School of Civil and Mechanical Engineering

Numerical Modelling of Subsea Cables and Pipelines

Ahmed Reda

**This thesis is presented for the Degree of Doctor of Philosophy
of
Curtin University**

August 2020

DECLARATION OF AUTHORSHIP

I, Ahmed Reda, declare that this thesis entitled "Numerical Modelling of Subsea Cables and Pipelines" and the work presented in it are my own. I confirm that:

- To the best of my knowledge and belief this thesis contains no material previously published by any other person except where due acknowledgment has been made.

- This thesis contains no material which has been accepted for the award of any other degree or diploma in any university.

- Where I have consulted the published work of others, this is always clearly attributed.

- Where I have quoted from the work of others, the source is always given. Except for such quotations, this thesis is entirely my own work.

- I have acknowledged all main sources of help.

- Where the thesis is based on work done by myself jointly with others, I have made clear exactly what was done by others and what I have contributed myself.

Signed:

_____

Date:
                                28/10/2020
_____

DEDICATION

To the loving memory of my father.

To my beloved wife, Nashwa, who endured my absences and supported my passion for this research.

To our kids, Maya, Yaseen and Yousef who make our life beautiful.

To all those who have contributed to this thesis.

ABSTRACT

There is currently a large demand for the global installation of subsea cables. Subsea cables play an integral role in the harnessing of offshore hydrocarbon resources and wind farm energy, among many other uses. Pipelines are used to transport oil and gas from offshore production platforms to export lines, while submarine power cables transmit generated power to consumers inland. Needless to say, an inadequate pipeline or cable design can lead to disastrous environmental damage and significant economic loss. To prevent such catastrophic outcomes, subsea cable designs must take into account many crucial aspects of the lifecycle of pipelines and cables.

This thesis identifies five critical design and performance issues associated with pipelines and cables and provides guidelines to improve the design process. This is achieved through cable testing programs and finite element analyses using the software package ABAQUS.

As part of this thesis, the compression limit of high voltage alternating current (HVAC) cables was investigated. This is because the behaviour and consequence of axial compression loads on HVAC cables has not received adequate attention from the offshore cable industry. Cable manufacturers often only specify that HVAC cables should not be subjected to any compressive forces which not only restricts design parameters but also causes installation to be both impractical and prohibitively expensive. In reality, the development of compressive forces in flexible submarine cables is inevitable and was confirmed as such in this thesis by performing a dynamic analysis of the lay operation using the software OrcaFlex. This thesis presents a testing arrangement and inspection method to determine the axial compression limit of submarine cables under both axial compression and bending moment conditions. The testing results were synthesized into an empirical method to determine the compression limit of a given cable.

As the majority of failures in submarine cables can be attributed to cable field joints, the second area of research involved the development of a testing scheme to improve cable joint integrity. Current standards suggest the use of sea trials to determine the integrity of cable field joints however, sea trials are often excessively expensive and time consuming.

Additionally, the high failure rate suggests that these standards are also grossly inadequate. This thesis presents a set of standardised onshore testing regimes that improve both the reliability and affordability of cable jointing for in-line and Omega joints. The proposed testing arrangement offers an alternative to subsea immersion testing for subsea cable joints and offshore deployment simulations.

Another area in which current subsea design codes are severely lacking is in relation to subsea crossings. This is in spite of the fact that the deterioration of subsea cable, umbilical and pipeline crossings occurs frequently due to movement between crossing components. In particular, when the crossed pipeline is used as a support, the contact load and lateral movement of the crossing components under severe environmental loading conditions can compromise the integrity of the field joint coating. The third area of research examined in this thesis was the potential of employing articulated paddings as a means to obviate the need for extra supports to protect a crossed asset. The results presented herein confirm the benefits of the articulated padding technique and provide a basis for the development of future industry standards incorporating articulated padding designs.

Another important topic investigated as part of this thesis was the pipeline walking and anchoring considerations in the presence of steel catenary riser (SCR) motion and inclined seabeds. Steel catenary risers are becoming increasingly common in many deep-water field developments however, the effective tension in the SCR at the touchdown point on the seabed can contribute to axial walking of the pipeline connected to the SCR. The contribution of the SCR to pipeline axial walking was examined through rigorous finite element analyses using ABAQUS. The results herein show pipeline walking due to SCR bottom tension as the dominant walking mechanism when compared to the effects of thermal transients and seabed slopes. Based on the results, it was recommended that an anchor be installed towards the pipeline end termination (PLET) side away from the SCR transition point in the case of a short pipeline where lateral buckling does not occur. Furthermore, it was shown that there may be conflicting requirements between the anchor loads imposed by the SCR and the pipeline operating loads and that the anchor location has a significant impact on the load imposed on the anchor. Fatigue loading on the SCR anchors due to pipeline start-up and shut-down events and SCR tension variations, must all be evaluated during the anchoring system design. A roadmap to determine the

requirements for anchoring a short pipeline connected to a SCR in the absence of lateral buckling is presented herein.

The final topic investigated in this thesis was the pipeline slug flow dynamic load characterization. It is known that the multiphase slug flow inside oil and gas pipelines can give rise to fluctuating forces within the pipeline. In the unsupported span of a pipeline, these fluctuating forces induce vibrations and cyclic stress that can cause fatigue. The effect of pipeline slug flow was investigated by modelling it as a moving force along a pipeline span, with emphasis on the effect of the span out-of-straightness which induces centrifugal forces. A non-dimensional centrifugal force parameter was developed to assess whether the combination of out-of-straightness and slug velocity has a tangible influence on the pipeline vibration. The results showed that for a non-dimensional centrifugal force parameter of less than 10%, the out-of-straightness has an insignificant effect. The analysis also showed that the stress pattern over the pipeline span is relatively complex, even when the non-dimensional centrifugal force parameter is less than 10%. This indicates that if detailed stress values are required along the pipeline, a finite element analysis should be conducted.

All previous work undertaken in the area of pipeline vibrations under the passage of slug flow treat the slug as a moving force where the inertia of the slug is disregarded. It is widely accepted however, that when the mass of the slug is not significantly smaller than the pipe span mass, this simplified model will not completely capture the dynamic effects of the system. Quantification of the mass ratios where these effects become significant has not been previously studied and is developed in this thesis. Lastly, the thesis provides guidelines regarding when the moving mass model or the moving force model should be considered and at what slug speed a dynamic analysis becomes necessary.

ACKNOWLEDGMENTS

PUBLISHED PAPERS ENCLOSED AS CHAPTERS OF THE THESIS

Journal articles

1) Reda, Ahmed, Gareth L. Forbes, Faisal Al-Mahmoud, Ian M. Howard, Kristoffer K. McKee, and Ibrahim A. Sultan. "Compression limit state of HVAC submarine cables." *Applied Ocean Research* 56 (2016): 12-34.

2) Reda, Ahmed, Ali Mothana Saleh Al-Yafei, Ian M. Howard, Gareth L. Forbes, and Kristoffer K. McKee. "Simulated in-line deployment of offshore rigid field joint–A testing concept." Ocean Engineering 112 (2016): 153-172.

3) Reda, Ahmed, Ahmed Abu-Siada, Ian M. Howard, and Kristoffer K. McKee. "A testing platform for subsea power cable deployment." Engineering Failure Analysis 96 (2019): 142-157.

4) Reda, Ahmed, Ian M. Howard, Gareth L. Forbes, Ibrahim A. Sultan, and Kristoffer K. McKee. "Design and installation of subsea cable, pipeline and umbilical crossing interfaces." Engineering Failure Analysis 81 (2017): 193-203.

5) Reda, Ahmed, Ibrahim A. Sultan, Ian M. Howard, Gareth L. Forbes, and Kristoffer K. McKee. "Pipeline walking and anchoring considerations in the presence of riser motion and inclined seabed." International Journal of Pressure Vessels and Piping 162 (2018): 71-85.

6) Reda, Ahmed, Kristoffer K. McKee, Ian M. Howard, and Ibrahim A. Sultan. "When is a subsea anchor required for a short pipeline/SCR system?" International Journal of Pressure Vessels and Piping 171 (2019):278-298.

7) Reda, Ahmed, Gareth L. Forbes, Ibrahim A. Sultan, and Ian M. Howard. "Pipeline slug flow dynamic load characterization." Journal of Offshore Mechanics and Arctic Engineering 141, no. 1 (2019): 011701.

Conference Proceedings

8) Reda, Ahmed, Gareth Forbes, Kristoffer McKee, and Ian Howard. "Vibration of a curved subsea pipeline due to internal slug flow." In Proceedings of the 43rd International Congress on Noise Control Engineering. Australian Acoustical Society, 2014.

Table of Contents

List of Figures

List of Tables

1 Chapter-1

1.1 INTRODUCTION

Harnessing offshore hydrocarbon resources and wind farm energy requires the construction and installation of critical subsea assets such as pipelines and cables among other apparatus. Pipelines transport oil and gas from offshore production platforms or subsea wellheads to export lines, while submarine power cables transmit the power generated by the wind farms to consumers inland. Inadequately designed pipelines or cables can lead to both disastrous environmental damage and significant economic losses. To guard against these adverse outcomes, pipeline and cable designs must account for many critical aspects before installation and during the lifespan of the pipelines and cables. This thesis identifies five critical design and performance issues associated with pipelines and cables. The thesis provides guidelines to improve the process by which cables are tested using finite element analysis and the software package ABAQUS. Additionally, The thesis highlights the vital topics that are not by current industry standards and practices and develop new testing methods for subsea cables.

The five main areas of research are listed below and will be discussed in further detail in the following chapters.

Topic 1: Compression limit of high voltage alternating current cables

Topic 2: Development of a testing scheme to improve cable-joint integrity

Topic 3: Design and installation of subsea cable, pipeline and umbilical crossing interfaces

Topic 4: Pipeline walking and anchoring considerations in the presence of riser

motion and inclined seabeds:

Topic 5: Pipeline slug flow dynamic load characterization.

As part of this thesis, the following experimental works were also undertaken:

1- Compression testing on subsea power cables:

This experimental work was carried out by conducting full scale bending as well as pure compression testing. The experiment was conducted in order to develop a new testing arrangement for determining axial compression limits of subsea cables. The output from this compression test was also used during the simulated in-line/Omega deployment of offshore rigid field joints as well as in the novel crossing design.

2- Simulated in-line/Omega deployment of offshore rigid field joint- A test concept:

These experiments were undertaken on full-scale cables to establish new testing arrangements for the subsea joints to increase the level of reliability of said joints. The simulated testing was performed on two subsea joint configurations: Omega and in-line joints. The proposed testing arrangements can be employed in industry to ensure that the subsea joints do not fail under the mechanical loads and stresses associated with installation.

3- Physical testing to qualify the new crossing concept:

A testing program was conducted on the articulated padding to ensure that it was fit for the intended surface. The following tests were conducted on the articulated padding:

1- Axial load test
2- Radial load test
3- Abrasion test

1.2 PROBLEM STATEMENT, MOTIVATION AND OBJECTIVES

Topic 1: Compression Limit of High Voltage alternating Current Cables:

Currently, there is a huge demand for the global installation of subsea cables. Often the installation takes place in a hostile environment and, in areas associated with strong surface currents, the cable might experience high compression loads at the touchdown point. As such, a specific test is required to understand the allowable compression limit of

the subsea cable in order to reduce the weather downtime of the installation vessel while ensuring that the integrity of the cable is not compromised.

Determining the compression limits of a subsea cable is not considered a standard type test. In fact, there are currently no accepted industry standards for determining compression limits in subsea power cables leading cable manufacturers to state that the cables are not allowed to be axially loaded at all during compression. This results in longer installation times and higher costs.

The industry does not provide any guidance regarding the compression that develops over time in the subsea cable nor the consequences of compression on the integrity of the cable. Consequently, industry standards and recommended practices are silent regarding test arrangements which can be used to determine the allowable axial compression level for a subsea cable.

Submarine cable crossings are a common feature in offshore hydrocarbon field development and the instances of them are increasing with development density. Cable crossings add costs to new submarine cable systems and should be obviated wherever possible but not at the expense of increasing cable length. This is because increasing cable length may (a) increase potential hazards along the cable route, (b) increase transmission losses and (c) increase cost.

It is often a requirement of the codes and standards to maintain a positive vertical separation between the crossing cable and the crossed assets. The common concept for a submarine cable crossing is to raise and support the new cable up and over the existing pipeline/cable/umbilical. The support is pre-installed on the seafloor and the new cable is laid over the support. Common support concepts include pre-cast concrete mattresses and sleepers as well as grout in-situ fabric formwork.

The positive vertical separation between the crossing subsea cable and crossed assets can also be achieved via the use of articulated padding as shown in Figure 1-1. The articulated padding is lightweight and installed around the cable which is comprised of two polyurethane half shells attached via corrosion resistance alloy banding. The entire length of the subsea cable is post-trenched, for the protection of the subsea cable, except at the crossing locations. As such, the subsea cable is required to be installed with low

3

touchdown tensions in order to enable the post-trenching operations and avoid free spans from high cable tension. A lower bottom tension can cause the cable to build loops or snake which could compromise the integrity of the sub-sea cable. The post-trenching contractor recommends a bottom tension ranging between 5 and 10 kN to reduce the possibility of free spans, to ease the post-burial operation and to reduce the stress induced in the cable during the post-burial operations. In the following example, a scenario of low-tension cable lay operation is described. Simulation of the dynamic motion during installation was performed using OrcaFlex software, 2014. The installation analysis starts, as shown in Figure 1-2, when the trailing bend restrictor is in the splash zone and ends when approximately 10 m of cable has been laid after the articulated padding, as in Figure 1-3.
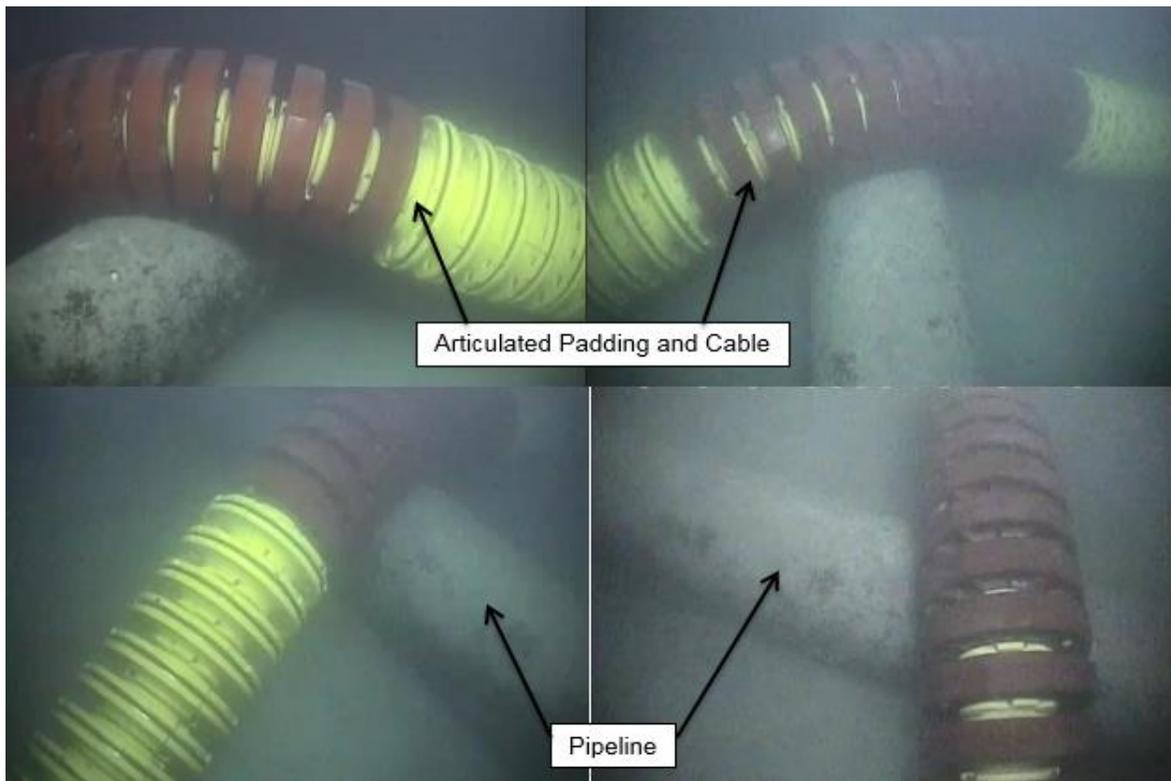
Figure 1-1: General arrangement of articulated padding crossing system.

During this dynamic analysis it was shown that the proposed articulated padding sections and associated displacement, when subject to the design wave and current environment associated with the location of the crossings, could impose additional residual tension in

4

the laid cable on the seabed as well as compression issues at the touchdown point as shown in Figure 1-3 and Figure 1-4. This is due , in part , to the heave and yaw motions of the installation vessel as it lays the cable.
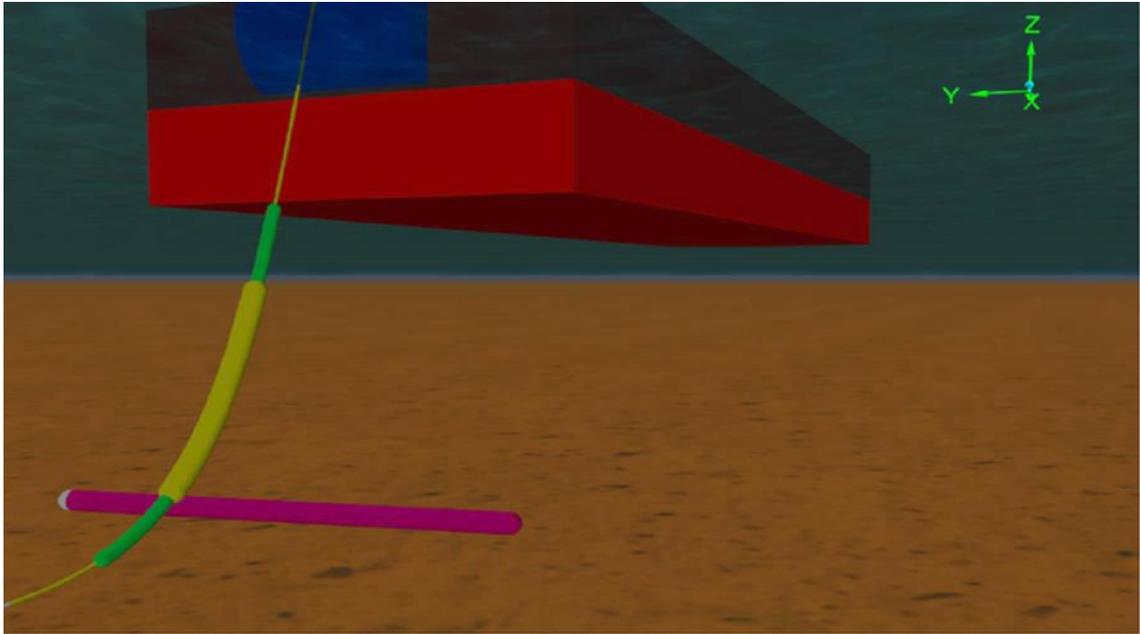
Figure 1-2: Illustration for starting position of articulated padding installation analysis.
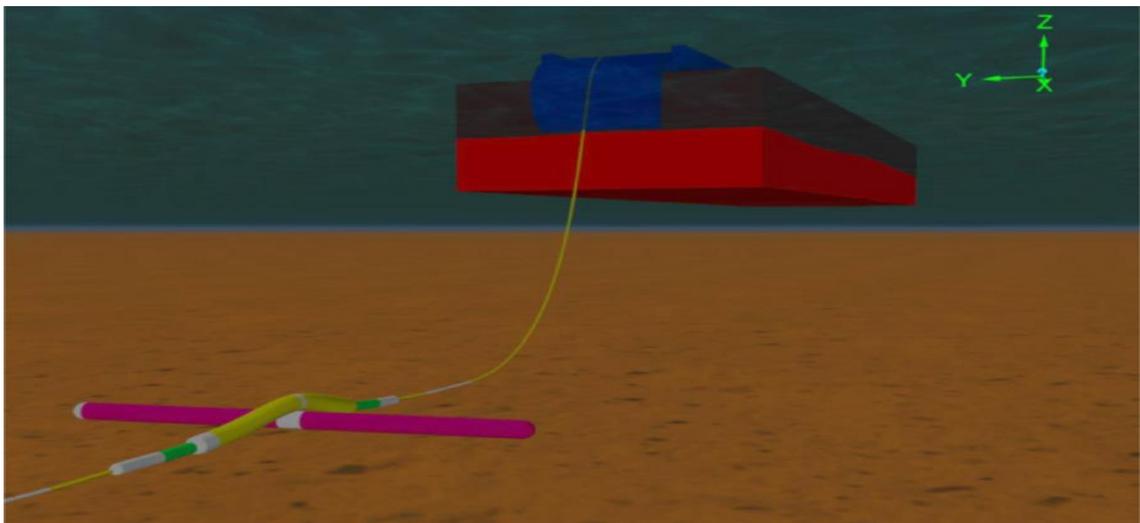
Figure 1-3: Illustration for end position of articulated padding installation analysis.
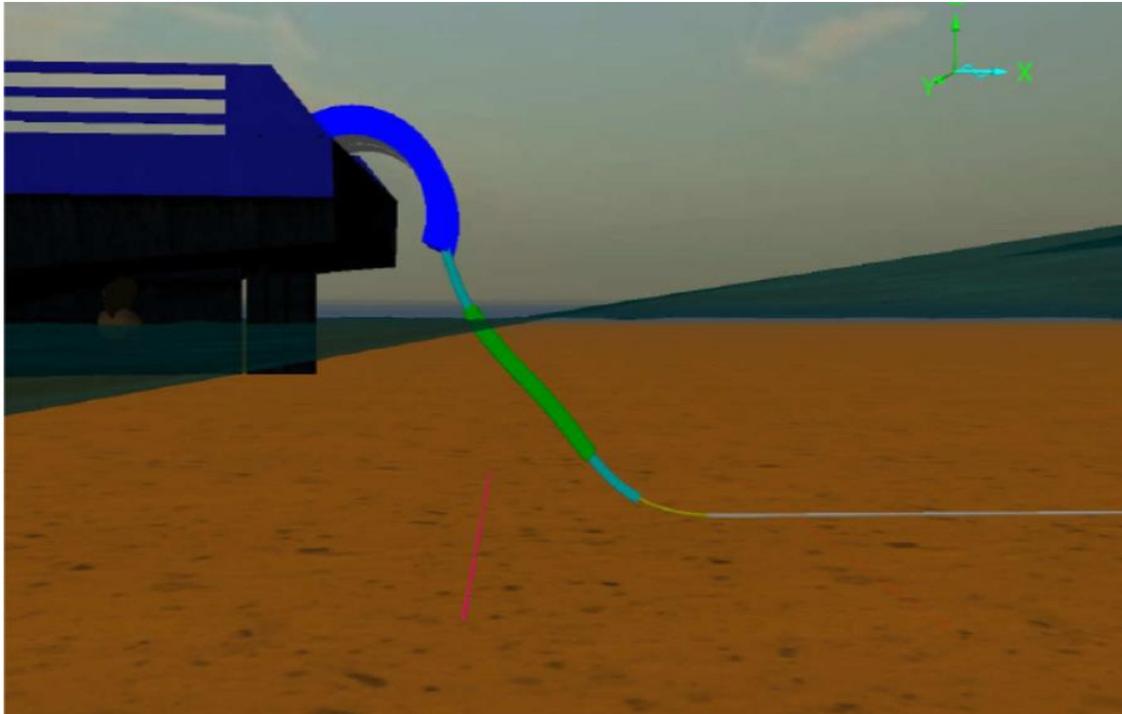
Figure 1-4: Rendered side view at maximum compression peak.

Additionally, a negative heave displacement of the vessel was shown to cause compressive loads within the cable which can result in a kink effect. This is often followed by steel armour wires lifting in the form of a "bird-caging" effect which leads to the displacement of the armour wires and consequently weakens the cable strength. Figure 1-6 shows an example of a bird-cage failure of a flexible pipe (Bectarte et al, 2004).

In addition to the vessel motion, the submerged weight of the articulated padding introduces an increase in the bottom tension at the touchdown point even in a static equilibrium condition. An example can be visualised in Figure 1-7 and Figure 1-8. A green, bare cable and an orange cable with the articulated padding attached to it are visible. Both cables have the same length and are constrained on top of the chute. In this example, a 1000 m length of cable has been laid in front of the articulated padding with an as-laid (residual) tension of 5 kN for both cases.
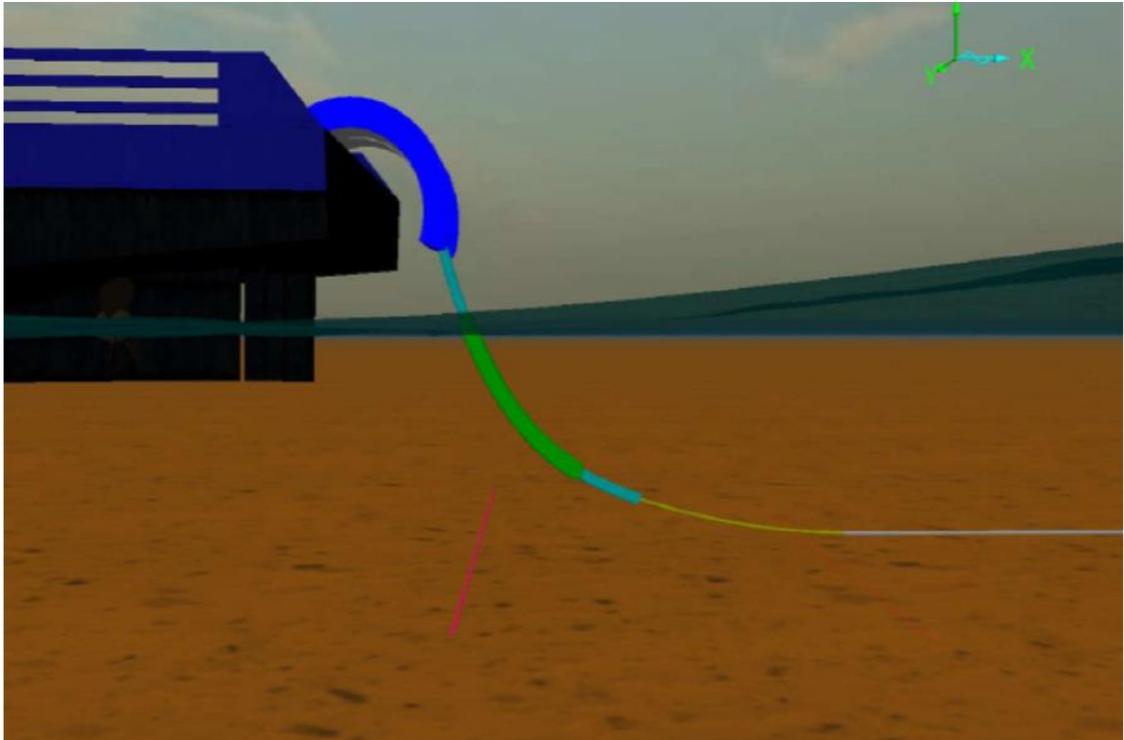
Figure 1-5: Rendered side view at maximum tension peak.

Figure 1-6: Bird-cage failure of flexible pipe (Bectarte et al, 2004).
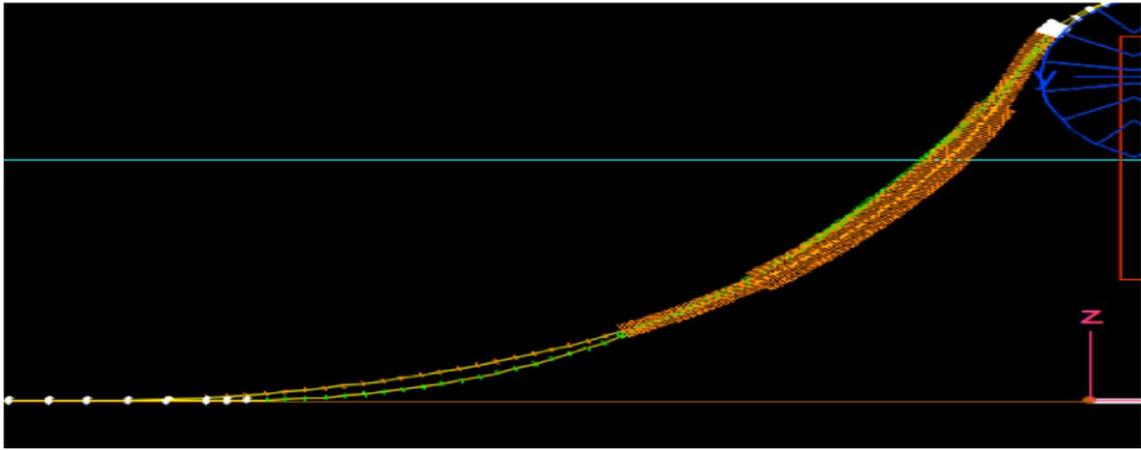
Figure 1-7: Bottom tension comparison – side view (first white node is touchdown point).
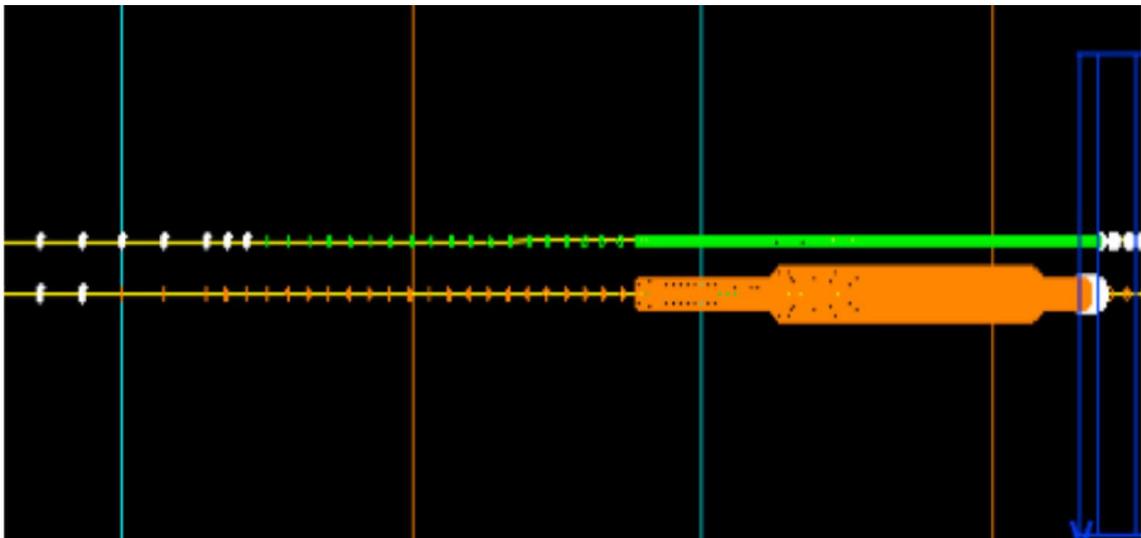
Figure 1-8: Bottom tension comparison – top view (first white node is touchdown point).

Table 1-1 illustrates the effect of the articulated padding on the residual bottom tension in the static equilibrium condition case. The analysis indicates a significant increase in top tension due to the articulated padding and a bottom tension value that is twice as high as that of the bare cable. It also takes about 300 m after the articulated padding is laid before the tension in the cable is reduced to 5 kN. The mechanics of the increased residual tension

can be explained by a simple model as shown in Figure 1-9. This figure shows the influence of the submerged weight of the articulated padding (F_{AB}) on the bottom tension (F_{bottom}). It can be seen that the weight of the cable combined with the weight of the articulated padding generates tension.

Table 1-1: Residual Bottom Tension

Item	Bare Cable	Cable + articulated padding
Residual bottom tension	4.9 kN	10.0 kN
Layback distance from chute	19.9 m	24.2 m

It can be seen from the force diagram in Figure 1-9, that horizontal equilibrium requires that F_{bottom}= Fh.

1-1

Also, in the vertical direction, this gives

$F_v = F_{AB} + \text{CABLE WEIGHT}$.

1-2

This gives

Fh= Fv· tan(θ),

1-3

and hence it can be seen that the bottom force is given by

$F_{bottom} = F_v \cdot \tan(\theta) = (F_{AB} + \text{CABLE WEIGHT}) \cdot \tan(\theta)$

1-4

Therefore, an increase in padding weight, F_{AB}, causes a direct increase in the bottom tension, F_{bottom}.

The location of the crossing in this example was also associated with strong currents with 1-year return surface currents reaching 3.5 knots. The result from the dynamic installation analysis highlighted several potential issues with the articulated padding for some water depths and sea-states. Furthermore, the dynamic installation analysis indicated that the

bare cable experiences high compression loads at the touchdown point. This was the result of applying low tension and movement of the installation vessel under the hydrodynamic loads. The resulting axial compression was consequentially outside the allowable design criteria of typical submarine cables.
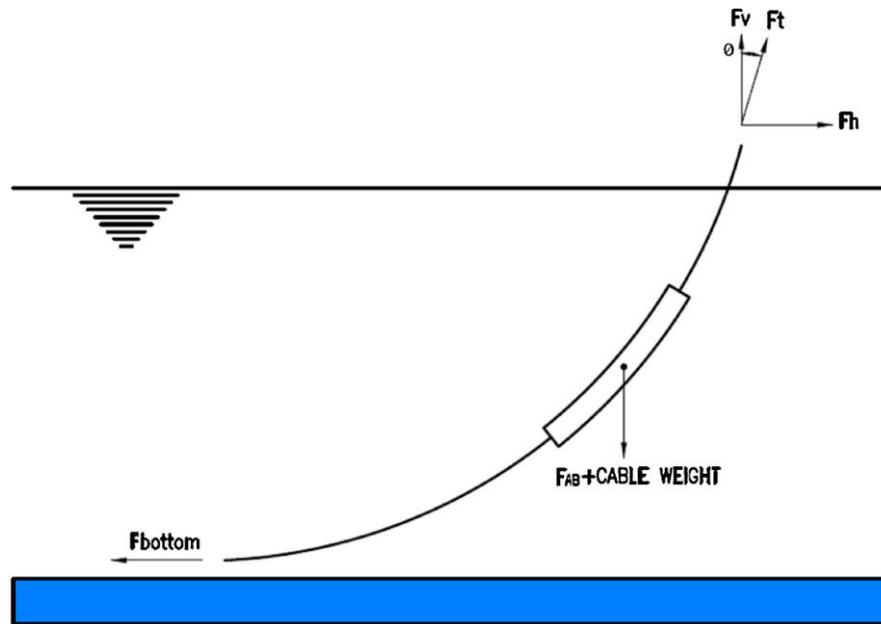
Figure 1-9: Free body diagram of the cable with articulated padding at the middle of the catenary.

A further increase in the top tension would resolve the compression issue, but would introduce even higher levels of residual tension which would adversely affects the post-trenching operation. Alteration of several of the parameters influencing the lay tension and/or compression was thus considered to find an optimal configuration. For instance, the possibility of increasing the weight of the articulated padding to alleviate the compression values at the touchdown point was considered. However, this option requires a corresponding increase in the top tension. Many other options have been investigated by the thesis such as the use of reduced current profiles based on the seasonal probability of occurrence. The directionality of the current and waves was also considered rather than assuming that the current and waves act in the same direction. However, the analysis of compression values at the touchdown point was beyond the allowable design criteria for typical submarine cables.

The compression limit is also required as an input for Chapters 4, 5 and 6. This is to ensure that the integrity of the cable is not compromised under the compressive loads.

The objective of this work is to:

1. Establish a standardised testing scheme which can be incorporated in the industry standards to determine the allowable compression limit of subsea cables and umbilicals. The test programme should include both pure axial compression tests and bended compression tests, in order to mimic the installation of the cable.

2. Provide guidance for the acceptance criteria of the compression loads on submarine cables during installation. These acceptance criteria could be used in the absence of project specific data.

3. Provide sufficient data which can be used by others to achieve the best possible outcome for cable design and installation and to understand the compression limit state of a subsea cable.

4. Use the results presented here and from future tests to develop analytical models to determine the allowable axial compression limit. The analytical model can be calibrated by gathering results from many tested umbilicals and cables.

5. Use the outcomes of the compression tests in other areas of research related to subsea cables such as that seen in Chapters 4, 5 and 6.

Topic 2: Development of a Testing Scheme to Improve Cable-Joint Integrity:

Failure of submarine power cables have been attributed to cable field joints in 18% of all cases. This high failure rate at the jointing location indicates that the current accepted testing of these joints is inadequate. The failure mode of these joints is believed to be entirely due to water ingress at the field joint location. Field joints are unavoidable and must be employed when joining insufficient factory-made cable lengths, during cable repair, or when the cable installation process must be abandoned due to rough weather or other unplanned events.

Current design practices for subsea cable field joints recommend offshore simulations or trials to demonstrate the long-term performance of the joint under the expected mechanical loads during cable installation and to demonstrate whether the planned field jointing practice is satisfactory. However, offshore simulations are costly and therefore a set of standardized onshore testing schemes would be an advantageous alternative.

Current design guidance for cable field joints also recommend sea trials to determine if the proposed field jointing technique is acceptable. However, like the offshore simulations, sea trials too, are often prohibitively expensive. For these reasons, it is clear that a set of standardised onshore testing regimes which improves both the reliability and affordability of these tests would be advantageous.

The deployment of a rigid joint on the seabed is probably the trickiest and most complicated operation of cable installation. This is in part due to the fact that during the deployment operation the two jointed cables must be handled with the rigid joint. Neither over-bending nor over-tensioning must occur or the cable arrangement risks being stuck in other structures on-board (Worzyk, 2009).

Recently, a type test for an offshore rigid field joint (OFJ) was conducted three times. In the first and the second type tests, the OFJ passed all the mechanical and electrical tests successfully however, the OFJ did not meet the criteria defined in CIGRÉ TB490 (2012) for the radial water penetration (RWP) test. It was therefore decided to undertake a trial laying test of the OFJ in addition to the third RWP test as required as part of the type test. It should be mentioned that after the investigations and using the results from type tests 1 and 2, it was concluded that the OFJ during the two type tests were not dismantled carefully enough. Moreover, stresses were introduced to the pre-moulded joint during the release from the compound filling before conducting the RWP tests. The OFJ failed the two RWP tests due to one of the pre-moulded joints containing incomplete fillings at two locations of the copper housings. During the third test, the OFJ was dismantled cautiously and it was ensured that no additional stresses were introduced to the pre-moulded joint during the release from the compound filling before the execution of the RWP test. Additionally, it was ensured that adequate measures were implemented to ensure that the copper housing of the pre-moulded joint was filled completely.

Water penetration tests can be conducted to measure the ability of the rigid joint to resist water penetration up to the maximum water depth of the submarine joint. Water tightness is a crucial feature for a high-quality power cable system. The International Council on Large Electric Systems also known as Conseil International des Grands Réseaux Électriques or CIGRÉ outlines in their TB490 (2012) recommendations that acutal sea trials be conducted to ensure the quality of the repaired joints.

The loading conditions during the deployment of the rigid joint on the seabed are also critical. Previously, many joint failures occurred in the first few days following installation or during early operation. By controlling loading conditions during the deployment operation, the joints do not have to be regarded as a weak joint anymore. Due to time constraints as well as logistical issues, it was decided to replace the sea trial tests with simulated on-land deployment. These were used to verify the mechanical integrity of the OFJ and to identify OFJ weak points under deployment conditions.

The repeated failure in the type test proved that inadequate joint design and poor joint assembly work could lead to joint failure. It must be taken into consideration that the joint was made in a well-controlled environment and would be taken offshore on a vessel in less than ideal conditions. It is important to ensure that quality control procedures for the jointing procedure are well established and account for the offshore field jointing process.

This thesis presents a new testing arrangement and testing procedure which can be used to simulate the deployment of inline rigid offshore field joints which is critical to the integrity of the OFJ. Particular interest is paid to the weak point of the OFJ such as the plumbing point between the power cable metallic sheath and the copper tube of the pre-moulded joint as shown in Figure 1-10.

The onshore testing scheme presented in this thesis is a viable alternative to sea trials. The proposed testing arrangement can be employed to verify the design of the offshore field joint and to prove the functionality of the field joint under installation loads.

The thesis focuses only on the stiff joints which have a rigid outer casing. This rigid joint serves as a connection point for the armouring wires of each cable end.

Figure 1-10: Plumbing area after in-line test and water penetration test.

Topic 3: Design and Installation of Subsea Cable, Pipeline and Umbilical Crossing Interfaces:

As mentioned in Subchapter 1.2, Topic 1, submarine pipeline, umbilical and cable crossings are a common feature of offshore hydrocarbon field development. For a variety of reasons mentioned earlier, these crossings should be obviated wherever possible, but not at the expense of increasing the cable length, as doing so poses its own problems (see Subchapter 1.2, Topic 2 for further details).

The selection of the crossing method is normally based on technical feasibility, cost, safety and environment. The possible crossing methods are as follows:

1. Lower the existing pipeline/umbilical/cable prior to crossing. This will enable the new cable to cross flush with the seafloor or trenched on a pre-defined trench profile.

2. Raise the new crossing pipeline/umbilical/cable above the existing pipeline/umbilical/cable using supports as shown in Figure 1-11. This will enable the new pipeline/umbilical/cable to be installed without interfering with the existing crossed pipeline. The separation between the crossed pipeline and the crossing pipeline/umbilical/cable will depend on the settlement of the support over time as shown in Figure 1-11. Prediction of such settlement is uncertain and typically requires geotechnical sampling for design. Any intervention required to increase the separation during the operation phase is costly and difficult.
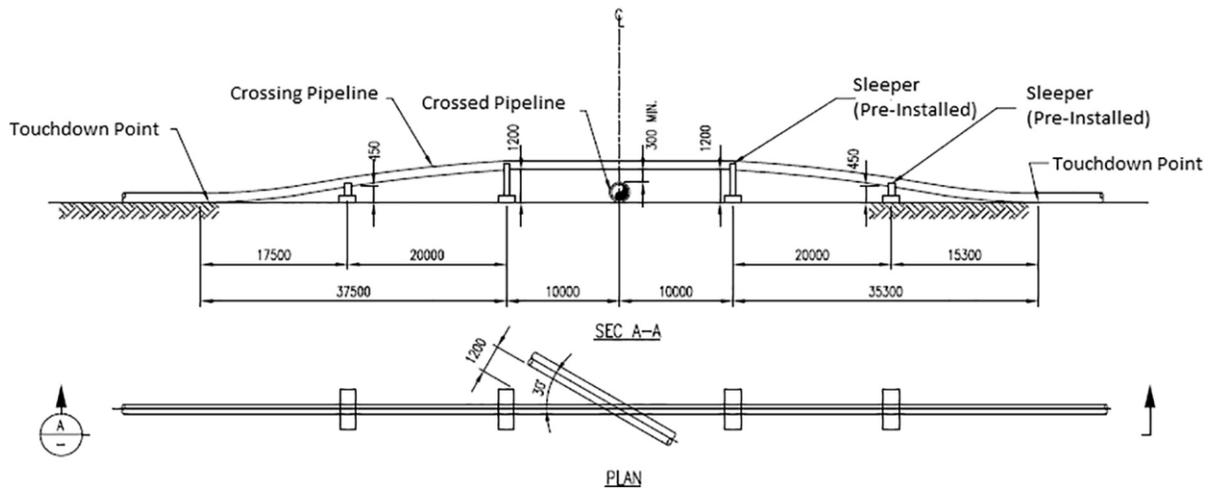
Figure 1-11: Discrete supports (Reda et al., 2017).

3. Using the existing crossed pipeline as a support provided that:

- The loads imposed on the crossed pipeline are within the allowable limits.

- The crossing cable does not bear directly on the crossed pipeline (i.e. the required vertical separation between the crossed and crossing assets is maintained).

- The integrity of the coating of the crossed and crossing assets are not impaired.

- The cathodic protection of the crossed and crossing assets are not jeopardised.

- Thermal expansion induced by the operating pressure and temperature can be accommodated by the crossed pipeline without compromising its integrity.

Figure 1-12 and Figure 1-13 show examples of crossing designs where the existing pipelines are utilised as a support. In Figure 1-12, the crossing umbilical is laid on the crossed pipeline. The required vertical separation between the crossing umbilical and the crossed pipeline is achieved by the use of a concrete mattress. A portion of the weight of the new umbilical and the mattress is supported by the crossed pipeline. Figure 1-13 shows a rock cover placed on the existing crossed pipeline with the new pipeline laid on the rock cover. Some designs may subsequently add rock covers over the crossing pipeline as well. The design of this top rock cover reflects the requirements of secondary stabilisation of the crossing pipeline, upheaval buckling hold down and protection against

15

trawl boards or dragging anchors. The design of the rock cover will account for the stability of the rock as well as the potential settlement of the rock.
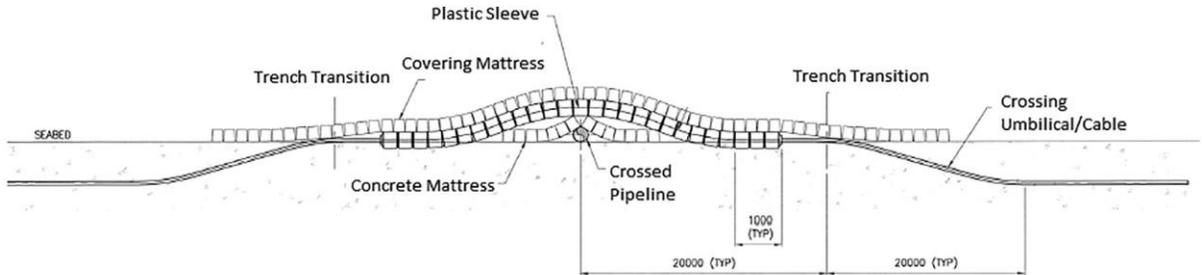
Figure 1-12: Using the crossed pipeline as a support (Reda et al., 2017).

Current subsea design codes are not explicit in the criteria for subsea crossings, beyond recommending pipeline separation distances. Additionally, an industry accepted standard for the design and construction of cable crossings does not currently exist when the crossed pipeline is used as a support.

The work within this thesis describes two case studies that employ the novel use of articulated padding applied to the crossing member, the first of which uses the crossed pipeline as a support while the second has the articulated padding resting on traditional grout-bag supports. This thesis highlights gaps in the current industry practice guidelines in the field of subsea pipelines and cables.

A recent failure which occurred to the field joint coating of crossed pipelines, and the subsequent underwater repair, is also described, thus demonstrating the critical importance of establishing industry standards and practices regarding the above.

Topic 4: Pipeline walking and anchoring considerations in the presence of riser motion and inclined seabeds

The connection of floating production vessels to subsea pipelines requires careful consideration of the stresses placed on the steel catenary riser (SCR), subsea spool and pipeline end termination (PLET). Due to vessel motion, environmental conditions, flow

conditions and pipeline temperature gradients during start-up, shut-down and operation, the forces on all sections of the subsea pipeline system may deviate from their static configurations.
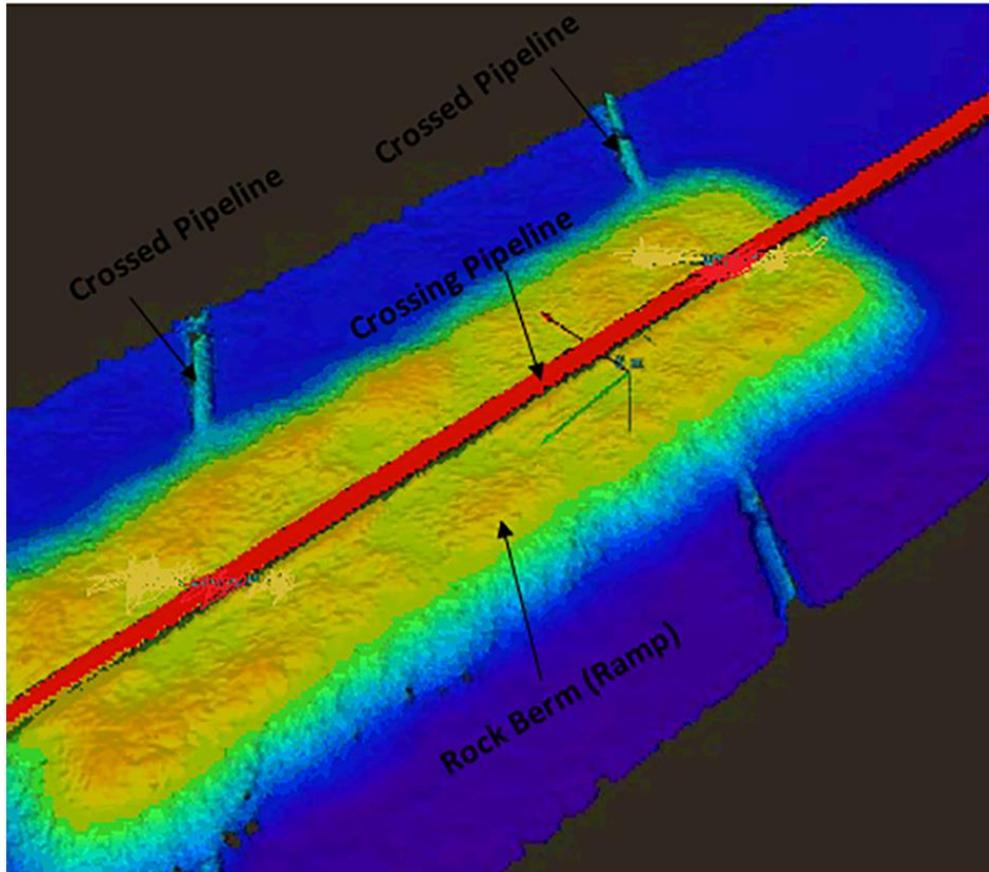
Figure 1-13: Rock dump concept.

Steel Catenary Risers (SCRs) are becoming an increasingly attractive option for many deep-water field developments. They are typically used to transport fluids between floating production vessels and pipelines. Other common uses include the transport of fluids from a subsea production system to a floating production vessel or the transport of gas or water for reinjection into the producing reservoirs. The floating production vessel on which the SCR is supported will be subject to motion caused by environmental loads and influenced by the mooring system and other risers. Horizontal movement of the vessel causes changes in the riser catenary configuration in near, mean, and far positions. On the seabed, the riser is connected to a pipeline that extends for some distance from the riser

17

touchdown point to its tie-in point on a pipeline or other facility. Effective tension at the touchdown point is necessary to maintain the riser configuration however it may cause the pipeline to walk in the axial direction. The development of axial walking is in part due to the pull experienced by the pipeline at the touchdown point from the SCR tension.

Pipeline risers, PLETs and spools all have design limits that must not be exceeded in order to ensure the integrity of the pipeline/SCR system. The operational and dynamic loads on the pipeline/SCR system cause expansion and contraction of the pipeline at the riser and free end locations, and these too, need to be kept within the pipeline system design limits.

The most appropriate method to account for the pipeline system movement is to either ensure the pipeline has sufficiently long run-out, to accommodate the pipeline system loading, or to provide anchoring locations for the pipeline section.

The failures that occurred at two pipelines located in Canada and the North Sea respectively (Knouk, 1998; Tornes et al, 2000) were both attributed to axial walking. Expansion towards the SCR should be kept within the allowable maximum axial displacement specified by the SCR design. Excessive slippage of the touchdown point will result in reducing the static tension and changing the curvature in the sag-bend region. This can cause a non-recoverable condition as an effective tension is required to maintain the shape of the catenary.

Pipeline walking and excessive expansion towards the SCR could lead to SCR failure. Conversely excessive SCR tension could pull the spool and consequently overstress it. Excessive SCR tension in the horizontal direction can change the field architecture and introduce lateral imperfections in the pipeline and a lateral buckle can consequently be triggered in the pipeline.

As the host platform moves, the SCR touchdown point shifts with the motion of the floating production vessel and is subject to the influence of environmental factors. At the touchdown zone, the pipe is subjected to fluctuations in curvature. This will therefore give rise to the sensitivity of SCRs to fatigue damage.

The current literature is silent regarding a roadmap to determine requirements for anchoring a short pipeline connected to a SCR. Additionally, there currently exists no criteria by which one can determine the optimal location for an anchor.

This thesis provides a guideline for anchoring a short pipeline connected to a SCR. Furthermore, the thesis provides guidance in regards to the selection of the optimum location for the hold-back anchors to ensure pipeline walking does not compromise the integrity of neither the SCR nor the pipeline system.

The thesis provides insight into the driving mechanisms behind pipeline design when connected to a SCR. The factors considered which could result in variations of the mean position of the touchdown point are 1) pipeline expansion combined with the SCR bottom tension during different load cases, 2) thermal transience due to cyclical heat-up and cool-down, and 3) seabed gradients along the pipeline route.

This research intends to fill the gaps in the literature regarding interfaces between the pipeline and the SCR. Additionally, The thesis presents the criteria and design approach that must be considered when determining the requirements for the hold-back anchors to successfully mitigate jeopardising the integrity of the SCR as well as the tie-in spool. The criteria and requirements for anchoring are valid for the combined conditions of a short pipeline, route bend and no lateral buckling.

The thesis explains the mechanics of pipeline expansion and describe the development of the analytical solution used to validate the results from the finite element analysis. The potential methods available to anchor the pipeline and limit the axial feed-in towards the SCR are also discussed.

Topic 5: Pipeline Slug Flow Dynamic Load Characterization.

Subsea oil and gas pipelines undergo vibration due to "slug" flow within the internal fluid contents of the pipeline. Flow of gas in pipelines is subject to thermodynamic conditions which produces two-phase bulks (i.e. slugs) within the axial pipeline flow. This slug flow is generated by the differences in density of the internal fluid. It acts as a traversing force along the length of the pipeline and causes structural vibrations of unsupported pipeline spans. The resulting vibration of the pipeline may cause high cycle fatigue due to these fluctuating forces.

The moving slugs apply a moving load on the free spanning pipe sections, which consequently undergo variable bending stresses and flexural deflections. Both the

maximum pipeline stress and deflection due to the slug flow loads, need to be understood in the design of pipeline spans. However, calculation of a moving mass on a free spanning pipeline is not trivial and the required mathematical model is burdensome for general pipeline design engineering.

Currently, there are no guidelines for when dynamic analysis is required and to what extent the analysis procedure must be performed for different slug flow conditions. To date, all work presented on the topic of pipeline vibrations under the passage of the slug flow, ignores the inertia of the moving slug.

Current literature specifies that the moving force model may be used when the mass of the moving load is small compared to that of the structure and vice versa for the moving mass model. However, the term "small" has not yet been given a quantitative definition.

Previous modelling of a moving slug flow in a pipeline has generally been presented for straight (non-curved) spans (Reda et al., 2011; Copper et al., 2009). As unsupported pipeline spans are often curved, understanding the impact this curvature has on the traversing fluid load is important. The inclusion of the pipeline curvature introduces centrifugal forces and produces additional vertical and axial forces in the pipeline that vary when the slug traverses the unsupported pipe span. This variation in the force, produced by the moving slug across a curved span, changes the dynamic motion and thus the stress within the pipeline during the slug motion.

This thesis investigates the limitation of each of the aforementioned models and attempts to present a guideline regarding the applicability of both the concentrated moving mass and the concentrated moving force models. This is in an effort to determine when it is appropriate to simplify the problem of a pipeline spanning as a concentrated moving force, or indeed under what conditions a dynamic analysis may not even be required. The thesis sets out to identify when the inertia of the load is important and needs to be taken into account in the analysis.

Furthermore, this thesis presents a finite element method to investigate the effect pipeline curvature has on the slug flow induced forces, resultant vibrations and possible fatigue damage to the pipeline structure. Additionally, The thesis presents a technique for using

commercial finite element packages for analysing the dynamic response of curved beams to time variant moving loads.

This thesis goes on to address buckle mitigation measures of local vertical out-of-straightness using a sleeper underneath the laid pipeline. The obstacle placed under the pipeline is usually called a sleeper and is sometimes made from a section of pipe, the diameter of which is normally in the range of 0.5m to 1.2 m. As the height of the sleeper increases, the probability of a lateral buckle forming also increases, as does the length of unsupported span along the pipeline on either side of the sleeper. A pipeline laid over a sleeper acting as a lateral buckling initiator can be seen in Figure 1-14 .
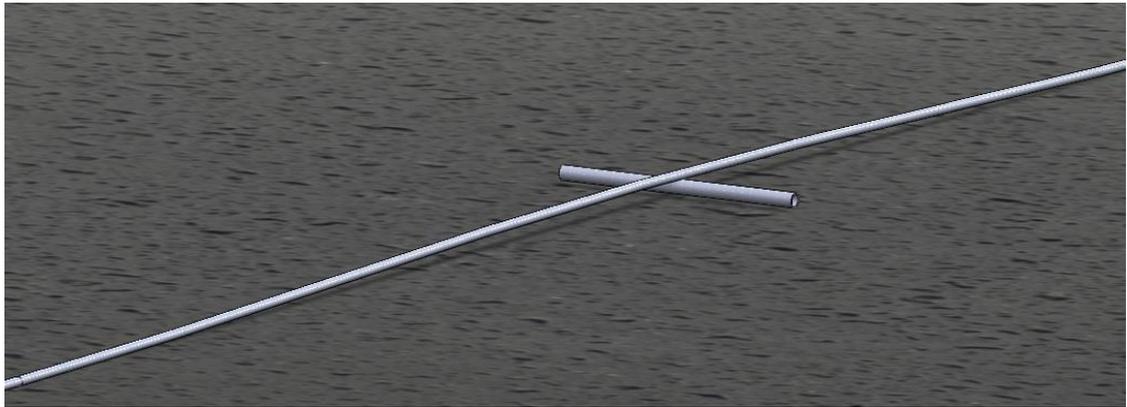
Figure 1-14: Schematic diagram of a pipeline over a sleeper type buckle initiator

The work in this thesis will present the modelling of an unsupported pipeline span length under slug flow conditions which can lead to cyclic fatigue. The thesis will highlight the effect of the span vertical out-of-straightness due to the sleeper, as well as show when this vertical out-of-straightness has a significant influence.

1.3 GLOSSARY OF TERMS

The following terms are used in this thesis and are defined as follows:

- **<u>Bottom tension:</u>**
   Tension in the cable at the touchdown point.

- **Departure angle:**

  This is the angle between the horizontal plane and the angle of the cable during lay operations. Refer to Figure 1-15.
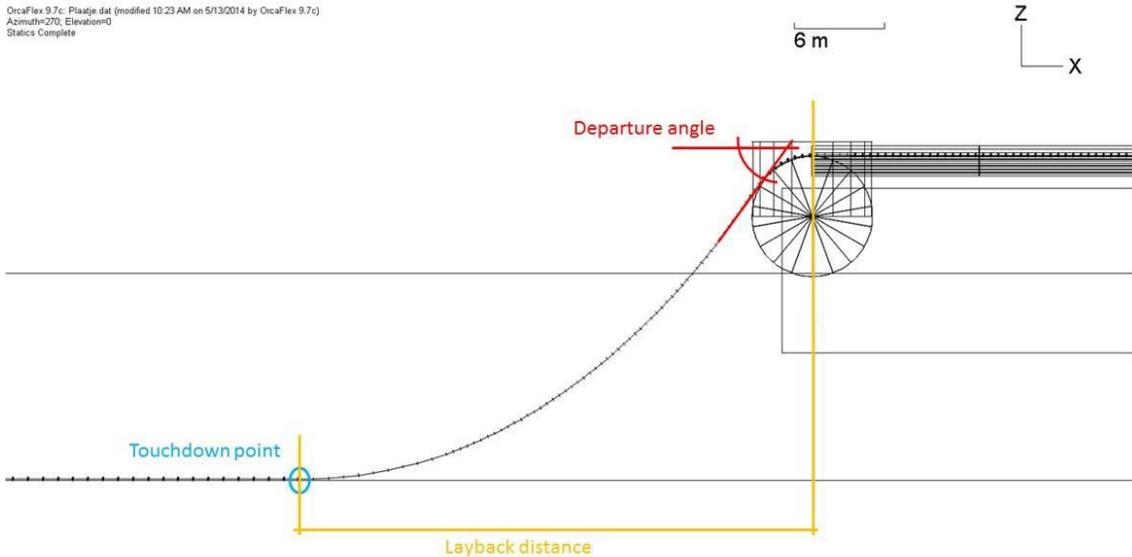
Figure 1-15: Visual depiction of terms.

- **Catenary length:**

  The length of the cable from touchdown point up to the chute.

- **Critical Speed:** the speed of a force travelling across a simply supported beam at the first mode of vibration as obtained by Equation (1-5):

$$u_{cr} = \frac{\pi}{L}\left(\frac{EI}{\rho A}\right)^{1/2}$$

<div align="right">1-5</div>

- **Field joint:**

A joint made on board a cable laying vessel or barge, or in the beach area, between cable lengths which have been armoured. They are generally used to connect two delivery lengths offshore. The design principles of field joints are generally the same as for repair joints and are treated as such.

- **Layback distance:**

  The horizontal distance between the touchdown point of the cable and the location of the chute. The touchdown point of the cable is defined as the first point where the cable touches the seabed from the vessel. Refer to Figure 1-15.

- **Moving Force Model:**

  In this model, the mass of the moving load compared to the mass of the simply supported beam is small. Thus, the inertial effect of the moving load can be disregarded.

- **Moving Load:**

  Used to describe the collective moving force and moving mass models.

- **Moving Mass Model:**

  In this model, the mass of the moving load cannot be regarded as small when compared to the mass of the simply supported beam. Therefore, the inertial effect of the moving mass must be considered.

- **Minimum occurring bend radius:**

  The radius of the cable between the chute and the touchdown point.

- **Normalized Dynamic Load Factor (DLF) of Bending Moment:**

  The maximum possible dynamic bending moment response in relation to the static bending moment that would be produced by the same load at the center of the beam. The maximum bending moment does not necessarily occur at the mid-point of the span.

- **Normalized Dynamic Load Factor (DLF) of Displacement/Deflection:**

  The maximum possible dynamic displacement/deflection response in relation to the static displacement/deflection that would be produced by the same load at the centre of the beam. The maximum displacement/deflection more or less occurs at the mid-point of the span.

- **Speed Parameter/ Ratio:**

  This is a non-dimensional parameter defined as the ratio of the frequency of excitation of the moving load to the first mode of natural frequency of vibration of the simply supported beam. Mathematically, it can be expressed as per Equation (1-6):

  $$\alpha = \frac{u}{u_{cr}} = \frac{uL}{\pi} \left(\frac{\rho A}{EI} \right)^{1/2}$$

  <div align="right">1-6</div>

- **Steps:**

  The results are presented per step. Ten steps are chosen between the start of the operation (beginning of the articulated padding system at the chute) and the situation in which 10 meters of bare cable has been laid down behind the articulated padding system.

- **Radial water penetration test:**

  The test conducted to measure the ability of the rigid joint to resist water penetration up to the maximum water depth of the submarine joint. Water tightness is a crucial feature for a high-quality power cable system.

- **Repair joint:**

  A repair joint is a joint between cable lengths that have been armoured. They are generally used in repairing a damaged submarine cable or joining two delivery lengths offshore or in factory.

  In principle there is no difference between a field joint and repair joint.

  - **Top tension:**

  The tension in the cable section on board the vessel as calculated by OrcaFlex.

  - **Type test:**

  The test performed to qualify the design and the manufacturing of the cable system against the conditions of the intended application.

- **Vessel offset:**

  The distance the vessel has been displaced perpendicular to its heading to ensure the cable is laid within 1.5 m of the targeted position. Note that this offset is just an indication and that the actual value during installation depends on numerous factors.

1.4 OUTLINE OF THESIS

This thesis is composed of seven papers that have been published in peer-reviewed journals and one conference proceeding.

In Chapter 2, The thesis presents the literature review. In Chapters 3 to 7, the thesis presents the methodologies and main results of this body of work. While Chapter 11 comprises the discussion, outlook and recommendations for future work.

The published papers are attached as appendices.

2 Literature Review

2.1 COMPRESSION LIMIT STATE OF HVAC SUBMARINE CABLES

Submarine power cables are becoming increasingly common in offshore hydrocarbon field development. Submarine power cables have mechanical limitations regarding the loads experienced during their installation (Feld et al., 1995) and are not typically designed for negative axial tension (i.e. compression). Most submarine suppliers specify that the axial compression is limited to 0 kN in cables. This is due to the fact that submarine cables are flexible and therefore generating compressive loads through the cable cross-section is difficult. A compressive load applied axially onto the end of the cable will cause the cable to bend thereby relieving the compressive axial force.

To date, no work has been undertaken to understand the consequence of the short or long term application of axial compression loads on submarine cables. In a recent project, it proved difficult to completely eliminate compressive loads acting on subsea cables at the touchdown point due to the presence of the articulated padding that was used to achieve the positive vertical separation between the crossing subsea cable and crossed assets. Neither CIGRÉ (Conseil International des Grands Réseaux Électriques) TB490 (2012) nor Electra 171 (1997) discuss excessive compression as a failure mechanism for subsea cables nor recommend a test arrangement which could be used to determine the boundaries of the axial compression limit. The industry recommend practice DNV (Det Norske Veritas)-RP-J301 (2014) identified axial compression as a possible failure mechanism for subsea cables however, they too, did not give any recommendations for the allowable compression load nor recommend any test arrangement which could be used to determine the boundaries of the axial compression limit.

The IEEE (Institute of Electrical and Electronics Engineer) Standard 1120 (2004) emphasise that caution must be exercised to ensure that the compression due to water pressure is accommodated. Nevertheless, it does not specify any recommendations regarding the compression limit. Subsea cable umbilicals and flexible pipes can all be

treated as composite, with helical armouring layers and polymer sealing layers as the main components. This results in cross-sections with low bending stiffness and high axial tensile stiffness. The ISO (International Standards Organization)-13628-5 (2009) highlights that for subsea umbilicals equipped with fibre optics, excessive compression can result in increased fibre optic attenuation and excessive strain causes considerable deformation of the optics. The same standard specifies a crush test for the radial compression to verify the performance of the umbilical cross-section under the clamped forces expected from the tensioner pads. They indicate that during the global response analysis, the umbilical element should be as small as possible to obviate the occurrence of Euler buckling within the element. Furthermore, they recommend the avoidance of excessive bending which leads to buckling and consequently ovality and collapse. It is evident that though the ISO-13628-5 (2009) identifies compression as a failure mode, they do not recommend any test arrangement for the axial compression. Similarly, API (American Petroleum Institute) -RP- 17B (2014) state that flexible pipes may be subjected to two types of compression, namely axial, or true wall compression, and effective compression (negative effective tension). The former can result in bird-caging of the tensile armour layer. The latter causes the global stability of the pipe to be significantly reduced, resulting in significant deformation of the pipe through global buckling. Furthermore, API RP 17B (2014) state the following,

> "The potential for both types of compression to occur should be checked during the design of the flexible pipe system. In particular, compression is often an issue in the design of risers (e.g. at seabed touchdown), and effort should be made to design the riser in such a way to minimize compression. If compression is predicted to occur in the pipe, the maximum value predicted should be checked against the criteria specified in Table 8 of (API RP 17J,2014]) (refer to tensile armours buckling and anti-buckling tape) and against the criteria specified by the manufacturer for allowable compression in the pipe body and minimum bend radius (API RP 17B,2014)"

McCann et al. (2003) highlight that there are currently no industry recommendations regarding the modelling of flexible risers in compression, particularly for deep-water applications. The authors used Flexcom-3D (1999) engineering software to demonstrate

27

that it can be used to predict the onset of buckling, instability and post-buckling behaviour. For this verification work, they used a simplified structure comprising of a cylindrical column subjected to a vertical compressive load and a small lateral load. This simple model was adequate to predict the Bar (Euler) buckling but it was not suitable for cases where bending occurs in conjunction with tension.

Clarkston et al. (2009) stated that the ISO-13628-5 (2009) does not provide specific guidance for levels of compression, or its development or consequences. Alexander et al. (1999) indicated that based on extensive global analyses undertaken on dynamic flexible risers, the compression experienced by the flexible pipe should be eliminated by conducting further engineering studies. They also indicated that the compression load can be eliminated via the use of distributed weight collars to the sag-bend area of the riser.

Nesje et al. (1999) identified excessive axial compression limits as one of the possible causes of failure modes for flexible pipes. The same reference determined the following areas as the causes of excessive axial compression:

•Exceeding specified design.

       - Installation (vessel excursions).

       - Environmental loads larger than predicted.

       - Mooring failure.

•Improper design.

•Material defects.

The end effect for the excessive axial compression was specified as burst or collapsed. Yasseri et al. (2014) found that vessel movement associated with extreme events could pose a risk of compression and buckling at the touchdown point region of a dynamic riser connected to a vessel. Additionally, Aranha et al. (2001) indicated that there will be oscillations in the tension of the riser, installed between the vessel and the seabed, as a result of the vessel movement under the influence of waves and currents. The oscillatory dynamic tension can cause riser compression, as part of the wave cycle, and the riser would be subject to so-called dynamic compression. The authors developed a simple expression for the critical load of the maximum total compression that a riser is able to locally withstand for an excitation with a given frequency. They also derived the

wavelength and propagation velocity of the compression waves formed during the dynamic compression. Rabelo et al. (2015) pointed out that bird-caging of flexible pipes is an intriguing phenomenon requiring further study, and stated that dedicated design software should implement nonlinear plastic analytical models as a tool for bird-caging prediction.

The consequence of coupling the compression load with the bending loads is not known. Work undertaken by Feld et al. (1995) indicated that the bending strain in the wires due to combined bending and axial strain is determined solely by the geometry of the cable and the imposed bend radius. As such, the axial strains are dependent upon the interaction between the conductor and the insulation. This interaction is in turn influenced by global axial loading. The authors concluded that the results of the bending and combined tension tests for the same conductor samples were different. They claimed that the presence of the voids within the cable resulting from the manufacturing process would be responsible for significant and unpredictable changes in the cable behaviour and load sharing. In the same paper, the authors developed an iterative analytical solution for bending and combined tension. However, this solution catered only for the conductor and did not adequately cater for external elements of the cable, cables with asymmetric cross-section or cables with cylindrical elements.

Subsea cable manufacturers rely heavily on analytical and empirical models developed and validated over many years. A number of dedicated finite element packages (Reda et al., 2016, p.12-34) are used for the calculations of the load/stress and design optimisation. However, there are still uncertainties associated with finite element models regarding the accurate prediction of stresses and loads acting within the cable structures during compression or when the cable is bent in conjunction with experiencing tensile loads. This is in part because compression testing is not a standard test for subsea cables. Other mechanical properties of umbilical/cable assembly lay-up designs, such as bending stiffness, can be predicted using analytical models without the need for heavy finite element analysis (FEA) software (Reda et al.,2016, p.12-34). This is because the analytical models can be calibrated by gathering results from previously tested umbilical/cables.

The calibration factors can be used as constants to correlate the bending stiffness theory with measured test results. Similarly, with the finite element models, manufacturers tend

to develop models which can replace the standard tests specified in the codes and standards. Bend stiffness and tensile test models are both developed this way. The situation is different for compression testing as there exists an industry knowledge gap in determining the compression limits of HVAC submarine cables (Reda et al., 2016, p.12-34). This issue does not appear to have been adequately investigated by cable manufacturers or by third party technical assurance organisations. The submarine cable is comprised of metallic materials combined with a number of polymeric materials with different geometries and material properties (Worzyk, 2009). This results in dissimilar deformation responses that do not always exhibit linear elastic trends (Reda et al., 2016, p12-34). The parts of the cable can slip between each other due to the difference in the nature of the cable as a composite section. Also, as stated by Marta et al. (2015), the impact of the individual material surface finish on the overall mechanical properties can be the result of only minimal changes in the manufacturing processes. In conclusion, developing complex three-dimensional finite element models or analytical equations will require numerous experiments that will help in determining the following (Reda et al., 2016, p.12-34):

- The stress strain curve for each material as well as the shear and compression moduli of the insulation material.
- Friction factors between relevant material combinations.

Furthermore, ISO-13628-5 (2009), section F.1.2.4 indicates that the response in bending is even more complicated since relative displacements can also occur. The physical behaviour in bending can be divided into the following two regimes:

- Stick regime, where plane surfaces remain plane as in traditional beam theory; this behaviour dominates until the shear stress between components at the neutral axis of the umbilical exceeds the frictional resistance. This is governed by the friction coefficient and the internal reaction forces from tension and torsion or external loads.
- Slip regime, where the friction resistance is exceeded and relative displacements occur; for the constantly curved case, this means that helical components move by relative displacement from the compressive side towards the tensile side of the umbilical (ISO-13628-5, 2009).

This gives further impetus to the view that experimental testing is necessary and required to understand the behaviour of the cable under the combined bending and compression loading scenario.

Recently, Marta et al. (2015) undertook an investigation using a global analysis for a dynamic power cable connected to a floating host. The tensile load of the cable was always below the allowable tensile loads for all cases investigated. It was discovered that the axial compression loads were significant and posed the risk of causing buckling and/or bird-caging of the subsea cable in some cases. Other failures were also identified, such as bending failure due to extreme bending loads and related cable deformation below the specified allowable minimum bend radius. The two tests were conducted to assess fatigue life to ensure that the cable would not fail under the repeated cyclic bending load due to the change in the location of the touchdown point. The former test was used to measure cable bend stiffness and the latter to measure the axial and torsional stiffness. Tests were also undertaken to validate the numerical or analytical models, following the recommendations of Electra 171 (1997) and ISO-13628-5 (2009).

The first test undertaken involved bending against the template, following DNV-RP-F401 (2012), as illustrated in Figure 2-1. As highlighted in DNV-RP-F401, (2012), this test method is not suitable for long samples for practical reasons. Also, this test method is only valid for displacement-controlled situations.

The second test undertaken was for full dynamic pitch, roll and heave combined loading. During this test, the sample was subjected to a loading regime that replicated the force and motions associated with the vessel movement under controlled laboratory conditions. One end of the sample was subjected to tension and compression to replicate heave motion, while at the other end, the headstock had the ability to move with two degrees of freedom, to replicate pitch and roll. Electrical measurements were undertaken before and after two full dynamic tests. This was in part because the test cable area was 3 mm $\times$ 50 mm whereas the subject cable was 3 mm $\times$ 500 mm.

For the subject cable used in this thesis, high voltage electrical measurements were impossible due to the cable sample length and available resources. One should note that Det Norske Veritas-RP-F401, (2012) also proposes fatigue testing of a complete cross-section as shown in Figure 2-2. Although this test can be used to determine the allowable

axial compression, as highlighted by Det Norske Veritas -RP-F401 (2012), for long and or slender configurations, this test may not give sufficient control of the bending radius especially when a tensile preload is also added. Additionally, for practical reasons, the gauge section will have to be relatively short. Thus, this testing arrangement is not suitable for cases where bending occurs in conjunction with tension.
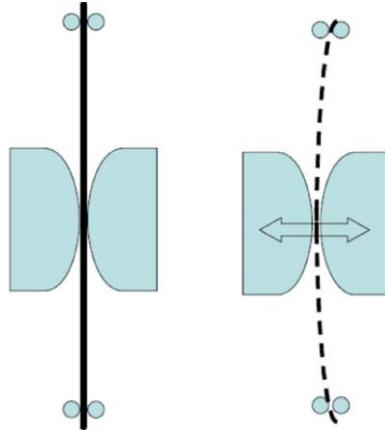
Figure 2-1: Bending against template. Source: (Courtesy of (DNV-RP-F401, 2012)).
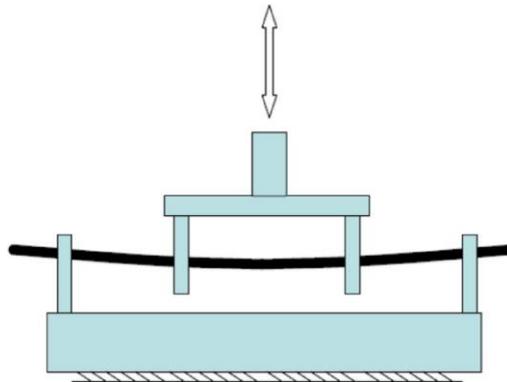
Figure 2-2: 4-Point bending test. Source: [Courtesy of (DNV-RP-F401, 2012)].

Balena et al. (2009) and Clarkston et al. (2009) both indicated that the outcome from the first cycle of analyses undertaken on Frade umbilicals was that the umbilical in the free hanging configuration was under threat from excessive bending and compression. As

32

such, the authors started to investigate another alternative option called "wavy-wave". This option utilises buoyancy modules close to the umbilical touchdown point in order to reduce the compression on the seabed. The downside of this option, however, is the cost involved in the procurement and the installation of the buoyancy modules. Due to this, it was decided to install the umbilical in the free hanging configuration and instead revise the compression acceptance of the umbilical. The authors carried out a pure axial compression test to evaluate the pure axial compression limit and to ascertain a safe level of acceptable compression for the Frade design.

Loos (2017) notably stated "Currently, there is no accepted industry standard for determination of compression limits in subsea power cables. The result is that most manufacturers specify that subsea cables are not allowed to be axially loaded in compression (Reda et al., 2016, p.12-34). This poses a problem for cable installation companies since compression can occur if the cable is heaved in a rapid motion. With the current installation methods, compression is often the limiting factor for operable conditions."

2.2 SIMULATED IN-LINE/OMEGA DEPLOYMENT OF OFFSHORE RIGID FIELD JOINT - A TESTING CONCEPT

According to Worzyk (2009), a study on subsea power cable failures was undertaken in 1986 by CIGRÉ. This study indicated a typical failure rate of 0.32 failures/year/100km. Furthermore, 82% and 18% of the failures occurred in the cables and the joints, respectively. The study did not specify the exact causes of the failures, however, the three major causes for submarine cable joint failures are known to be 1) inadequate joint design, 2) poor joint assembly work onboard the vessel, 3) adverse weather conditions during jointing, and 4) inadequate installation procedures.

Other causes of failures to subsea power cables can be attributed to many factors such as fishing, anchors, and dredging. According to the International Cable Protection Committee (2009), anchors represent the largest portion of submarine cable damages.

Contact between a cable and an anchor is often disastrous as the forces applied by a moving anchor can be extremely high. The anchoring hazard may result from:

- Emergency anchoring (where an anchor is deployed to prevent collision or grounding).

- Negligent anchoring.

- A vessel being anchored inadequately with a resultant dragging session.

- Accidental anchoring (where an anchor falls unexpectedly from a vessel due to equipment failure or operator error).

- Insufficient protection for the cable.

- Component damage.

Figure 2-3 shows a proportion of cable faults by cause, from a database of 2,162 records spanning 1959–2006 (Reda et al., 2016, p. 153-172).

It can be seen from Figure 2-3 that cable failure components represent 7.2% of the statistical distribution of damages.

Worzyk (2009) indicated that while many failure statistics account for failures during operation, the statistics normally do not include damage to the cable that happens before commissioning. Cable damages during the installation might call for expensive and time-consuming repair operations.
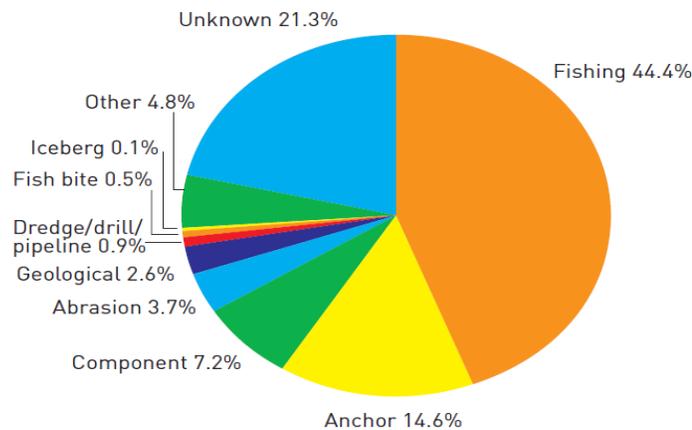
Figure 2-3: Proportion of cable faults by cause. Source: Tyco Telecommunications (US) Inc.

Worzyk (2009) also stated that "The failure of some early installation joints during service shaded the reputation of submarine power cable joints. Failures in the joints were usually caused by poor engineering or inadequate installation procedures."

A CIGRÉ study conducted in 2009 revealed that there were only four joint failures out of 49 failures in total in 7000 km of installed submarine cable. The study stated that 19 of the 49 reported faults could be repaired within one month. The ratio of joint failures changed from 0.22 to 0.095 failures/year/100 km, from 1986 to 2009, respectively which concurs with Worzyk (2009). This demonstrates that the design of submarine cables has improved over the years and that cable joints are safer and more reliable today than in 1986.

Worzyk (2009) and a CIGRÉ study conducted in 2010 highlighted that manufacturing of a reliable joint is often the most difficult undertaking during the development of a susbsea joint. Joints must be able to withstand the mechanical stress and strains associated with installation deployment.

Conseil International des Grands Réseaux Électriques (CIGRÉ) TB490 (2012) emphasised the importance of paying attention to repair joints as part of the AC submarine cable system. Det Norske Veritas (DNV) -RP-J301 (2014) indicated that all joints and terminations should be subject to a testing programme in accordance with the applicable standards. Since subsea installation field joints and repair joints connect the cable parts along the cable route to form one integrated cable, the joint has to withstand the varying loads that are typically experienced during its service life in the same way that the cables are expected to withstand them (Karlsdóttir, 2013). The deployment of the rigid joints requires a complicated crane arrangement due to the stiffness of the joints as well as the increased diameter of the joint compared to that of the cable. The stresses experienced by the joints during deployment on the seabed are most likely the maximum stresses experienced by the joint during its service life. It is therefore, all the more important to verify the mechanical integrity and reliability of the rigid joint during deployment.

Jointing operations (Worzyk, 2009; Reda et al., 2016, p.153-172; Reda et al., 2019, p. 142-157) are challenging and require valuable vessel time, good planning, highly qualified personnel, proper equipment for deployment, jointing facility container loads on the vessel as well as good coordination between the jointing crew and the vessel crew. Jointing

operations typically take one to several days, depending on the cable joint and joint design, and a good weather window is required to complete the jointing operation. Cable and joint repair are impossible during storm seasons as suitable weather windows rarely hold up long enough. Good weather conditions are essential to ensure adequate workmanship of the joint and to obviate cable fatigue damage of the hanging cable sections. It is thus essential to ensure the reliability of offshore installation joints and repair joints. This is in part due to the fact that any failure in the joint could lead to black-outs in offshore platforms resulting in financial and reputation impacts on the offshore platform operators. It should be highlighted that "installation joint", "field joint" or "repair joint" denotes a joint of the complete submarine power cable including the conductor insulation system, armouring and all other intermediate layers as shown in Figure 2-4 (Worzyk, 2009; Reda et al., 2016, p.153-172; Reda et al., 2019, p. 142-157).
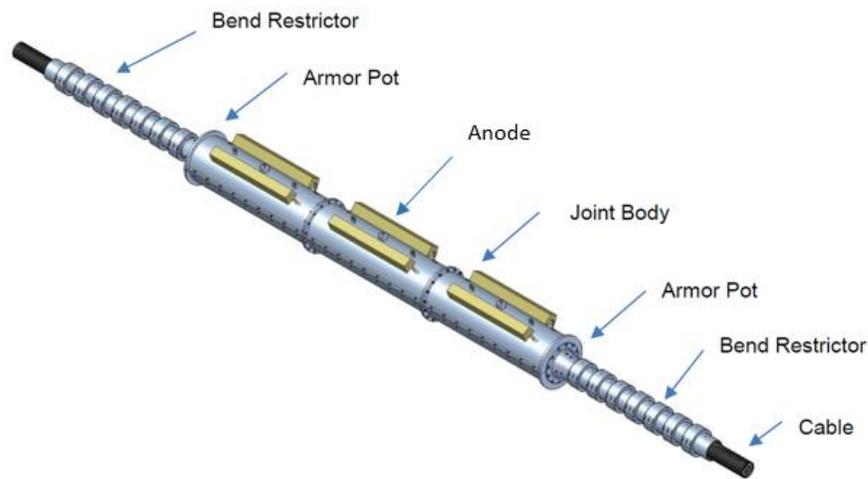
Figure 2-4: Offshore Field Joint (OFJ).

Subsea cable offshore rigid field joints have to be designed and correctly installed otherwise the offshore field joint will present a weak point and often the only source of seawater ingress. This seawater ingress will subsequently lead to electrical failures. For reliability, offshore field joints should be avoided wherever possible, as they are a potential source of failure. However, in some situations it is impossible to avoid offshore

field joints, as in the case where the subsea cable becomes damaged or the cable laying operation must be temporarily stopped.

For the offshore pipeline installation industry, abandonment of the laying operation takes place when the weather conditions do not allow cable lay activities to continue or due to unforeseen circumstances in the pipeline field area. In this situation, normally a temporary abandonment head is welded to the end of the pipeline (Reda et al., 2016, p.153-172; Reda et al., 2019, p. 142-157). The tension is then transferred from the tensioners to the abandonment and recovery (A&R) winch and the abandonment of the pipeline can begin. The barge is moved ahead a sufficient distance to allow the abandonment to hard rest on the seabed as illustrated in Figure 2-5. However, the situation can be different with the laying of subsea power cables (Reda et al., 2016, p.153-172; Reda et al., 2019, p. 142-157).
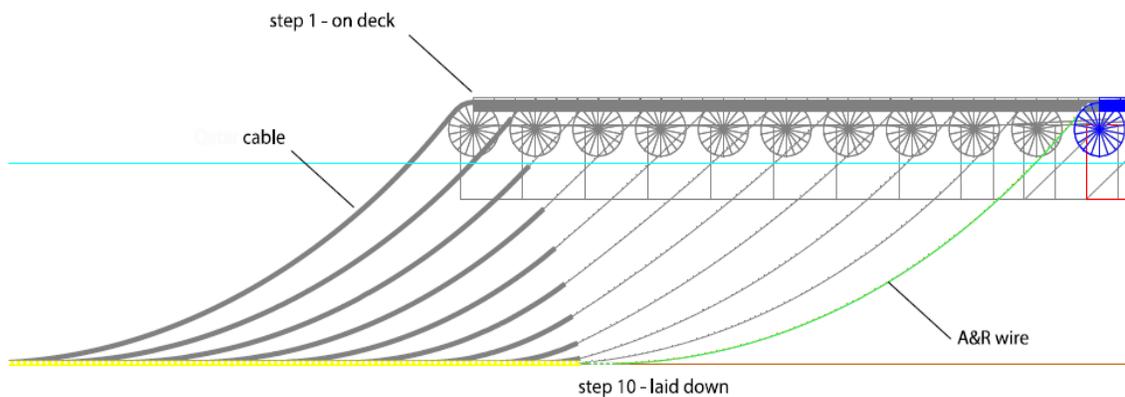
Figure 2-5. Abandonment operations.

Depending on the kind of emergency, there will be a different procedure for the sealing of the subsea cable according to time availability. The cable will, however, still be cut for each of these possible scenarios. Once the weather conditions improve, the recovery procedure will be undertaken in the reserve in order to continue the deployment operation. It is then that the in-line jointing will take place using an offshore field joint (OFJ). Det Norske Veritas (DNV)-RP-J301 (2014) recommends that the repair joint should, if possible, be laid in line with the cable.

Conseil International des Grands Réseaux Électriques (CIGRÉ) TB490 (2012) defines a field joint as a joint which is made onboard the cable installation vessel between the cable lengths, whereas, it defines the repair joint as the joint used to repair a damaged submarine cable or the jointing of two delivery lengths offshore. In principle there is no difference between a field joint and repair joint. The subject joint can be considered as either a field joint or a repair joint. The subject joint shall only be used in the situation where a repair joint is required during the cable installation, and Omega laying, shown in Figure 2-6, is not viable due to the seabed configuration or crossing conditions. In the offshore industry, the U shape that is deployed on the seafloor is also known as "Omega" (Reda et al., 2016, p.153-172; Reda et al., 2019, p. 142-157).

Figure 2-6: Omega joint deployment.

Previously, many joint failures occurred in the first few days following installation or during early operation (Worzyk, 2009; Reda et al., 2016, p.153-172; Reda et al., 2019, p. 142-157). This is simply due to the fact that these joints were not subjected to sea trials to mimic the installation loads experienced by the field joints during deployment (Reda et al., 2016, p.153-172; Reda et al., 2019, p. 142-157). It is clear that by controlling loading

conditions during deployment, the joints do not have to be regarded as a weak joint anymore. Due to time constraints as well as logistical issues, it was decided to replace the sea trial tests with simulated on-land deployment. This was used to verify the mechanical integrity of the OFJ and to identify OFJ weak points under the deployment conditions.

In order to determine the loads which should be applied on the OFJ during the on-land simulation, dynamic simulations using OrcaFlex software (2014) were undertaken to calculate all the relevant loads and stresses expected during the over-boarding and deployment procedure. OrcaFlex is a standard industry three-dimensional non-linear time domain finite element program specifically developed for marine dynamics and suited to the dynamic analysis modelling of cable catenaries.

Similar to the deployment simulation undertaken by the authors of this thesis to mimic the deployment of the in-line rigid joint offshore, Woo et al. (2015) carried out an experiment to verify that the anchor collision caused no damage to the power cable covered by rock berm. Additionally, Yoon et al. (2013) performed a safety assessment of mattress type submarine power cable protectors under the dragging forces of a 2-ton anchor through field tests on land.

2.3   A TESTING PLATFORM FOR SUBSEA POWER CABLE DEPLOYMENT

Several previous studies (Worzyk, 2009; Reda et al., 2016, p.153-172; Reda et al., 2019, p. 142-157; Karlsdóttir, 2013; Skog et al., 2010) have highlighted that jointing operations are complex and involve valuable vessel time. As discussed in the previous Subchapter, jointing operations undertaken offshore require good planning, highly qualified personnel and an installation vessel fit out with the proper equipment required for handling and deployment. Jointing operations can last for several days depending on the subsea joint design as well as the type of the joint. As pointed out earlier, cable repair may not be possible during rough seas or windy conditions. It is thus, that Det Norske Veritas (DNV) -RP-J301 (2014) proposes that cable joints as well as terminations should be subjected to a testing scheme as per industry standards.

(Reda et al.,2016,p.153-172) presented a testing platform for the in-line offshore field joint (Figure 2-7 and Figure 2-8) which can replace the sea trials undertaken offshore. In this thesis, the thesis goes on to propose a testing scheme applicable only for the Omega offshore field joints. The Omega offshore field joint refers to a joint that will be deployed on the seabed in a "U" configuration, in an over length loop (Figure 2-9 and Figure 2-10). It is also defined as an Omega joint because the joint mimics the symbol Omega "Ω" from the Greek alphabet.
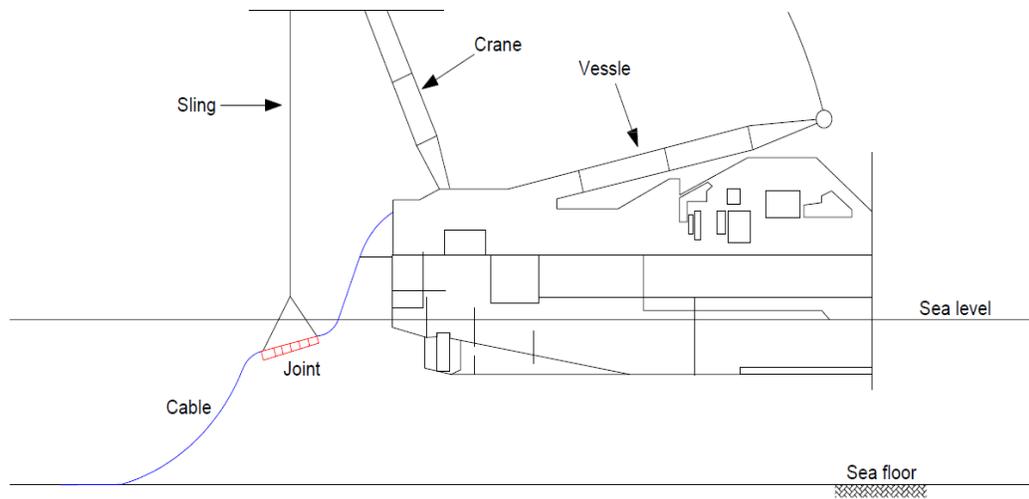
Figure 2-7: In-line offshore field joint deployment.
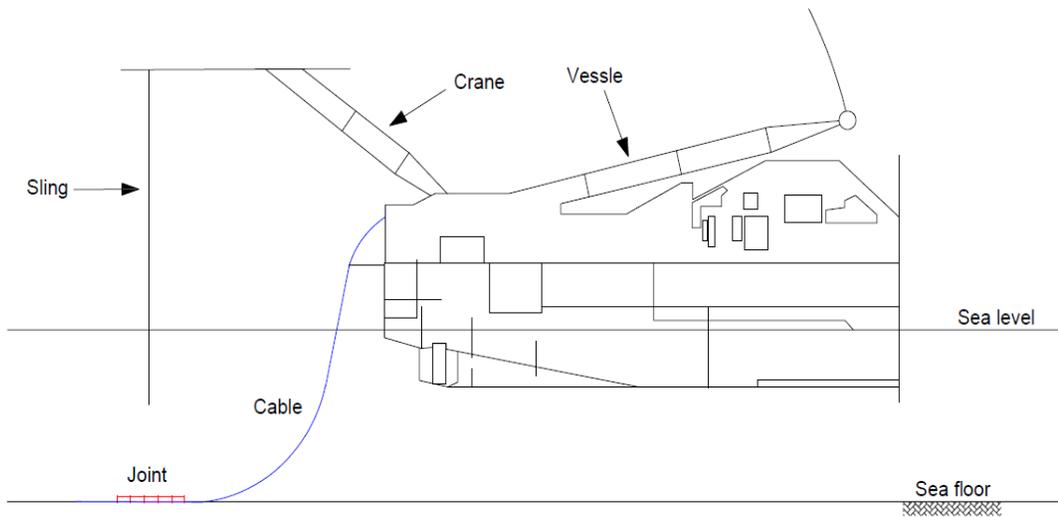
Figure 2-8: In-line offshore field joint-final position.
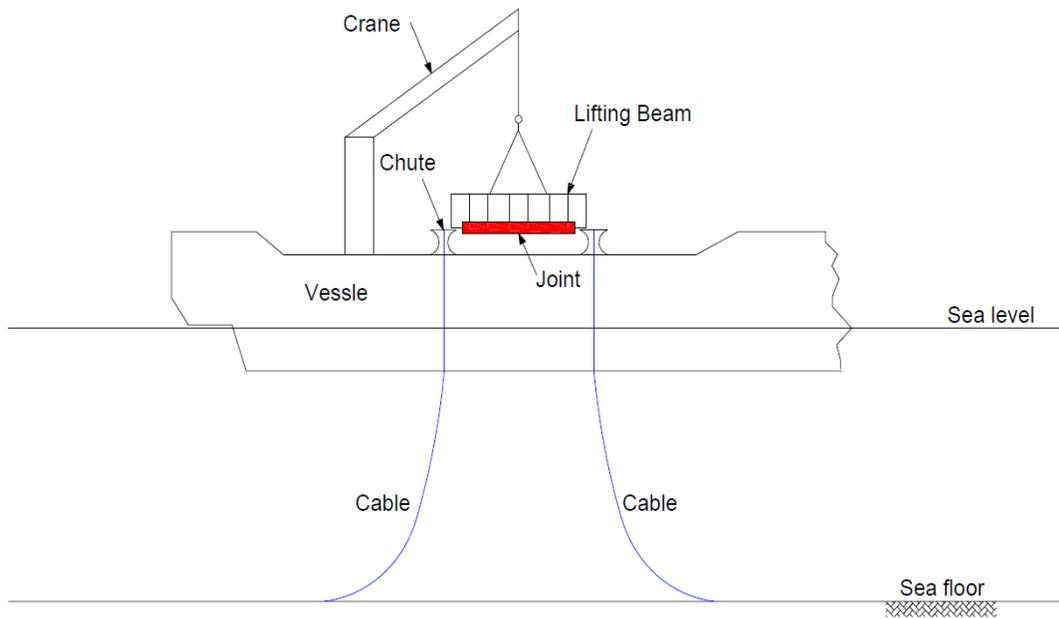
Figure 2-9: Omega offshore field joint deployment.
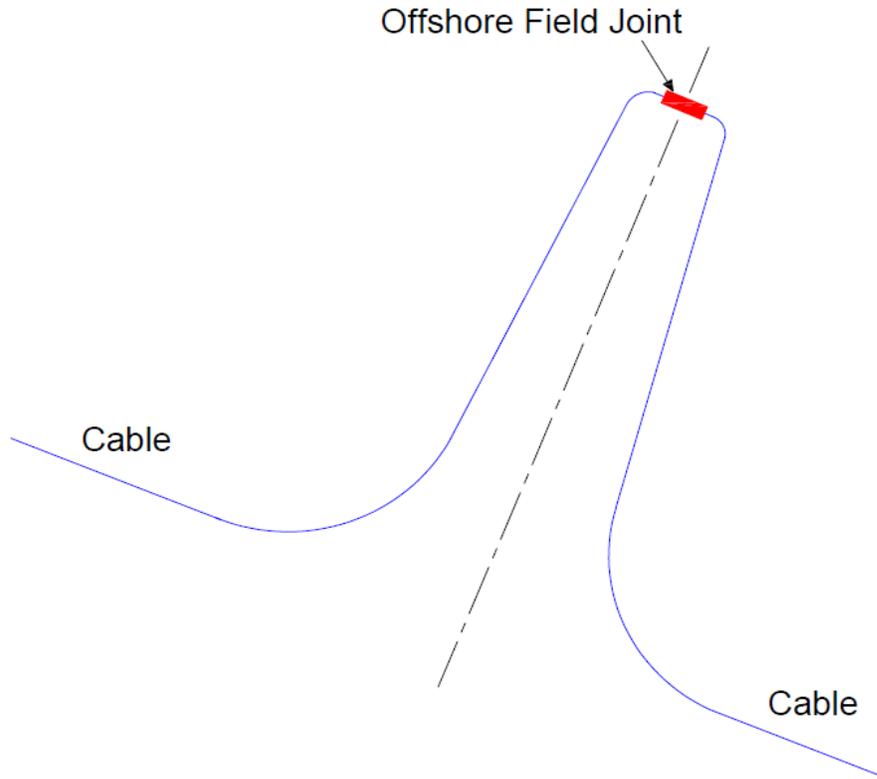
Figure 2-10: Omega offshore field joint-final position.

General statistics on land cables show a high fault rate caused by joints. This figure is mostly driven by poor workmanship rather than design defects. Ventikos et al. (2013) indicated that 10.4 % of the failures within the medium voltage subsea power cable system in Greece, is related to joints, as highlighted in Figure 2-11.

Featherstone et al. (2001) indicated that although the failure rate in subsea power cables has recently improved, joint failures are still taking place. It was reported that for a single core cable, the failure rate is 0.024 failures/100km/year in which joint failure rate is 0.01 per 100 components per year (Ericsson et al., 2003).
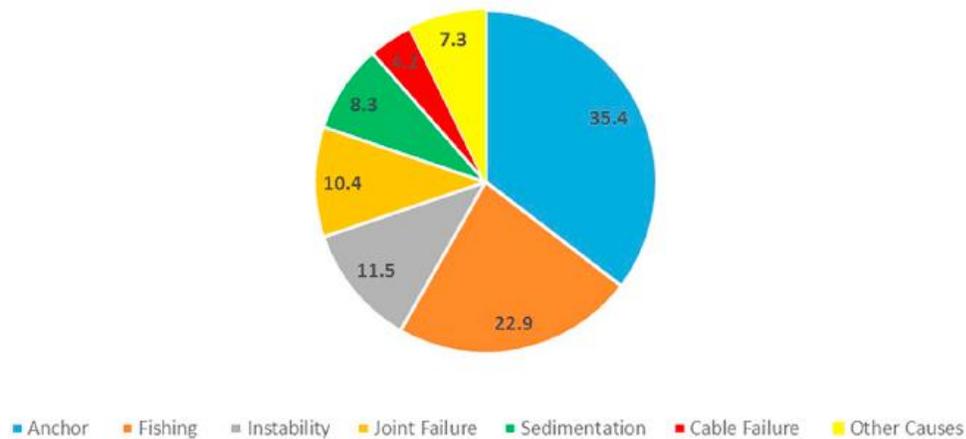
Figure 2-11: Proportion of cable faults in Greece.

2.4 DESIGN AND INSTALLATION OF SUBSEA CABLE, PIPELINE AND UMBILICAL CROSSING INTERFACES

High voltage submarine cables are being installed with increased frequency in existing and new offshore oil and gas fields for power supply and control purposes. High voltage power cables have a relatively large diameter and mass which can present a challenge when designing safe, economical, fit for purpose crossing-solutions that will be maintenance free during the asset and crossing life (Reda et al.,2017).

Damage of subsea pipeline crossings due to the deterioration of crossing supports, field joint materials and cover components are well known in the industry, particularly with old pipelines.

The crossing of one pipeline over an existing pipeline or cable should be avoided wherever economically and practically possible. However, in some situations the crossing design requires using the existing pipeline, laying unburied on the sea floor, as the crossing support when a new cable or umbilical is installed over it. In these situations, the crossing of the cable or umbilical over an existing pipeline may be a cost-effective solution and should be considered. However, the industry accepted standards and recommended practices for the design and construction of crossings are not explicit in the criteria for subsea crossings beyond recommending pipeline separation distances (Reda et al.,2017;

43

Palmer et al.2004; Bai et al., 2014; DNVGL-ST-F101, 2017; API-RP-1111, 2015; ISO 15589-2, 2012; ISO 13623, 2009; ICPC Recommendation 3, 2014).

The size of the cable, umbilical or pipeline being crossed and their burial condition are important factors in selecting the crossing design concept. Cost, complexity and engineering effort all increase with increased cable/umbilical/pipeline size (Reda et al., 2017; Palmer et al., 2004; Bai et al., 2014). For example, a cable/umbilical/pipeline crossing involving a non-buried large diameter pipeline is considerably more complex than that involving a partially buried, small diameter pipeline. Furthermore, the selection of the crossing design depends on the construction method, especially when the crossing design involves burial, trenching or rock dumping. In this case, the cost of the construction vessel and equipment will have a significant impact on the choice of crossing design and alternative crossing designs must be envisaged (Reda et al., 2017).

Deterioration of subsea pipeline crossings is also a common issue (Reda et al., 2017). Most of the problems have been primarily related to the long-term integrity of crossing supports and cover components. It is imperative to ensure that the crossing design is a sound and fit for purpose solution that will be maintenance free over the life of the crossing.

Det Norske Veritas Germanischer Lloyd (DNVGL)-ST-F101 (2017) requires that crossing pipelines/cables/umbilicals should be separated by a minimum vertical distance of 0.3 m.

American Petroleum Institute (API)-RP-1111 (2015) states that "Pipeline crossings should comply with the design, notification, installation, inspection, and as-built records requirements of the regulatory agencies and the owners or operators of the pipelines involved. A minimum separation of 12 inch is required".

International Organization for Standardization (ISO) 15589-2 (2012) states that "A separation of 0.3 m is normally adequate, but smaller separation distances may be acceptable if it can be demonstrated that CP interference between the lines is insignificant."

International Organization for Standardization (ISO) 13623 (2009), Section 6.9.5 states that "Physical contact between a new pipeline and existing pipelines and cables shall be

avoided. Mattresses or other means of permanent separation should be installed, if necessary, to prevent contact during design life of the pipeline".

In view of the above, when a 0.3 m thick mattress or similar protection is placed over the crossed pipeline at the crossing point, then the required positive vertical separation is guaranteed throughout the crossing life. This is providing the mattress remains in place and does not deteriorate or collapse.

International Cable Protection Committee (ICPC) Recommendation 3 (2014) states that basic questions should be answered carefully before considering any crossing design. These questions are applicable for the cases where an existing pipeline is crossed by a power cable. The questions are "Will it require an artificial separation to be installed between the pipeline and the power cable? Will the power cable owner consider artificial separation necessary in order to avoid chafing damage to the power cable?"

Furthermore, ICPC Recommendation 3 (2014) asks some questions in regards to the cathodic protection of the existing pipeline crossed by a power cable. These questions are "Does the pipeline have cathodic protection? If so, what is the distance between anodes? Are the anode positions accurately known? Can the cable lay be arranged so that the cable is in the mid-50% distance between anodes?"

It is evident that for cases where the crossed pipeline is utilized as a support, the codes and recommended practices are not explicit in prohibiting the installation of a cable crossing at a field joint-coating site of a pipeline.

2.5 PIPELINE WALKING AND ANCHORING CONSIDERATIONS IN THE PRESENCE OF RISER MOTION AND INCLINED SEABEDS

A subsea pipeline, laid on the seabed, operated at a temperature greater than the installation temperature will tend to axially expand (Palmer et al., 2004; Bai et al., 2014; Reda et al., 2014). The term "pipeline walking" is used to describe the movement of the pipeline in the axial direction (Reda et al., 2018, p. 71-85; Reda et al., 2019, p. 278-298; Guha et al., 2019, Burton et al., 2008; Perinet et al., 2011; Carr et al., 2003; Carr et

al., 2009; Knouk; 1998; Tornes et al., 2000). The effect of pipeline walking should be considered in pipeline design.

Pipeline walking occurs in pipeline sections not anchored by seabed axial soil resistance when there exists one or more of the following conditions (Reda et al., 2018, p. 71-85; Reda et al., 2019, p. 278-298; Burton et al., 2008; Perinet et al., 2011; Carr et al., 2003; Carr et al., 2009;Knouk, 1998; Tornes et al., 2000).

- Pipeline slope.

- SCR tension at the pipeline end.

- Pipeline length.

- Internal pressure of the pipeline.

- Frequency of start-up and shutdown.

- Thermal transients along the pipeline during warm-up and cool-down.

- Pipe-to-soil longitudinal friction coefficient.

Repetitive heat-up and cool-down cycles may lead to a significant global displacement of the pipeline, resulting in overstressing of the expansion spools and jumpers as well as loss of SCR tension (Reda et al., 2018, p. 71-85; Reda et al., 2019, p. 278-298; Burton et al. , 2008; Perinet et al., 2011; Carr et al., 2003; Carr et al., 2009; Knouk, 1998; Tornes et al., 2000).

Tornes et al. (2000) indicated that the outcome of monitoring some relatively short high temperature flowlines in the UK sector of the North Sea revealed that the net axial displacement of the flowlines towards the outlet ends gradually increased over time. As a result, one of the tie-in spools ruptured and had to be replaced. It is thus evident that pipeline walking can cause failures in tie-in spools or riser connections if not controlled or eliminated. Furthermore, Knouk (1998) attributed the buckling of a pipeline in Canada to pipeline walking.

Burton et al. (2010) explained that pipeline walking is sensitive to the axial friction factor. The same reference indicated that the Safebuck Joint Industry Project is currently working on understanding axial friction mechanisms. There is uncertainty associated with predicting the range of axial friction and in particular with the lower axial friction factor.

Steel catenary riser (SCR) systems can represent a significant portion of the field development costs of a floating system. For many projects, SCRs have been shown to have more advantages over flexible risers. Some of the advantages are listed in Phifer et al. (1994), Quintin et al. (2007), Drumond et al. (2018), Wu et al. (2007), Belik (2016), and Ogbeifun et al. (2019).

A major problem with SCRs is the high bending stress where the SCR touches down on the seabed. Tension near the touchdown point is lower than the top tension, so the SCR is easily bent. In addition to a high static curvature at the touchdown, the high bending stress and curvature at the touchdown is exacerbated by the dynamic response associated with waves travelling down the SCR (Mekha et al., 2013; Mansour et al., 2014; Clukey et al., 2017; Shoghi et al., 2019; Taheri et al., 2017).

Many studies have been devoted to investigating the fatigue damage at the touchdown point due to environmental effects (Serta et al., 1996; Wang et al., 2014; Wang et al., 2014; Elosta et al., 2013; Li et al., 2012; Shiri et al., 2014; Hawlader et al., 2015).

The effects of the floating vessel's motion, environmental effects and thermal loads that cause pipeline expansion all lead to the slipping of the mean position of the touchdown point towards the vessel. Expansion towards the SCR should be kept within the allowable maximum axial displacement specified by the SCR design (Reda et al., 2018; Reda et al., 2019, p. 278-298). Excessive movement of the touchdown point could result in reduced static tension in the SCR and a change in curvature of the sag-bend region (Reda et al., 2018, p. 71-85; Reda et al., 2019, p. 278-298).

Axial friction governs the expansion of a pipeline (Reda et al., 2018; Reda et al., 2019, p. 278-298; Carr et al., 2003; Carr et al., 2009, Knouk, 1998; Burton et al., 2008). The effective force is dependent on the axial friction. Effective axial force can be defined as the summation of all externally applied axial forces acting on a pipeline (Reda et al., 2018, p. 71-85; Reda et al., 2019, p. 278-298; Carr et al., 2003; Carr et al.,2009, Knouk, 1998; Burton et al., 2008). A high frictional resistance will give rise to a high effective force (Reda et al., 2018, p. 71-85; Reda et al., 2019, p. 278-298; Carr et al., 2003; Carr et al., 2009, Knouk, 1998; Burton et al., 2008).

Current literature is silent regarding the criteria which should be considered when selecting the optimum anchor location in the presence of SCR motion, thermal transients

and inclined seabeds. This thesis intends to fill the design guidance gap regarding the interfaces between the pipeline and the SCR.

2.6   WHEN IS A SUBSEA ANCHOR REQUIRED FOR A SHORT PIPELINE/SCR SYSTEM?

A subsea pipeline, laid on the seabed, operated at elevated temperatures and pressures invariably undergoes expansion (Reda et al., 2018; Reda et al., 2019, p. 278-298; Burton et al., 2008; Perinet et al., 2011; Carr et al., 2003; Carr et al., 2009; Knouk, 1998; Tornes et al., 2000). The straining actions associated with this phenomenon must be determined.

In a recent study (Reda et al., 2018), the thesis provided design criteria that could be adopted for the selection of the optimum anchor location in the presence of SCR motion, thermal transients as well as seabed inclination. However, the cited criteria are only applicable to straight, short pipelines that do not undergo lateral buckling. Axial walking occurs when the pipeline moves incrementally overtime. This can result in progressive movement towards the SCR, downhill or towards the cooler end of the pipeline.

Reda et al. (2018) and Knouk (1998) indicated that pipeline walking causes gradual axial displacement of the entire pipeline towards one end, due to the repeated start-up and shut-down pressure and temperature cycles. The accumulated axial displacement over time can eventually lead to overloading of the spool piece or jumper.

2.7   PIPELINE SLUG FLOW DYNAMIC LOAD CHARACTERIZATION

As indicated by Sultan et al. (2012), Sultan et al. (2013), Reda et al. (2012), and Reda et al. (2014), slug flow induces a vibration in pipelines, which may in some scenarios, result in fatigue failures associated with the dynamic stresses. This slug flow acts as a traversing force along a length of an unsupported pipeline span and causes structural vibration of the unsupported pipeline span as illustrated in Figure 2-12.
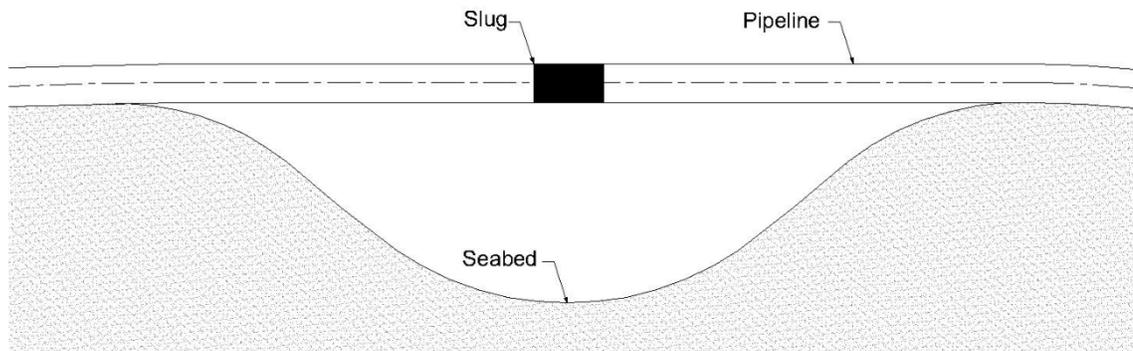
Figure 2-12: Slug schematic model.

When the slug of fluid passes over this unsupported length of a pipeline, dynamic motion can ensue. This results in force amplification within the pipeline and possible fatigue related issues if multiple slugs of fluid pass over this unsupported length of a pipeline over the period of its design life (Sultan et al., 2012; Sultan et al., 2013; Reda et al.,2012; Reda et al.,2014; Reda and Forbes ,2011).

Reda and Forbes (2011) indicated that many types of slender or thin walled structures experience forces which traverse across them. For example, vehicles passing over a bridge, overhead crane operations and liquid "slug" movement in spanning pipelines. This moving force can initiate a large axial dynamic stress within the structure and is often important for assessing structural fatigue.

Previous research has investigated the dynamic response of pipelines under the influence of slug flow (Reda and Forbes, 2011, Rieker and Trethewey, 1999; Rieker et al., 1996; Casanova et al., 2009; Casanova et al., 2010; Kansao et al., 2008; Lin et al., 1990). These studies have counted on the use of finite element analysis of specific pipeline systems with increasing complexity to account for the non-linear seabed. Reda et al. (2011) presented the fundamental analytical solution of a simply supported beam under the influence of this loading type along with a discussion regarding the structural response with the level of detail necessary to help those working in this field to grasp the complex phenomena involved.

49

In the same paper (Reda et al., 2011), the thesis posed the following four questions that may arise when presented with the issue of unsupported span lengths and flow conditions conducive to slug flow patterns:

    i.   What size does a slug need to be for a dynamic analysis to be undertaken?

    ii.   At what speed does slug flow produce increased dynamic amplification over and above the static loadings?

    iii.   At which location on the span does the highest bending moment exist?

    iv.   Does a moving mass or moving force analysis need to be undertaken?

The thesis covered questions i–iii as follows:

    i.   When a concentrated moving force model can appropriately describe the system, the size of the slug is independent of the analysis.

    ii.   With the size of slug being independent of the analysis, the greatest increase in force amplification occurs at approximately 60% of the critical speed of the system.

    iii.   The location of the maximum bending moment is dependent on the damping of the system but generally does not occur at the mid-span.

Consequently, this leaves question (iv) to be answered: "when is a moving concentrated force model not appropriate"? It is one of the objectives of this thesis to provide a quantifiable answer to this question.

To date, all work presented on the topic of pipeline vibrations under the passage of the slug flow, ignored the inertia of the moving slug (Casanova et al., 2009; Casanova et al., 2010; Kansao et al., 2008; Cooper et al., 2009).

Conventionally, research on the topic of vibration of structures under moving loads has been focused on the dynamic response of the structure under either a moving force or a moving mass (Reda and Forbes, 2011; Rieker and Trethewey, 1999; Rieker et al., 1996; Casanova et al., 2009; Casanova et al., 2010; Kansao et al., 2008 ; Cooper et al., 2009; Lin et al., 1990). Current literature specifies that the moving force model can be used

when the mass of the moving load is small compared to that of the structure and vice versa for the moving mass model. However, the term 'small' has not yet been given quantitative terms (Reda and Forbes, 2011; Rieker and Trethewey, 1999; Rieker et al., 1996; Casanova et al., 2009; Casanova et al., 2010; Kansao et al., 2008; Cooper et al., 2009; Lin et al., 1990).

2.8 VIBRATION OF A CURVED SUBSEA PIPELINE DUE TO INTERNAL SLUG FLOW

As the oil and gas industry moves towards deep-water development, subsea pipelines are being increasingly required to operate at higher levels of pressure and temperature especially with wellheads moving further away from processing facilities (Reda et al., 2018 p. 71-85, Reda et al., 2019, p. 278-298; Reda and Forbes, 2012). This has led to the two design challenges (Reda et al., 2018 p. 71-85, Reda et al., 2019 p. 278-298; Reda and Forbes, 2012, Carr et al., 2003; Carr et al., 2003; Knouk, 1998; Burton et al., 2010; Cooper et al.,2009) outlined below.

1. If not properly mitigated, high pressures and temperatures can result in large axial pipeline expansion as well as uncontrolled lateral buckling.

2. Larger distances between the wellhead and processing plant can cause multiphase internal 'slug' flow resulting in dynamic forces as the oil and gas passes through the pipeline.

In terms of the first design challenge, a subsea pipeline laid on a seabed tends to axially expand and contract under the repeated operating cycle of start-ups and shut-downs (Reda et al., 2018 p. 71-85, Reda et al., 2019 p. 278-298; Reda and Forbes, 2012, Carr et al., 2003; Carr et al., 2003; Knouk, 1998; Burton et al., 2010; Cooper et al., 2009). This axial expansion is the result of the internal operating pressure as well as the raised wall temperature in relation to the seabed ambient temperature. As the axial expansion is restrained by the frictional restraint of the seabed, an effective axial force can develop in the pipeline. If the effective axial force exceeds the buckle initiation force, the pipeline

will undergo Euler buckling to relieve the resultant high axial forces in the pipe wall (Reda et al., 2018; Reda et al., 2019 p. 278-298; Reda and Forbes, 2012; Burton et al.,2008 , Perinet et al., 2011; Carr et al., 2003; Carr et al., 2006; Knouk, 1998; Tornes et al., 2000).

Uncontrolled buckling can have serious implications on the integrity of the pipeline. Buckle mitigation can be achieved by providing controlled lateral pipeline movements in instances where the response of the in-service buckled pipeline exceeds any ultimate and fatigue limit states (Reda & Forbes, 2012).

Buckle mitigation measures are intended to induce lateral deformations at designated locations thereby sharing expansion between the adjacent buckle locations. A number of buckle mitigation measures have been employed or proposed (Reda and Forbes, 2012; Burton et al., 2008; Carr et al., 2003; Carr et al., 2006) to initiate buckling at the defined locations and include:

- Local vertical out-of-straightness (i.e. sleeper and zero radius bend).

- Imposed local curvatures (snake lay).

- Local buoyancy.

Laying the pipeline over a vertical buckle initiator may generate significant unsupported span lengths depending on the height of the vertical initiator, as shown in Figure 1-14.

In an earlier paper (Reda et al., 2011), the paper described how fatigue due to slug flow in pipelines, which would normally require dynamic analysis, can be quantified using simplified quasi-static analysis. The thesis also presented a design process which could be adopted to determine the level of analysis required before embarking on more complex and expensive dynamic finite element.

In the same paper, it was recommended a design process to calculate the axial stress and stress range required to perform the fatigue assessment at the girth weld located at the mid-point of the straight span.

With respect to the second challenge, multiphase internal flow in the pipeline can cause "slugs" or fluids of differing densities, to pass through these unsupported span lengths causing dynamic motion, cyclic stress and fatigue events in the pipeline. Both of these

pipeline design challenges are investigated in this thesis, with particular attention given to the curved path the internal flow must pass as it traverses the unsupported span over a sleeper type buckling mitigation design.

3 Chapter-3 – Paper No. 1

Title: "**Compression limit state of HVAC submarine cables**".

Authors: **Ahmed M Reda, Gareth L Forbes, Faisal Al-Mahmoud, Ian M Howard, Kristoffer K McKee and Ibrahim A Sultan.**

Journal: **Applied Ocean Research**

3.1 INSTALLATION ANALYSIS

The purpose of this section is to:

1. Present the finite element analysis undertaken on the cable and articulated padding to understand the parameters which impose compression loads on subsea cables at the touchdown points.

2. Investigate the dynamic response of the articulated padding during the installation phase of the system. From the performed analyses, installation parameters are obtained, and the cable is analysed in different sea states to check its integrity.

As indicated earlier, the crossing of power cables with existing objects requires a minimum separation to be maintained between the power cable and the crossing object. This separation can be achieved via the installation of articulated padding around the cable.

3.1.1 Analysis Methodology

The analyses performed for this chapter are divided into two parts:

1. Static analysis
2. Dynamic analysis

The static analysis contains the installation parameters while the results of the dynamic analysis is used as inputs to check the integrity of the cable. Both are discussed in more detail in the following subchapters. For all crossing analyses the software package OrcaFlex (2014) was used. OrcaFlex takes the following relevant physical phenomena into account:

- Bending stiffness of the cable

- Axial stiffness of the cable

- Weight (submerged and dry) of the cable

- Relative soil friction normal and lateral to the seabed

- Contact forces between the seabed and the cable

- Friction between the cable and the tensioner

- Hydrodynamic properties

- Non-linear wave modelling depending on wave train

- Cable lay vessel motion

- Current profile

The complex shape of the articulated padding cannot be modelled in OrcaFlex. This is because OrcaFlex calculates the submerged weight of a line element by subtracting the buoyancy from its dry weight. To account for this, the following solution has been used. The line attachments in OrcaFlex are set to be free flooding. By setting the inner diameter of the line attachment, a porous tube is created. The inner diameter can be adjusted so that the submerged weight exactly matches the given specifications. In this way the important hydrodynamic properties are modelled correctly. This method has been approved by Orcina, the developers of OrcaFlex .

The complex shape of the spacers makes them difficult to model correctly in OrcaFlex . The approach used in this analysis involves using an average outer diameter of the modelled articulated padding system. The average outer diameter is calculated using the dimensions of the spacers, the bend restrictor, the effective pitch and the nominal gap between the spacers. The contact diameter in the model is the actual outer diameter of the spacers. The diameters used can be found in Table 3-1.

Table 3-1: Diameters of Articulated Padding System as Modelled

Item	Value for articulated padding + bend restrictor	Value for bend restrictor	Unit
Outer diameter	825	600	mm
Inner diameter	548	309	mm
Contact diameter	1050	600	mm

The bend restrictor adds additional bending stiffness to the system. The bend restrictor properties are shown in Table 3-2.

Table 3-2: Bend Restrictor Properties

Item	Value for Bend restrictor	Unit
Minimum bend radius at 0 kN	3.5	m
Minimum bend radius at locked out state under 20 kN of load	3.0	m
Contributing to effective bending stiffness in unlocked state	0	kNm²
Contributing to effective bending stiffness in locked-out state (20 degrees)	800	kNm²

These properties are modelled in OrcaFlex with a variable bending stiffness of the line attachments that represent the bending restrictors and articulated padding. The bend restrictors do not contribute to the effective axial stiffness or to the effective torsional stiffness.

3.1.2 Static Analysis

The purpose of the static analysis is to form a starting point for further dynamic analysis based on known criteria such as cable limits, water depths, vessel response amplitude operators (RAOs), without taking into account the effects of current. That is, the static approach analyses the continuous installation of the cable and articulated padding system without the effect of waves. The analysis starts when the first section of the bend restrictor is placed upon the chute and ends when ten meters of bare cable is installed behind the articulated padding system.

The static analysis consists of the following steps:

- Building the model based on the geometry of the crossings.

- Optimising the model for the required target bottom tension.

- Optimising the model and determining the vessel offset.

- Running the simulations.

- Obtaining installation parameters.

- Optimising the model in such a way that the bottom tension during normal lay operations is equal to the target bottom tension. The model has to be optimised for each crossing to meet multiple target bottom tensions that range from 5kN to 30kN (5-8-10-15-30kN).

Currents act on the cable and the articulated padding system to cause a lateral offset at the touchdown location. The increase in outer diameter due to the installation of the articulated padding system causes a larger offset compared to normal cable installation. The models are optimised by including a vessel offset that ensures the touchdown location is within 1.5 m of the intended location.

Finally, from the analysis the following installation parameters are obtained:

- Layback distance

- Departure angle

- Top tension

- Bottom tension

- Minimum bending radius

- Catenary length

These parameters are obtained over ten steps per case. Additionally, the free span length and the contact force at the crossing are also determined.

In Figure 3-1, Simulation 1 is shown, as modelled in OrcaFlex, at the beginning of the analysis (step 1). The articulated padding system lies completely on the vessel's deck. The crossing object can be seen on the seabed.

The 10 steps are divided equally over the duration of the simulation from the start, where the entire articulated padding system is on deck, to the finish, the point where 10 m of bare cable is laid upon the seabed after the crossing. This is illustrated in Figure 3-2.
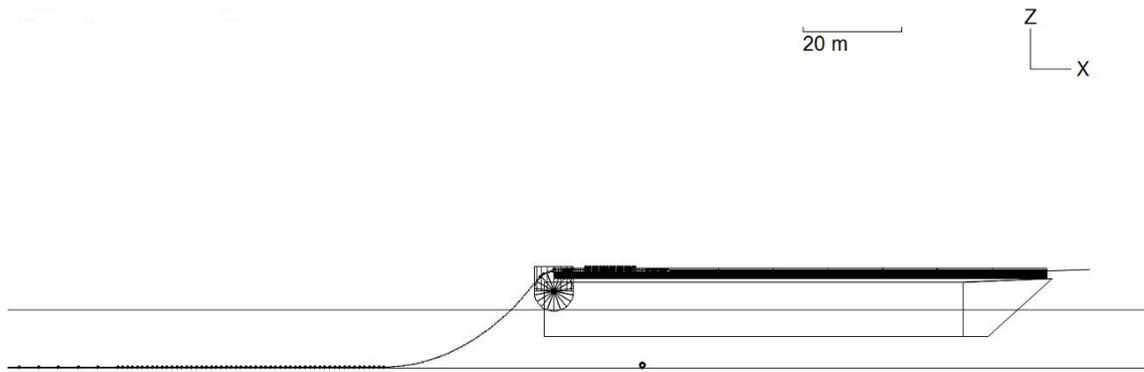
Figure 3-1: Simulation 1 as modelled in OrcaFlex, side view.

Figure 3-2: The 10 simulated steps.

3.1.3   Dynamic Analysis

The dynamic analysis includes the effect of waves on the vessel-cable system and is performed using a time-domain analysis. In the case of continuous installation, DNV recommends keeping the object fixed in selected positions for a minimum of 30 minutes (DNV-RP-C205,2014). Therefore, for each case, the 10 steps are simulated with a 30 minute JONSWAP wave spectrum. From these dynamic analyses, the following results are obtained:

- Maximum tension in the cable in front of the spacer

- Minimum tension in the cable in front of the spacer

- Minimum occurring bend radius

- Maximum contact force at the crossing

- Maximum occurring top tension

- Minimum occurring bottom tension

3.1.4   Input Data

3.1.4.1   Vessel RAOs

Vessel motions are simulated by means of Response Amplitude Operators (RAOs). The RAO files provide the response with six degrees of freedom for incoming waves with a defined height and period. The RAOs are calculated using a wave direction interval of 11.25 degrees. The vessel characteristics that were used for the determination of the RAOs are presented in Table 3-3.

Table 3-3: Vessel Particulars for RAO Calculations

Parameter	Unit	Value
I_{XX}	kg.m^2	7.68E+08
I_{YY}	kg.m^2	7.12E+09
I_{ZZ}	kg.m^2	7.33E+09
LCG	m	50.78
TCG	m	0.0
VCG	m	7.37

3.1.4.2   Vessel Layout

The relevant parameters for the static and dynamic analyses are summarized in Table 3-4.

Table 3-4: Vessel Parameters

Parameter	Unit	Value
Vessel width	m	23
Draft	m	5.4
Length	m	106.75
Chute radius	m	4.0
Chute distance from aft	m	2.0
Chute offset centre line	m	1.5

3.1.4.3   Installation Limits

To ensure the safe installation of the cable, the following cable limits are set:

• The maximum top tension must not exceed 100kN.

• The minimum bend radius is limited at 2.9 m.

• The maximum axial compression is

     o 17.3kN at 5.0 m minimum bend radius, and

     o 10.2kN at 2.9 m minimum bend radius.

61

It should be noted that these installation limits were determined by the results of the compression tests undertaken as part of this thesis. The results from the tests are explained further in Section 3.4.

3.1.5   Static Analysis Input

The sections below provide information on the input parameters that were used for the static installation analysis.

3.1.5.1   Currents

The analyses were performed for two current velocities; zero velocity and the 1-year maximum surface current. The data is summarised in Table 3-5 and consists of the omnidirectional current velocities.

Table 3-5: Maximum Surface Current Velocities (1 Year Maximum)

Parameter	Unit	Value					
		Section 1	Section 2	Section 3	Section 4	Section 5	Section 6
Maximum surface current- 1 year	m/s	0.97	0.71	0.97	0.64	0.64	1.29

Current variation over depth is modelled using the $1/7^{th}$ power law of velocity reduction as shown in Figure 3-3:

$$\frac{U}{U_R} = \left(\frac{d}{d_R}\right)^{\frac{1}{7}}$$

where:

U = current velocity (m/s)

d = distance above mud line (m)

U_R = surface current velocity (m/s)

d_R = water depth (m)
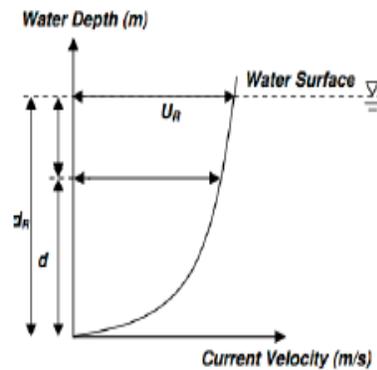
Figure 3-3: The 1/7th power law of velocity reduction.

It is obvious that for the zero current velocity case the current direction is irrelevant. For the maximum surface current, seven directions were analysed ranging from 0 to 180 degrees in increments of 30 degrees. The definition of the directions can be found in Figure 3-4.
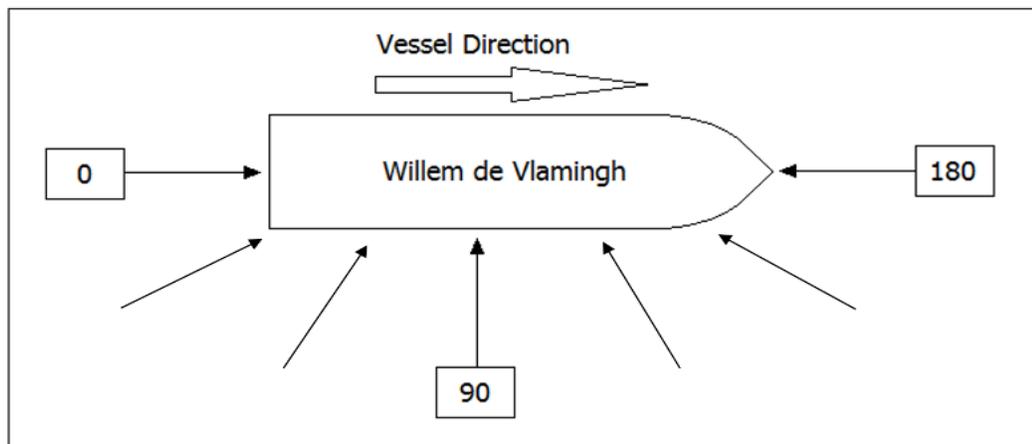
Figure 3-4: Definition of current directions.

3.1.5.2 Waves

The wave loading in the static analysis was set to zero, that is, no waves are present.

3.1.5.3 Bottom tension

The models were optimised to incorporate the correct bottom tensions for normal lay operations. The target bottom tensions for normal lay that were used as input for the models were 8, 10, 15 and 30kN. If no workable solution was found within the range of 8-30kN, due to excessive compression or top tension, a bottom tension of 5kN was analysed as well.

3.1.6 Dynamic Analysis Input

The sections below provide information on the environmental input parameters that were used in the dynamic installation analysis. The dynamic analyses were performed for two current velocities; zero velocity and the 1-year maximum surface current. Both velocities were considered for seven different directions ranging from 0 to 180 degrees in increments of 30 degrees.

3.1.6.1 Waves

All simulations were performed with significant wave heights of 1.5 m, 1.0 m or 0.5 m . The waves were modelled with a JONSWAP wave spectrum. As discussed in Subsection 3.1.3, each step was analysed for 30 minutes using this spectrum.

The direction of the waves were set in the same as the direction of the current, as this leads to the largest response.

For each sea state, the corresponding peak period was calculated using the following formula:

$$T = \sqrt{30.H_s}$$

where H_s is the significant wave height. This is based on the range of T_p that is proposed in the report of the International Ship and Offshore Structures Congress Committee I.1 and suggested by GL Noble Denton (2016, 7.4.2):

$$\sqrt{13.H_S} \leq T_P \leq \sqrt{30.H_S}$$

This leads to a peak period of 6.7s for these simulations.

In the first simulation, all of the crossings were simulated with a significant wave height of 1.5m. However, it turned out that some crossings were not installable under the given limits. As such, those crossings were simulated again with a significant wave height of 1.0 m. Where necessary, the significant wave height was further lowered to 0.5m.

3.1.7   Results

The results presented here are only samples of the compression load at the touchdown point due to the presence of the articulated padding system. Note that not all simulations resulted in axial compression at the touchdown point. Table 3-6 shows the cases for which the results are presented.

It is worth mentioning that many cases did not satisfy the installation limits indicated in Sub subsection 0.

In the results, location A refers to "30 m clear of crossing" and location B refers to "150 m clear of crossing".

Figure 3-5 to Figure 3-8 show snapshots from the finite element simulations undertaken using OrcaFlex to determine the forces in the cable during the laying process.

Table 3-6: Cases Presented

Case	Head case (degree)	Wave height (m)	Wave period (s)	Water depth (m)	Layback[1]
1	0	1.5	7.6	11	Minimum
2	0	1.5	7.6	11	150% layback
3	90	1.5	7.6	11	Minimum

Case	Head case (degree)	Wave height (m)	Wave period (s)	Water depth (m)	Layback[1]
4	0	1.5	6.3	11	Minimum

Note:

1- The horizontal distance between the touchdown point of the cable and the location of the chute. The touchdown point of the cable is defined as the first point where the cable touches the seabed, as seen from the vessel.
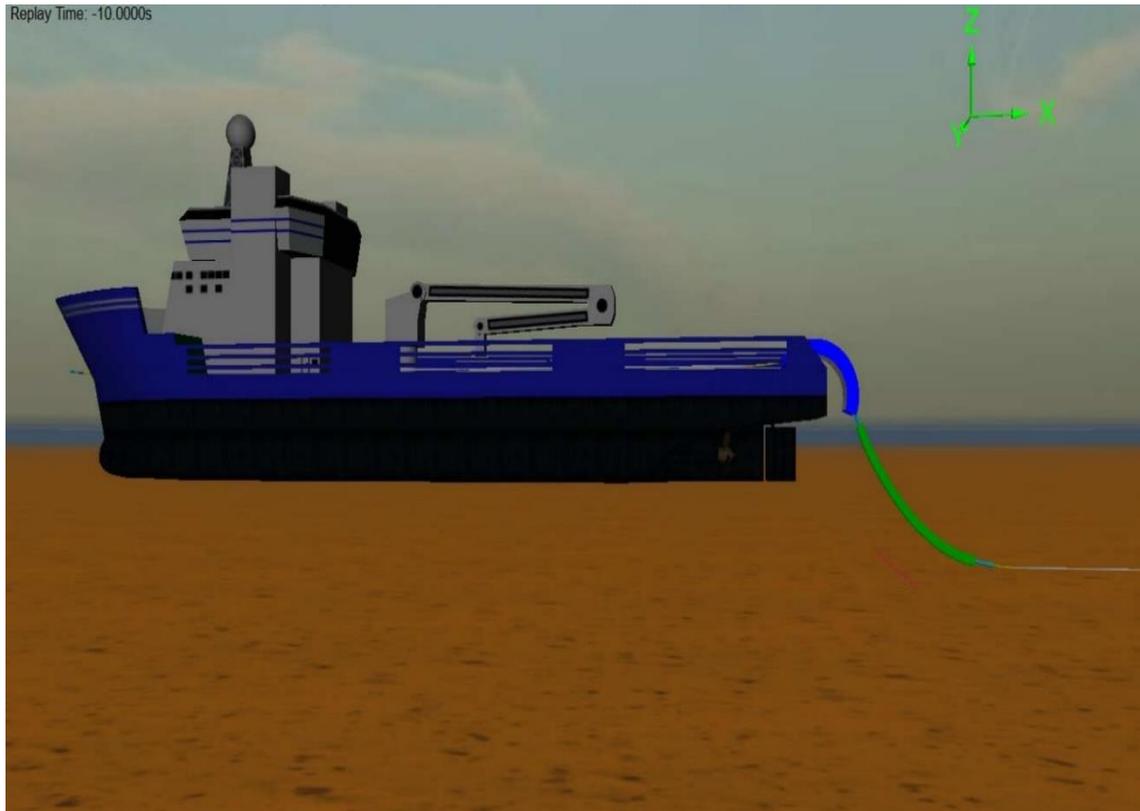
Figure 3-5: Cable crossing -side profile-at start.
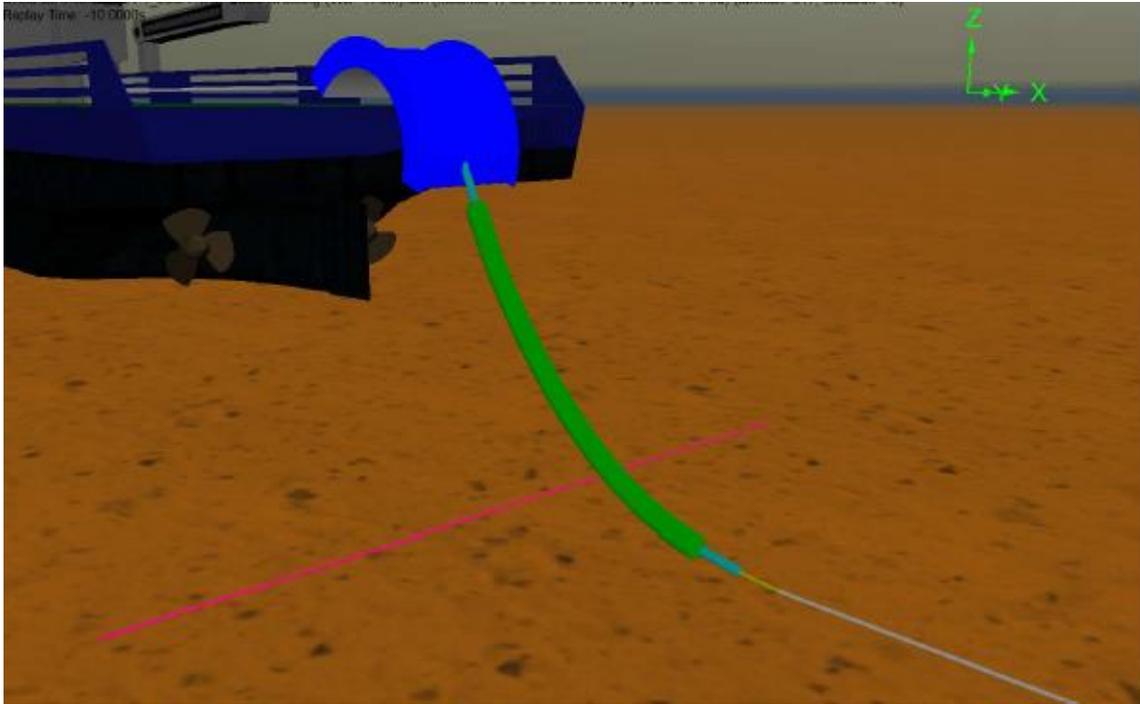
Figure 3-6: Cable Crossing –isometric profile-at start.
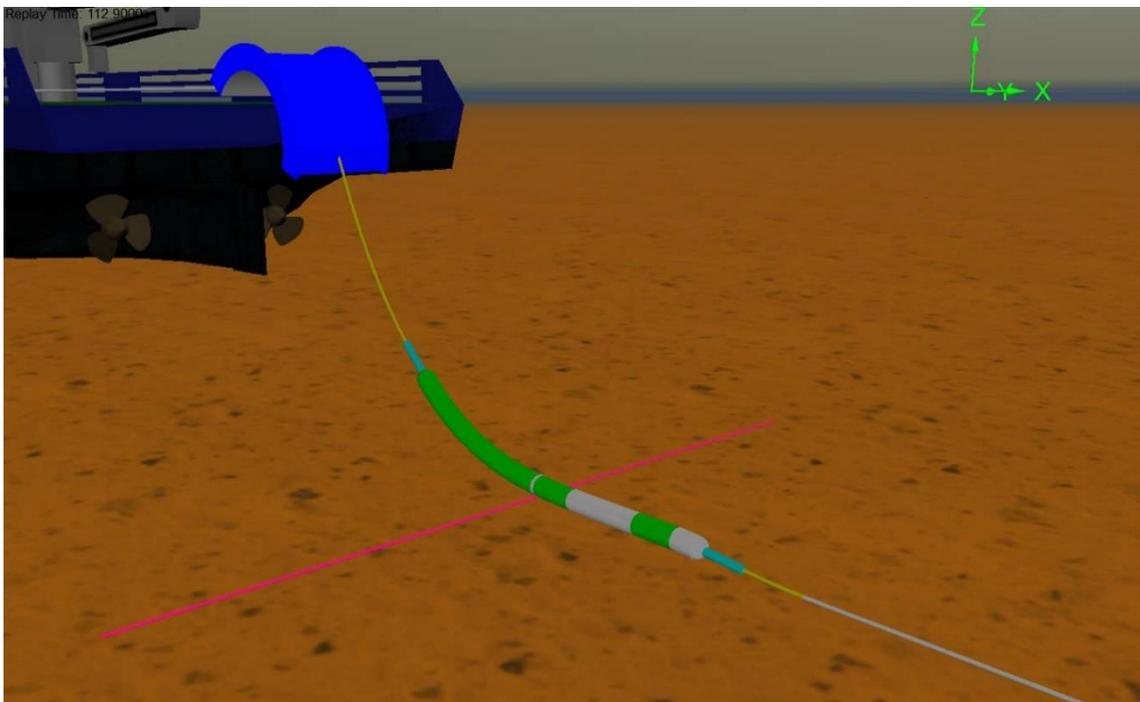
Figure 3-7: Cable crossing –isometric profile-at 50% laying process.
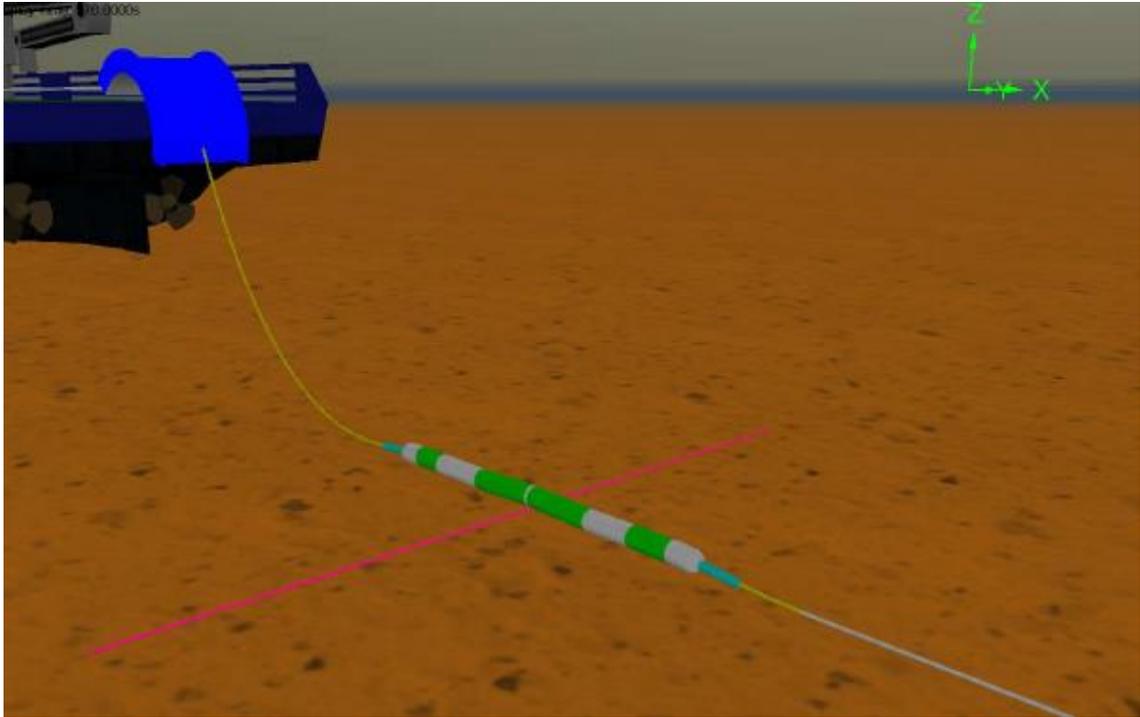
Figure 3-8: Cable crossing –isometric profile-at 100% laying process.

The results shown in Figure 3-9 to Figure 3-20 indicate that the cable experiences axial compression loads at the touchdown point due to the presence of the articulated padding.
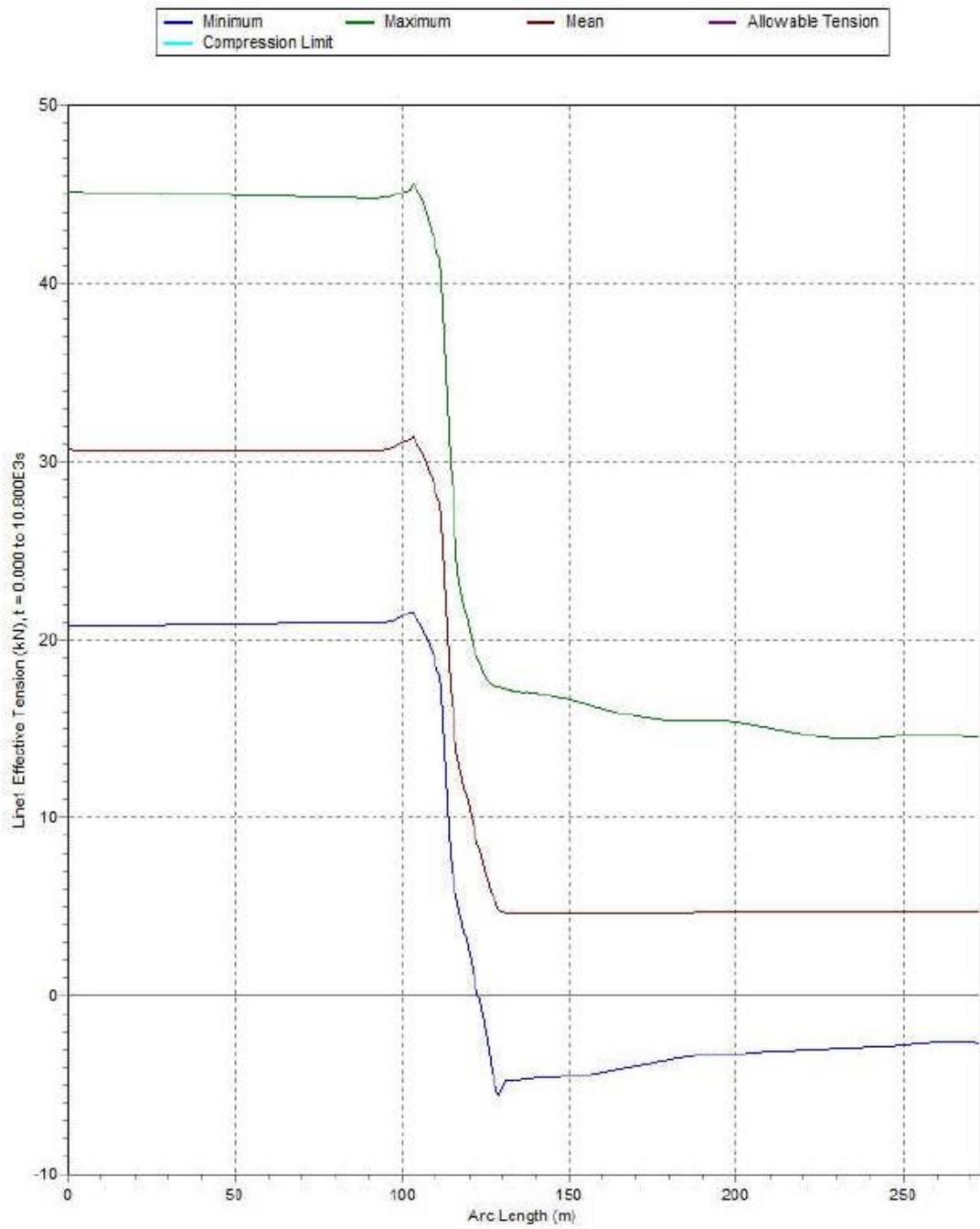
Figure 3-9: Cable tension along the catenary and straight section of the cable on the seabed - Case 1.
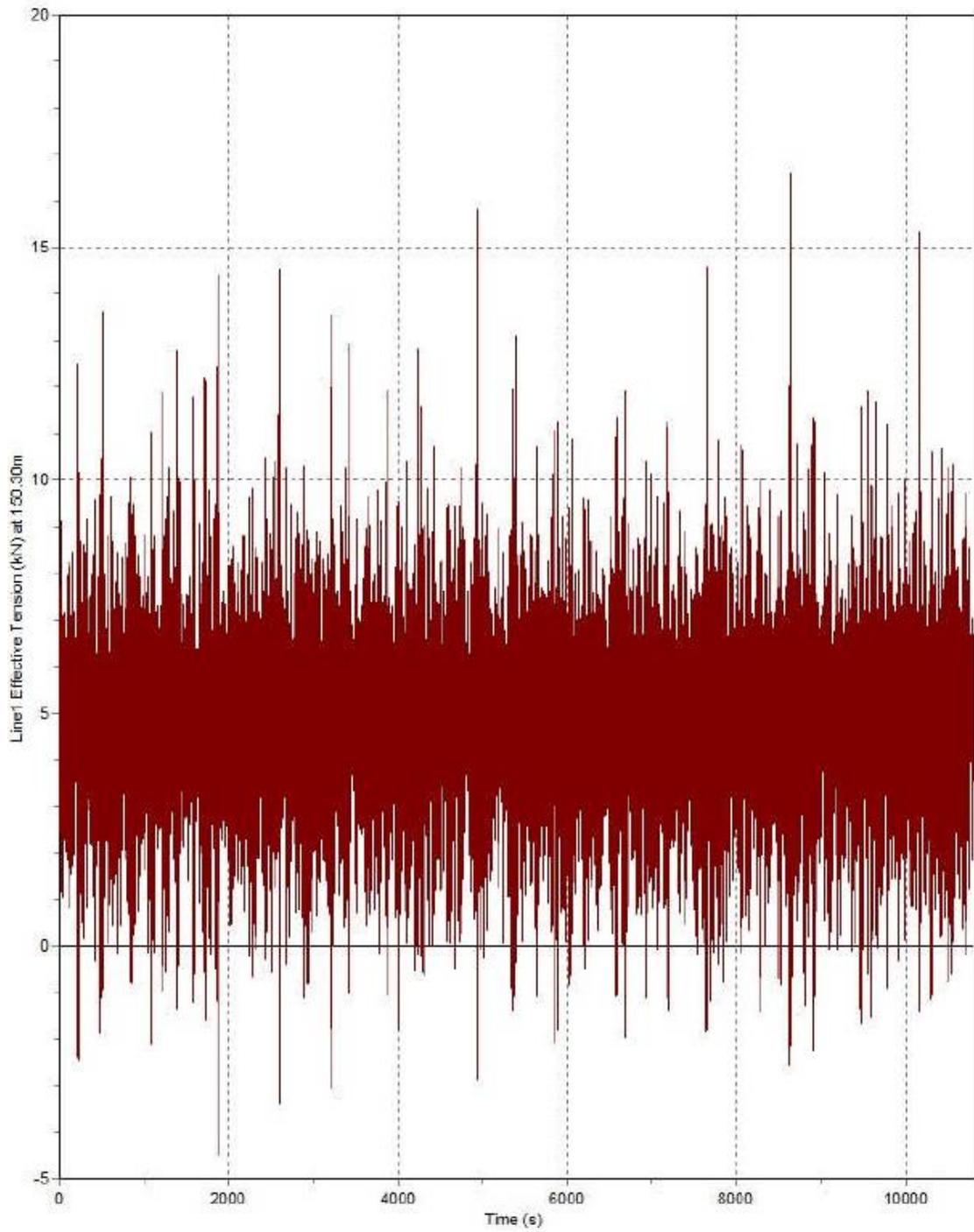
Figure 3-10: Tension history at the touchdown point- Location A - Case 1.
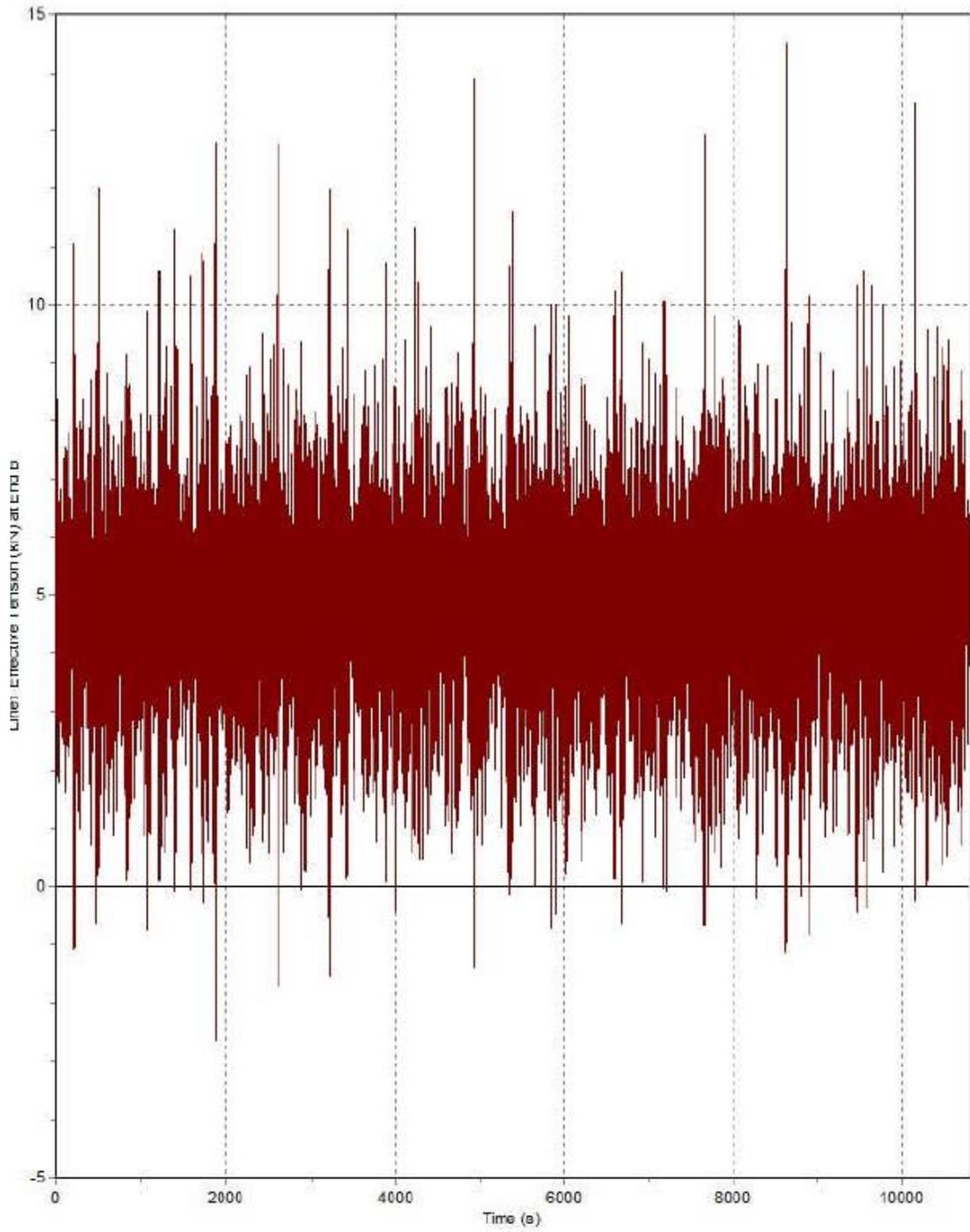
Figure 3-11: Tension history at the touchdown point - Location B – Case 1.
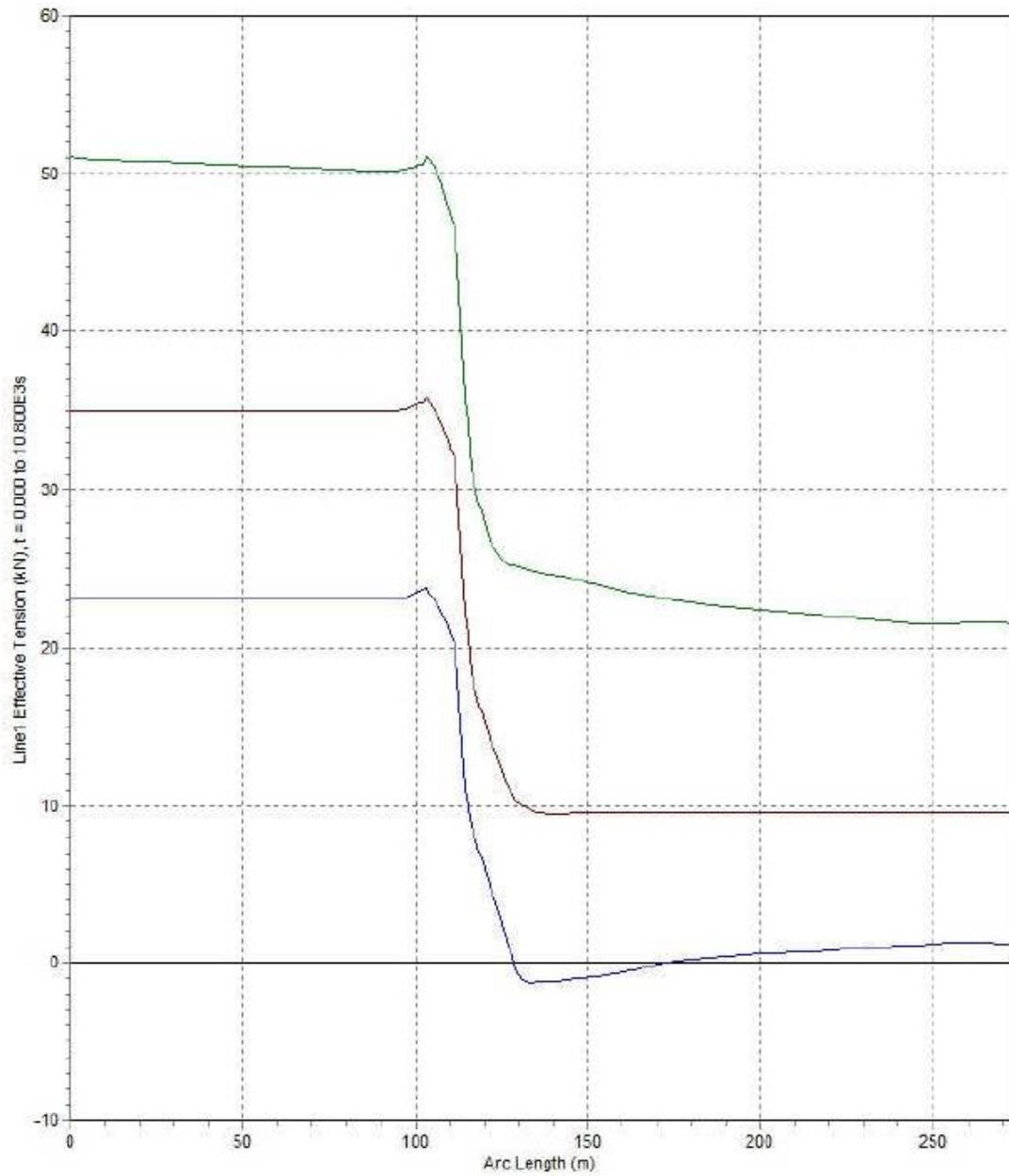
Figure 3-12: Cable tension along the catenary and straight section of the cable on the seabed – Case 2.
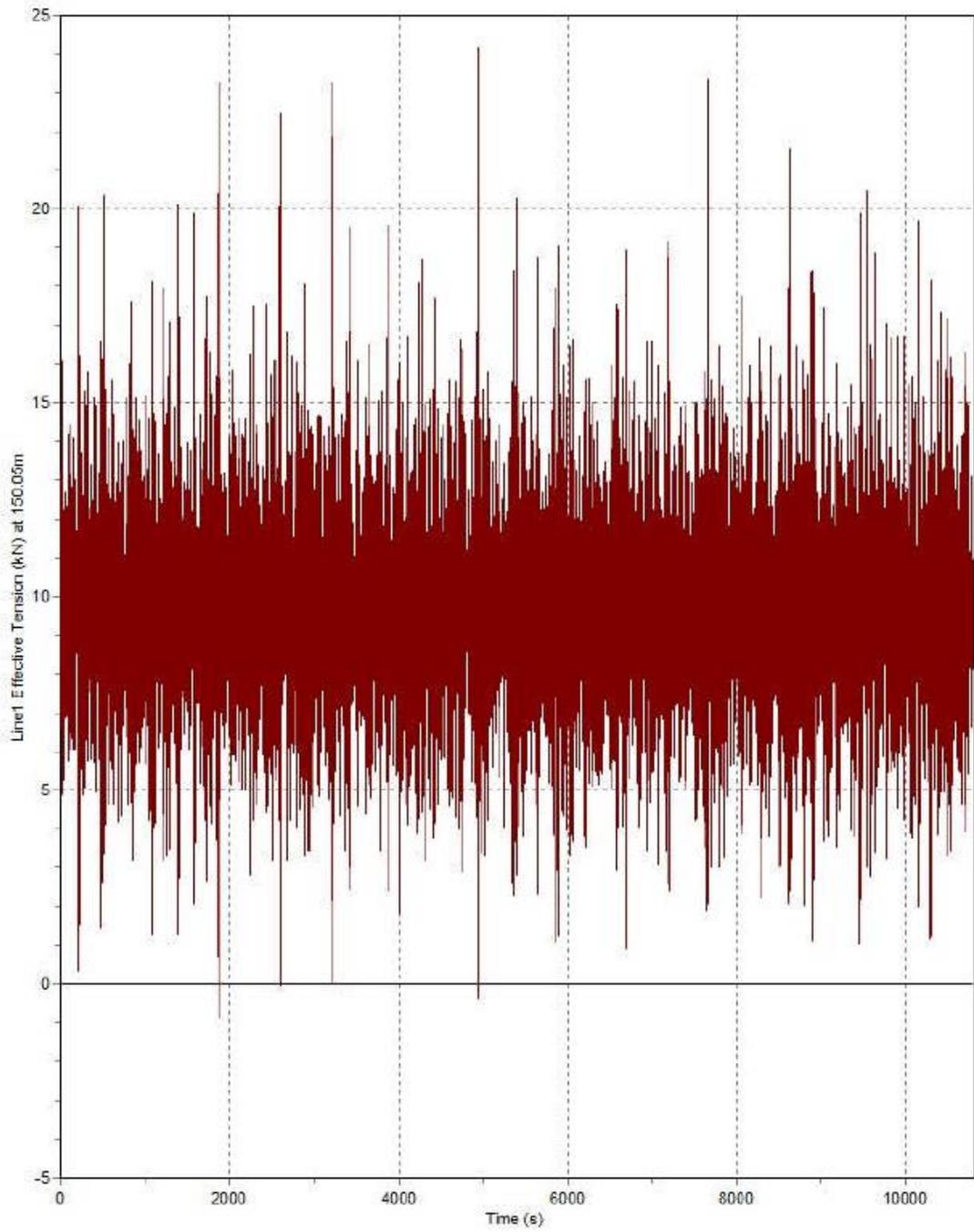
Figure 3-13: Tension history at the touchdown point - Location A – Case 2.
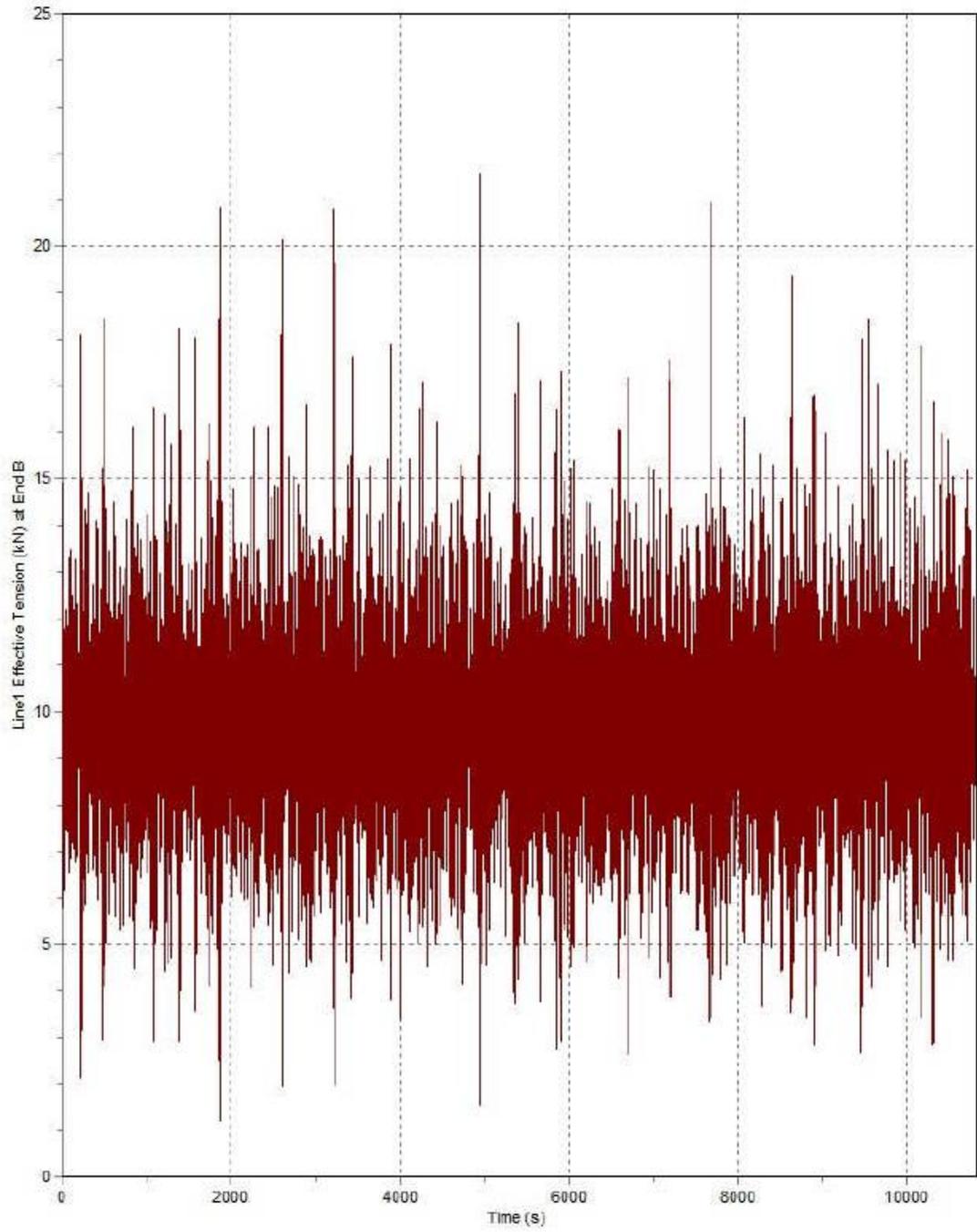
Figure 3-14: Tension history at the touchdown point - Location B – Case 2.
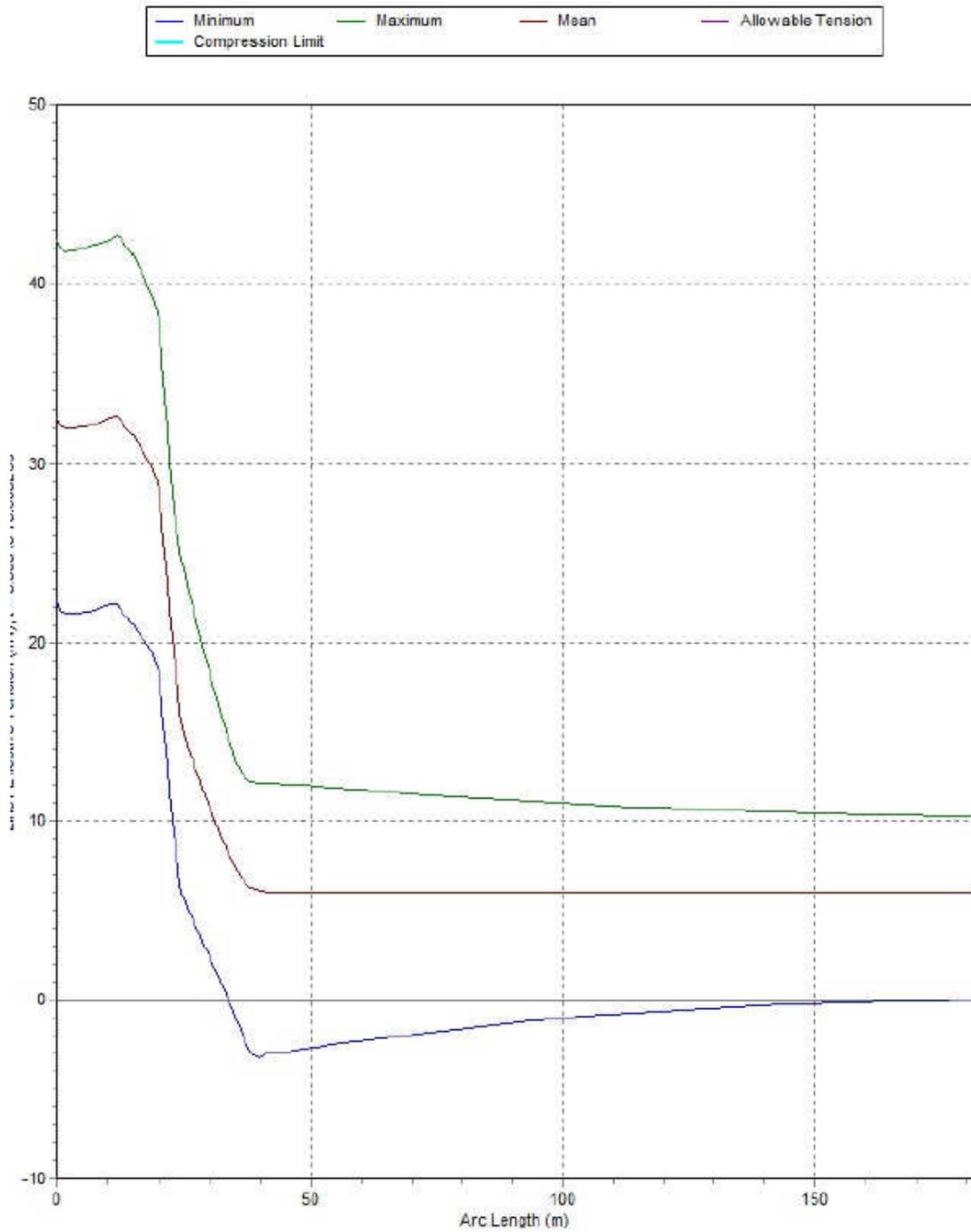
Figure 3-15: Cable tension along the catenary and straight section of the cable on the seabed – Case 3.
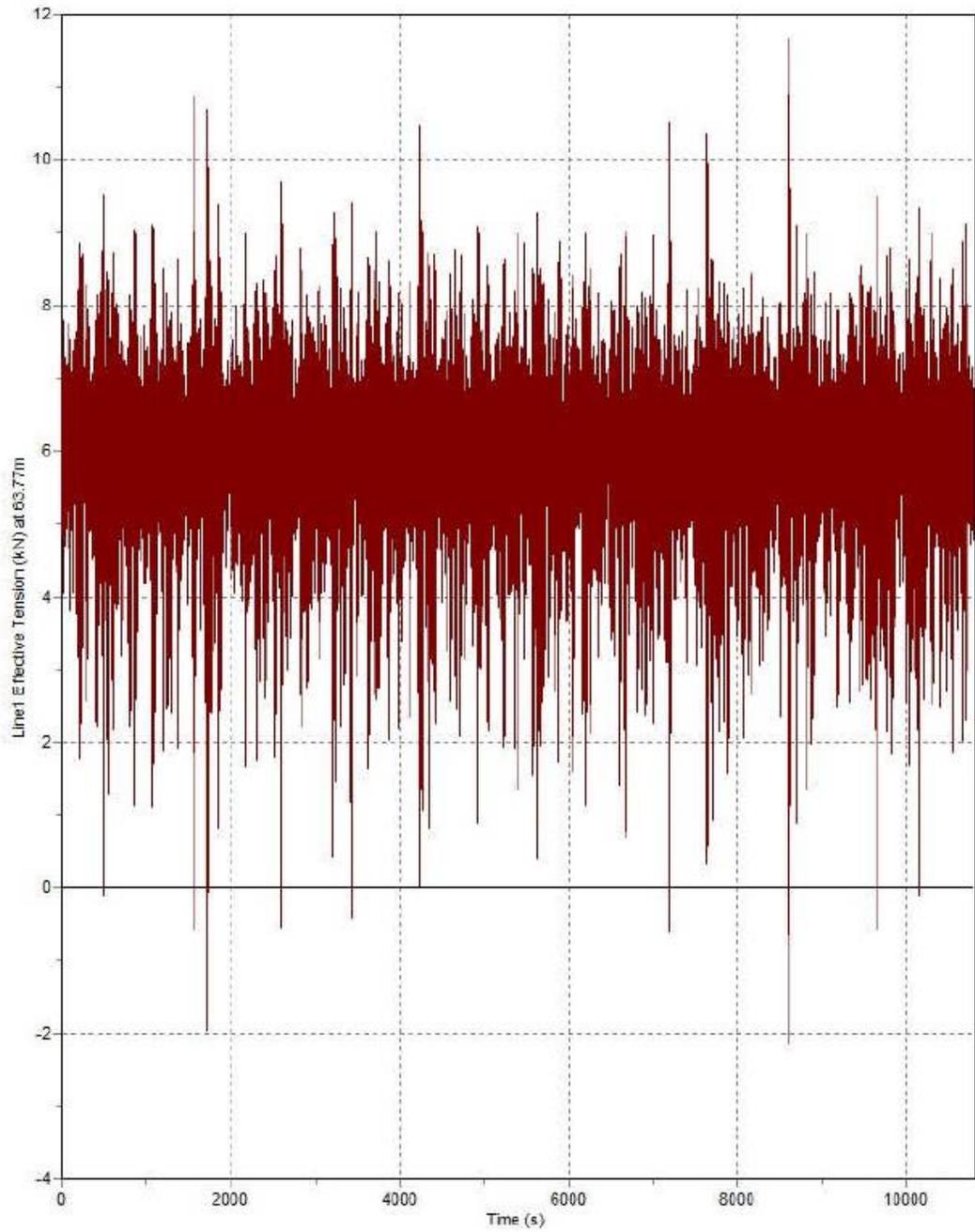
Figure 3-16: Tension history at the touchdown point - Location A – Case 3.
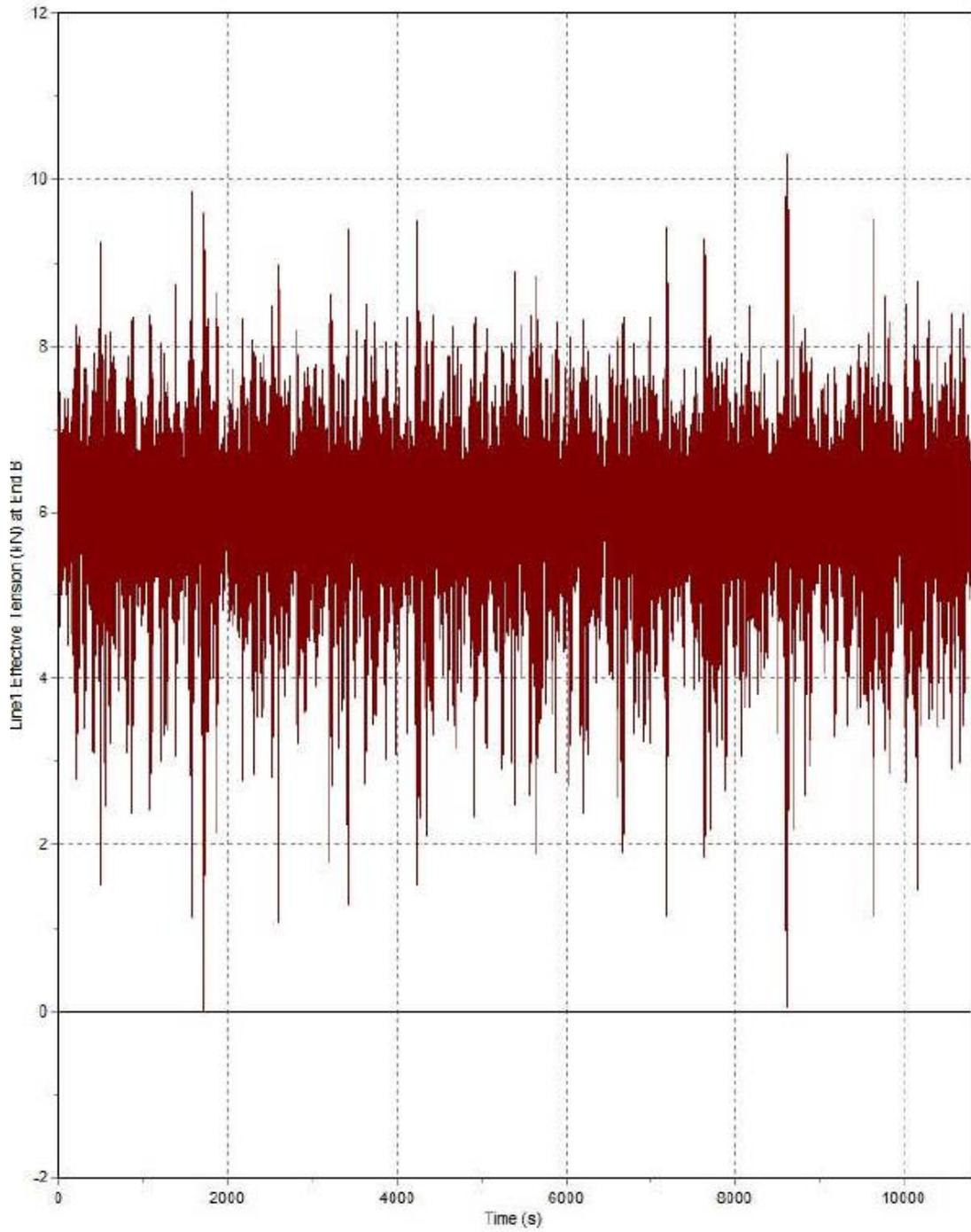
Figure 3-17: Tension history at the touchdown point - Location B – Case 3.
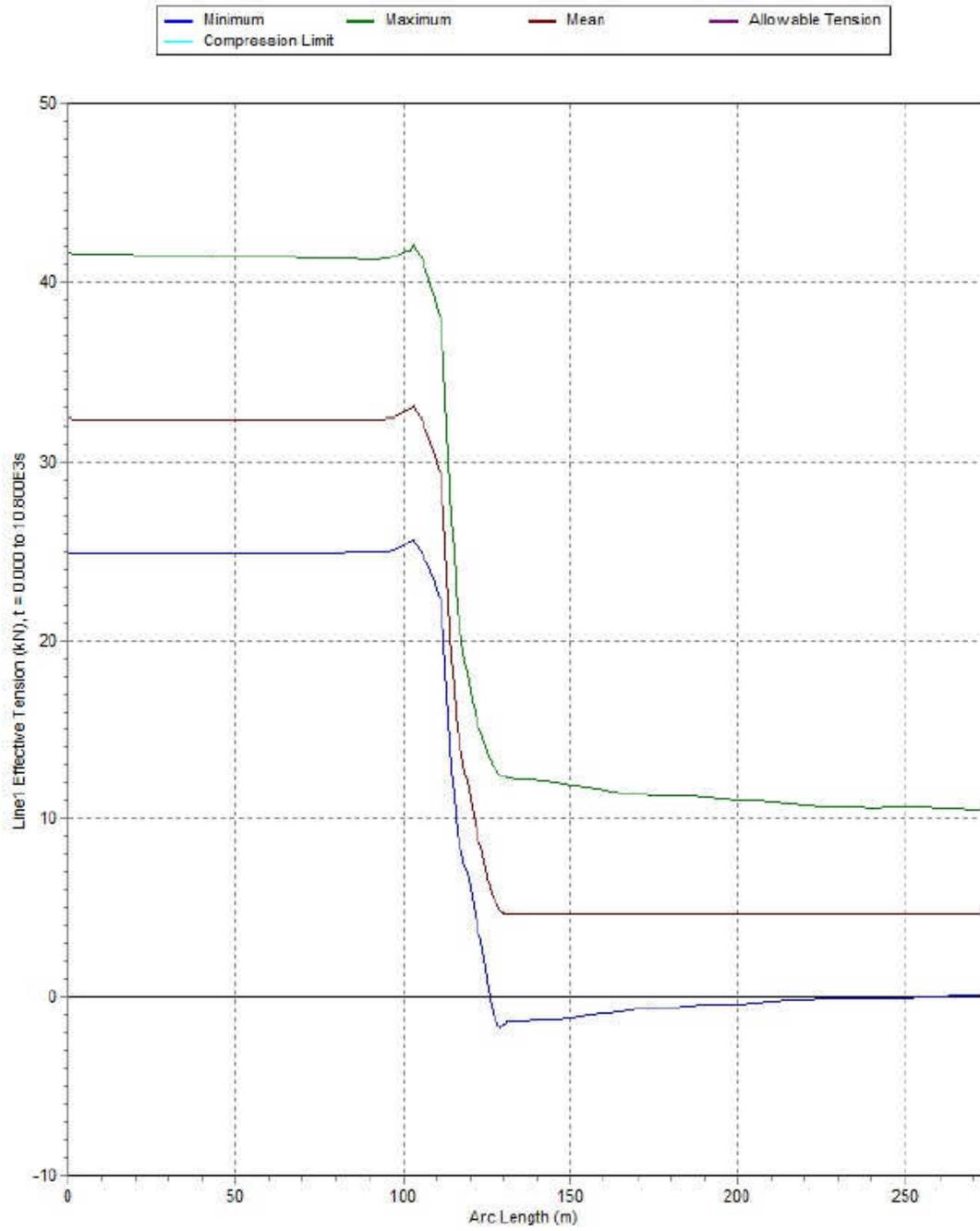
Figure 3-18: Cable tension along the catenary and straight section of the cable on the seabed - Case 4.
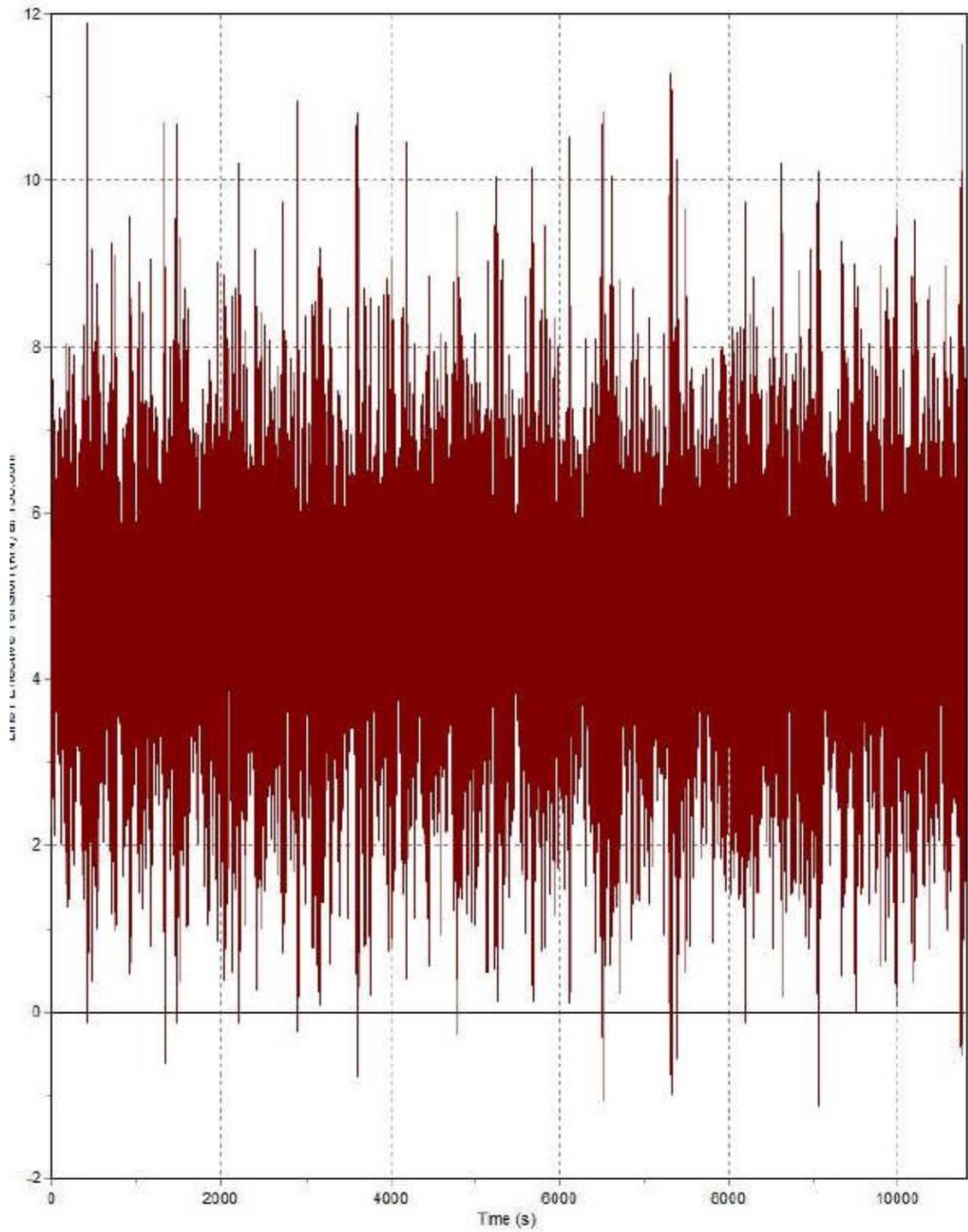
Figure 3-19: Tension history at the touchdown point - Location A – Case 4.
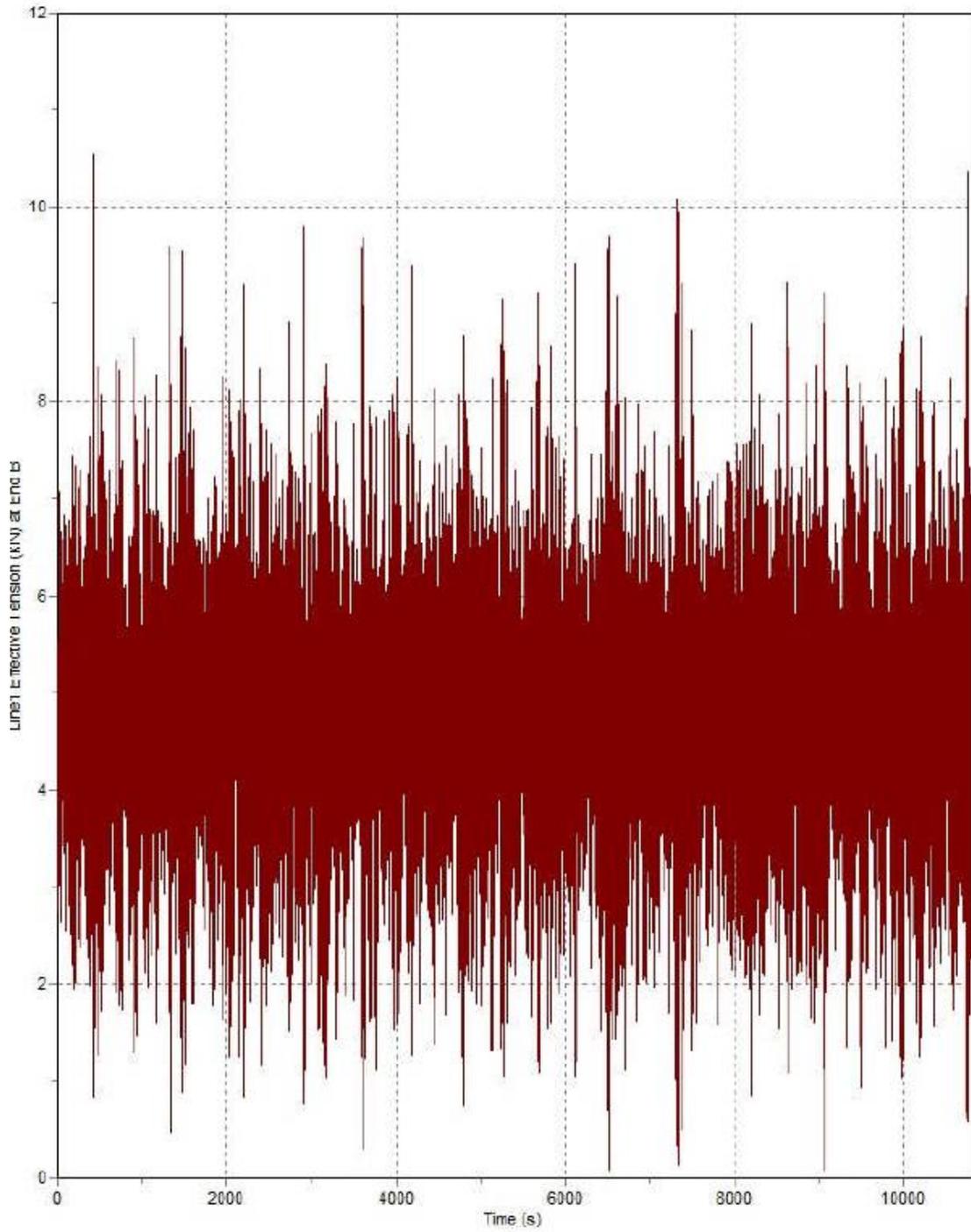
Figure 3-20: Tension history at the touchdown point - Location A – Case 5.

3.1.8 Workability Matrices

To analyse whether the cable and its crossing protection system can be installed for each specific case, given the environmental conditions, workability matrices were created. These matrices quickly show whether or not the cable can be installed. An example of such a matrix is shown in Table 3-7.

Table 3-7: Workability Matrix Example

Dir		V0					Vmax			
Hs (m)		0.5	0.5	1.0	1.0	Hs (m)	0.5	0.5	1.0	1.0
			Bt					Bt		
	Step	8	10	15	30	Step	8	10	15	30
	1	0.0	0.0	0.0	0.0	1	0.0	0.0	0.0	0.0
	2	0.0	0.0	0.0	0.0	2	0.0	0.0	0.0	0.0
	3	0.0	0.0	0.0	115.6	3	0.0	0.0	0.0	118.3
	4	-18.4	0.0	121.3	153.3	4	-24.5	0.0	121.9	154.0
0	5	-3.4	0.0	113.8	142.8	5	-5.0	0.0	113.2	143.6
	6	-10.5	0.0	0.0	103.8	6	-6.1	0.0	0.0	103.5
	7	-0.2	0.0	0.0	0.0	7	0.0	0.0	0.0	0.0
	8	0.0	0.0	0.0	0.0	8	0.0	0.0	0.0	0.0
	9	0.0	0.0	0.0	0.0	9	0.0	0.0	0.0	0.0
	10	0.0	0.0	0.0	0.0	10	0.0	0.0	0.0	0.0

The Table is divided into three main sections: the first section indicates the acting wave and current direction, the second section presents the results per step for a range of bottom tensions without the effect of currents, while the third section provides the results per step for a range of bottom tensions with the effect of currents.

It is possible that for different bottom tensions, different wave heights were analysed. The significant wave height that was investigated is indicated in the header of Table 3-7.

The dark grey cells indicate where the cable limits were exceeded.

If the maximum top tension exceeds the specified limit at the same time that non-allowable compression occurs, the value for compression is given rather than the top tension value. With the use of these matrices one can quickly determine whether a path can be found within the installation parameters for the safe installation of the cable.

The thesis points out that the vessel has the ability to adjust its heading up by to 30 degrees and still be able to install the cable. Thus if a given wave and current direction indicates that the limits will be exceeded, it may very well be possible to change the vessel's heading and install the cable safely with a different wave and current direction.

3.1.9   Discussion of Installation Results

It was found that the compression loads experienced at the touchdown point is governed by the following:

- Crossing object diameter: bottom tension is reduced when the articulated padding settles on a crossing object with a large diameter and hence high compression can take place.

- Weight of the articulated padding: it was noticed that increasing the submerged weight reduced the sensitivity of the articulated padding to vessel and wave motions and high tension or compression did not occur at the touchdown point. In other words, increasing the submerged weight of the articulated padding made the articulated padding less susceptible to environmental loading.

- High layback distance: increasing the layback distance increased the effective tension across the cable to unacceptable levels in the post-burial operation. However, no compression took place.

It was observed that the current acting on the cable and articulated padding system caused a lateral offset of the touchdown point. The significantly increased diameter of the articulated padding system caused a larger offset compared to the offset that occurs during normal cable lay. Needless to say, significant offset from planned routes is undesired.

This can be further explained by Figure 3-21 and Figure 3-22.
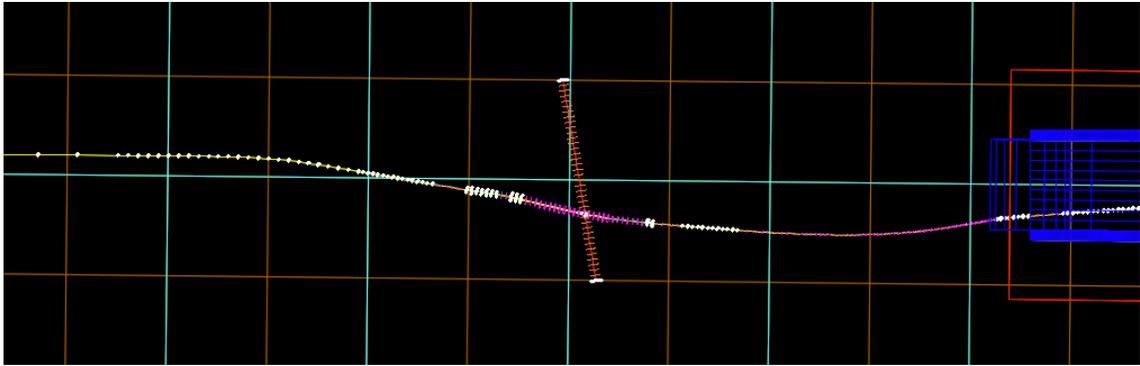
Figure 3-21: Lateral offset of 5.5m due to current, water depth = 11 m.
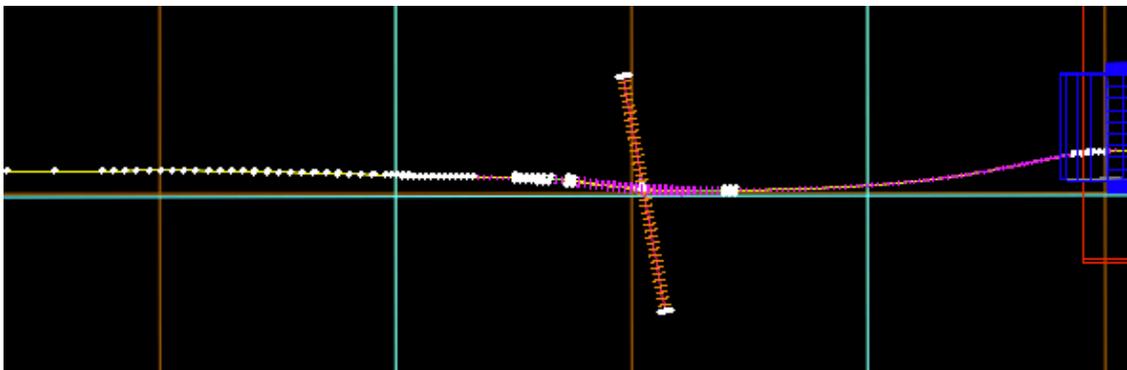
Figure 3-22: Articulated padding installation including current and predetermined required vessel offset.

- **Wave and current direction**

The cable laying vessel used in the numerical simulations were found to be sensitive for waves acting in the direction of 60 and 120 degrees, where pitch, roll and heave motions were combined. Pitch and heave motions cause vertical velocities and acceleration at the stern of the vessel, which are directly transferred to the cable-articulated padding system. The results indicated that the installation limits were exceeded for these directions at almost every crossing.

The significant response can be visualized by looking at the Response Amplitude Operators (RAO) graphs. The peak in the RAO plot (Figure 3-23) is at a period of approximately 6.7 s, which coincides with the peak period of the wave spectrum, which

is also 6.7s. However, the selected vessel is capable of adjusting its heading with 30 degrees of freedom while continuing the lay operation. This would enable the selected vessel to perform a safe installation at a different wave and current direction, as long as that direction did not exceed the installation limits.
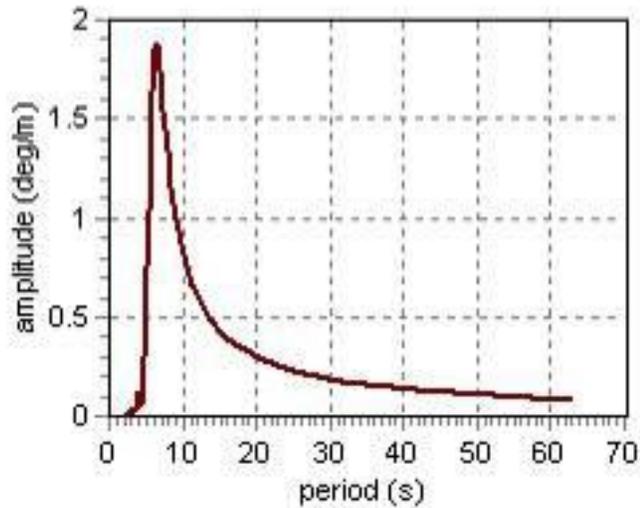
Figure 3-23: RAO for pitch

- **Geometry articulated padding systems**

The results indicate that the length of the articulated padding system in the catenary significantly influences the results of the simulation. The longer the articulated padding system was, especially the articulated padding section, the more undesirable the results were, in terms of compression loads, effective tension and minimum bend radius. A longer articulated padding system not only introduces additional mass, but the area sensitive to waves and current is also extended. This leads to exceeding installation limits and the inability to install the cable with its protective system for a large proportion of crossings at a simulated significant wave height of 1.5m. These crossings were therefore simulated with a lower significant wave height (H_s).

- **Distance between crossings**

For some simulations, the distance between one crossing and the next was less than 60 m. This means that the articulated padding system of the next crossing has an influence on the results from the simulated crossings. The presence of the second articulated padding system dampens out some of the tension, with possible positive effects on the bottom tension and consequently negative impacts on trenching operations.

- **Water depth**

It was observed that installing the articulated padding in deep water introduces additional dampening of the system. It was determined that the installation of the articulated padding system in shallower water resulted in larger compression values, but these did not necessarily exceed installation limits. Some of the other rejected simulations were those in deeper water with longer articulated padding systems, which resulted in the installation limits being exceeding.

3.2 TESTING SCHEME

Two tests were developed to test the compressive limits of a subsea cable. The two tests were:

1.   A standard compressive test of a short length of cable. This was considered a supplementary test.

2.   A test with both compression and bending applied to a longer length of cable. This more accurately represents the type of loading a cable will experience during installation.

During normal lay operations, the tension is highest at the tensioner, which is located on the vessel. The tension then reduces along the cable catenary towards the touchdown point and reaches a minimum at the area illustrated in Figure 3-24. The movement of the vessel under the influence of the hydrodynamic loading combined with the low applied tension

at the tensioner results in a) bending combined with axial compression loads at the area close to the touchdown point and b) pure axial compression just after the touchdown point. At the touchdown point there is negligible bending in addition to axial compression however it is the axial compression that is dominant.
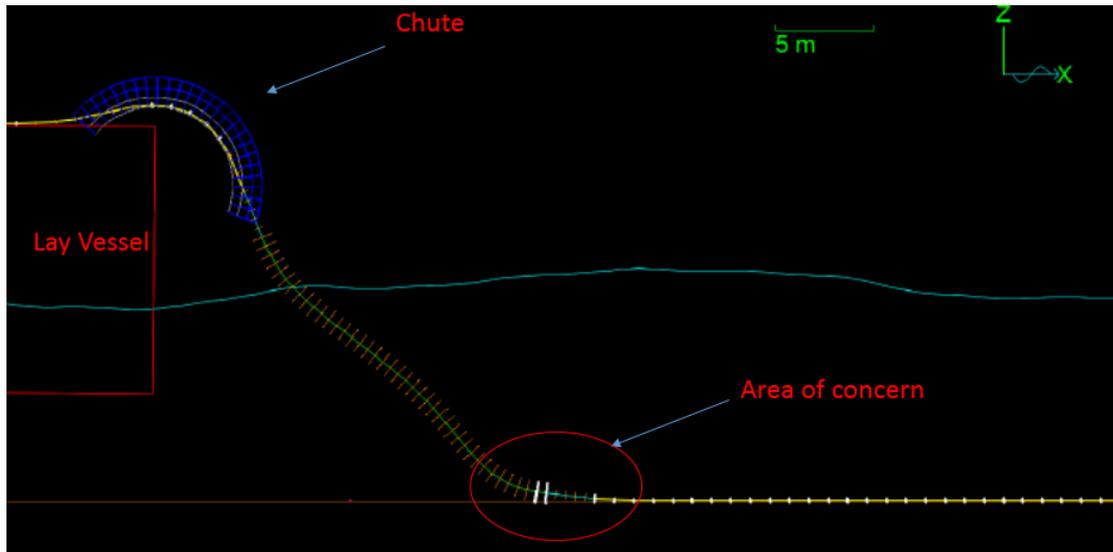
Figure 3-24: Schematic representation of cable installation.

3.2.1 Axial Compression Test

The axial compression test was used to a) validate the axial load at the middle of the test length and near End-2 in the bending compression test (see Section 3.2.2 for more details) and b) determine the pure axial compression limit of the cable. The results from this test were used to ensure that the cable does not buckle in the small area just after the touchdown point. In that area, the bending moment is negligible and can be considered to be zero and thus the load is purely in the axial direction.

The test was performed as depicted in Figure 3-25. In this test, the cable sample was only subjected to axial compression loads (P_c). During the test, strain gauges were positioned in the middle of the cable.
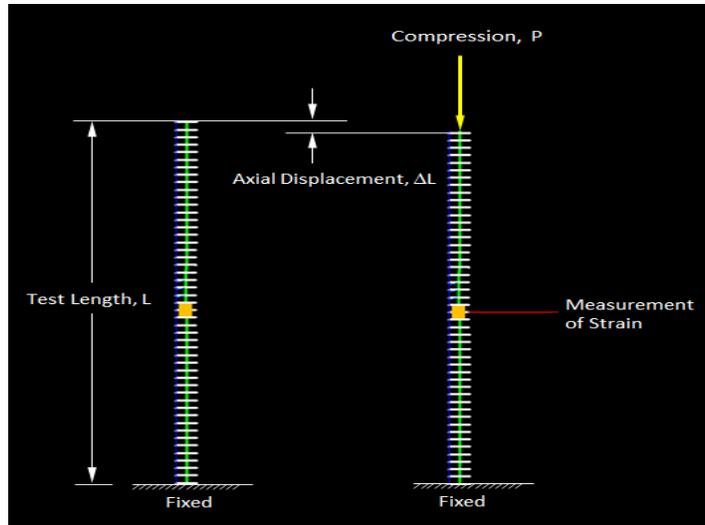
Figure 3-25: Axial compression test.

3.2.2 Bending Compression Test Concept

Figure 3-26 to Figure 3-28 illustrate the concept of the bending compression test employed during this investigation. This test was performed to determine the compression limits of the subsea cable. As shown in Figure 3-26 and Figure 3-27, one end is connected to the tensile machine and will be denoted throughout this thesis as End-1. The other end is clamped, in order to mimic the sag bend zone of the cable above the seabed and will be referred as End-2.

As per Figure 3-26 and Figure 3-27, the compression load was applied to the test cable sample via the tensile test machine. The tensile test machine was connected to the cable end via a grip. This grip was attached to the cable that was connected to the tensile test machine via a shackle and a sling. The tensile test machine applies the load as shown in Figure 3-26 to Figure 3-28. The measurement of the pulling tension is achieved through a load cell installed in the tensile test machine.
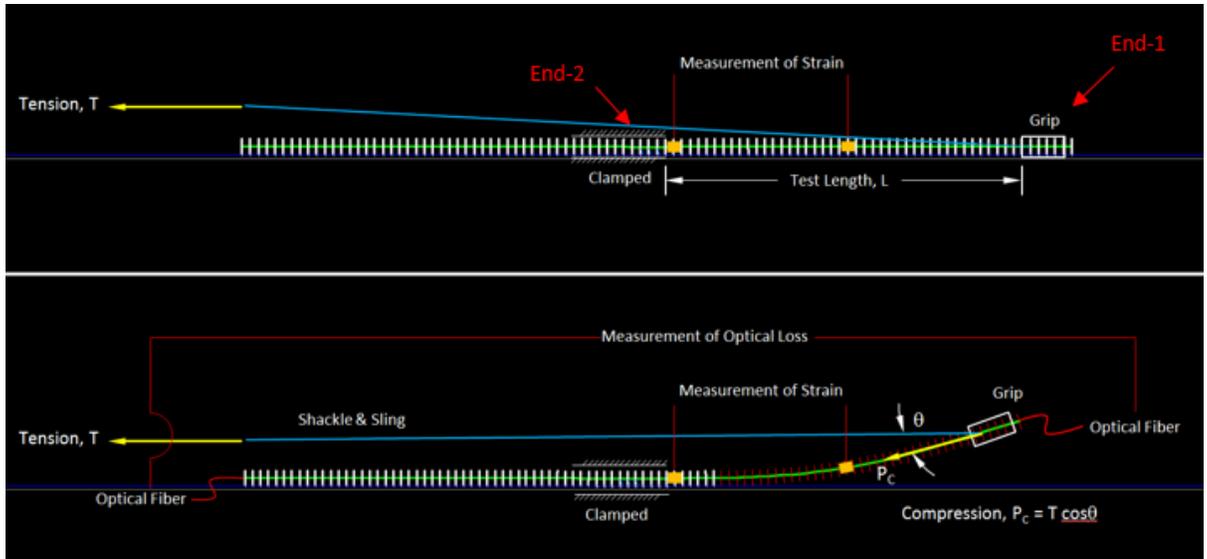
Figure 3-26 : Concept of bending compression test.

Figure 3-27: Test rig used during bending compression test.

Figure 3-28: Photo of the grip attached to the cable.

The compression load, P_C, is determined from the applied tension, T, and the angle, θ, between the pulling wire and the cable at the gripping location. The cable sample length, L, was measured from End-1 to End-2 and excludes the grip length.

During the test, strain gauges were positioned at two locations, as shown in Figure 3-26. The first location is at the centre of the test length, while the second location is close to End-2. During the entire test, the integrity of the cable was monitored by continuous measurement of the fibre optical power. The bending compression test was undertaken for two different cable lengths.

3.2.3 Methodology

The following section describes the methodology adopted in order to determine the allowable axial compression load of the submarine cable. The measured parameters, during the bending compression test as well as the axial compression test, were utilised to provide the compression limit state of the submarine HVAC cable. The compression load, P_C, at the gripping location, is shown in Figure 3-29 and can be calculated using Equations (3-1) and (3-2).
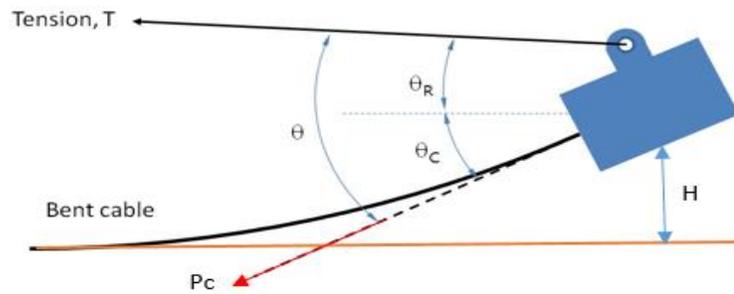
Figure 3-29: Angle (θ) between pulling sling and cable.

Resolving the applied tension into the direction of the cable gives,

$$P_C = T \cos\theta,$$

3-1

where,

$$\theta = \theta_C + \theta_R,$$

3-2

and,

   T: pulling tension [kN] applied via the tensile machine,

   θ : angle between pulling wire and cable at gripping location [deg],

   θ_R : angle of pulling wire [deg],

   θ_C : angle of cable [deg].

The bending moment at the clamped location, M_C, as highlighted in Figure 3-30, is given by,

$$M_C = T_H H = T \cos\theta_R\, H,$$

3-3
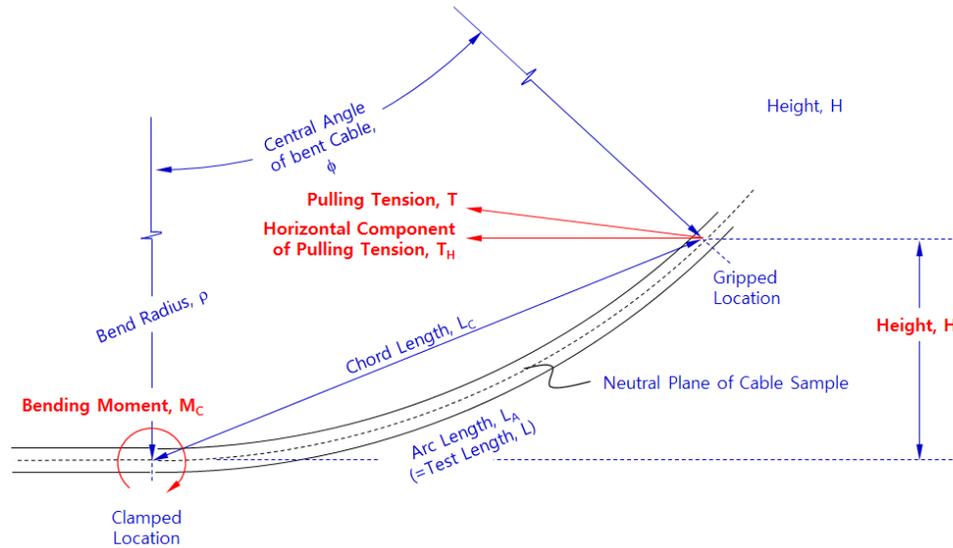
Figure 3-30: Geometry of bent cable.

The central angle of the bent cable can be approximated by measuring the chord length, L_C, using the expression:

$$\frac{L_A}{L_C} = \frac{\phi}{2\sin\frac{\phi}{2}},$$

3-4

where

ϕ: central angle of bent cable [rad],

L_A: arc length of bend cable [mm],

L_C: chord length of bent cable [mm].

The central angle, ϕ, can also be determined, as it is equal to the cable angle, θ_C, as shown in Figure 3-31.
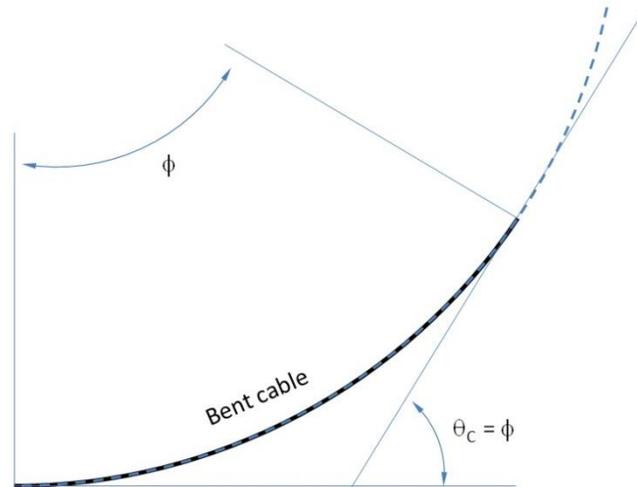
Figure 3-31: Relationship between central angle, ϕ, and cable angle, θ_C.

The bend radius, ρ, of the test sample can be determined from the following:

$$\rho = \frac{L_A}{\phi}.$$

<div align="right">3-5</div>

It can be seen from Figure 3-32 that the strain gauges can be utilised to determine the following:

- The compression load at the middle length of the test sample (P_{CM}),

- The compression load near End-2 (P_{CC}).

The compression loads, P_{CM} and P_{CC}, are identified using the load-strain relationship derived from the axial compression test.
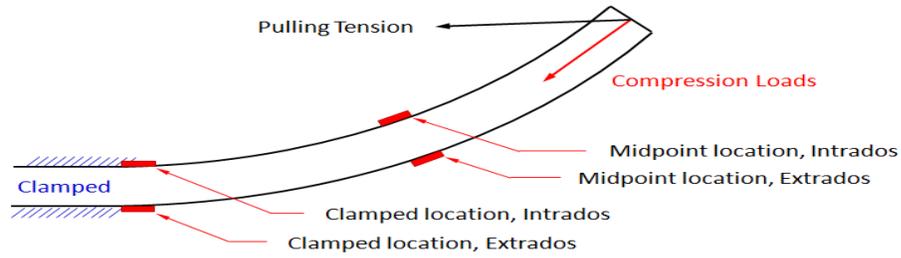
Figure 3-32: Locations of strain gauges in the bending compression test.

Using the measurements from the axial compression test, the axial stress and axial strain can be calculated as per Equations (3-53-6) and (3-7) respectively,

$$\sigma_{eff} = \frac{P_C}{A},$$

3-6

$$e = \frac{\Delta L}{L},$$

3-7

where,

σ_{eff} : effective stress [MPa],

P_C : compression load [N],

A : cross section area [mm²],

e : axial strain [-],

ΔL: axial displacement [mm],

L : length of cable sample [mm].

3.3   TEST SET-UP

3.3.1   Submarine Cable Data

The cross section and the mechanical properties of the tested submarine cable are highlighted in Figure 3-33 and Table 3-8 respectively.
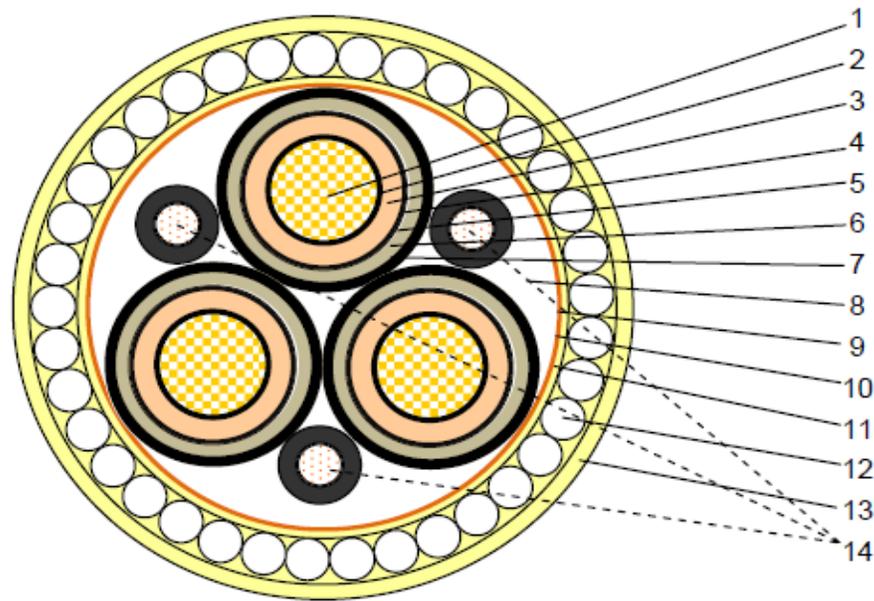
Figure 3-33: Configuration of 132kV HVAC submarine cable.

Table 3-8: Mechanical Properties of 132kV HVAC Submarine Cable

Item	Value	Unit
Outer diameter	191	mm
Weight in air	70	kg/m
Weight in seawater	41	kg/m
Axial stiffness	650	MN
Bending stiffness	26	kN.m^2
Allowable tension (straight pull)	160	kN
Allowable tension (on MBR pull)	115	kN

Item	Value	Unit
Minimum bending radius (for installation)	2.9	m
Minimum bending radius (for storage)	4.0	m

Subsea cables are composite structures consisting of helical armouring layers, polymer layers and copper conductors. The result is a cable with high axial stiffness and low bending stiffness. Insulated conductors are twisted together to form the cable assembly giving a high degree of flexibility and good electrical properties. A layer of galvanised round steel wire armour provides enhanced tensile axial strength and impact and crush resistance to the fibre cable. Technical specifications of the cable regarding layer interaction properties are presented in Table 3-9.

Table 3-9: Technical Specification of 132kV HVAC Submarine Cable

No.	Description	Details	Thickness (mm)	Indicative Diameter (mm)
1	Conductor	Annealed copper, circular compact, watertight	-	26.3
2	Conductor screen	Extruded semi-conducting compound	1.3	31
3	Insulation	Extruded cross-linked polyethylene	16	63
4	Insulation screen	Extruded semi-conducting compound	1	65
5	Water blocking layer	Semi-conducting swelling tape	0.9	-
6	Metallic sheath	Lead alloy sheath	2.6	72
7	Oversheath	Extruded semi-conducting polyethylene	2.0	76
8	Filler	Polypropylene yarn	-	-
9	Binder tape	Polymeric tape	0.45	166

No.	Description	Details	Thickness (mm)	Indicative Diameter (mm)
10	Anti-teredo protection	Cooper tape	0.16x2	167
11	Armor bedding	Polypropylene yarn with bitumen	2.0	171
12	Wire armour	Galvanised steel wires with bitumen	Diameter 5.6	182
13	Serving	Polypropylene yarn	4.0	191
14	Optical fibre unit	-	-	-

3.3.2 Axial Compression Set-Up

An axial compression test on a cable sample of length 1.6 m was conducted as illustrated in Figure 3-34. The universal testing machine INSTRON 5982, which has a capacity of 100kN, was utilized for the performance of the axial compression test. The test was conducted as per the following steps:

1. Both ends of the cable sample were milled carefully to ensure that the axial load was applied uniformly across the cross-section of the cable.

2. Two strain gauges were attached to the middle of the test sample.

3. The cable sample was placed vertically between two steel plates. It was ensured that the steel plates were aligned and that both cable ends were placed at the centre of the steel plates. This was to ensure that the load was concentric.

4. The load capacity and test speed were checked. The load and displacement were then adjusted for initial readings.

5. The test started with an initial axial load of 0kN, which was increased at a rate of 1.0 mm/min. The compression load was increased to 90.0 kN.

6. During the test, the compression load and the corresponding axial displacement were continuously recorded. Furthermore, the strain from the strain gauges were

continuously measured with respect to the compression load. The strain gauges were then attached to the wire armours at two different locations (6 o'clock and 12 o'clock).

Figure 3-34: Axial compression test arrangement.

3.3.3   Bending Compression Set-Up

The tensile test machine, used in the bending compression test, has a capacity of 100 tonnes, as shown in Figure 3-35 and Figure 3-36. The tensile load machine was equipped with load cells to measure the axial tension and the displacement stroke of the tensile load machine.

Figure 3-35: Tensile test machine (100 metric tonne capacity).

Figure 3-36: Photo of the tensile test machine.

The following steps were followed during the bending compression test:

1. A cable sample 2.0 m in length was placed at the bottom of the test rig.

2. Strain gauges were attached at two locations with two strain gauges at each location (one at the intrados and the second one at the extrados). The first location

was at the centre of the test length, L, while the second location was close to End-2.

3. End-1 and End-2 were connected to a power meter to measure optical power, α. The initial value of the optical loss was measured to set up a baseline of the fibre optical losses.

4. End-1 was gripped while End-2 was clamped by means of fixtures.

5. End-1 was connected to a shackle, located at the cross-head of the tensile machine, via a sling.

6. Electrical connectivity of all the wiring and sensors were confirmed.

7. The test commenced by movement of the cross-head connected to End-1. This pull increased the curvature of the tested cable as shown in Figure 3-37 to Figure 3-39. The pulling test speed was 1 mm/sec to ensure that the loading was applied in a quasi-static fashion.

Figure 3-37 : Initial position of End-1 before commencing the test.

Figure 3-38: End-1 during the test.

8. During the test, optical light power, α, was continuously monitored to detect any damage to the cable.

9. Every 10 or 20 mm of pulling displacement, the test was paused in order to measure the following parameters (see Figure 3-39):

   - Chord length, L_C
   - Height, H
   - Tension, T
   - Angle, θ

10. The strain gauges near End-2, e_C, and at the middle length of the test sample, e_M, were continuously monitored.
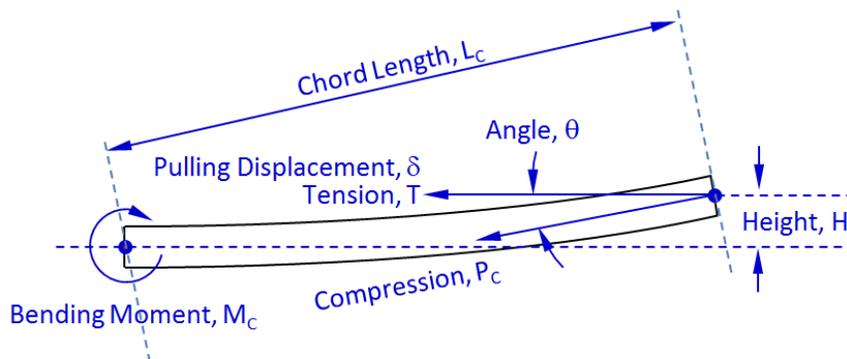
Figure 3-39 : Parameters measured during the bending compression test.

100

11. The test was progressed until the fibre optic loss was indicated to be 0.2 dB.

12. The bending compression test sample of length 1.3 m, and steps 1 to 10 were repeated.

3.4   TEST RESULTS AND DISCUSSIONS

3.4.1   Axial Compression Test

Figure 3-40 presents the relationship between axial compression load and axial displacement for a 1.6 m cable length as derived from the axial compression test. It can be seen from the figure that when the axial compression load was 90 kN, the corresponding axial displacement was 7.3 mm. As expected, there are slight variations in the slope of the curve of Figure 3-40. This is because the submarine cable consists of multiple layers made from different inhomogeneous materials. It is obvious from Figure 3-40 that there is no sign of yielding or material failure.
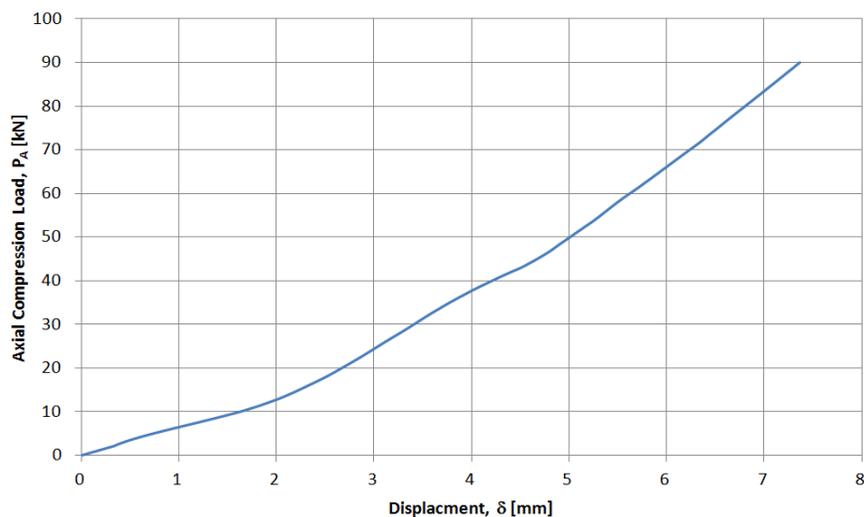
Figure 3-40: Relationship between axial compression load and axial displacement for a 1.6m cable sample.

Figure 3-41 illustrates the relationship between axial stress and axial strain as calculated using Equations (3-6) and (3-7). It is evident from the figure that the axial compressive

strain, e, can be used to determine the allowable axial compression load. Current industry standards do not provide any guidance or recommendations for how to determine the axial strain limit of submarine cables. For this specific submarine cable, we may assume 0.2% (or 0.002) as the allowable compressive strain limit based on the offset method. The offset method is the well-known method to determine the yield point or elastic limit of a material which does not have an obvious yield point (Gere & Timoshenko, 1984). The axial stiffness was calculated based on Figure 3-40 where the average slope from 0 to 90 kN was taken. The resulting calculation is

$$\text{Axial Stiffness (EA)} = \frac{Stress}{Strain} \times A = \frac{\frac{(P_F - P_0)}{A}}{\left(\frac{\text{Displacement}_F - \text{Displacement}_0}{L}\right) \times A}$$

$$= \frac{(P_F - P_0) \times L}{(\text{Displacement}_F - \text{Displacement}_0)} = \frac{90\text{kN x } 1620 \text{ mm}}{7.368 \text{ mm}} = 19.8 \text{ MN}$$

The result for axial stiffness was shown to be lower than the value specified in Table 3-8 (650MN). This is because the value presented in Table 3-8 was obtained from a tension test. It can be seen that the axial stiffness for compression is 32 times lower than the axial stiffness reported in Table 3-8. It is recommended that analyses should use different values for axial stiffness depending on whether it is for tension or compression.
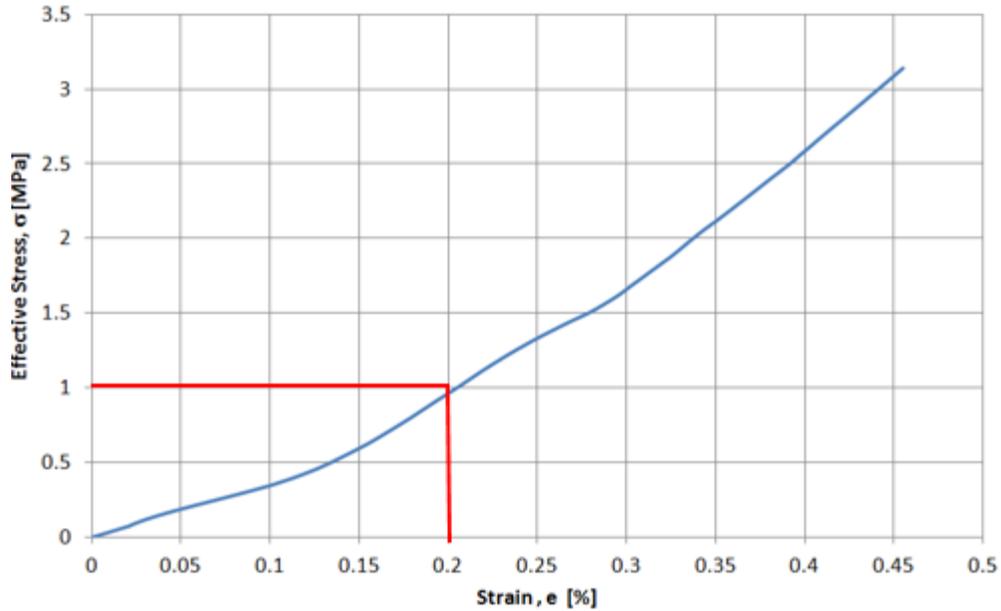
Figure 3-41. Stress and strain relationship of 1.6m cable sample under pure compression.

It can be seen from Figure 3-40 and Figure 3-41 that the stress-strain relationship exhibits non-linear behaviour. Non-linearity on stress-strain can be caused by many factors such as material non-linearity and the effects of the interaction between adjacent components of the cable so that the strain distribution within the cable cross-section is not constant.

Figure 3-42 illustrates the resulting stress of the wire armours under the pure compression load. The stresses are calculated by multiplying the strain values, obtained from the strain gauges, and the Young's modulus of the wire armour. The figure shows that one wire armour indicates tension whilst the second gauge indicates compression. This shows that the cable was bending due to the applied axial compression load. Although the test is intended to be an axial compression test, the bending could be due to the fact that the top end of the cable was not perfectly aligned. Nevertheless, the buckling failure mode did not take place during the test. This is simply because the axial compression load was not sufficient to initiate Euler buckling.

103
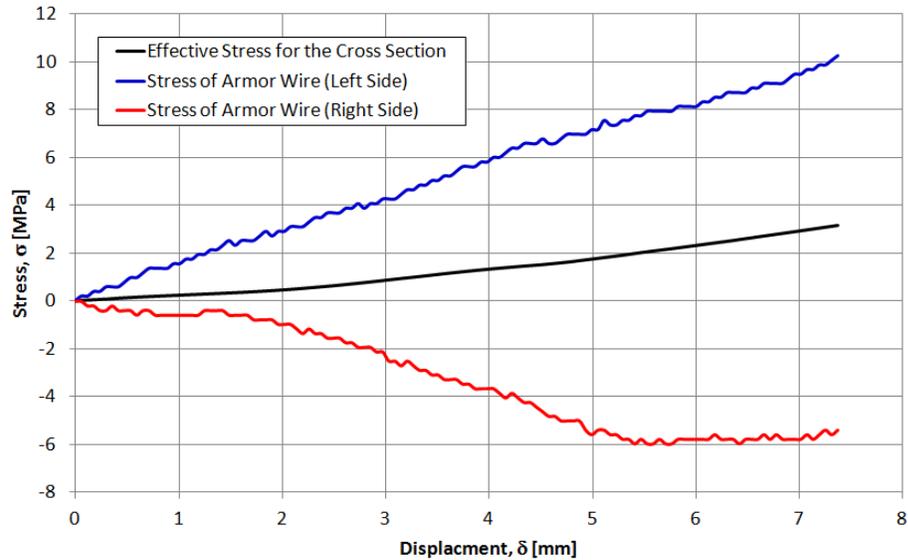
Figure 3-42.Stresses of armour wire during pure compression test.

It should be noted that upon completion of the axial compression test, the cable sample was subjected to a full inspection to ensure that no damage or excessive deformation occurred to the cable components. For more information, refer to the visual inspection results presented in Sections 3.5 and 3.6.

In addition to the above test, a sample of electric core was prepared newly from an unspoiled power cable of length 100 mm. This sample was prepared in order to perform an axial compression test as shown in Figure 3-43. The results of this axial compression test are presented in Figure 3-44 and Figure 3-45 .
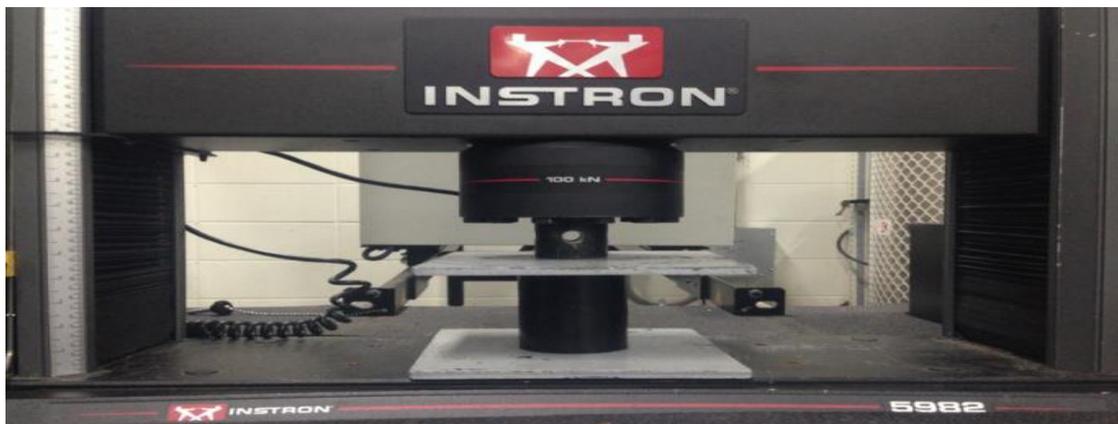
Figure 3-43. Electrical core axial compression test.
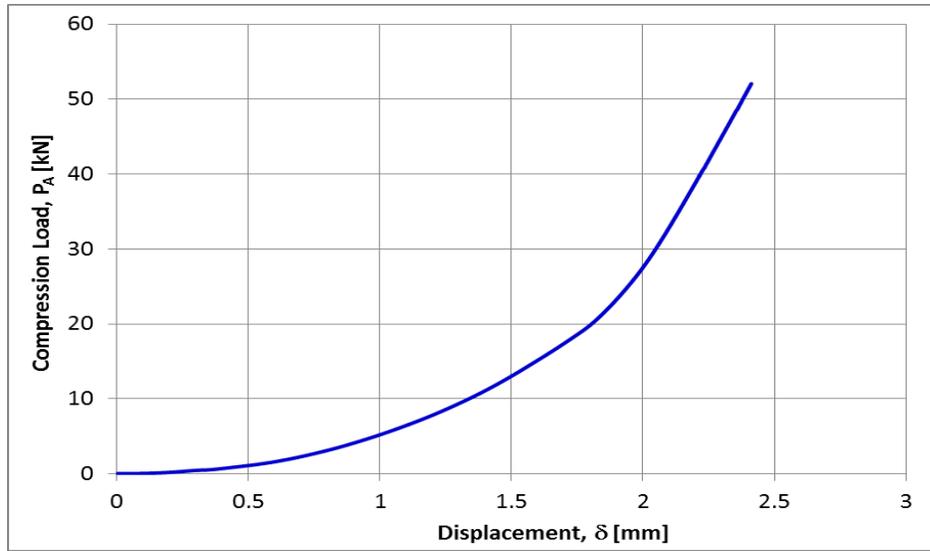
Figure 3-44: Relationship between axial compression load and axial displacement for a 100 mm electrical core sample.
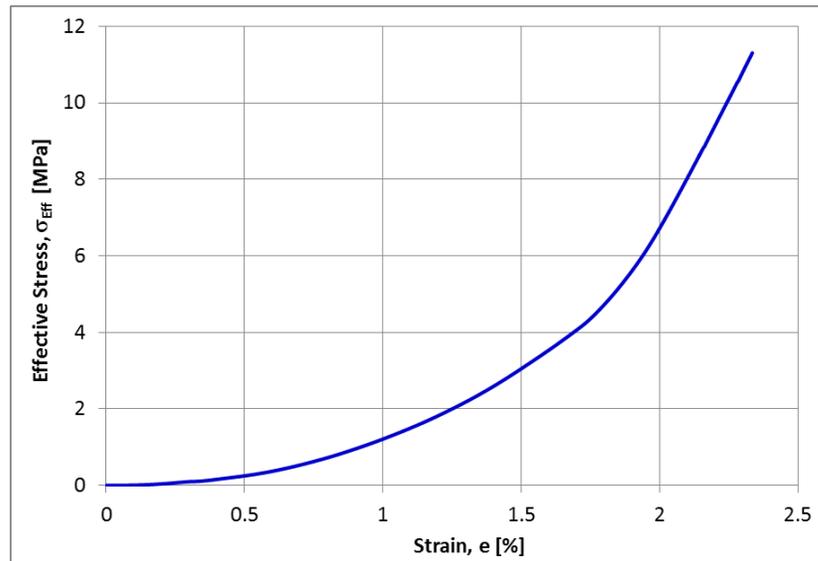
Figure 3-45 .Stress and strain relationship of 100 mm electrical core sample under axial compression.

Figure 3-45 shows that the slope of the stress-strain curve increases gradually as per the normal trend of the axial compression test. During the test, it was observed that a slight

change in slope occurred at a strain of 1.7%. It should be noted that no signs of damage or excessive deformation was observed before the strain reached 1.7%.

3.4.2   Approach to Determine Compression Failure Load

The pure axial compression load simulation was conducted in order to better understand the response of the cable to pure axial compression loads and hence ascertain the allowable compression limit for cable installation at crossing locations. The pure axial compression test was undertaken for a cable sample of 1.6 m. The maximum axial compression applied to the sample was 90 kN. During the course of the test no buckling or deformation was noticed in the cable sample. During the cable installation, as shown in Figure 3-46, the tension was at its peak at the tensioner and decreased along the length of the cable catenary before reaching a minimum at a location just after the touchdown point. At the touchdown point, the cable movement is held by the friction factor associated with the seabed. Based on this observation, the test concept was developed in order to replicate the bent and straight cable conditions at the touchdown point. In this section, an OrcaFlex model was developed to investigate the allowable compression load as shown in Figure 3-47. OrcaFlex (2014) is a standard industry three-dimensional non-linear time domain finite element program specifically developed for marine dynamics and suited to the dynamic analysis modelling of cable catenaries. The boundary conditions assumed in the model were fixed for one end and free at the other. This boundary condition is conservative to cover the likely range of expected seabed axial friction factors. The winch element was utilized for the application of the compression load. The critical load of the cable was measured by the winch load.
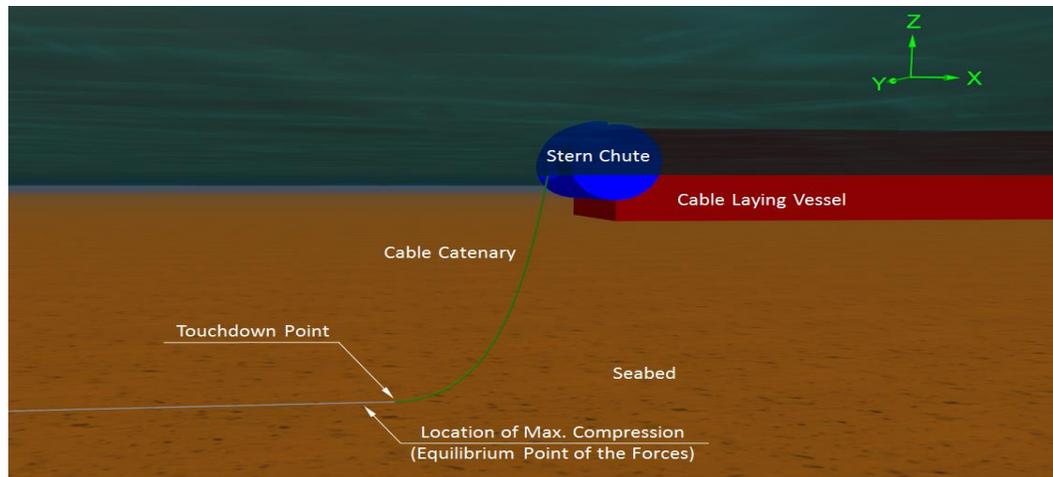
Figure 3-46. Boundary conditions and corresponding formula for critical load.
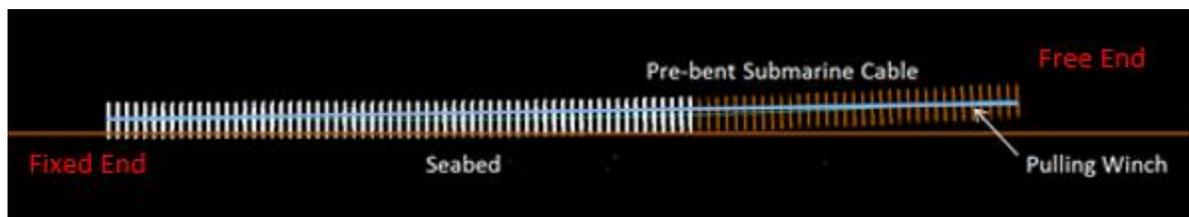
Figure 3-47. OrcaFlex model to investigate allowable compression loads.

Figure 3-48 presents the results of the compression failure load for different cable spans obtained from the OrcaFlex model shown in Figure 3-47. The compression load decreases with an increase in intermediate span and reaches its lowest level at the compression span of 5.0 m. The compression load then increases slightly and remains constant for longer spans.

It can be seen from Figure 3-48 that for the span length of 1.6 m, the compression failure load is approximately 114 kN. It should be noted that during the pure axial compression test, the maximum axial compression load reached 90 kN without any sign of damage. The reason for limiting the test load to 90 kN was the limitation of the machine capacity which was 100 kN. However for the sake of comparison with OrcaFlex results shown in Figure 3-48, it was assumed that the cable sample would fail if the compression load was to increase to a value greater than 90 kN.
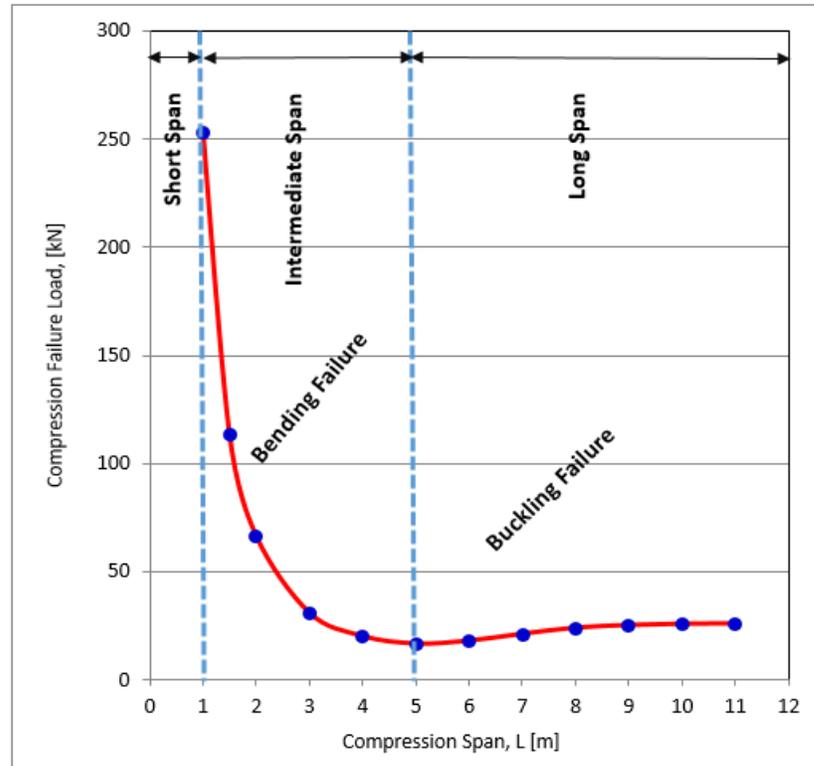
Figure 3-48. Compression failure load as a function of compression span

The OrcaFlex model can be used in the early stages of the project to determine the allowable compression limit of a subsea cable. Another comparison was undertaken where the results obtained from the OrcaFlex model, shown in Figure 3-47, were compared with the Euler Buckling theory for a Pinned-Pinned column. The comparison is shown in Figure 3-49. It can be seen that the results from the theory and the OrcaFlex model are in good agreement. Starting from the span length of 5.5 m, the results from the Euler Buckling theory tend to reduce to zero, whereas the results from OrcaFlex tend to increase slightly before stabilising. This is in part due to the difference in boundary conditions as well as the fact that in the OrcaFlex model the cable was laid flat on the seabed with an axial friction factor.
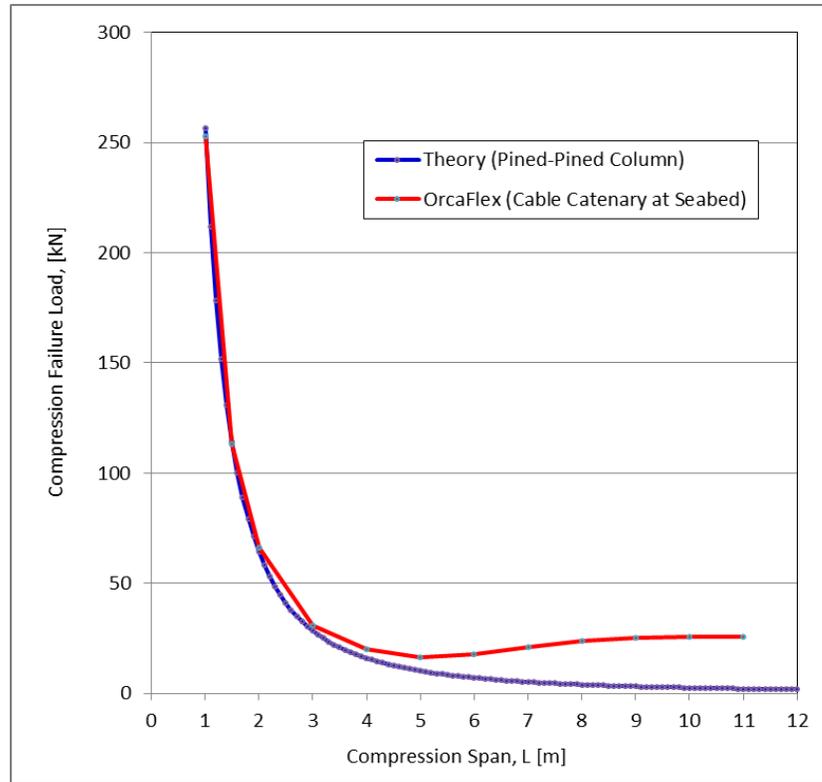
Figure 3-49. Comparison of compression failure load.

3.4.3   Bending Compression Test

Figure 3-50 illustrates the submarine cable during the bending coupled with compression test. It should be noted from this figure, that the cable was bent with a certain radius of curvature due to the application of the tension load. The tension load was converted into a compression load as per Equation (3-1). Figure 3-51 illustrates the relationship between the compression load, PC, and the pulling displacement, δ, for the tested cable samples.

Figure 3-51 illustrates the results from the bending compression tests. During the bending compression test, two tests of different lengths were performed. Figure 3-51 indicates that the compression load, P_C, increases at the early stage of the test but decreases later. This is because the bending becomes dominant in the cable as the pulling displacement increases.

Figure 3-50 . Submarine cable subjected to compression and bending.

The results shown in Figure 3-51 show that the cable exhibits the same response as those obtained from the bending of a steel tube (Ju & Kyriakides, 1992). Ju & Kyriakide s (1992) indicated that soon after reaching their maximum moment, the tubes started to kink and the moment dropped off significantly. The relationship between the axial compression load and the bend radius of the cable is shown in Figure 3-52.

The bend radius is calculated as per Equation (3-5). The drop in the ultimate compression load is due to:

- An increase in axial compression stresses
- An increase in bending stresses in the in-plane and out-of-plane moments,
- Yielding of steel armours at End-2, as shown in Figure 3-55,
- The helical nature of the steel armour wires which causes an increase in bending stress on one side of the cable and a reduction on the other side.

110

- Restrained radial movement of the armour by the outer serving layer (yarn). The armour wires are thus forced to slip and the spacing between them is reduced. This was noticed from a visual inspection of the outer sheath at that location.
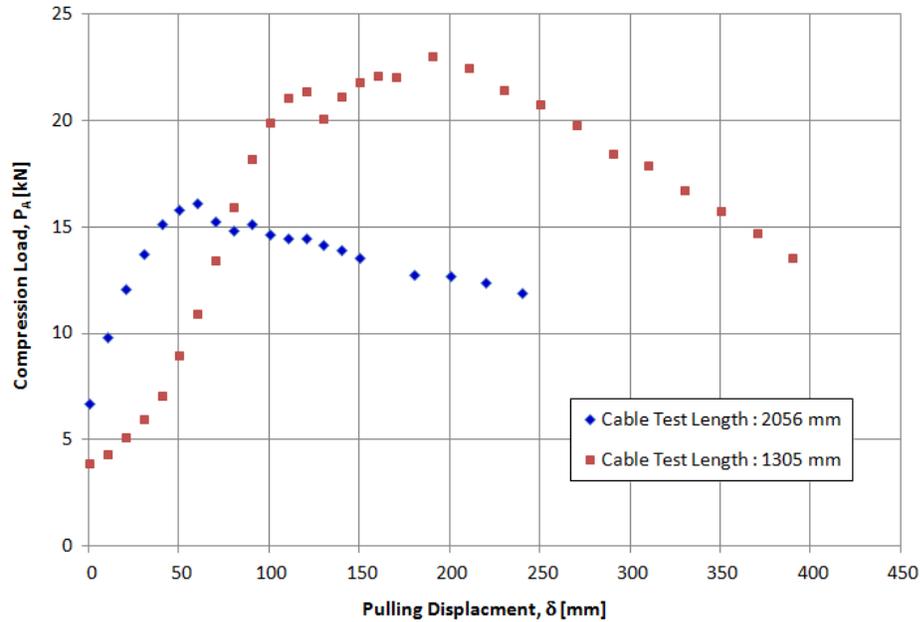
Figure 3-51. Compression load and pulling displacement of tested samples.

It can be seen that the cable sample of length 1305 mm shows higher compression loads than the sample with a length of 2056 mm. This is consistent with buckling theory.

Figure 3-53 presents the bending moment at the clamped location, M_C, versus curvature, κ. Both samples show an increase in bending moment with an increase in curvature. It supports the observation that the bending is dominant during the test.

The data shown in Figure 3-51 and Figure 3-52, which was obtained from the compression load at the beginning of the test, does not represent the allowable compression limit for the subsea cable. The reason being that at the beginning of the test, there was a slight axial compression force in the subsea cable and the bend radius of the cable was infinite. In this case the axial compression force in the cable does not represent the maximum axial compression limit that the cable can withstand.

Figure 3-54 and Figure 3-55 presents the axial stresses of the armour steel wire which were calculated from the measurement of the strain gauges. The strain gauges were used

to record the axial strain values during the bending test at four different locations as indicated before in Figure 3-26. The two strain gauges attached to the extrados were measuring positive axial stresses. This means that the steel armours at both locations were under tension as a result of the bending.

The intrados strain gauges indicated a negative axial stress at End-2, while the strain gauges at the middle of the test sample indicated a positive axial stress. This is because the armour wire has a helical structure. The movement of the armour wire near the clamped location is restricted by the clamping fixture while the movement of the steel wire in the mid location is relatively free. This causes stress relaxation in the steel wire armour. This observation reveals that the stress on the cable components located at the intrados direction, could be relieved under bending. The positive axial stress at the mid length could be the result of the deflection of the cable to one side instead of bending in the plane of the test sample.

A closer look at the results in Figure 3-55 reveals that:

- The cross section exhibits smaller stiffness at the intrados of the mid location as well as at the extrados of the clamped location of the steel armoured wire.

- As a result, the combined stress at the intrados of the mid location fluctuates from negative to positive and back to negative due to the smaller stiffness at that location.

- Further, the combined stress at the intrados clamped location was greater than the extrados clamped location as a result of the smaller stiffness at the extrados clamped location.

- The bending stress at the extrados was dominant. The axial stress at the extrados was roughly 90 MPa whilst the overall combined stress was approximately 300 MPa. This shows that the testing duplicates the real-life situation where bending stresses are expected to exceed axial stresses for such lengths.

Cable Test Length : 1305 mm

Cable Test Length : 2056 mm
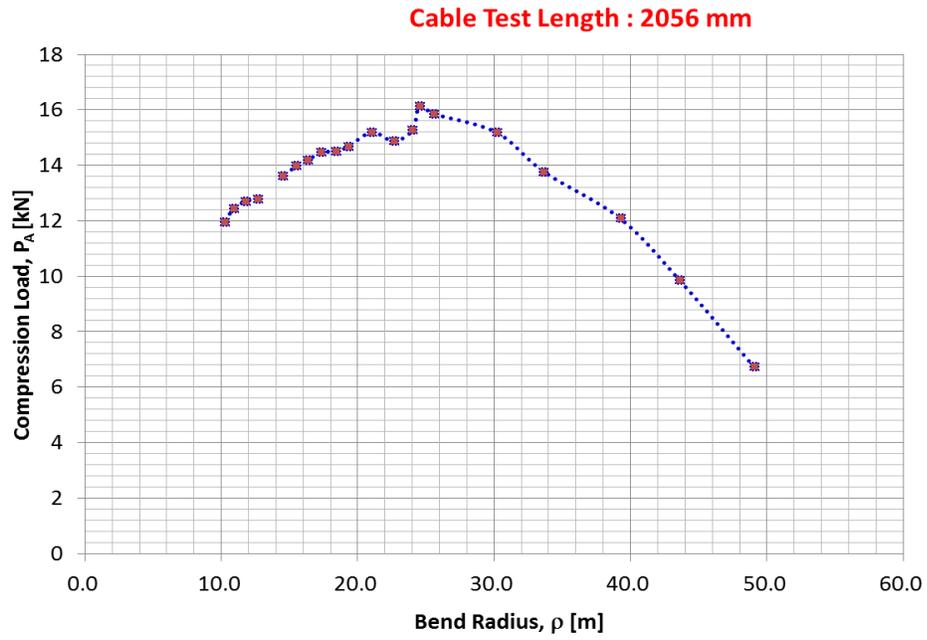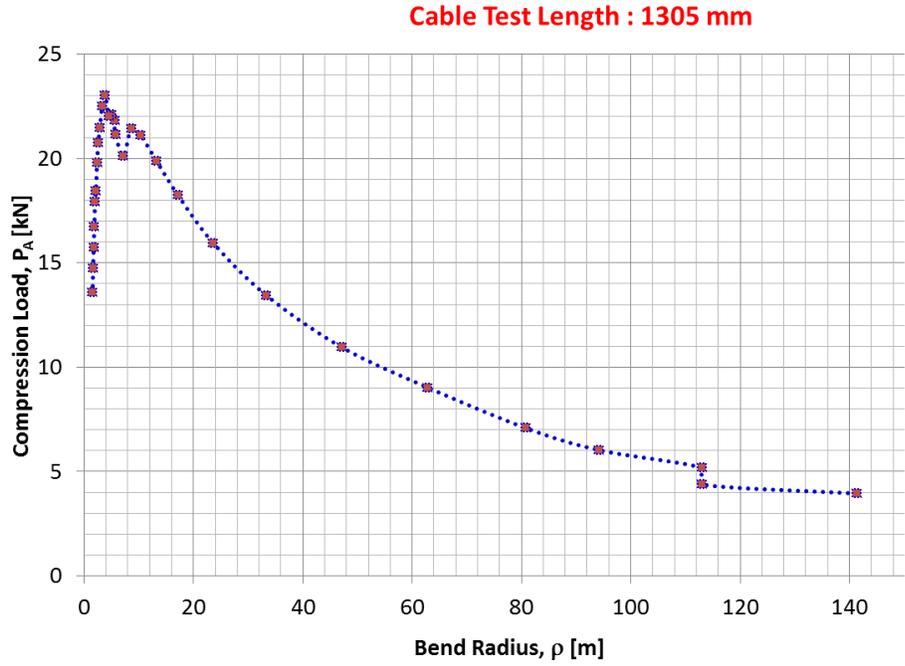
Figure 3-52. Compression load and bend radius relation for tested samples.
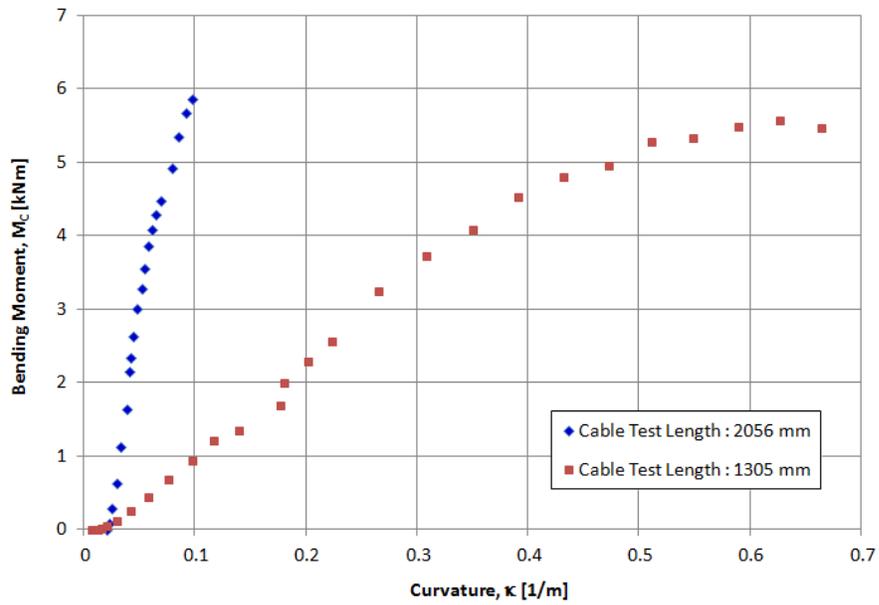
Figure 3-53. Bending moment at clamped location vs. curvature.
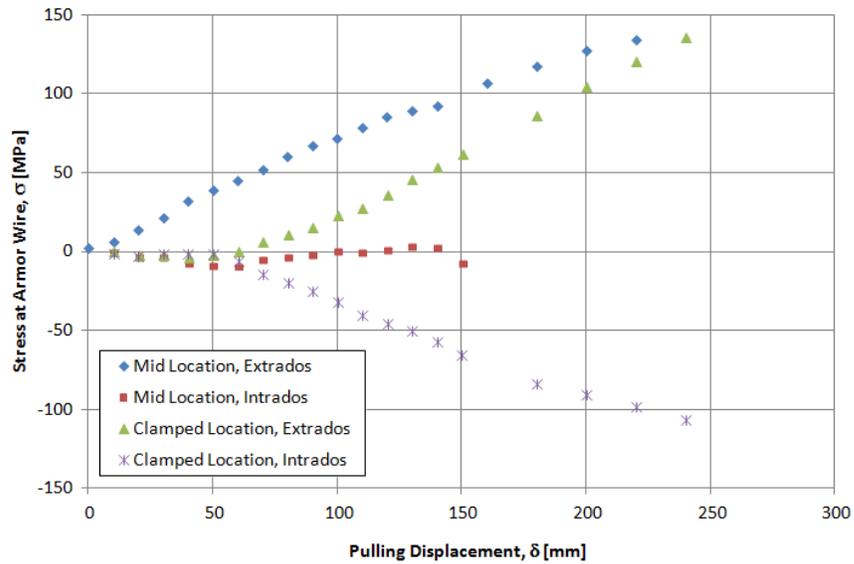
Figure 3-54. Stress of armour wire during bending compression test (cable length: 2056 mm).
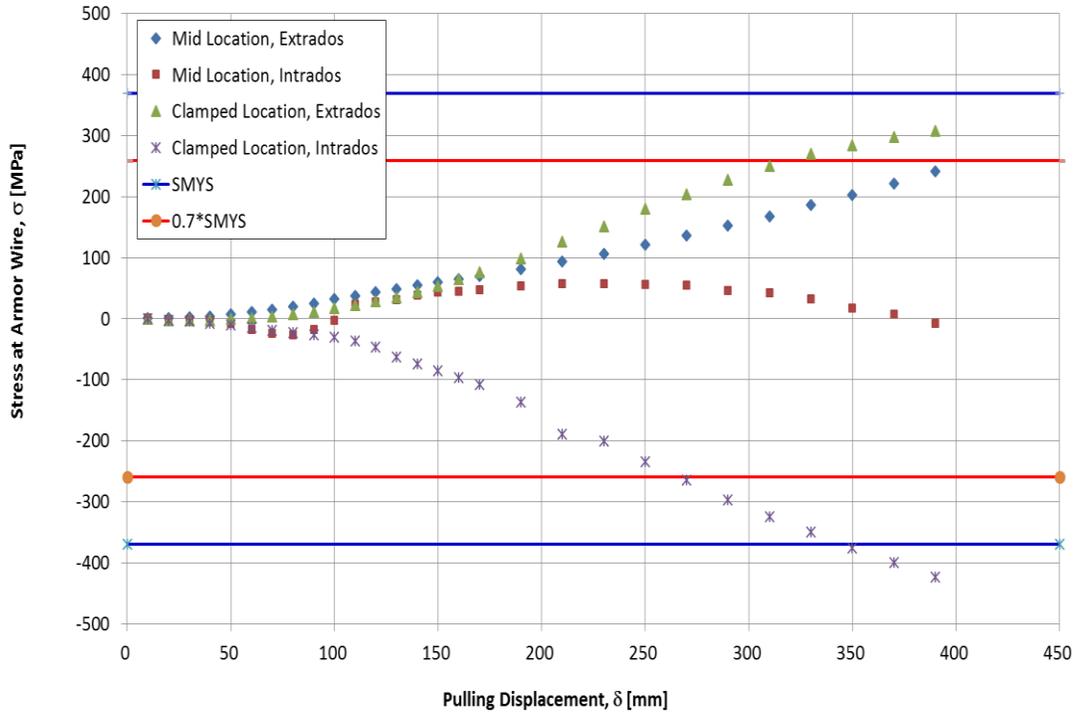
Figure 3-55 : Stress of armour wire during bending compression test (cable length: 1305mm).

The same observations can be made from the results shown in Figure 3-54. However, in this case, no yielding was taking place for the armours as the cable did not reach a tight enough bend radius during the bending test.

Figure 3-56 shows the reading from the fibre optics during the bending compression test. The fibre optics indicated that the changes in light power was less than 0.02 dB under the axial compression load which ranged from 3.5 to 23.0 kN. Therefore, no significant optical distortion was observed within the submarine cable during the tests.

It can be seen from the results presented in the previous section, that no signs of damage or excessive ovalisation were noticed for the duration of the bending test.

It is widely accepted that a cable is considered to fail if the stresses in the armour reach 70% of the specific minimum yield stress of the steel armour. The reason being that the

115

armour should not be yielded in order to keep enough mechanical strength left for operation and for instances where the cable has to be retrieved to the vessel for repair.
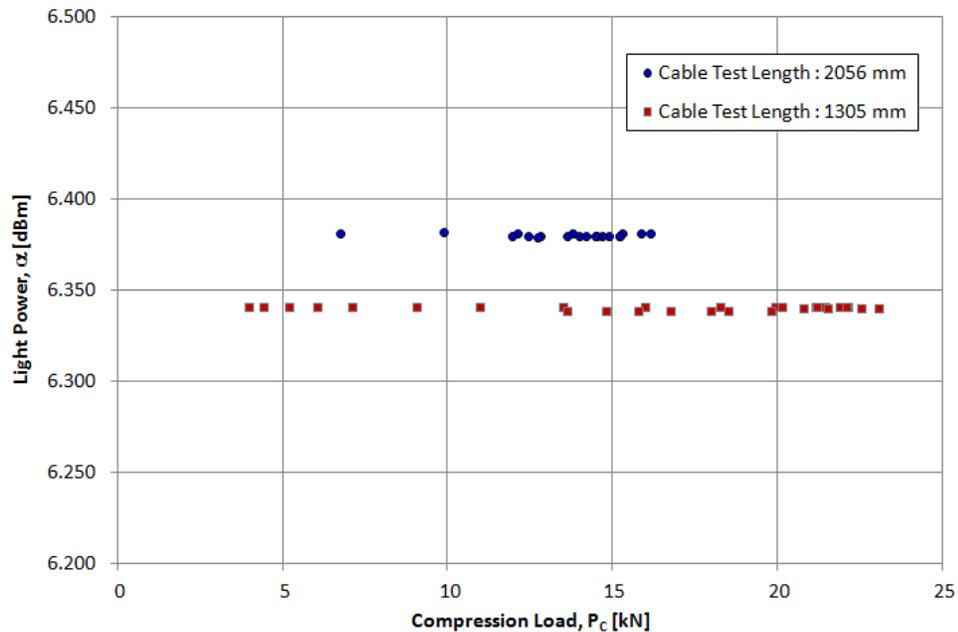
Figure 3-56. Light power measured during bending compression test.

Based on this acceptance criterion, the cable cannot withstand an axial compression smaller than the bend radius of 2.9 m. This value is given by the cable manufacture as the minimum bend radius of the cable. However, the cable supplier advised that the cable cannot withstand any compression as the cable is not designed for negative tension (compression).

Figure 3-57 presents a schematic diagram for the results shown in Figure 3-52. These results were obtained during the bending compression test of the submarine cable. For the installation analysis, the maximum compression against the bend radius is often used by the design engineer to check the cable integrity.
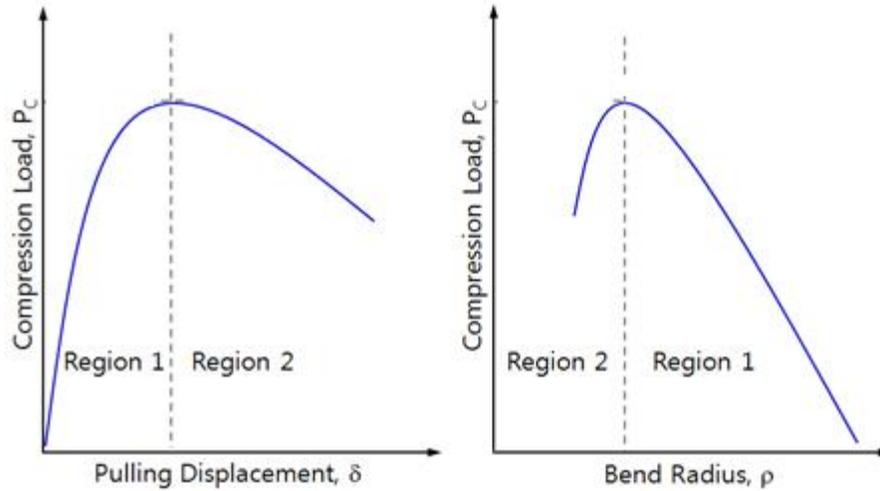
Figure 3-57. Schematic diagram of cable behaviour during bending compression test shown in Figure 3-52.

Figure 3-58 presents the maximum allowable axial compression plotted against the bend radius for the installation of the cable. The figure presents the envelope of allowable axial compression versus the bend radius for the subsea cable. The data presented in this figure are based on the data shown in Figure 3-52. The cable starts with a bending radius of 2.9 m. A safety factor of 1.33 (safety margin: 25%) is considered for the maximum axial compression load only. There are no stringent criteria regarding safety factors and they can be altered to suit any given operating scenario.

Based on the results shown in Figure 3-52, it was suggested to adopt a practical allowable axial compression versus bend radius for the installation of the submarine cable as shown in Figure 3-58. Alternatively, Table 3-10 can be used.

It can be concluded from Table 3-10 that for a bend radius greater than 5 m, the pure axial compression test is sufficient or the OrcaFlex model results presented in section 3.4.2 are also sufficient. The OrcaFlex model showed a compression failure load of 16.5 kN. Additionally, for a large bend radius greather than 5m , the pure axial compression can replace the allowable bending compression limit.
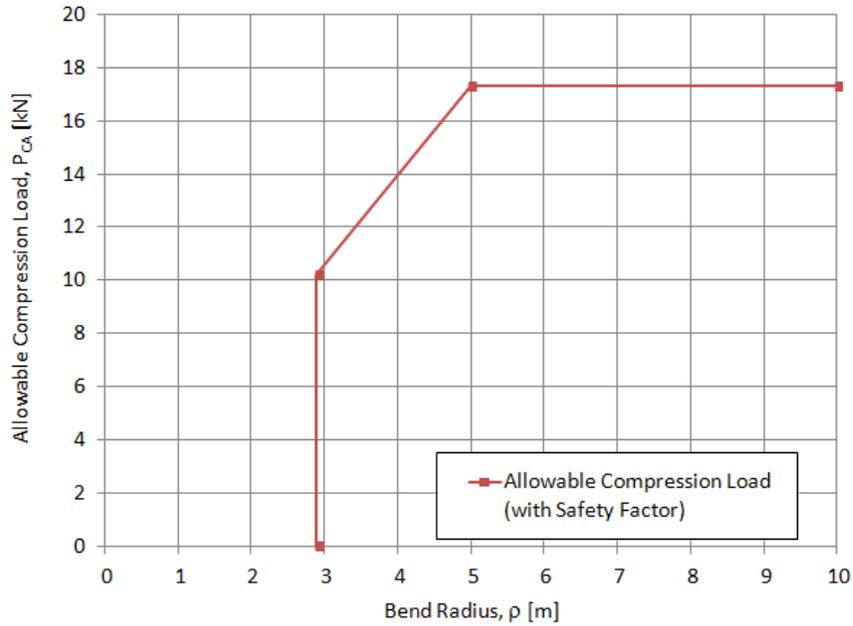
Figure 3-58. Allowable compression load.

Table 3-10. The Allowable Compression Loads

Bend Radius, ρ [m]	Allowable Compression Load, P_A [kN]
$\rho < 2.9$	$P_A = 0$ (Not allowed)
$2.9 \leq \rho \leq 5$	$10.2 \leq P_A \leq 17.3$ (Linear relation with bend radius)
$5 < \rho \leq 10$	$P_A = 17.3$ (Constant value) The allowable compression load under the infinite bend radius was proved by the pure compression test.

3.4.4 Comparison of the Bending Compression Test with OrcaFlex Analysis

This section compares the results from the bending compression test to that obtained from the OrcaFlex simulations. An OrcaFlex model, shown in Figure 3-59, simulating a compression test was used to compare bending in conjunction with tension. The model

118

consisted of a single line with several constraints applied as static winch elements along its length. A load was applied to the unconstrained end (End B) via a separate winch element which caused the line to bend back on itself and go into compression. The model was found to suffer from instability because of the way the load was applied. It was found that the constraints did not keep the cable in the plane of interest and an unwanted out of plane response occurred. In order to counter this, OrcaFlex shapes were added to the model to fully constrain the cable laterally. This meant that the cable remained within a single plane throughout the simulation. A further vibration or instability was observed at the start of the OrcaFlex simulation. To remove this vibration, the speed of the winch pay-in was reduced which created a smoother transition from the static to the dynamic state thereby removing the unwanted vibration. The boundary conditions employed in this model were identical to those from the physical bending compression test.

In the test arrangement, there was a clamp on End B with a shackle for the attachment of the sling. In the OrcaFlex model however, the load was applied directly on the cable centre line. The load applied in the centre line of the cable generates a pure axial load with small geometric imperfections to start the bending behaviour, resulting in unstable behaviour or a buckling effect. As highlighted above, the unstable behaviour was obviated via the use of OrcaFlex shapes.
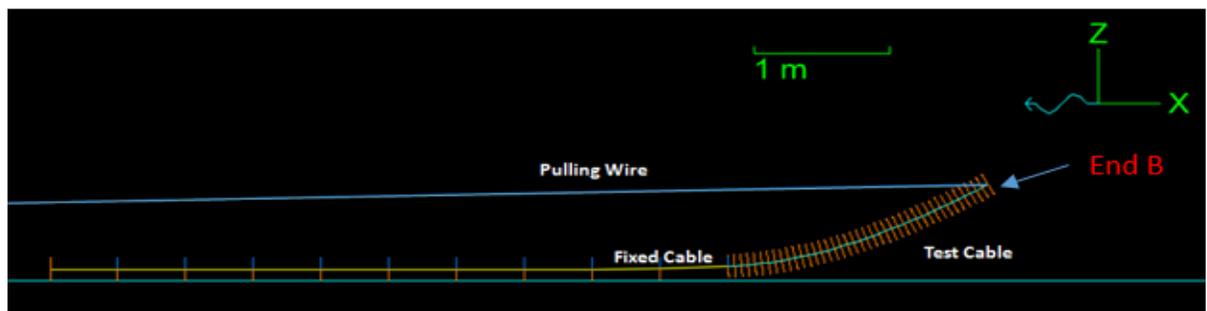
Figure 3-59. OrcaFlex model for bending compression test.

Figure 3-60 highlights the results from the comparison undertaken between the numerical modelling and the physical testing of the subsea cable. The input data employed in the OrcaFlex model was taken from Table 3-8.

119
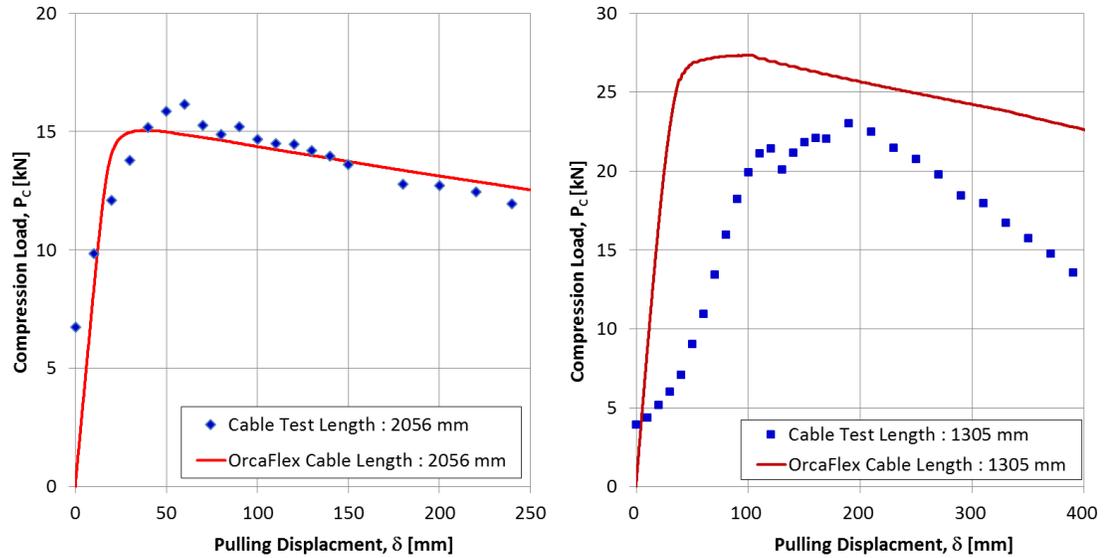
Figure 3-60. Comparison of cable behaviour.

It can be seen from Figure 3-60 that for the cable test length of 2056 mm, the results from the OrcaFlex model and the test results are in a very good agreement.

For the cable test length of 1305 mm, the onset of the limitpoint predicted by OrcaFlex is earlier compared to that predictedby the physical testing. OrcaFlex results illustrate different post-buckling behaviour from that obtained by the physical testing.However, the correlation between the testing and OrcaFlex is still good.As indicated earlier, from the pure axial compression test, it was concluded that the axial stiffness to compression was 32 times lower than the axial stiffness reported in Table 3-8. In the OrcaFlex model, it was assumed that the axial stiffness was the same during tension and compression loads. The axial stiffness was also shown to be nonlinear during the physical testing and exhibited a significant non-linear response.

Further, the onset of the limit point was earlier in the OrcaFlex model as compared to the physical test. The OrcaFlex results for the shorter sample illustrated different post-bucklingbehaviour from that obtained from the physical testing. However, the correlation between the testing and OrcaFlex was still reasonable.

The cable test length of 2056 mm was bent to a bend radius ranging from 10 m to 49 m. That is, the cable was almost straight and did not exhibit a strong geometrical non-linearity. It is worth indicating that the OrcaFlex method uses a beam element and assumes

120

homogenous, elastic material for the cable rather than using proper strain curves for the relevant materials. Additionally, OrcaFlex does not account for the friction between the relevant material combinations and the viscous damping due to the polymeric materials.

In spite of this, it can be concluded that the OrcaFlex model is sound and may be suitable for this type of combined loading. The proposed modelling of the combined bending plus tension scenario can be used in the early stages of design to determine the allowable compression limit for a subsea cable after considering a safety factor. Testing a large number of samples and comparing those results against the OrcaFlex model results will further improve the confidence of the simulation tools.

Solid modelling could not be used in this validation as it requires the following accurate input:

- Friction factors between relevant material combinations
- Load deformation and stress-strain curves for relevant materials

The only way to determine the above inputs is via small scale tests. The mechanical behaviour of the cable is known to be highly dependent on the constitutive materials. Thus, the solid finite element modelling will not provide accurate results and may not be acceptable in lieu of the actual tests.

3.5   VISUAL INSPECTION OF 1.6 M CABLE SAMPLE AFTER THE AXIAL COMPRESSION TEST

It is essential to determine whether the cable sample was damaged during the axial compression test. A high voltage test would be the appropriate way to ensure that the integrity of the cable was not jeopardized. However, in practice, high voltage testing may be impossible due to the cable sample length and available resources.

The visual inspection was undertaken on the various layers of the cable as shown in Figure 3-61 to Figure 3-69. This was inclusive of cable cores and optical fibres. Upon completion of the test, the cable sample was measured again. The measurements showed that the properties of the sample length were unchanged. This indicates that the cable remained

within the elastic region and that no plastic deformation occurred within the cable sample. Overall, no sign of damage or permanent deformations were observed during the course of the axial compression test.

The fibre optics did not indicate any power loss during the entire duration of the test. In addition, during the visual inspection there were no signs of cracks or damage to the cable components nor were there any signs of wrinkles in the metallic screen.

During the test, it was noticed that the cable, after some pulling motion, started to deflect to one side (torsion) instead of bending in the plane of the catenary (the test sample) due to the helical nature of the steel armour wires. This is also what often happens in practise during installation. The following figures show the steps of the visual inspection undertaken for the cable to ensure that that the cable layers were free from any observable damage. During the visual inspection, a magnifying glass was used to detect any tiny deformations.
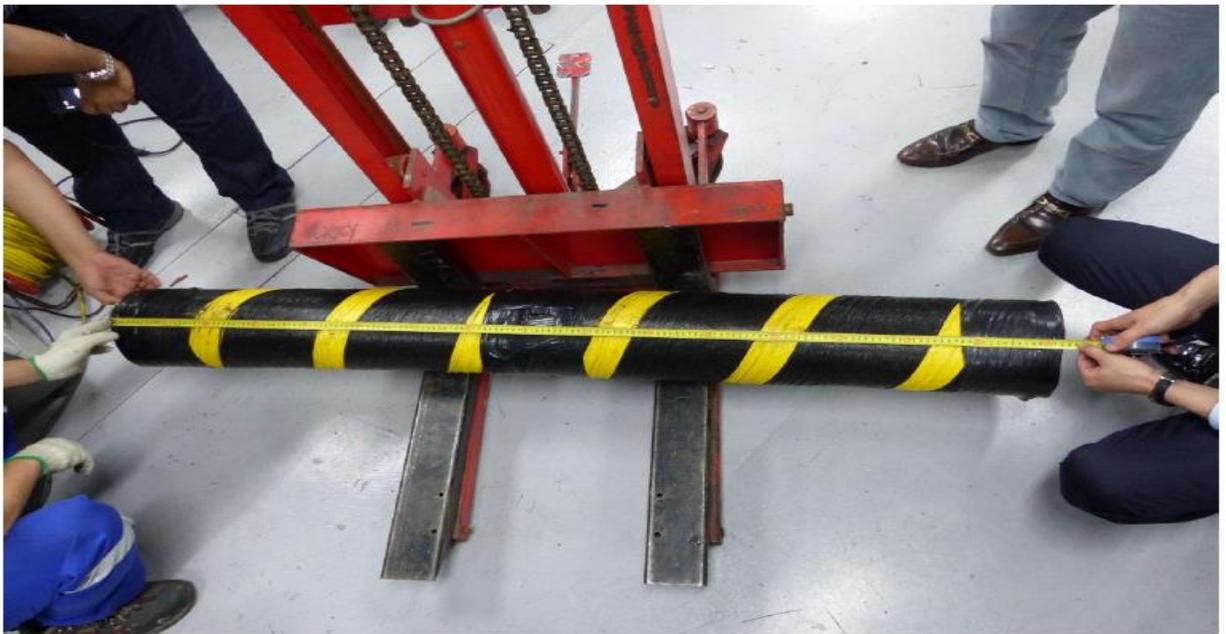
Figure 3-61: Length measurement of cable sample upon completion of pure axial compression test. No deformation or damage was observed.

Figure 3-62 : Removal of serving sheath and steel amour wires. No deformation or damage was observed.

Figure 3-63: Armour bedding after removal of steel armour wires. No deformation or damage was observed.

Figure 3-64: Anti-teredo layer after removal of armour bedding.

Figure 3-65: Binder tape after removal of anti-teredo layer.

Figure 3-66: Three cable cores and optical fibres.

Figure 3-67: Lead sheaths of cable cores after removal of core outer sheaths.

Figure 3-68: Water absorbing layer after removal of lead sheath.

Figure 3-69: Cable conductors after removal of insulation and semi-conductor screens.

3.6 VISUAL INSPECTION OF 2 M CABLE SAMPLE AFTER THE BENDING COMPRESSION TEST

Upon completion of the bending compression test, the 2 m cable sample was cut and prepared for visual inspection. During the visual inspection test, two locations of the cable sample were inspected as illustrated in Figure 3-70 to Figure 3-79. The two locations were

- The cable section adjacent to the fixation point
- The middle of the bended part

Overall, no sign of damage or permanent deformations were observed during the course of the axial compression test. The following figures show the steps of the visual inspection undertaken for the cable to ensure that that the cable layers were free from any observable damage. During the visual inspection, a magnifying glass was used to detect any tiny deformations.

Figure 3-70: Cable sample after cutting.

Figure 3-71: Steel armour wires after removal.

Figure 3-72: Armour bedding after removal of steel armour wires.

Figure 3-73: Anti-teredo layer after removal of armour bedding layer.

Figure 3-74: Binder tape after removal of the anti-teredo layer.

Figure 3-75: Three cable cores.

Figure 3-76: Lead sheaths of cable cores after removal of core outer sheaths.

130

Figure 3-77: Insulation screens.
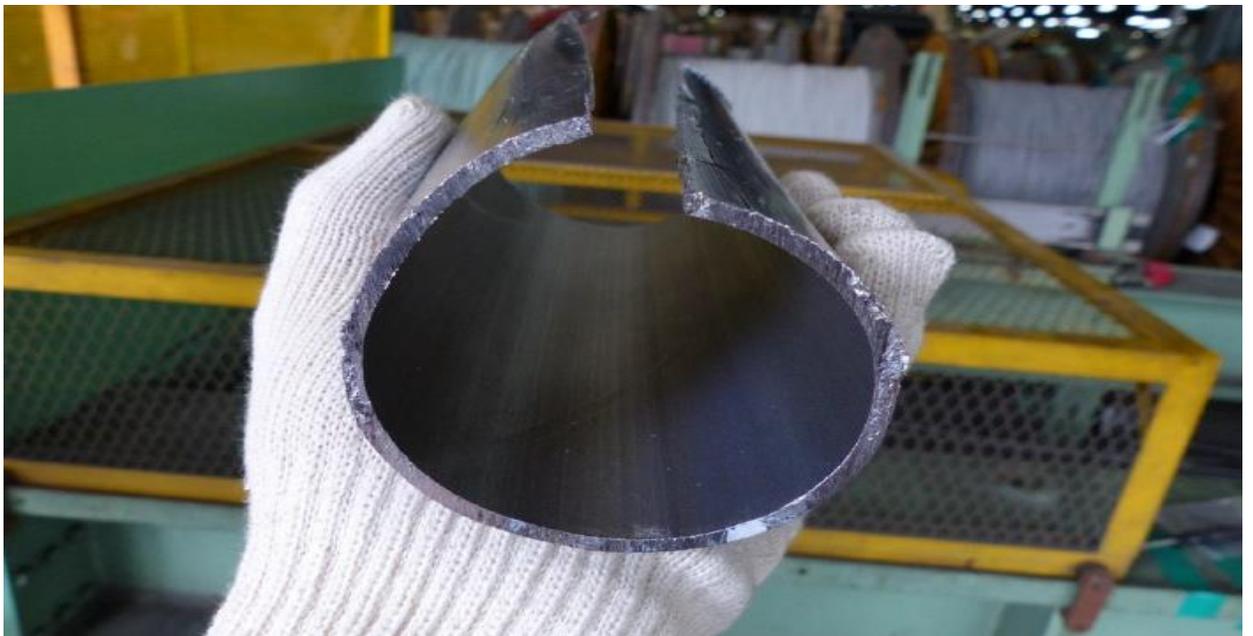
Figure 3-78: Inspection of inner surface of a lead sheath. No sign of wrinkles.

131

Figure 3-79: Cable conductors after removal of insulation and semi conducting screens.

In addition to the visual inspection performed on the subsea cable within the composite construction, a dimension check of the various components of the subsea cable was also conducted. The measurements were not performed according to any standards, but was conducting on the basis of determining the minimum and maximum values using a calibrated calliper. The main objective of this exercise was to ensure that the values were between the minimum and the maximum and did not deviate greatly. This was also to determine whether or not deformation had taken place as a result of the bending test.

The measurement revealed that differences between the minimum and maximum values were very small (well within allowed ranges). The measurements indicated that the three phases had hardly any variations. In conclusion, the measurements of the cable parts indicated that no deformation had occurred as a result of the bending tests.

4 Chapter-4 – Paper No. 2

Title: **"Simulated in-line deployment of offshore rigid field joint–A testing concept".**

Authors: **Ahmed Reda, Ali Mothana Saleh Al-Yafei, Ian M Howard, Gareth L Forbes, Kristoffer K McKee.**

Journal: **Ocean Engineering**
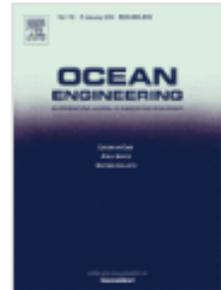
4.1 TESTING DESIGN PROCESS FOR DEPLOYMENT SIMULATION

The testing design process for the deployment simulation involves a series of steps as shown in Figure 4-1.

1. Define cable, crane hoist, eye-bolt, or joint acceptance criteria (i.e. allowable tension, minimum bend radius, crane hoist load, eye-bolt load, allowable bending moment for the joint body). More details of this step can be found in Section 4.3.

2. Select the optimum layback and departure angle. In this step, OrcaFlex Software (2014) dynamic simulations should be undertaken to determine the layback which results in the highest dynamic workability (low tension, compression and curvature exceedance). Refer to Section 4.4.

3. Perform still water analysis at zero wave using OrcaFlex Software (2014). The objective of this step is to investigate whether the acceptance criteria defined in Step 1 are met with a wide enough margin to allow for the subsequent addition of wave actions. Refer to Section 4.8.

4. Perform dynamic simulations using OrcaFlex Software (2014) to determine the limiting weather criteria. Refer to section 4.9.

5. Perform a stress analysis using ABAQUS (2012) for the OFJ body to ensure that the allowable bending is not exceeded during deployment. In this step, the bending moment from Steps 3 and 4 shall be used. Should the stresses from ABAQUS be beyond the allowable stresses, the limiting weather criteria should be relaxed and the dynamic simulations run again to define the relaxed weather criteria, as discussed in Section 4.10.

6. Define loads from dynamic simulations using OrcaFlex to perform the mechanical test on the OFJ. Refer to Section 4.11.

7. Conduct the mechanical test followed by visual inspection and radial water penetration (RWP) tests as per section 4.15. Should the RWP test and in-line test items not be acceptable after the completion of the mechanical test, then another joint should be prepared and the limiting weather criteria relaxed. If the

RWP test and in-line test items are acceptable then the OFJ design can be deemed acceptable.

4.2 OFFSHORE FIELD JOINT INLINE DEPLOYMENT PROCEDURE

This section highlights the steps which should be used to deploy the in-line joints as an integral part of the emergency contingency procedure during cable installation. Figure 4-2 to Figure 4-5 show some of the required steps and a brief description of the operation. The joint schematic is shown in Figure 2-4.

Figure 4-2 shows the use of the vessel crane to lift the joint outboard. The tensioner pays out the cable to ensure sufficient slack during operation. The joint is then lowered through the splash zone area.
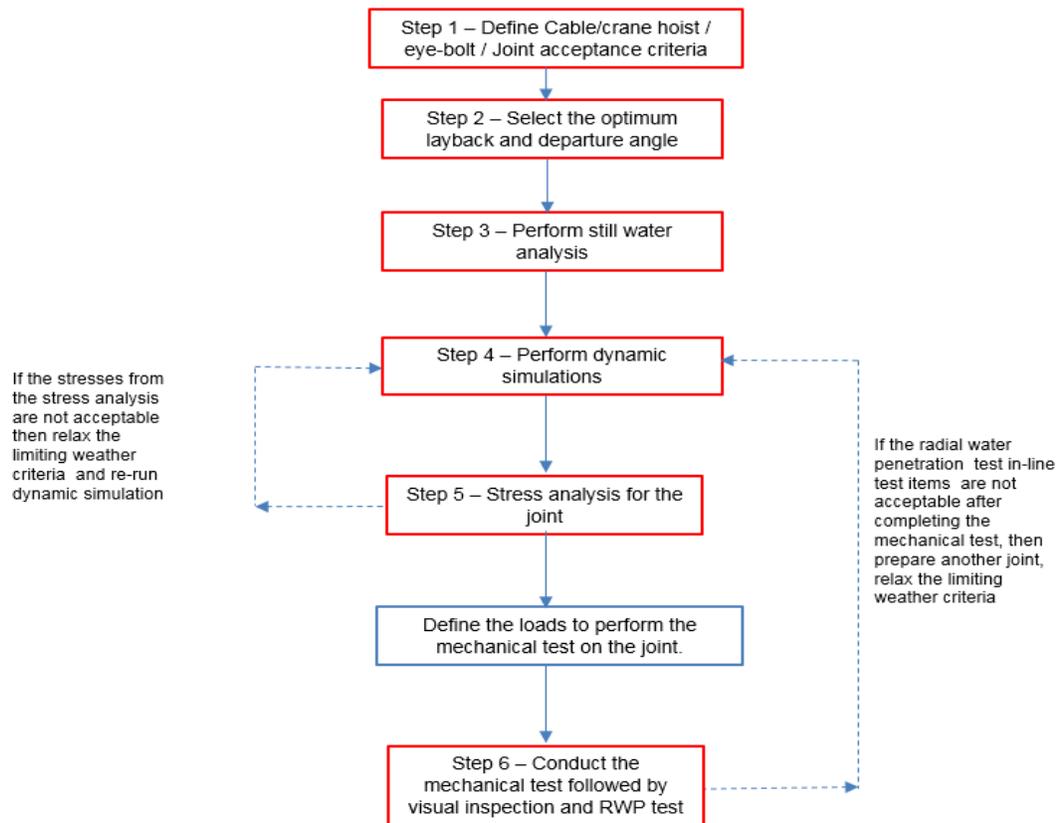
Figure 4-1: Testing design process.
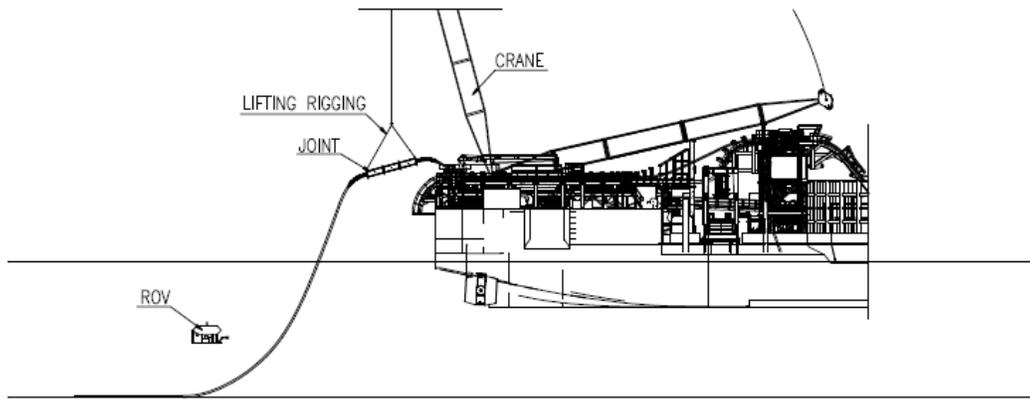
Figure 4-2: Lift the joint outboard. Tensioner to pay out cable to ensure sufficient slack during operation.

Figure 4-3 shows that as soon as the joint is fully submerged, the tension on the crane wire will be removed. The crane wire will only be detached from the joint when the joint reaches the seabed. Until then, nominal tension shall be maintained to ensure that the crane wire does not become entangled with the joint. During this step, it is important to ensure that the departure angle is in accordance with the dynamic simulations undertaken.
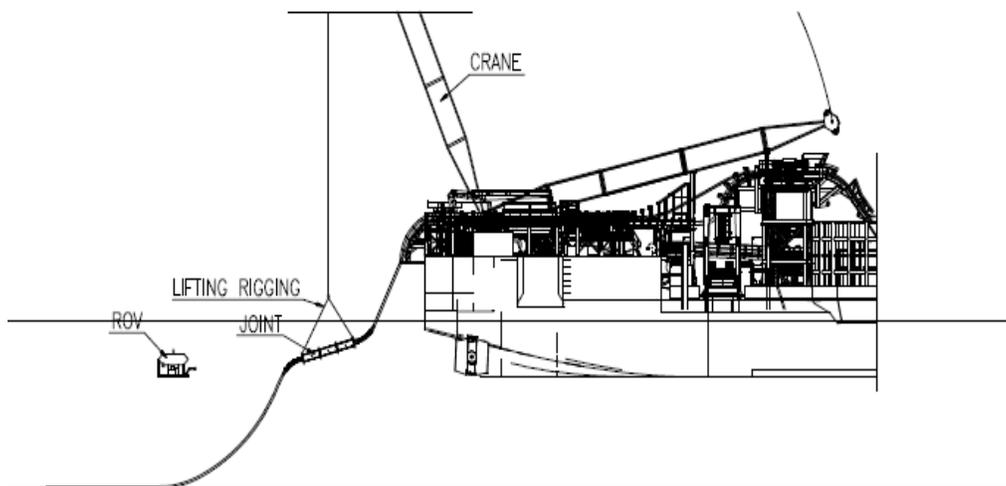
Figure 4-3: Lower the joint through the splash zone area.

Figure 4-4 illustrates the lowering of the joint until it rests on the seabed. The remote operated vehicle (ROV) will confirm proper set down. As before, it is important to ensure that the departure angle is in accordance with the dynamic simulations undertaken. The installation vessel then proceeds with the laying of the remaining cable as illustrated in Figure 4-5.
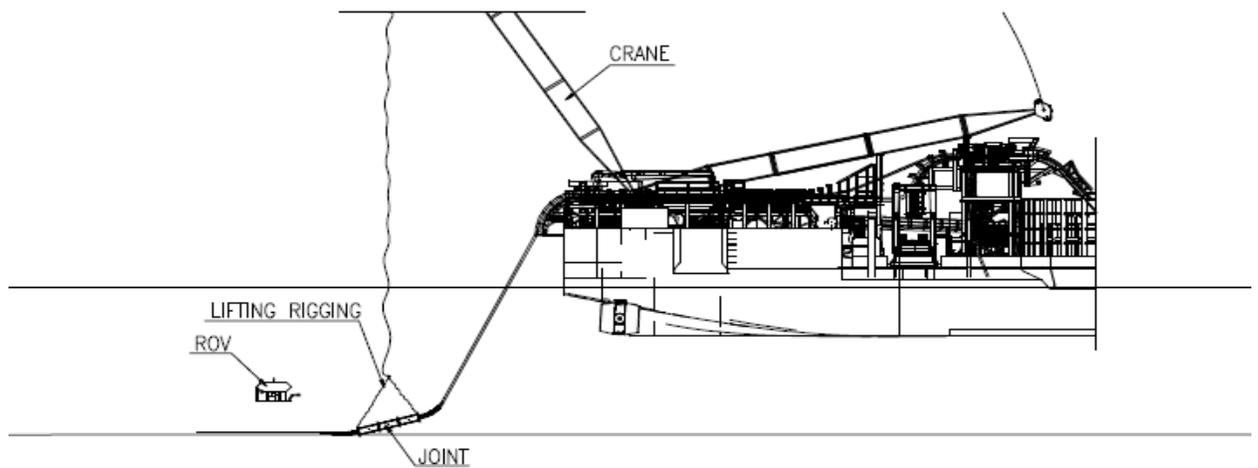
Figure 4-4: Keep lowering the joint until it rests on the seabed.
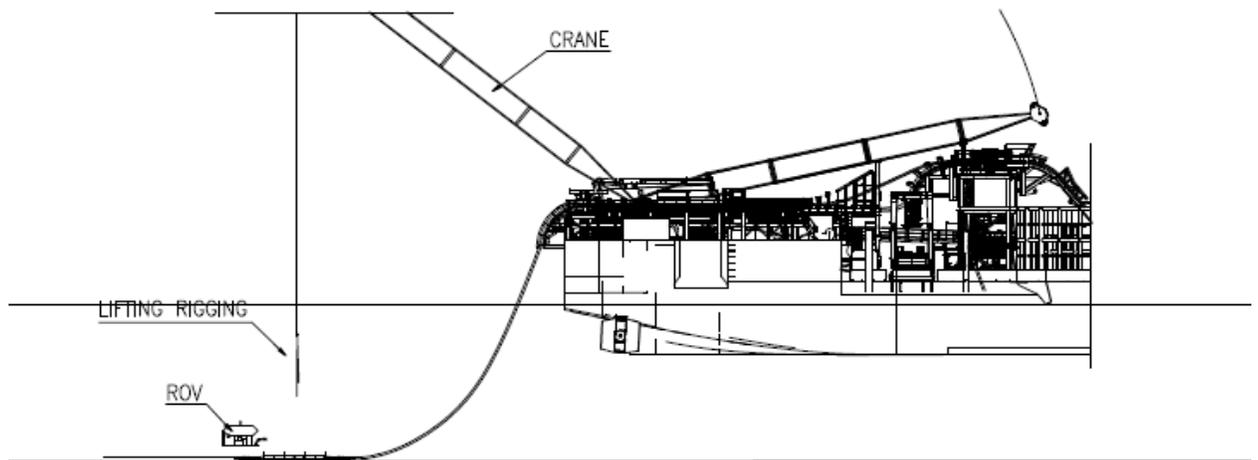
Figure 4-5: Installation vessel to resume normal cable laying operations.

137

4.3   STEP 1 – DEFINING CABLE, CRANE HOIST, EYE-BOLT AND JOINT ACCEPTANCE CRITERIA

Figure 4-6 presents the cable lay conventions which are used throughout this thesis. The results presented are parametric with respect to the departure angle, layback length, cable, chute and touchdown point. The simulations undertaken in this section were made using OrcaFlex Software (2014).
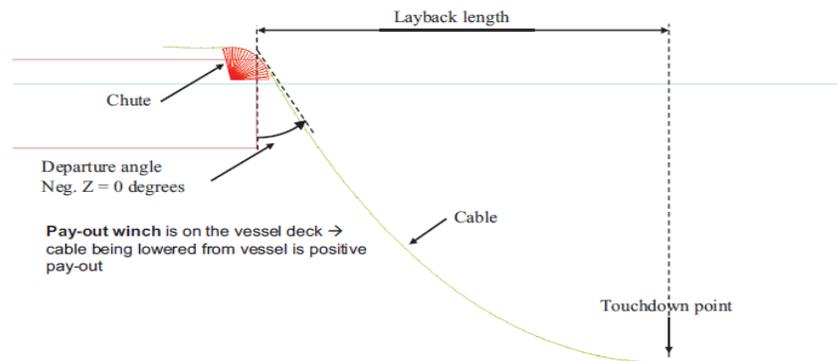
Figure 4-6: Cable lay conventions.

Figure 4-7 illustrates the environmental conventions used throughout the simulations. The wave direction is also illustrated. The environmental conventions are indicated as follows:

- Stern wave   (0 degree)
- Starboard   (90 degrees)
- Head wave   (180 degrees)
- Portside   (270 degrees)
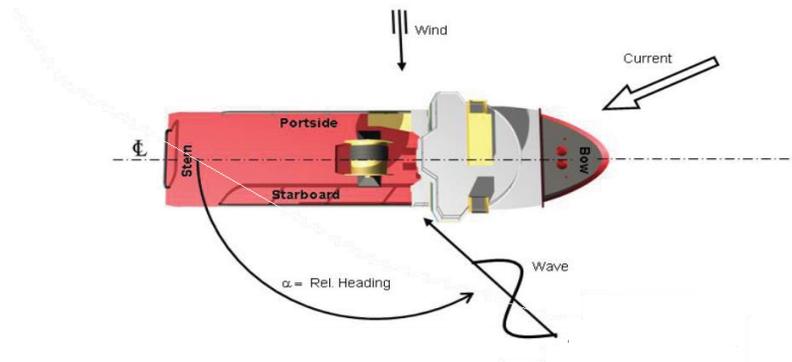
Figure 4-7: Environmental conventions.

4.3.1 Cable Data

The cross section and the mechanical properties of the submarine cable are highlighted in Figure 4-8 and Table 4-1.

1. Conductor
2. Conductor Screen
3. Insulation
4. Insulation Screen
5. Water blocking layer
6. Metallic Sheath
7. Oversheath
8. Filler
9. Binder tape
10. Anti-teredo protection
11. Armor bedding
12. Wire armor
13. Serving
14. Optical fiber unit
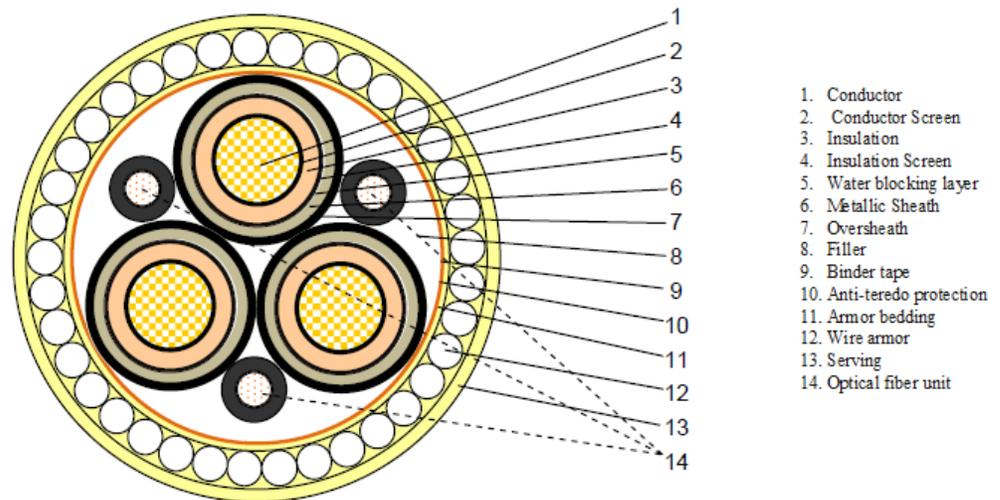
Figure 4-8: Configuration of 132 kV HVAC submarine cable.

Table 4-1: The Mechanical Properties of 132 kV HVAC Submarine Cable

Item	Value	Unit
Outer diameter	191	mm
Weight in air	70	kg/m
Weight in water	41	kg/m
Axial stiffness	650	MN
Bending stiffness	26	kN.m^2
Allowable tension (straight pull)	160	kN
Allowable tension (on minimum bend radius (MBR) pull)	115	kN
Allowable compression (straight pull)	-17.3	kN
Allowable compression (on MBR pull)	-10.2	kN
Minimum bending radius (for installation)	2.9	m
Allowable curvature (for installation)	0.345	Rad/m

It should be highlighted that the compression limit was identified by physical testing as outlined in Chapter 3.

4.3.2 Joint Data

The joint is comprised of the actual joint, armour pot and bend restrictor. The joint schematic is shown in Figure 2-4. Table 4-2 to Table 4-4 present the properties of the actual joint, armour pot and bend restrictor, noting that the joint is not a rigid body but a flexible member having prescribed bending limits.

Table 4-2: Joint Body Properties

Item	Value	Unit
Length	5580	mm
Outer diameter	605	mm
Axial stiffness	2680	MN
Bending stiffness	88000	kNm^2
Bending moment	125	kNm
Weight in air	744	Kg/m
Submerged weight	449.3	kg/m

Table 4-3: Armor Pot Properties

Item	Value	Unit
Length per side	358	mm
Outer diameter	291	mm
Axial stiffness	3695	MN
Bending stiffness	36400	kNm^2
Bending moment	180	kNm
Weight in air	210.7	Kg/m
Submerged weight	142.5	kg/m

Table 4-4: Bend Restrictor Properties

Item	Value	Unit
Length per side	2129	mm
Outer diameter	291	mm
Axial stiffness	650	MN
Bending stiffness unloaded	26	kNm^2
Bending stiffness loaded	4600	kNm^2

Item	Value	Unit
Bending moment	100	kNm
Weight in air	281.4	Kg/m
Submerged weight	213.2	kg/m
Minimum bend radius	3.0	m

The allowable tension in the cable inside the bend restrictor varies with the angle of bending. Table 4-5 illustrates the relationship between the bending angle and allowable tension for the cable inside the bend restrictor.

Table 4-5: Bend Restrictor Allowable Tension

Angle	Allowable Tension (kN)
0	120
15	116
30	104
45	85
60	60
75	35
90	20

4.3.3   Crane Lifting Capacity

Table 4-6 highlights the maximum crane capacity limit used throughout the simulations.

Table 4-6: Crane Capacity

Item	Value	Unit
Crane lifting capacity at smallest reach	13	Tonnes
Crane lifting capacity at largest reach	4.9	Tonnes
Crane block lifting capacity	30	Tonnes

4.3.4   Lifting Aids Capacity

Table 4-7 highlights the maximum eye-bolt and shackle capacity limits used throughout the simulations.

Table 4-7: Lifting Aids Capacity

Item	Value	Unit
Shackle	9.5	Tonnes
Eye-Bolt	17.3	Tonnes

4.3.5   Wave Data

A range of significant wave heights, H_s, were applied in the simulations, varying from 0.5 m to 1.00 m, for water depth (WD) = 38.4m. A corresponding realistic range of peak period, T_p, is defined by $\gamma\sqrt{H_s.13} < T_p < \sqrt{H_s.30}$ as highlighted in GL Noble Denton (2016), which is the relation for wind driven seas. In the analysis, three T_p's were considered: upper bound, best estimate and lower bound time periods, as shown in Table 4-8. The best estimate time period is an average of the upper and lower bounds. The Joint North Sea Wave Project, JONSWAP, spectrum was analysed with the wave steepness value formulated from Section 3.5.5.5 of DNV-RP-C205 (2014) as shown below,

$$\gamma = 5 \; for \; T_p/\sqrt{H_s} \leq 3.6,$$

$$\gamma = \exp{(5.75 - 1.15\frac{T_p}{\sqrt{H_s}})} \; for \; 3.6 < \frac{T_p}{\sqrt{H_s}} < 5,$$

and

$$\gamma = 1 \; for \; 5 < \frac{T_p}{\sqrt{H_s}}.$$

Where : γ is the peakedness parameter

The influence of the steepness factor over the H_S can be seen schematically in Figure 4-9.

143
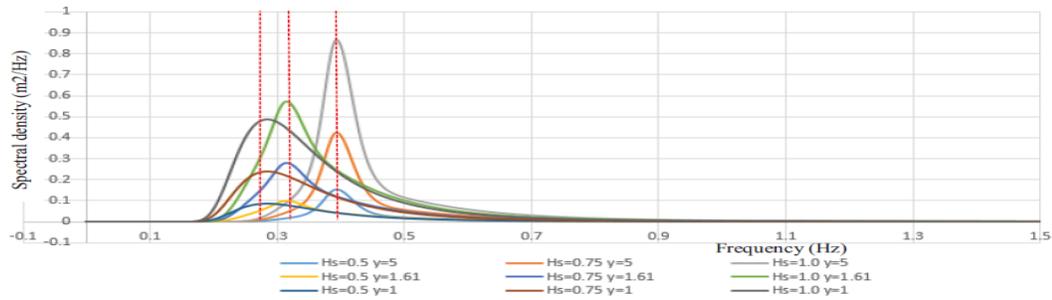
Figure 4-9: Effect of gamma and significant wave height on spectrum.

Table 4-8: Wave Data

Hs [m]	Lower Bound (LB) [s]	Best Estimate (LB) [s]	Upper Bound (UB) [s]
0.5	2.55	3.24	3.87
0.75	3.12	3.97	4.74
1.0	3.61	4.58	5.48

4.4   STEP 2 – SELECTING THE OPTIMAL LAYBACK AND DEPARTURE ANGLE

An intensive analysis was undertaken to determine the optimal layback distance and departure angle of the cable. The main criteria in selecting the optimal layback among the various options was to choose the layback which resulted in the highest dynamic workability (low tension/compression and curvature exceedance).

Figure 4-10 and Figure 4-11 present the cable curvature and the effective tension in the cable respectively. These results were extracted from OrcaFlex dynamic simulations undertaken at the same water depth but at different layback lengths. It can be seen from Figure 4-10 that the cable curvatures at layback lengths of 44 m (denoted as L44 in Figure 4-10) and 50 m (denoted as L50) exceed the allowable curvature limit. Furthermore, Figure 4-11 shows that the compression generated in the cable at layback lengths of 44 m and 50 m also exceeded the allowable axial compression limit. Additionally, Figure 4-11

shows that the effective tension for the layback length of 59 m (L59) was greater than that from the layback length of 54 m. Based on this, it can be concluded that the optimal layback is 54 m. This layback length resulted in low tension and curvature to the cable.
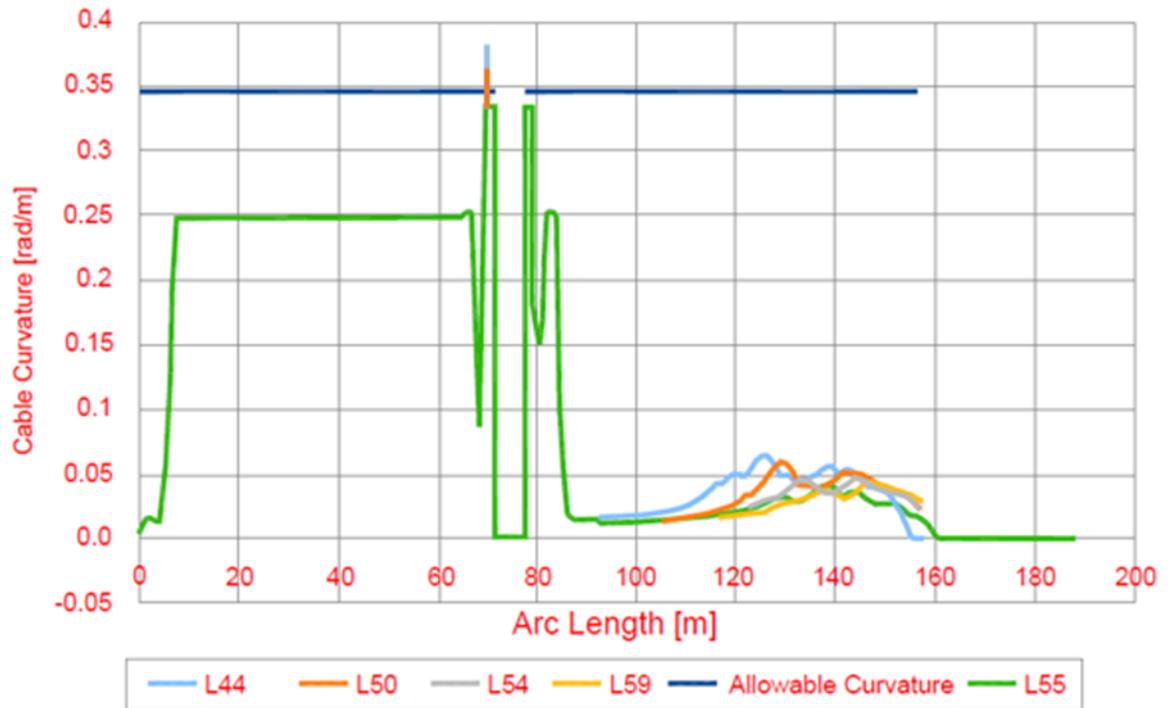
Figure 4-10: Cable curvature calculated at different layback lengths.
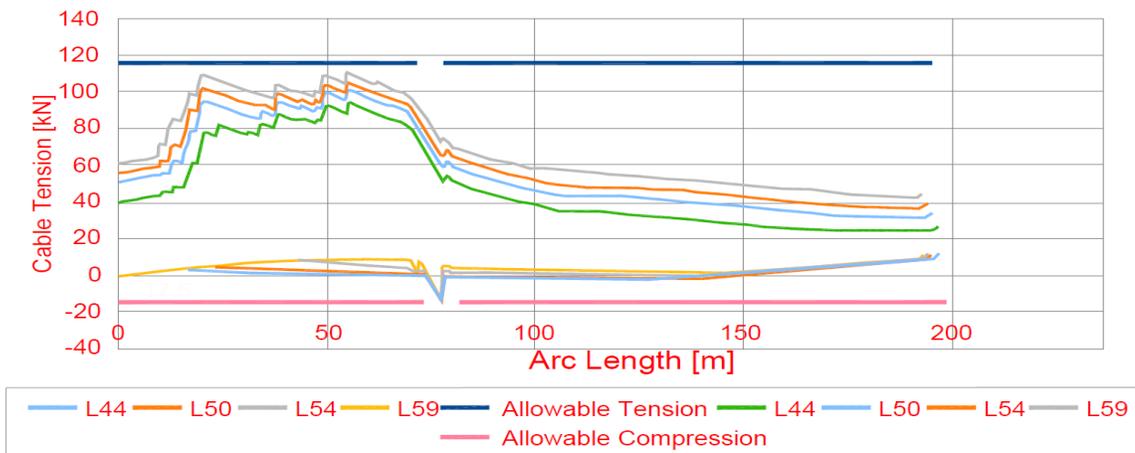
Figure 4-11: Cable tension calculated at different layback lengths.

145

4.5   INITIAL SET-UP

Figure 4-12 shows a snapshot from the OrcaFlex model used to calculate all the relevant loads and stresses expected during actual installation. These loads were applied to the OFJ during the on-land simulation. The initial set-up can be envisaged from Figure 4-13. In this example, the vessel, at its draft, was positioned so that the layback length was approximately 54 m for a water depth of 38.4 m.
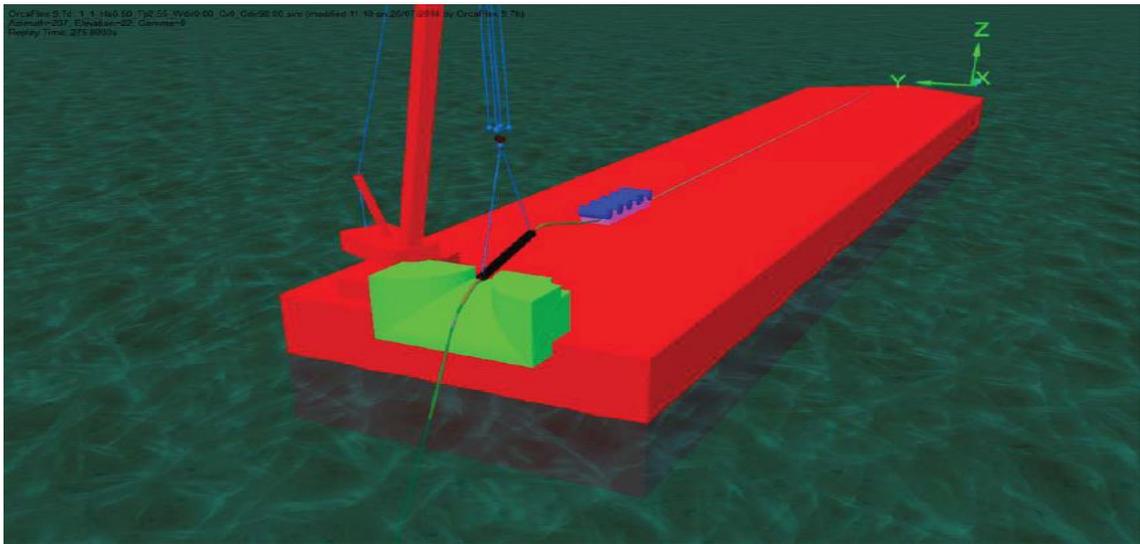
Figure 4-12: Snapshot of OrcaFlex model.

It is worth mentioning that the water depth of 38.4 m was selected as it represents the maximum water depth along the cable route. Deployment simulations are considered at water depths of 10 m, 20m and 30 m. It was concluded that the stresses experienced by the field joint increases with increased water depth.
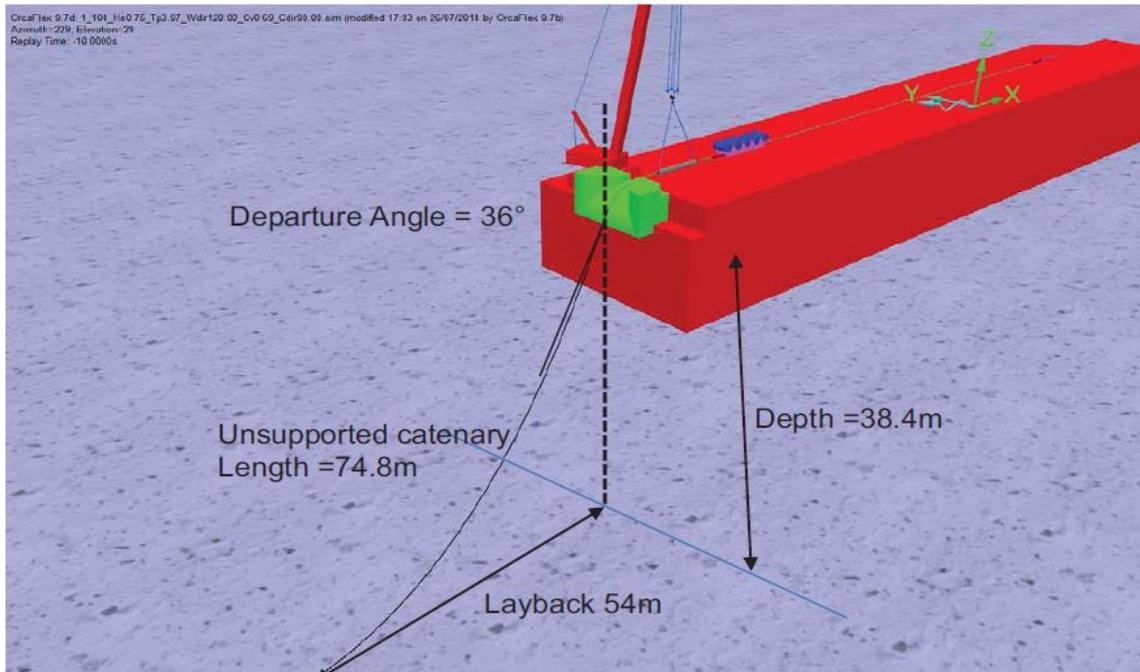
Figure 4-13: OrcaFlex model showing the starting point of the simulation.

OrcaFlex models were developed for the cable, joint, winch and vessel. The cable and joint were modelled as line objects in OrcaFlex using the input data described in Sections 4.3.1 and 4.3.2. The winch wire was modelled as a simple winch. One end of the cable was anchored to the seabed, while the end of the cable on the vessel was free.

The segmentation of the lines in OrcaFlex has considerable influence on the accuracy of the results. As such, a sensitivity study was carried out to establish how small the segments were required to be in order for the results to converge. This is particularly important for stress. The timestep size is crucial to the accuracy of the results but has a significant impact on the time it takes to run a simulation. For this reason, it is desirable to maximise the time steps without compromising the accuracy or stability of the model.

4.6   RIGGING SET-UP

In this step the in-line joint was lifted using a pulley arrangement where a sling was used to pass the joint over the pulley neatly into the crane hook location, as shown in Figure

4-14. For the OrcaFlex simulations, a 17 m steel sling was used. The selection and the details of the slings were based on the maximum dynamic force results. In the simulations, the pulley was held 7.6 m above the in-line joint as illustrated in Figure 4-15. Note that at this position, the joint is still located on the vessel desk with no lift from the cable.
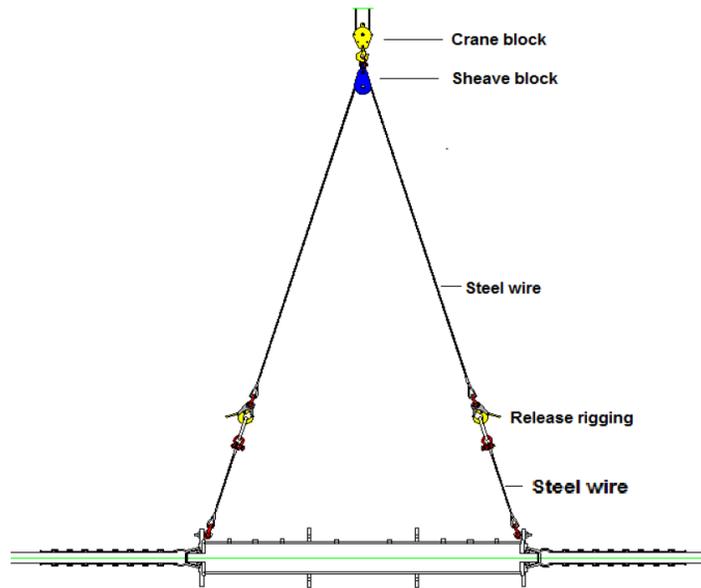
Figure 4-14. Lifting arrangement.
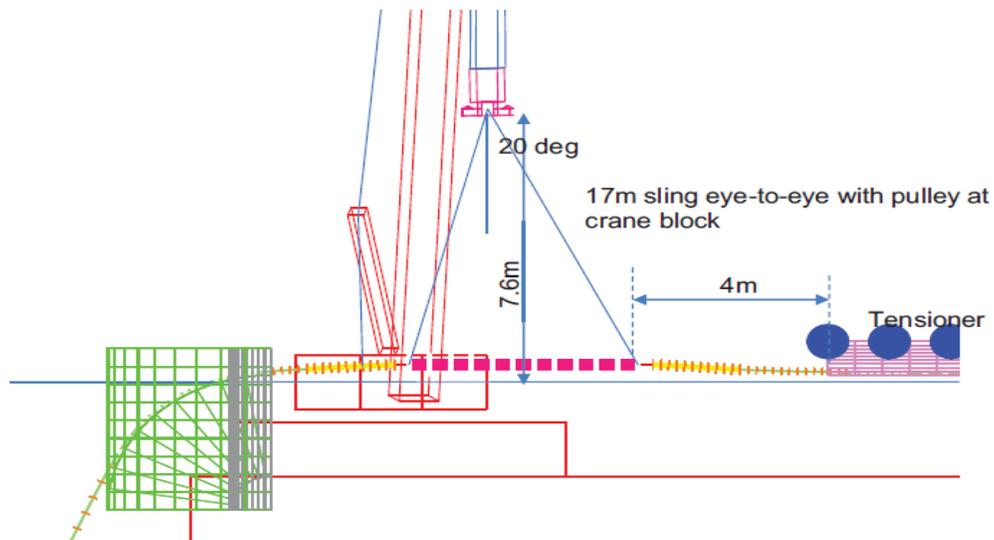
Figure 4-15. Initial position of the crane hook with reference to the in-line joint.

4.7   CRANE OPERATION AND VESSEL MANEUVERS

In this step, the in-line joint was lifted by the crane and the vessel was moved. The manoeuvres were done in such way that:

- The allowable tension, minimum bend radius, axial compression of the cable, etc. were not exceeded.

- There was no chance of immediate collision of the joint with the adjoining metal structures.

The total movement of the joint is displayed in Figure 4-16. Additionally, Figure 4-16 highlights the cable shape at different time increments of the dynamic simulation undertaken using the OrcaFlex software. This figure starts at the moment the crane lifts the in-line joint until the moment the in-line joint is laid on the seabed. It is worth indicating that the slings were released from the pulley once the in-line joint was laid on the seabed.
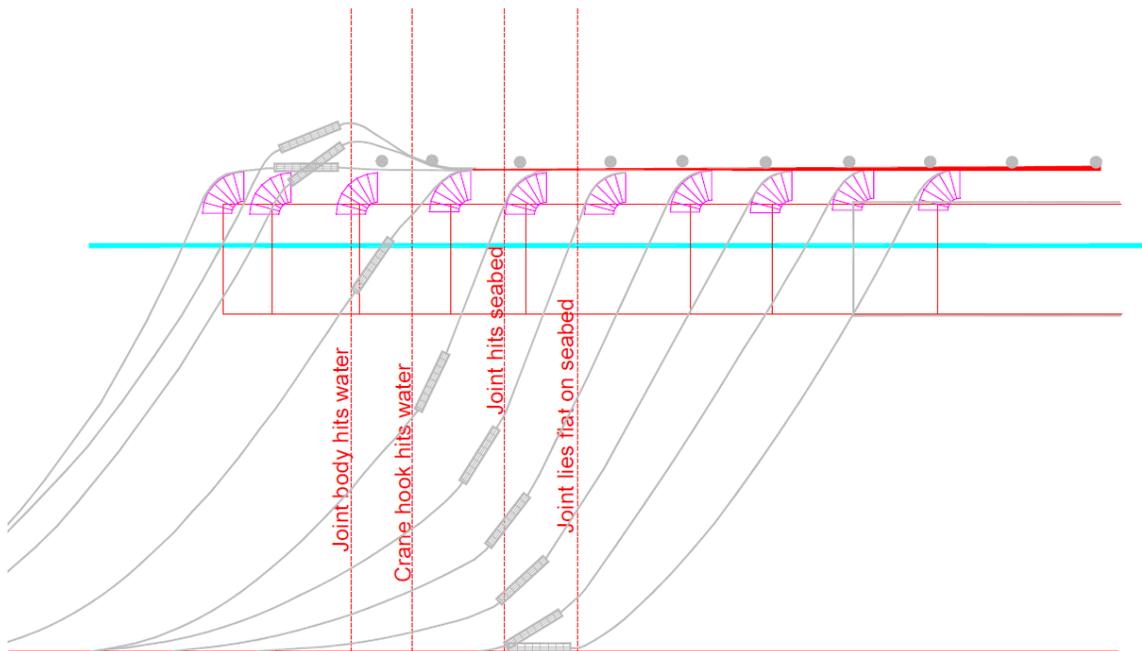
Figure 4-16. Cable shape at different time increments. Timeline of important events marked.

149

Figure 4-17 shows the operability curve for the depth 38.4 m. The upper graph is drawn corresponding to still water level. Four events are marked below:

- The MAROON line is when the joint hits the water.
- The RED line is when the sling is slack (this is when the crane block hits the water).
- The BLUE line shows when the joint touches the seabed.
- The GREEN line is when the joint lays flat on seabed.
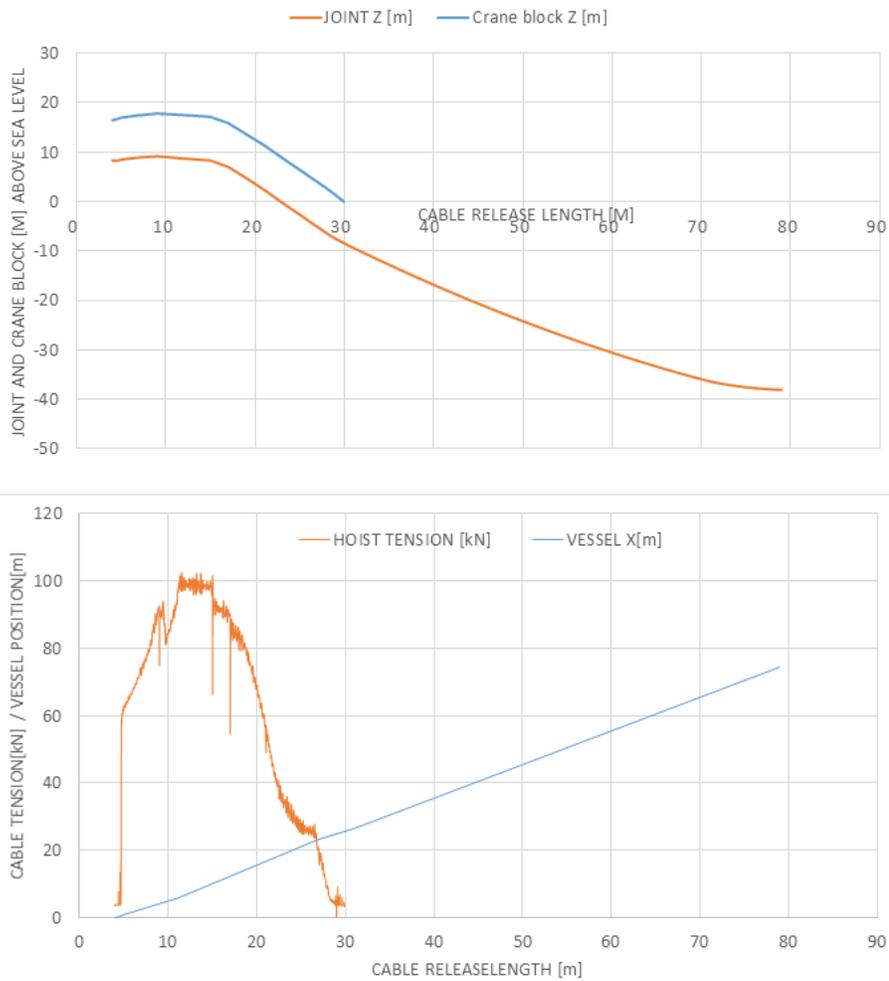
Figure 4-17: Vessel and crane operation for 38.4 m, based on slackness of sling.

4.8   STEP 3 – PERFORMING STILL WATER ANALYSIS

In this section, the analysis was undertaken ignoring the influence of waves to determine whether the requirements of tension, compression and curvature in the cable contained a wide enough margin to allow for the addition of wave actions.

For still water, the crane hook load was 10.0 metric tonnes as shown in Figure 4-18 .
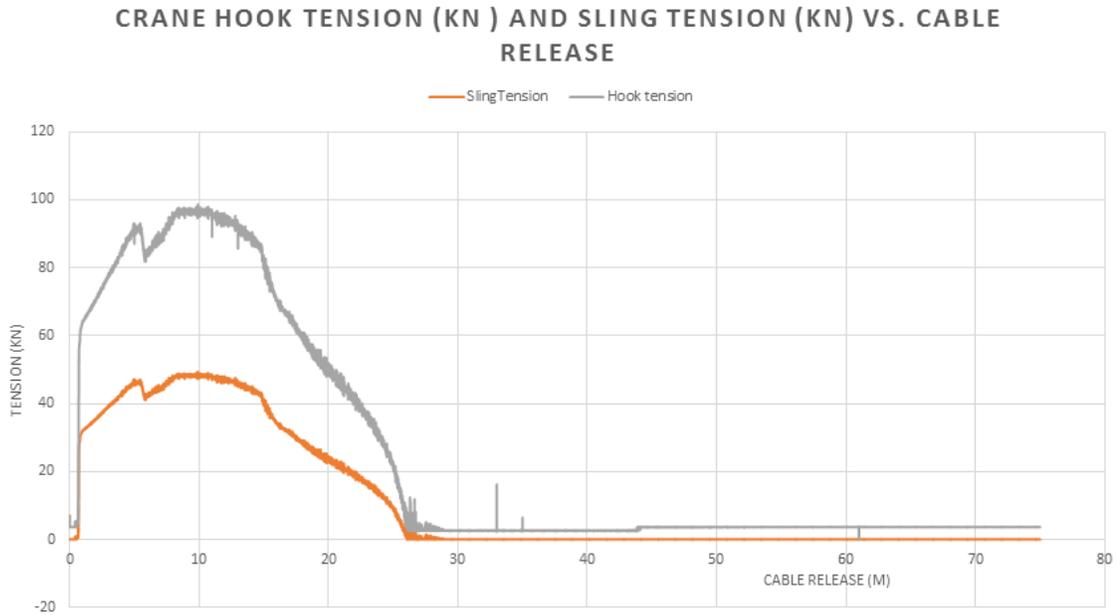
Figure 4-18: Crane hook load and sling load vs. cable release 38.4 m depth.

OrcaFlex was used to extract the range of tension values shown in Figure 4-19. It can be seen from the results that compression was occurring at the joint. The joint has been designed for these small compression loads and the compression in the OFJ is, in part, due to the rigging set-up.
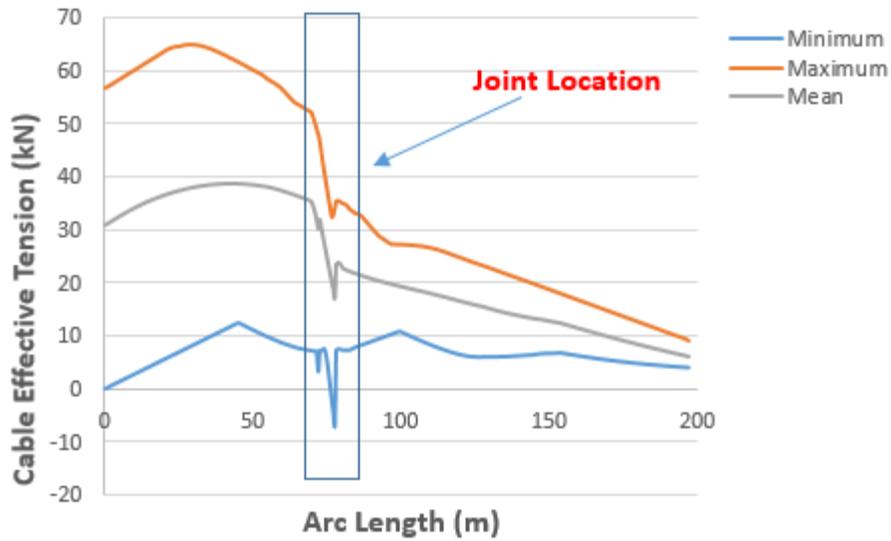
Figure 4-19: Cable tension over length 38.4 m water depth.

Figure 4-20 illustrates the maximum curvature of the cable. The figure demonstrates that the curvature requirement in the cable was not met. Moreover, the effect of the bend restriction was pronounced between the lengths of 69.5 m -71.6 m and 78.2 m-79.5m, where the curvature became reduced.

The bending moment along the cable is shown in Figure 4-21. It is evident that the bending moment requirement along the cable was not exceeded.
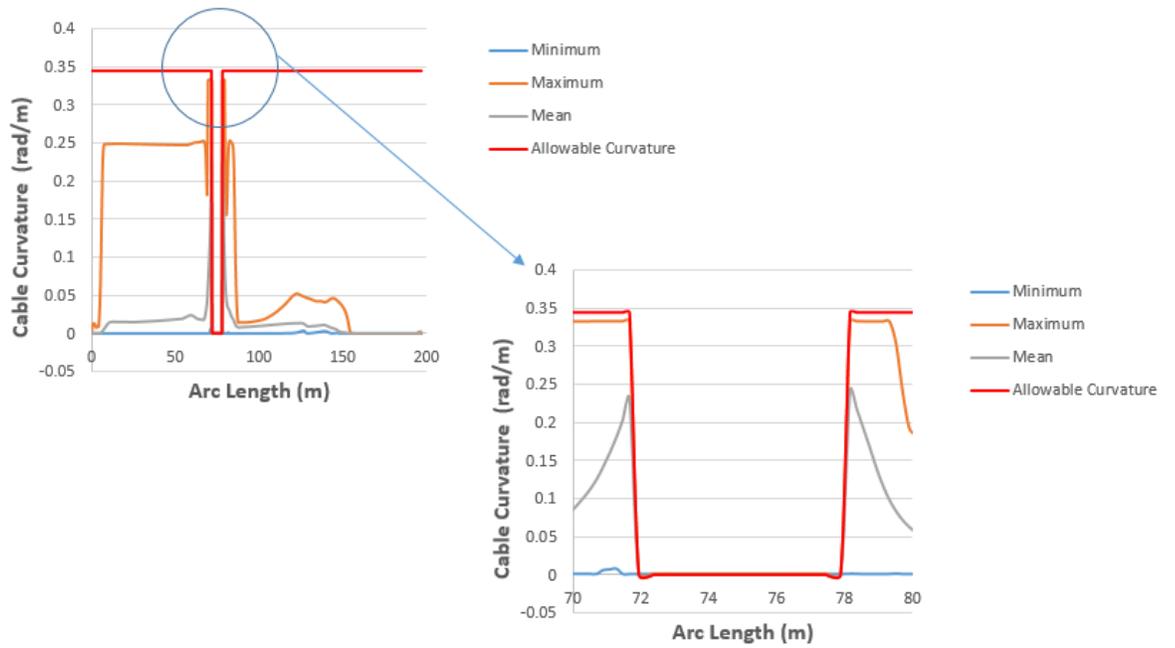
Figure 4-20: Cable curvature over length at 38.4m water depth.
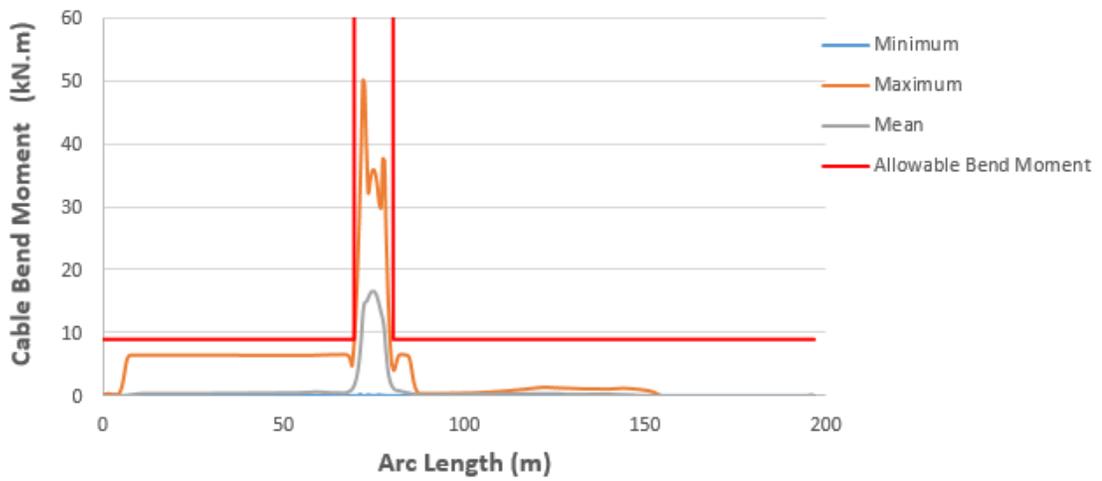
Figure 4-21: Cable bending moment over length at 38.4 m water depth.

153

4.9   STEP 4 – PERFORMING DYNAMIC SIMULATIONS

Upon completion of the still water analysis, a range of dynamic environments were introduced in the OrcaFlex model to investigate the deviation in the results due to the following environmental parameters:

- Wave height

- Wave Period

- Wave direction

- Current velocity

Dynamic simulations are required to determine the maximum sea state condition within which the vessel can safely deploy the joint and the cable. The following factors must be taken into consideration:

- Hoist wire tension

- Maximum tension/compression in the cable

- Maximum bending moment in the cable

- Maximum curvature in the cable

- Maximum declination in the hoist wire

Only the results of the maximum tension, maximum bending moment and maximum curvature in the cable will be presented here. The other results will not be presented due to limitations in thesis length.

Figure 4-22 presents the tension in the cable obtained from the range graph. In this figure, the maximum and minimum tensions are given as a function of environment. It can be seen from the figure that the significant wave height of 1 m at the upper bound wave period shows both tensions are beyond the acceptable limit of the cable.

From Figure 4-23 the limiting weather criteria for joint deployment can be determined.

Figure 4-24 and Figure 4-25 show the curvature of the cable as a function of environment. It can be seen from Figure 4-24 that the curvature of the subsea cable is above the allowable cable curvature for a significant wave height of 1 m and upper bound wave

period of 5.47 seconds. In these figures the red line refers to the cable allowable curvature and the green line refers to the bend restrictor allowable curvature.

The curvature of the cable was checked at a significant wave height of 1 m and upper bound wave period of 5.47 seconds for different wave directions as indicated in Figure 4-25. Figure 4-25 shows that the curvature is beyond the allowable limits for the wave directions of 60 and 90 degrees.

As indicated earlier, extensive OrcaFlex simulations were undertaken to determine the limiting weather criteria during the actual offshore jointing as well as to employ the likely maximum expected loads in the on-land simulation. This was in part to verify the mechanical properties of the OFJ under deployment conditions.

4.10 STEP 5 – STRESS ANALYSIS FOR THE JOINT

As the OFJ is subject to a bending moment during deployment, this section presents a stress analysis that was undertaken using the multi-purpose finite element package ABAQUS (2012). It can be seen from Figure 4-19 that the maximum tension obtained from the still water analysis at a water depth of 38.4 m was 70kN. The maximum dynamic tension from the OrcaFlex dynamic simulation was 100 kN.

This tension value is associated with the maximum sea state condition within which the vessel can safely deploy the joint and the cable. However, in order to be conservative, this dynamic tension was not used to calculate the dynamic amplification factor. Instead a tension value of 112 kN was used. This value represents the vessel's tensioner capacity. Based on this, the dynamic amplification factor, DAF, can be determined from the following equation:

$$DAF = \frac{Maximum\ Tension_{Dynamic}}{Maximum\ Tension\ for\ still\ water\ condition} = \frac{112}{70} = 1.6$$

It should be highlighted that this DAF will be used later in the hand calculations as part of the test procedure and requirements.
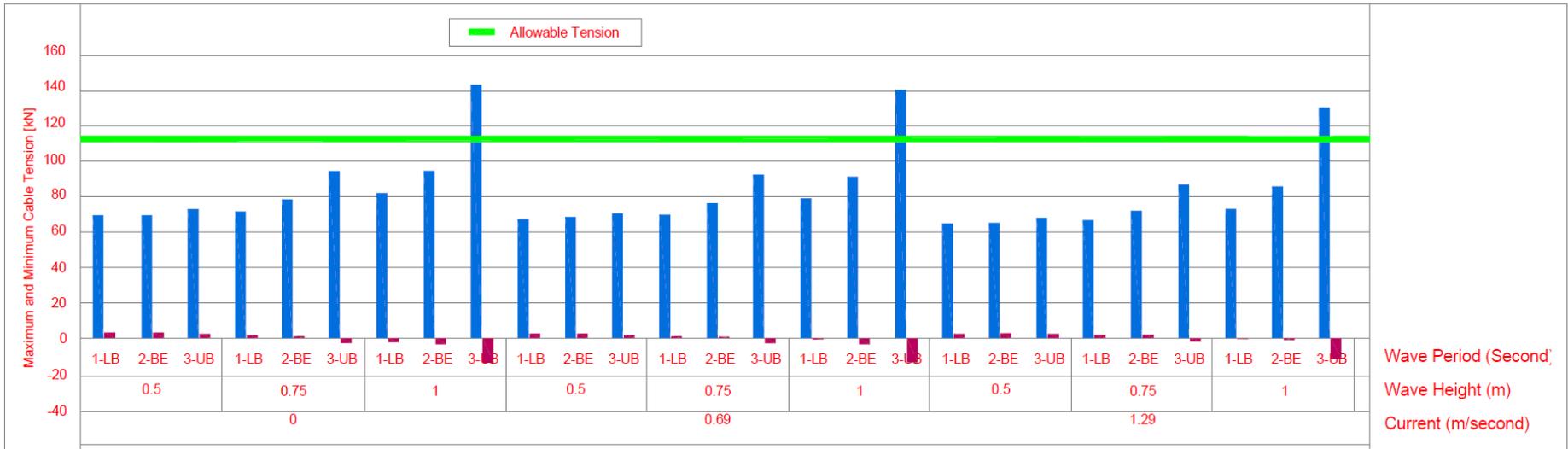
Figure 4-22. Cable tension value vs. significant wave height, peak period and steady current for the worst wave heading and current.

156
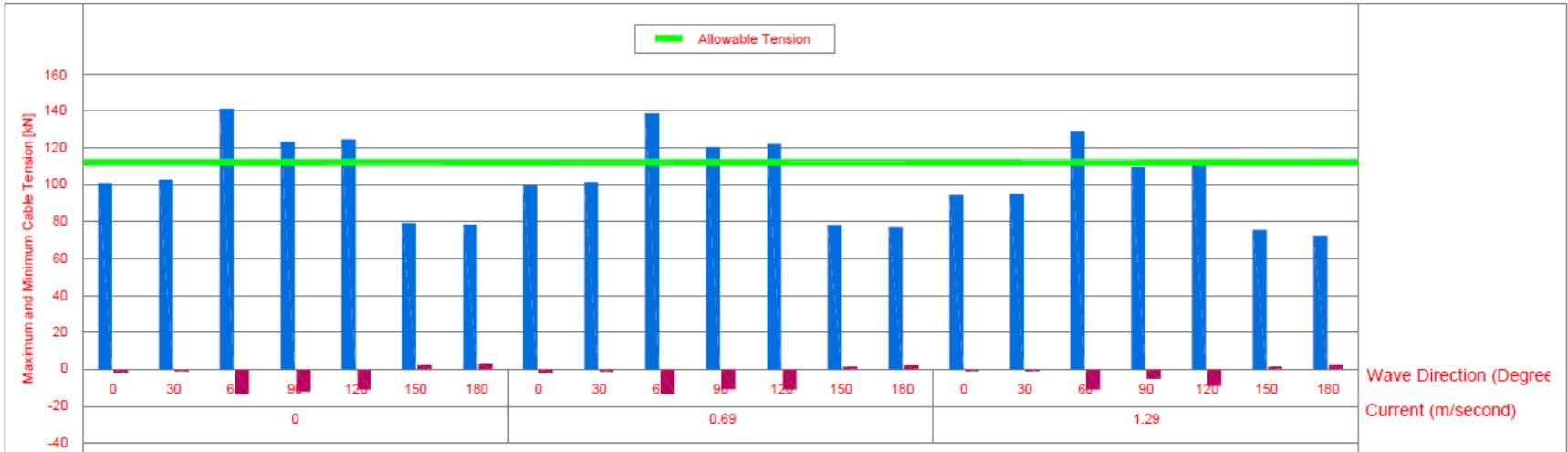
Figure 4-23. Cable tension value vs. direction and current for wave height=1 m and time 5.47 seconds.
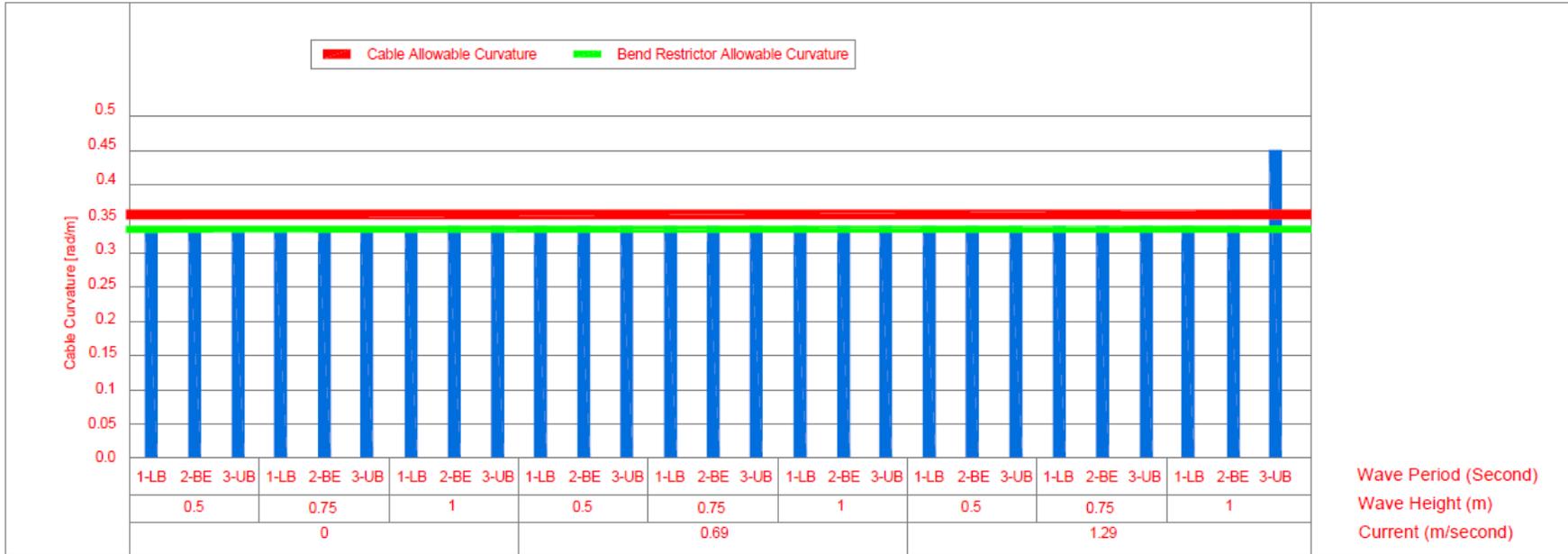
Figure 4-24: Cable curvature value vs. significant wave height, peak period and steady current for the worst wave heading and current.
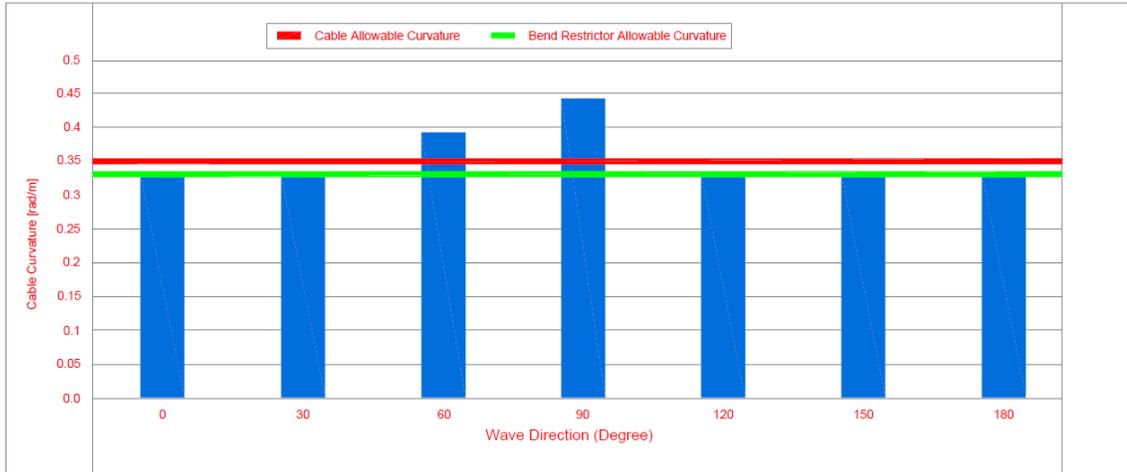
Figure 4-25: Cable curvature value vs. direction and current for wave height=1 m and time 5.47 seconds.

Table 4-9: Boundary Condition and Loading Condition of Analysis Cases

Analysis Case	Boundary Condition	Loads Applied
I	Fixed at upper hole of 2 main flange	Gravitational force of OFJ : 5.5 metric tonnes Bending moment at both armour pot: 125 kN.m
II	Fixed at upper hole of 2 intermediate flange	Gravitational force of OFJ: 5.5 tonne Bending moment at both armour pot: 125 kN.m

Figure 4-26 and Figure 4-27 show schematics for the two analyses undertaken using ABAQUS. As one can see, the bending moment of 125 kN.m was applied to the two ends of the OFJ. This bending moment value represents the allowable bending moment for the OFJ. Asides from the bending moment applied to the two ends of the OFJ, a gravity load of 5.5 tonnes was applied to the OFJ. The gravity load was applied as a distributed load along the OFJ length. During deployment, the crane lifts the OFJ using two main flanges as indicated in Figure 4-26. This way of lifting intends to relieve the bending moment in the main cylindrical body of the OFJ. For thoroughness, an OFJ with a different boundary

159

condition (as shown in Figure 4-27) was also investigated. This is in order to capture the likely maximum bending moment in the OFJ structure.
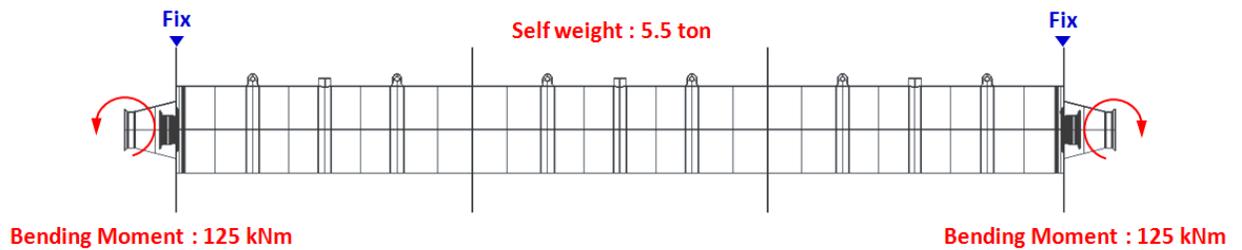
Figure 4-26: The boundary and loading conditions of Case I.
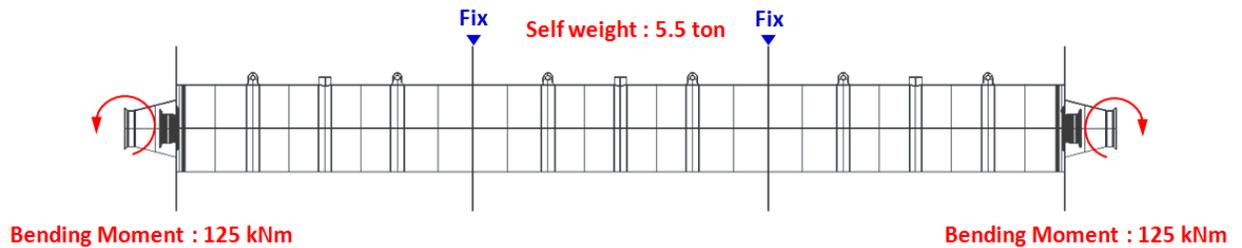
Figure 4-27: The boundary and loading conditions of Case II.

Figure 4-28 shows the stress contour extracted from ABAQUS for Case I. The maximum stress of 213.5 MPa occurs at the armour pot due to the load concentration. However, it still remains in an elastic state. The cylindrical body shows a low level of stress. Note that this result was drawn under the condition where 1.72 times the maximum bending moment was applied to the OFJ over the stern. The utilization factor is given as 0.80 (=213.5 MPa/265 MPa).

Figure 4-29 shows the stress contour for Case II. The maximum stress (219.2 MPa) occurs at the cylindrical body near the lifting point (intermediate flange). Again, yielding of the cylindrical body did not occur. It can be therefore ascertain that the allowable bending moment of the OFJ structure is at least 125kNm, which is harsher than the loading condition of the inline deployment. The utilization factor is 0.83 (=219.2 MPa/265 MPa).

160
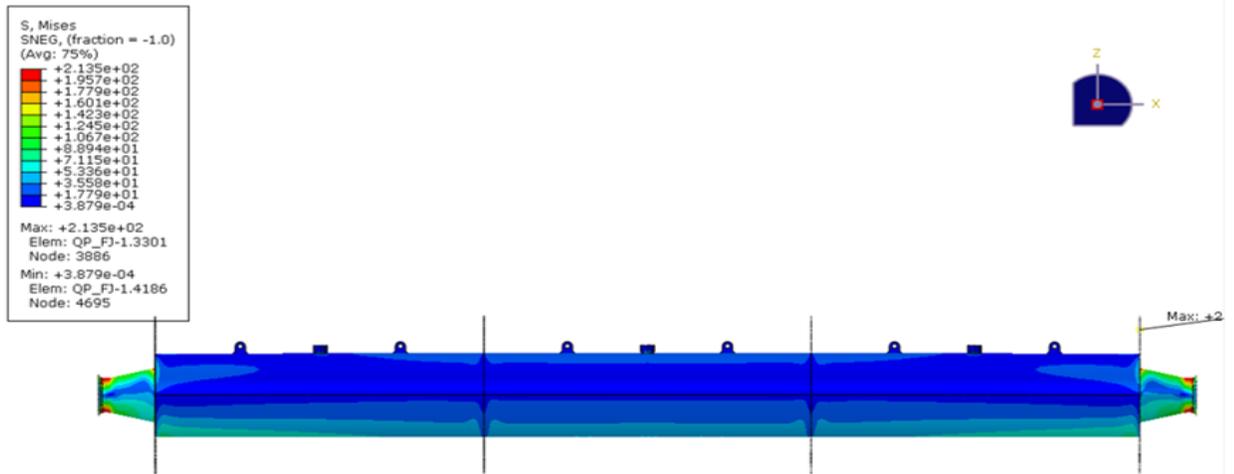
Figure 4-28: Stress contour of OFJ (Fixed at 2 main flanges, bending moment: 125kNm).
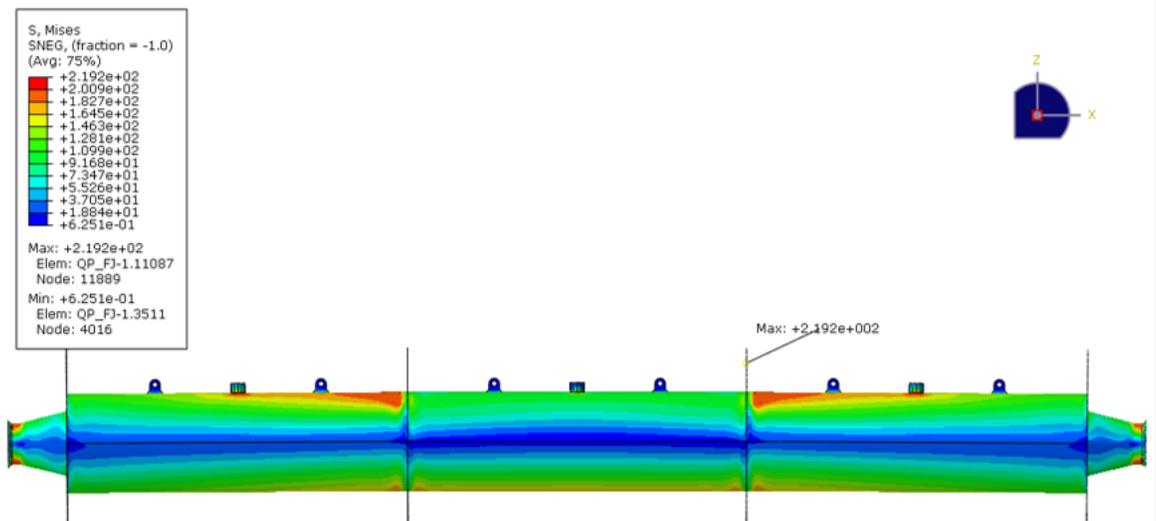
Figure 4-29: Stress contour of OFJ (fixed at 2 intermediate flanges, bending moment: 125kNm).

4.11 STEP 6 – CONDUCTING THE MECHANICAL TEST FOLLOWED BY VISUAL INSPECTION AND RWP TEST

4.11.1 Testing Concept for Simulated In-Line Deployment of OFJ

It was indicated from the OrcaFlex simulations that during the deployment operations, there are three critical stages which have high tension or bending moments, as illustrated in Figure 4-30. The loads given in this section are extracted from OrcaFlex simulations undertaken as part of the installation engineering.
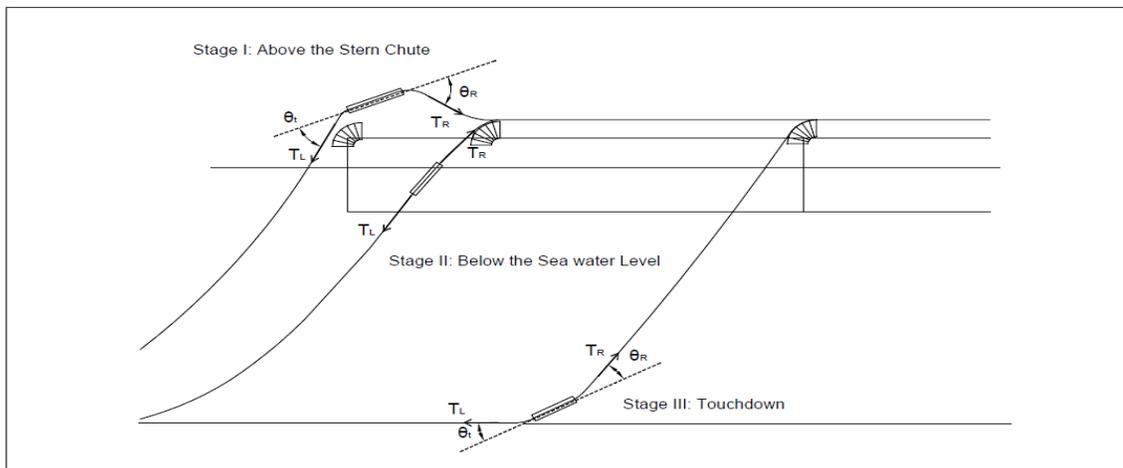
Figure 4-30. In-line deployment stages.

Before conducting the test, it was decided to compare the results obtained from OrcaFlex against the analytical calculations of residual tension. The detailed hand calculations of the mechanical load during the in-line deployment of the OFJ are presented below. The calculations are based on Electra 171 (1997).

CABLE AND OFFSHORE FIELD JOINT (OFJ) PARAMETERS

Cable weight in air, $W_{Air} = 70$ kg/m

Cable weight in water, $W_{water} = 41$ kg/m

OFJ weight in air, WOFJ, Air = 5500 kg (from bend restrictor to bend restrictor including the cable)

OFJ weight in water, WOFJ, water = 3517 kg (from bend restrictor to bend restrictor including the cable)

Length of OFJ, L OFJ = 10.55 m (from bend restrictor to bend restrictor)

INLINE DEPLOYMENT

For these calculations, refer to Figure 4-13.

Water depth, D = 38.6m (Max.)

Vertical distance from water level to centre of the joint body, d = 9.0m

Vertical distance from sea bed to centre of the joint body, D+d = 38.6 + 9.0 = 47.6 m

Unsupported catenary length, Lc=74.8 m

Departure angle, ϕ = 36°

Catenary factor, fc = Lc/(D+d) = 74.8/47.6 = 1.95

Residual tension factor, f_R= 0.2 (Based on Electra 171)

As mentioned earlier, there are 3 stages which have high tension or bending of the OFJ during in-line deployment, as shown in Figure 4-30. These are discussed in detail below.

STAGE I: Above the Stern Chute

Catenary length corresponding to air section, Lc, Air = fc x d= 1.95 x 9.0m = 17.53 m

Catenary weight corresponding to air section, Wc, Air = WAir x L C,Air= 70 kg/m x 17.53 m =1227.2 kg

Catenary length corresponding to water section, Lc,water = LC -L c,Air = 74.8 m - 17.53 m = 57.27 m

Catenary weight corresponding to water section, WC, water = Wwater x L c,water= 41 kg/m x 57.27 m =2348.0 kg

163

Total catenary weight, WC = WC,Air + W c,water= 1227.2 kg + 2348.0 kg = 3572.2 kg

Residual tension, Tres= fR x (WAir X d+ Wwater x D) = 0.2 x (70 kg/m x 9m + 41 kg/m x 38.4 m) = 440.9 kg

Dynamic Factor, f D= 1.6

Tension at left hand side of OFJ, TL = fDx (WC+ T res) = 1.6 x (3572.2 kg + 440.9 kg) = 6421 kg

Tension at right hand side of OFJ, TR= TL x sin ϕ = 8026.2kg x sin 36° = 3774.2 kg

Angle at left hand side of OFJ, θ L = +45° (from Figure 4-30)

Angle at right hand side of OFJ, θ R= -45° (from Figure 4-30)

STAGE II: Below the Sea Water Level

Catenary length corresponding to water section, Lc,water   W water,OFJ = 57.27 m

Catenary weight corresponding to water section, Wc,water = Wwater x (Lc,water – W OFJ) = 41 kg/m x 46.72m= 1915.5 kg

Residual tension, Tres= fR x (WAir X d + Wwaterx D) = 0.2 x (70 kg/m x 9m + 41 kg/m x 38.4 m) = 440.9 kg

Tension at left hand side of OFJ, TL= fD x (WC,water + T res) = 1.6 x (1915.5 kg + 440.9 kg) = 3770.24 kg

Tension at right hand side of OFJ, TR= fDx (WC,water + WOFJ, water + T res) = 1.6 x (1915.5 kg + 3517 kg +440.9 kg) = 9397.4 kg

Angle at left hand side of OFJ, θ L = 0° (from Figure 4-30)

Angle at right hand side of OFJ, θ R= 0° (from Figure 4-30)

STAGE III: Touchdown

Tension at left hand side of OFJ, TL = Fd x T res= 1.6 x 440.9 kg = 705.4 kg

Tension at right hand side of OFJ, TR = Fd x (WoFJ, water+ Tres) = 1.6 x (3517 kg + 440.9 kg) = 6332.64 kg

Angle at left hand side of OFJ, θ L = -45° (from Figure 4-30)

Angle at right hand side of OFJ, θ R= +45° (from Figure 4-30)

It is immediately discernible that the hand calculations yield conservative results as compared to those from OrcaFlex. During the simulation, the tensions from the hand calculations were used. The three critical stages can be summarized as follows:

1. Maximum bending: In this stage, the maximum bending takes place at roughly 45 degrees and with a maximum tensile stress of 6.4 tonnes exerted on the joint. This is when the joint is lifted from one side towards the end of the vessel deck as shown in Figure 4-30.

2. Maximum tensile force: The bending is negligible but but the tensile force encountered by the joint reached a maximum of 9.4 tonnes.

3. Opposite maximum bending: When the joint reaches the seabed, the cable will be bent in the opposite direction with a bending angle of approximately -45 degrees but without the occurrence of a tensile force. The upper side of the in-line joint also experiences a bending in the opposite direction with a tensile force of 6.3 tonnes.

Table 4-10 presents the values obtained from the hand calculations. These values will be employed during the on-land simulations.

Table 4-10. Load Applied During the On-land Simulations

Stage	Tension (Tonnes)		Bending Angle (Degrees)	
	Left Side	Right Side	Left Side	Right Side
1	6.4	3.8	+45	-45
2	3.8	9.4	0	0
3	0.7	6.3	-45	+45

4.11.2 In-Line Test Items and Acceptance Criteria

Table 4-11 highlights the tests undertaken during and after the on-land deployment simulation. The same table lists the acceptance criteria associated with each test.

Table 4-11. Summary of In-line Test Items and Associated Acceptance Criteria

Specific In-Line Test Item	Acceptance Criteria
1. **Fibre attenuation test** Fibre attenuation change during testing	Increase of attenuation per loop using power meter. During the test: maximum 0.1 dB After the test: maximum 0.05 dB
2. **Torsion test** Torsion of cable at end of bend restrictor	Change of torsion angle of the cable at bend restrictor is less than 5 degrees
3. **Radial water penetration test** Radial water penetration test on one pre-moulded joint including plumbing areas, 24 hours water pressure test	No water in the joint.
4. **Visual check of plumbing area** Visual check of plumbing area between cable sheath and copper housing (three joints)	No visible cracks. No holes in plumbing area. No visible gap between plumbing and lead sheath and copper housing.
5. **Measurement of internal displacement of cable** Check the measurements in axial and angular in the 3 dimensions	Information for further analysis and usage. The accuracy of the measurements was less than 5 mm.
6. **Visual checks** Visual check of armour pot and bend restrictor	No visible cracks or deformations.
7. **Dimensional/material check on pre-moulded and OFJ used**	This was done in accordance with the applicable manufacturing plans.

4.11.3 Testing Installation Set-Up

This section describes the set-up adopted during the simulation to mimic offshore installation. Note that the materials used in the simulation such as cables, housing and tools for installation, were identical to those used during offshore installations.

1. The OFJ was installed in a straight arrangement.

2. The inner cores of the joint were marked to determine any signs of axial movement, torsion or other displacement of the cable cores that might have occurred during the simulation. The position measurements were taken in three dimensions.

3. A visible straight mark was applied on the outside of the cable, outer yarn at the armouring pot, outer yarn at the end of bend restrictor, bend restrictor as well as on the OFJ housing. As before, this line was used to determine any signs of axial movement, torsion or other displacement of the cable cores that might occur during the simulation. During the simulation, all torsional variations in the testing assembly were monitored and listed.

4. The total length of the arrangement was 34 m. This was in part to perform the straight tensile test in a manner that most resembled the in-line laying. The armouring at both ends of the cable were terminated by pulling heads and a 1.5 m long fibre optics cable. This was fed out of the pulling head to monitor the fibre optics readings and ensure that the changes in the light power were within acceptable limits.

Note that the cable ends were fixed during the simulation. The cable ends were not allowed to rotate to ensure that any torsion in the cable due to bending or other factors remained in the test sample and did not leave the cable at the ends.

4.11.4 Stage-1 Tensile Bending Test

In this test, the following steps were performed to mimic stage-1 of the deployment procedure.

1. Before embarking on the test, the initial attenuation of the fibre optics was measured and recorded.

2. The torsion angle of the cable in front of the bending restrictor was measured, as shown in Figure 4-31 and Figure 4-32. Additionally, the torsional variation along the assembly length was measured and recorded.

3. The pulling force was increased slowly according to the values indicated in Table 4-10. The force was held for 15 minutes.

4. During the test, optical light power was continuously monitored to check for any cable damage.

5. Upon completion of the test, the torsion angle in front of the bending restrictor as well as the torsional variation were measured.
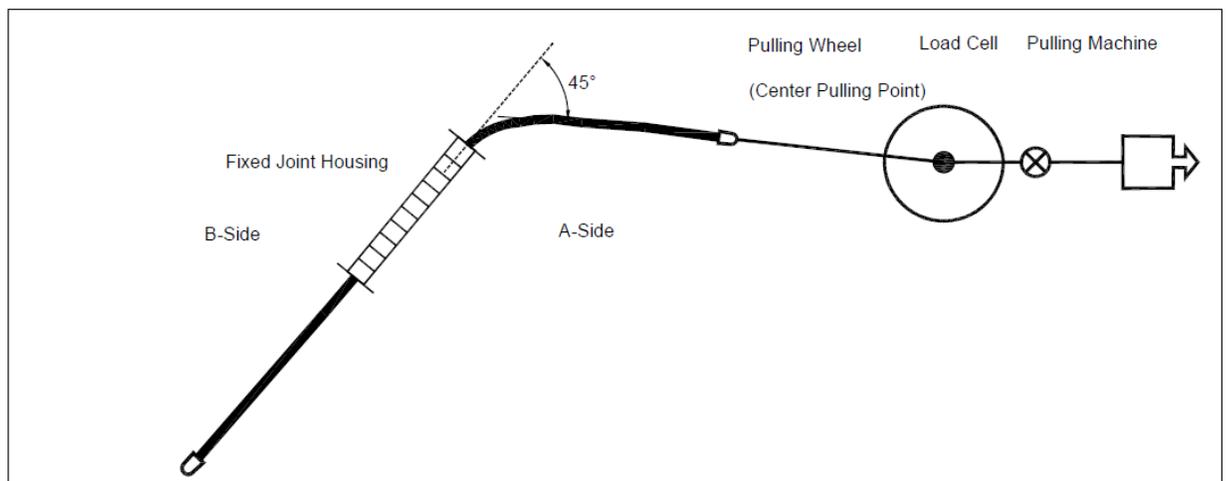
Figure 4-31. Tensile bending test (45 degrees) for in-line joint simulation.
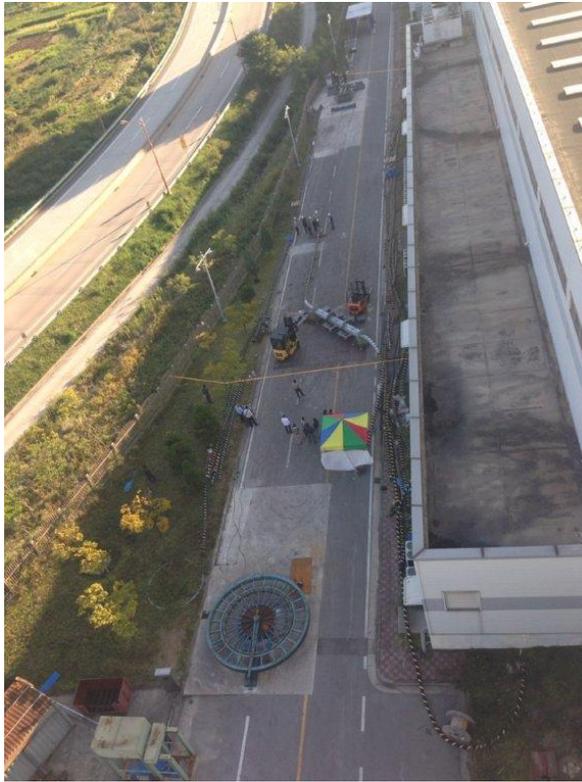
Figure 4-32.Testing set-up, +45 degrees pulling test.

4.11.5 Stage-2 Tensile Test

This test was undertaken to simulate stage-2 of the deployment procedure, as shown in Figure 4-33. The steps followed during this test were the same as those adopted in stage-1.
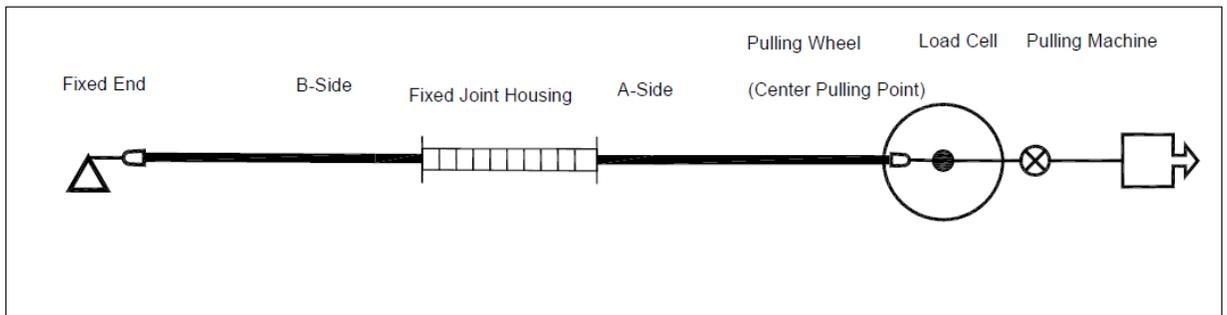
Figure 4-33. Tensile test for in-line joint simulation.

4.11.6 Stage-3 Opposite Bending Test

Stage-3 is where the opposite bending test was performed on the OFJ as illustrated in Figure 4-34 and Figure 4-35. The following steps were implemented during the simulation.

1. Upon completion of the tensile test, the OFJ housing was turned to a -45 degree direction and fastened to the ground to keep its position during the tensile bending test.

2. Before embarking on the opposite bending test, the initial attenuation of the fibre optics was measured and recorded.

3. The torsion angle of the cable in front of the bending restrictor was measured, as shown in Figure 4-34. Additionally, the torsional variation along the assembly length was measured and recorded.

4. The pulling force was increased slowly according to the values indicated in Table 4-10. The force was held for 15 minutes.

5. During the test, optical light power was continuously monitored to check for signs of cable damage.

6. Upon completion of the test, the torsion angle in front of the bending restrictor, as well as the torsional variation, were measured.
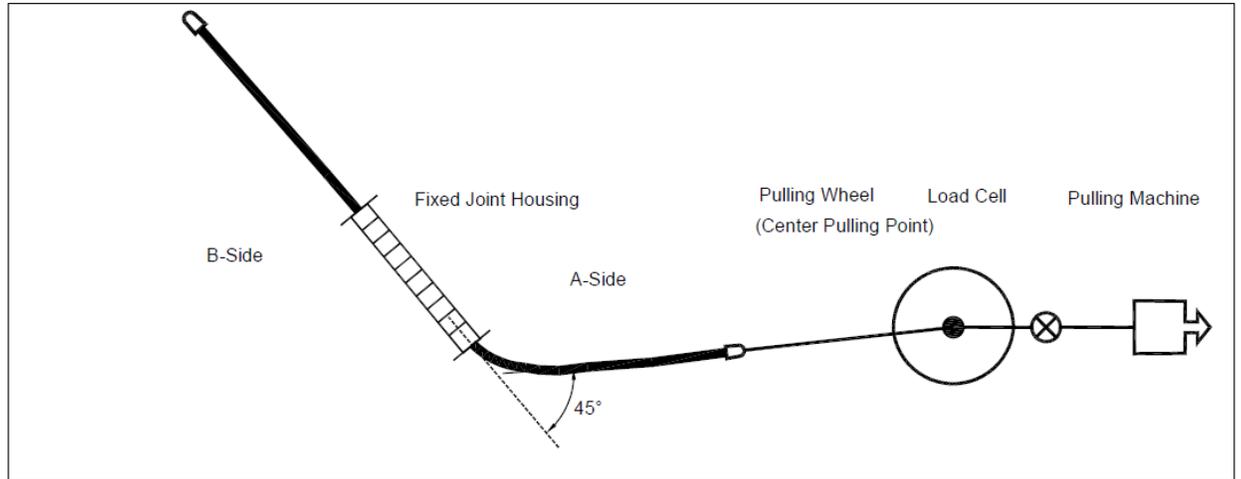
Figure 4-34. Tensile bending test (-45 degrees) for in-line joint simulation.

Figure 4-35. -45 degrees pulling test.

4.11.7 Visual Inspection

After completion of the three stages of the on-land deployment simulation, the OFJ was dismantled and inspected. The pre-moulded joint was released from the compound filling

without introducing any additional stresses. This was followed by the subsequent tests which were highlighted in Section 4.11.2.

Test item # 5: The axial and angular displacements of the cable cores were measured.

Test items # 4 and #6: The plumbing area between the cable lead sheath and copper housing were examined visually for any signs of cracks or deformation.

Test item # 3: For one pre-moulded joint a radial water penetration test was undertaken in order to check the tightness of the pre-moulded joint after the installation simulation test. The test was performed in accordance to Chapter 8.7.4 of CIGRÉ TB 490 (2012), with the exception of the heat cycle test for 24 hours under water. The end of the cable was sealed by plumbed metal covers. The joint was then placed under pressurised seawater in a pressure vessel. After 24 hours, the joint was released from the water and checked for water ingress and damage.

Item test # 7: A complete dimensional check was carried out on the pre-moulded joint and OFJ to ensure the tested object was in full accordance with the manufacturing plans.

The objects tested in this simulation included offshore field joints consisting of three pre-moulded joints and one fibre optics joint. They were found to pass the visual inspection and the test plan which comprised of a series of mechanical tests, fibre attenuation measurements and a water leakage test.

5 Chapter-5 – Paper No. 3

5.1 SUBSEA JOINTS

It was indicated in Chapter 4 that offshore rigid joints require complicated rigging arrangements for offshore deployment. Offshore rigid field joints should be designed and installed using the appropriate methods. If not, the joint will represent a weak point in the power cable that may lead to seawater ingress and subsequent electrical failures. As such, wherever possible, offshore field joints should be avoided. Having said that, this may not always be possible in real field applications, especially when dealing with long subsea power cables and when damaged cables require repair. As per Attwood et al. (1998), during the manufacturing process of Cross-Linked Polyethylene (XLPE), production has to stop after a certain number of days (typically 10 days). The stop in production is required in order to clean down the extruder. As such, it can be seen that the larger the cable, the shorter the extrusion run and hence, more field joints would be required. This substantially increases the probability of the cable having one or more faults during the cable's operational lifespan.

Figure 5-1: Offshore field joint after radial water penetration test during examination (water spouted-out of the test object).

The success of jointing operations, as well as the long-term integrity of the field joint is controlled by 1) the workmanship and quality control during manufacture, 2) cable/ joint design, and 3) welding of the copper sheath to the lead sheath, as illustrated in

Figure 5-2. This photograph was taken during the investigation of offshore field joints in the previous Chapter.

Figure 5-2: Soldering between copper sheath and lead sheath

5.2 MECHANICAL TESTS

Conseil International des Grands Réseaux Électriques (CIGRÉ) TB 490 (2012) introduced the following recommendations and modifications to the mechanical tests reported in Electra 189 (2000):

- A radial water penetration test of rigid repair joints: This test is required to ensure the ability of the joint to withstand water penetration up to the maximum water depth of the subsea cable. This test is an essential characteristic for a subsea cable.

- A scheme for mechanical tests for different types of repair joints.

Conseil International des Grands Réseaux Électriques (CIGRÉ) TB 490 (2012) emphasized that special attention must also be paid to mechanical tests for repaired joints under different installation conditions. The mechanical tests listed in Table 5-1 are typically conducted on rigid joints. According to CIGRE TB 490 (2012), these tests are representative of the mechanical stresses the joints are subjected to during installation and repair operations.

Table 5-1: Mechanical Test for Rigid joint

Tensile Bending Test	Tensile Test	Sea Trial Test
Electra 171, section 2.2	Electra 171, section 2.3	Electra 171, section 3
Not Mandatory Bending test only with radius R without load, if applicable.	Mandatory Straight tensile at T on the same joint assembly subjected to bend test at radius R without load.	Advisable

5.3   OFFSHORE FIELD JOINT DEPLOYMENT PROCEDURE

This section summarises the sequence in which an Omega joint should be deployed on the seabed. Figure 5-3 and Figure 5-4 are snapshots of the actual deployment of the offshore field joint. The loads experienced by the Omega field joint can be described in the following two stages:

- Stage-1: Lifting operation

- Stage-2: Lowering operation

Step-1 (Figure 5-5): Set-up the vessel at the given cable end position. Recover the cable ends to the vessel deck and secure the cable as required to facilitate jointing operations.

Step-2 (Figure 5-6 and Figure 5-7): After the completion of the jointing operation, raise the lifting beam and commence lifting of the cable joint.

Figure 5-3: Omega joint rigging arrangement during offshore simulation.

Figure 5-4: Omega joint rigging leaving the vessel during offshore simulation.

Step-3 (Figure 5-8): Lower the crane block by a certain distance and step the vessel back. Repeat this operation until the crane block is at certain level above the mudline. Stop the vessel movement and lower the crane until it reaches the required elevation.

Step-4 (Figure 5-9): Gradually lower the crane block until the cable is deployed on the seabed.
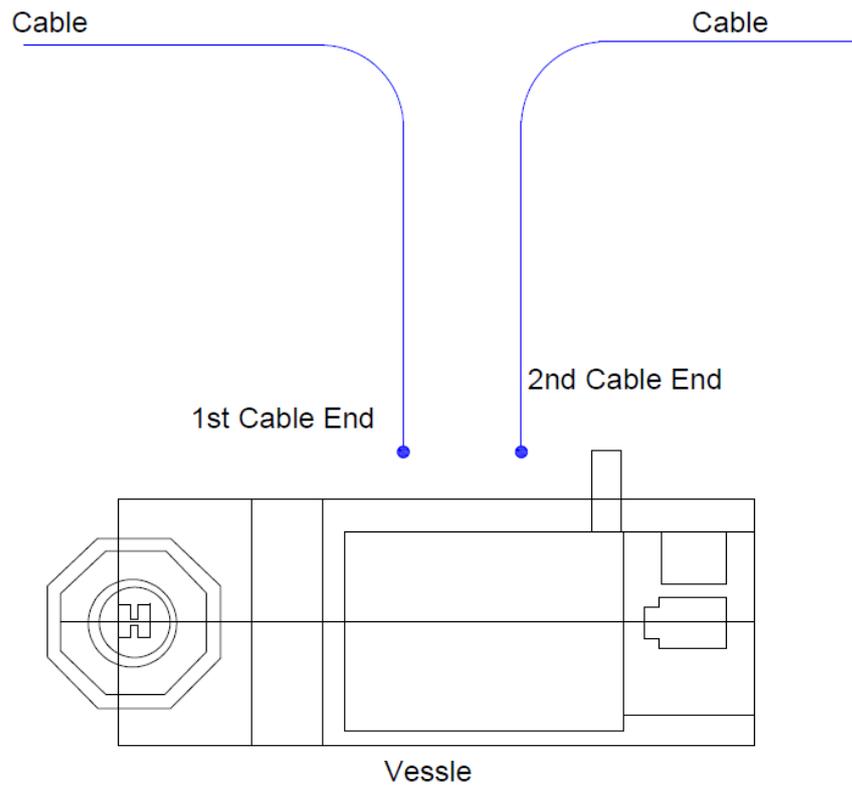
Figure 5-5: Schematic illustration of Step-1.
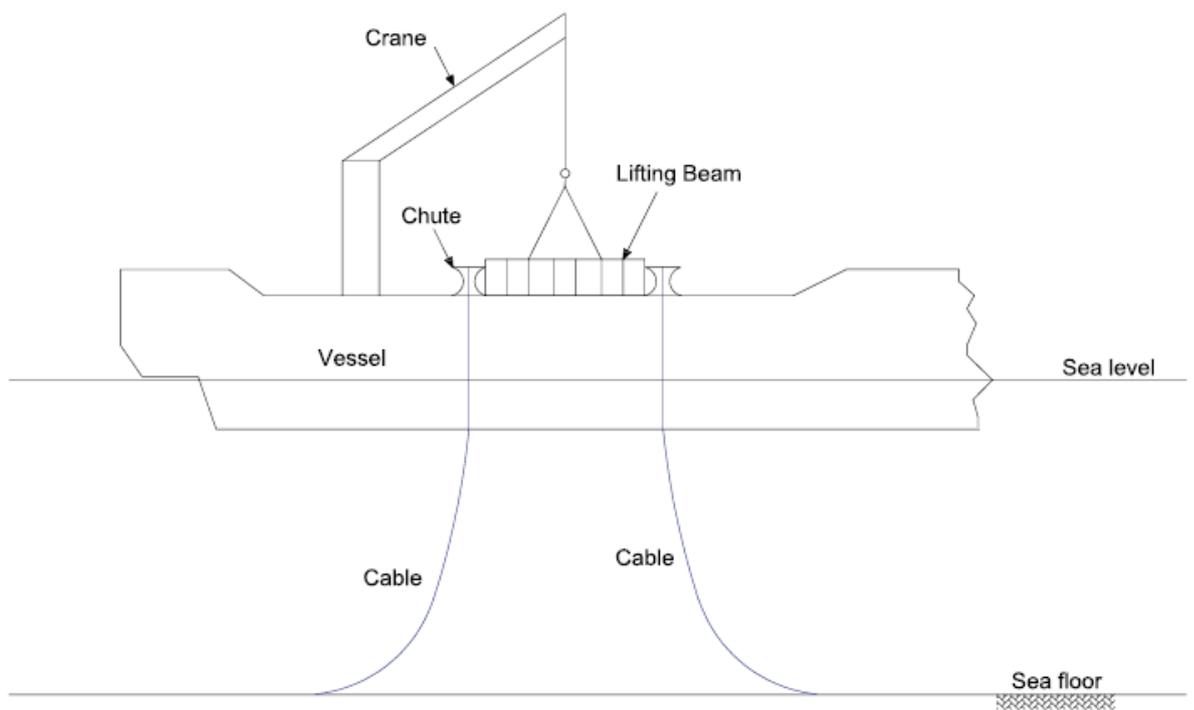
Figure 5-6: Schematic illustration of Step-2-a.
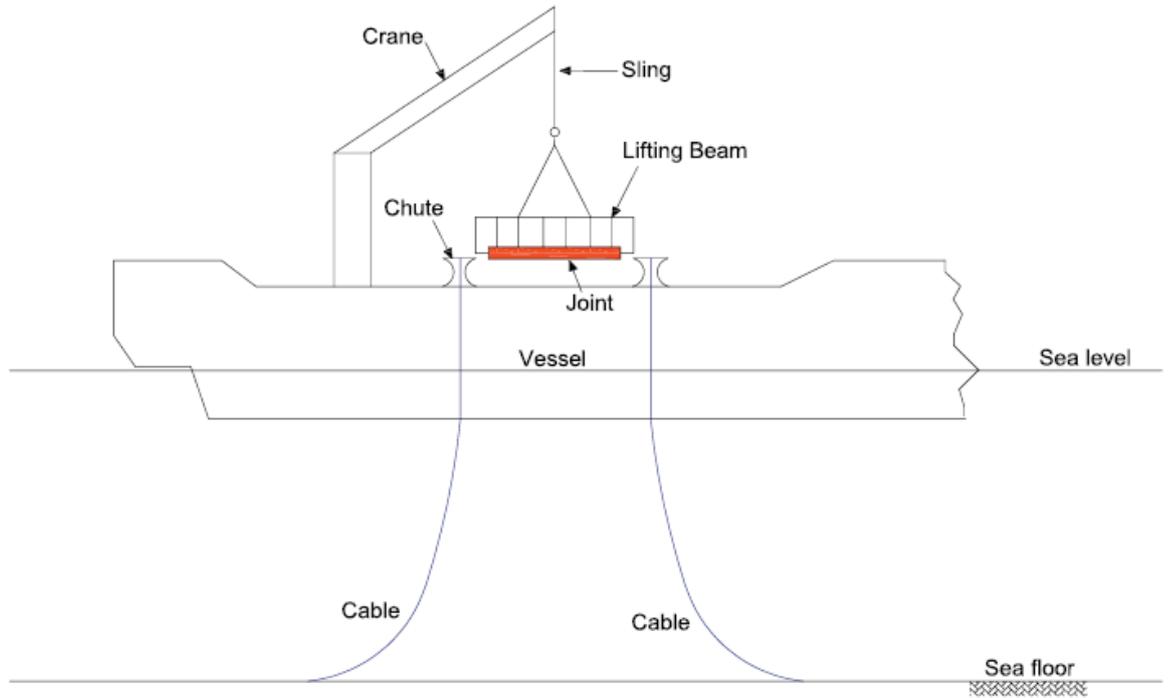
Figure 5-7: Schematic illustration of Step-2-b.
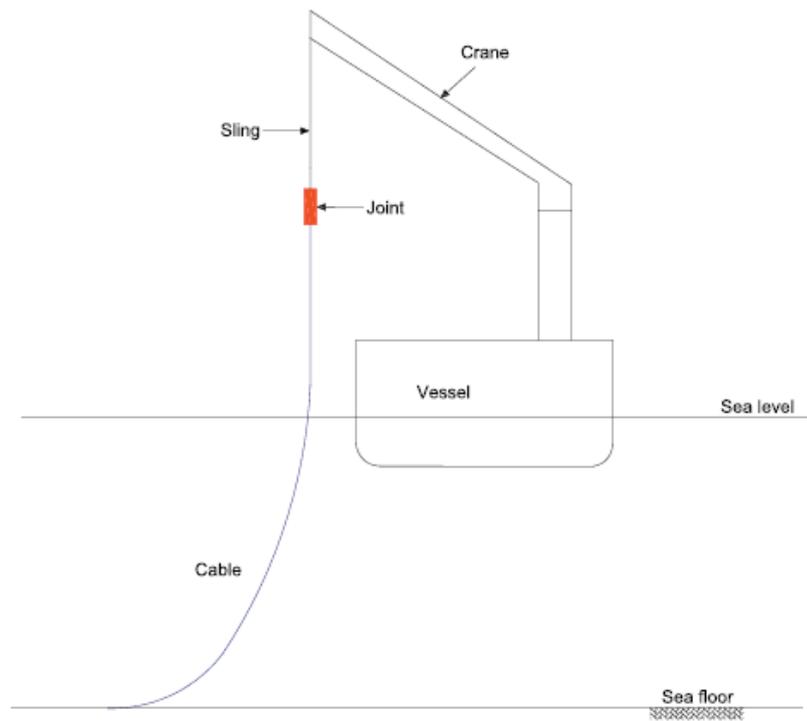
Figure 5-8: Schematic illustration of Step-3.
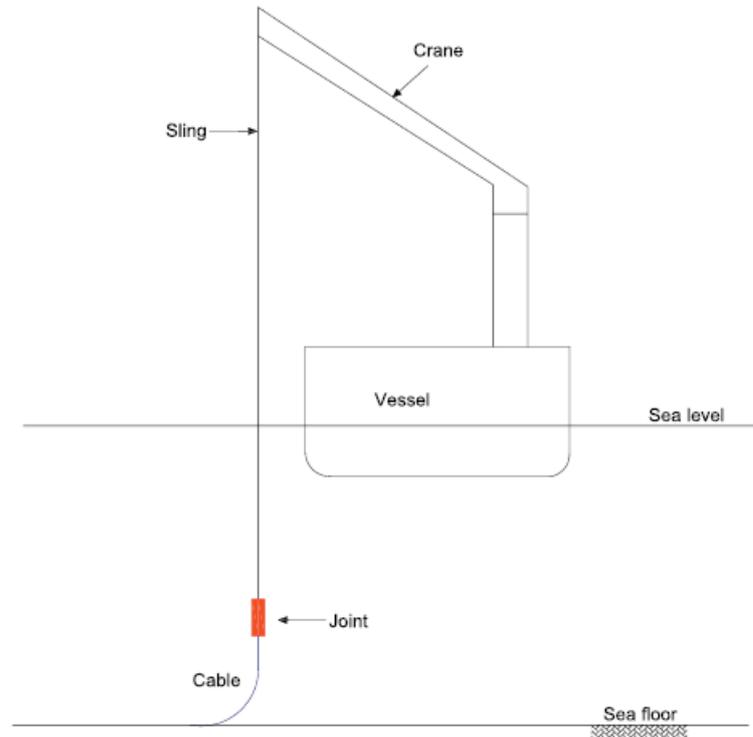
Figure 5-9: Schematic illustration of Step-4.

5.4 STRESS ANALYSIS DURING THE MID-LINE OMEGA DEPLOYMENT OF OFJ

The outer diameter of the HVAC (High Voltage Alternating Current) 132 kV submarine cable is 191 mm. A dynamic analysis, using finite element methods, was performed to determine the maximum axial load at the location shown in Figure 5-10 and Figure 5-11, during deployment operations.

Static and dynamic simulations were carried out to establish the likely maximum load expected on the cable as well as the joints. The dynamic analyses undertaken have considered the effects of wave, wind, and currents as well as vessel motion and displacement and has conservatively accounted for the worst-case scenario.

The loads obtained from the finite element analyses were then applied to the rigid joint during the on-land testing simulation. A load factor can be applied during the test to account for any uncertainties. As can be seen from Figure 5-10, the axial load was applied to the ends of the joint via the use of weights attached to the cable sections below the Chinese fingers.

180
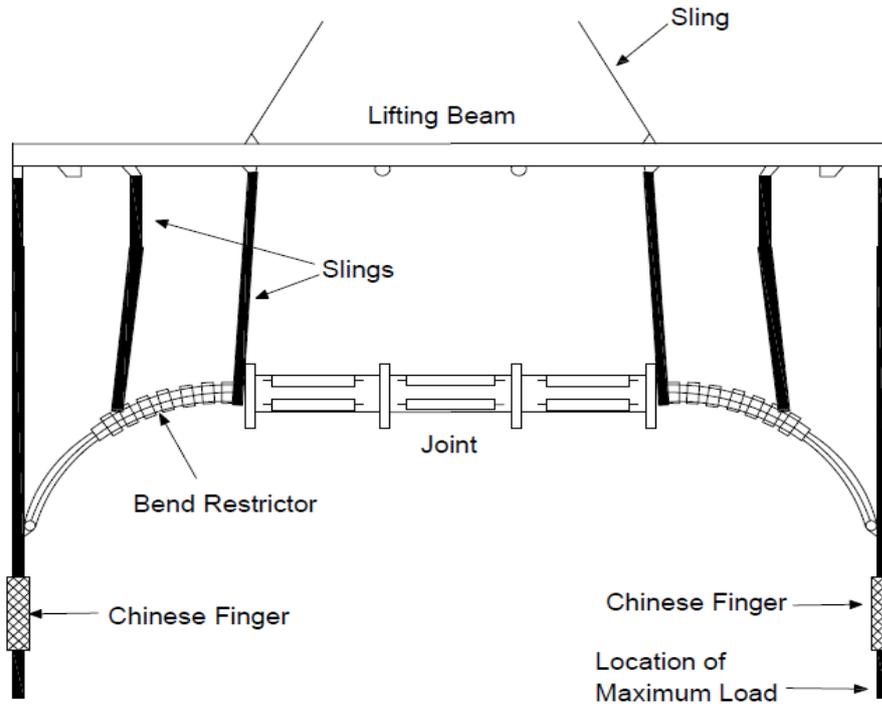
Figure 5-10: Location of maximum load.
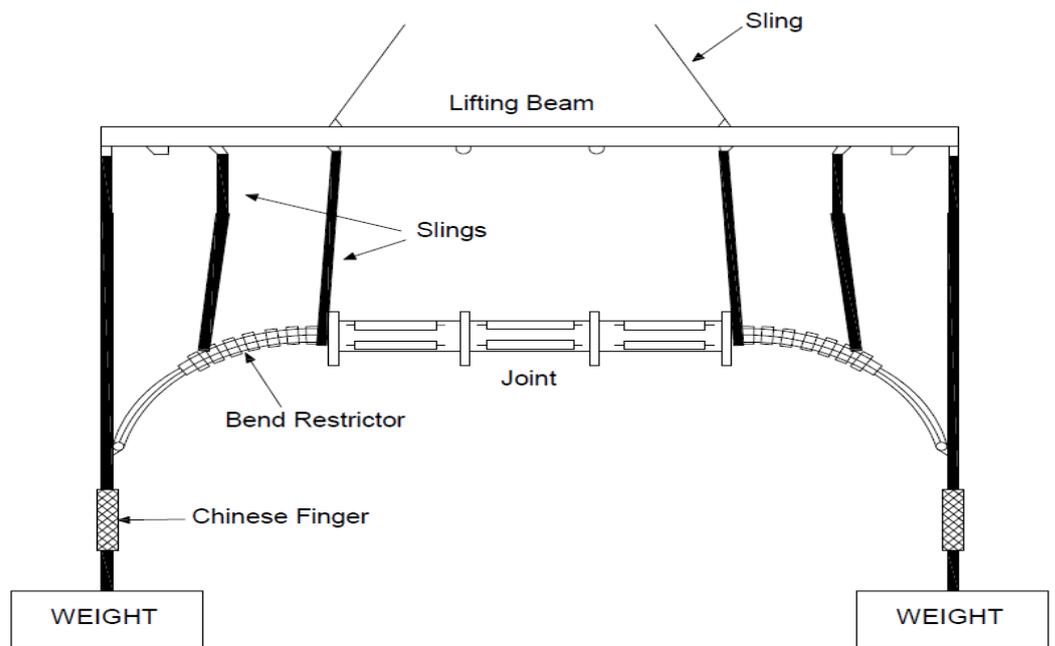
Figure 5-11: Offshore field joint deployment rigging arrangement for Omega laying (hanging position).

181

5.4.1   Analysis Methodology

Figure 5-12 to Figure 5-15 present the OrcaFlex model for the cable deployment operation. The cable is modelled as a line element in OrcaFlex. The winch wire is modelled as a simple winch and take-up of the winch wire during deployment operation is controlled to ensure the simulation period is sufficient to allow for the tension to rise and stabilise. Furthermore, the spreader bar, jointing head, corresponding slings, hook and chute were modelled in OrcaFlex.
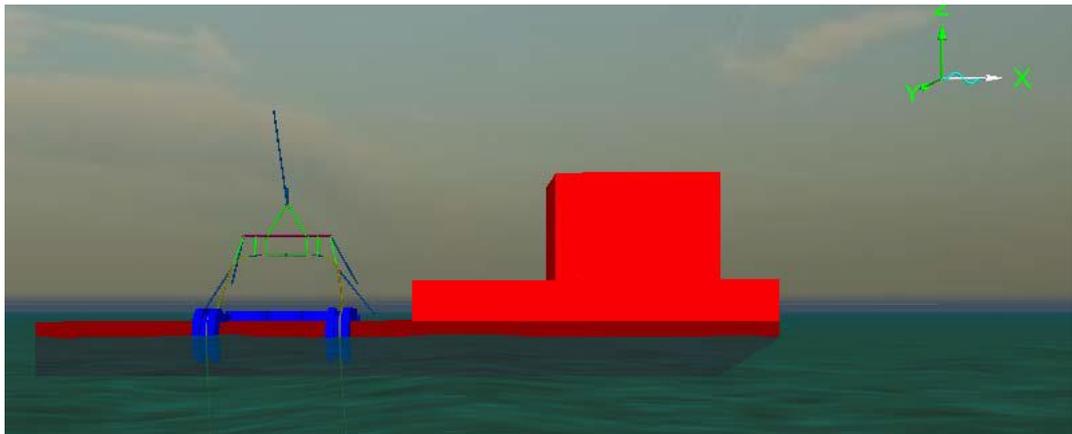
Figure 5-12: Cable joint lifting.
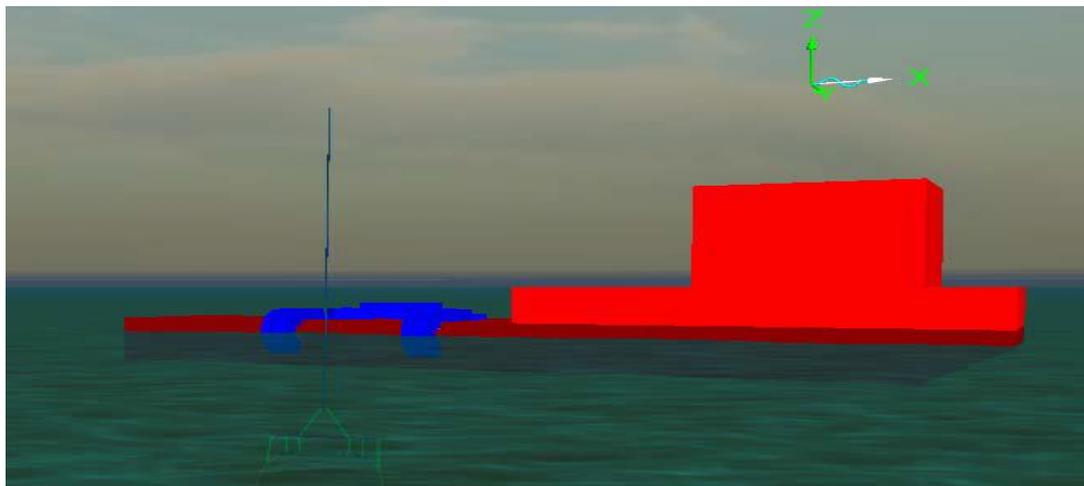
Figure 5-13: Cable joint lowering-Stage-1.
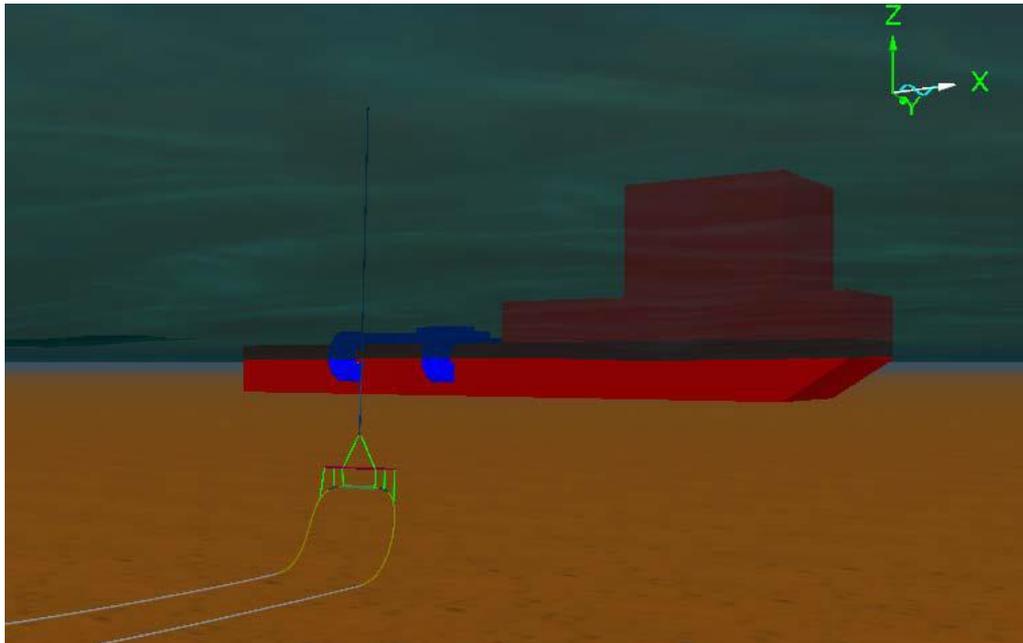
Figure 5-14: Cable joint lowering-Stage-2.
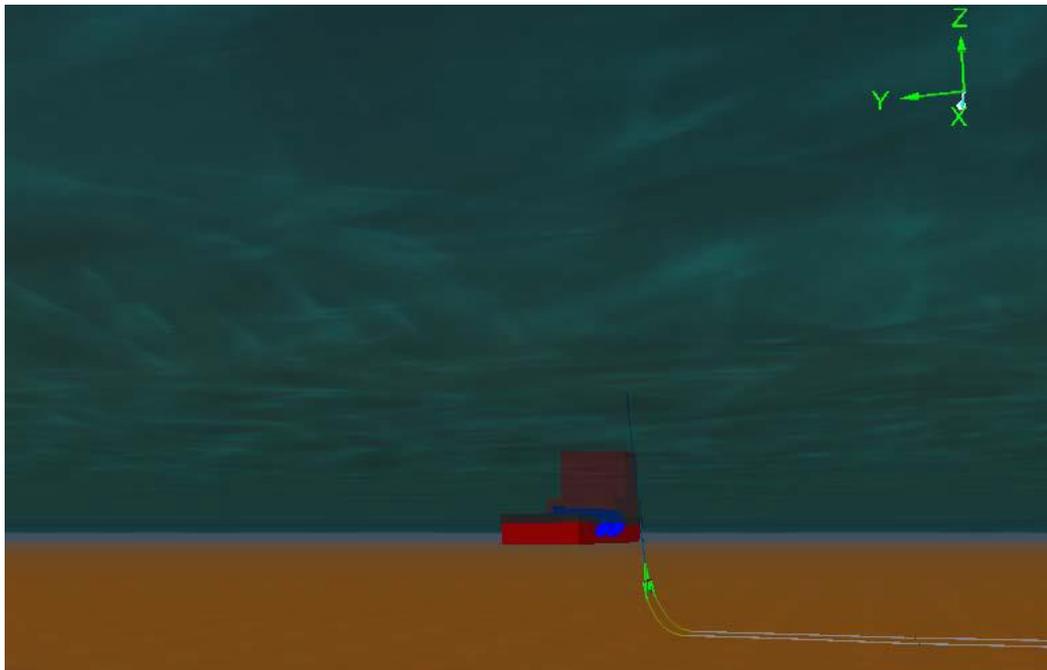
Figure 5-15: Cable joint lowering-Stage-3.

The cable was modelled as a line element in OrcaFlex with the properties as per the reference data. The water depth considered in the simulations was 32 m. Wind speeds

of 8 m/s and current speeds of 1.0 m/s were used for the analyses. The analyses were performed to determine tension and minimum bend radii for different environmental loading directions. Response Amplitude Operators (RAOs) were generated for wave headings of 0°, 45°, 90°, 135° and 180° degrees with wave periods varying from 1 to 25 seconds. Lastly, vessel motions were given six degrees of freedom using MOSES software. For the dynamic analysis of fluid umbilical installation, the significant wave height was 1.0 m. JONSWAP Spectrum with Peakedness parameter, γ, of 3.3 was used for the analysis. To simulate the worst possible wave response, the simulation time origin was shifted such that the wave with the highest crest or trough passed the vessel during the simulation.

The following steps were modelled in OrcaFlex to mimic the actual deployment of the field joint.

Lifting Operation

Step-1

Initial position, with additional restraints and cable joint house, approximately 1.25 m above the centre line of the tension machine. This step is only needed to obtain the correct cable position and was not included in the calculations.

Step-2

Lower the crane block by 1.25 m. This step was also only used to get correct cable position on deck and was not included in the calculations.

Step-3

Pick up the crane block by approximately 1 m. Gradually start taking tension on the tugger lines from the sides to prevent sag lines in the cable and to stabilise the spreader bar.

Step-4

Continue lifting the cable by approximately 6.5 m. At this stage, the total hook travelled 7.40 m upwards with respect to the start of step 3.

Step-5

Gradually rotate the crane outboard keeping the hook elevation the same and holding the cable with the tugger line. This step was not specifically modelled in OrcaFlex.

184

Step-6

Rotate the crane hook towards port and move the vessel starboard to clear the cable outboard. Approximate vessel movement of 15 m in deployment direction (this step was not specifically modelled in OrcaFlex). Approximate height of crane block was 21.4 m above the water line.

Lowering Operation

Step-7

Lower the crane block by 3 m and step the vessel back by 2.4 m. Repeat this operation until the crane block is 23 m above the mudline.

Step-8

Stop the vessel movement. Lower the crane block by 6.5 m.

Step-9

Gradually lower the crane block until the cable is deployed on seabed. Vessel position may be adjusted to suit the site condition. Estimated vessel movement was 5.0 m in the deployment direction.

5.5 INPUT DATA

The properties of the cable and joints used in the numerical simulations are given in Sections 4.3.1 and 4.3.2 of Chapter 4. The installation limits for the cable, crane lifting capacity and lifting aids capacity are given in Sections 4.3.3 and 4.3.4.

5.5.1 Results

5.5.1.1 Results for Lifting off from Deck

Table 5-2 and Table 5-3 show the results of the static and dynamic analyses, respectively, for the lifting of the joint from the deck.

Table 5-2: Results for Still Water Condition

Steps	Simulation Time	Bend Radius	Tension in Joint House (Max/ Min) (Note 1)	Max Cable Tension	Touch down at Start/e nd of Step (Note 2)	Centre of Cable Joint above Mudline at Start/En d of Step	Crane Hook above Waterlin e at Start/ End of Step	Crane Hook Paid out Length at Start/ End of Step	Crane Hook Load at Start/ End of Step (Note 3)	Vessel Horizontal wrt Step-1 at Start/ End of Step
	sec	m	kN	kN	m	m	m	m	kN	m
3	5-10	3.01	1.4/-5.4	24.1	15.7/15.7	36.5/36.5	13.0/13.1	10.2/10.2	76.3/ 76.1	0.0
4	10-40	3.01	1.4/-3.0	23.6	15.7/15.7	36.5/43.9	13.1/20.5	10.2/2.8	76.1/ 131	0.0
5	40	3.01	-0.7/-1.2	23.6	15.7	43.9	20.5	2.8	131	0.0
6	40	3.01	-0.7/-1.2	23.6	15.7/38.4[4]	43.9/45.7	20.5/22.1	2.8/16.1	131.2/ 117.5	0/15[7]

Note:
1. (-) ve indicates compression.
2. Touchdown with respect to barge side shell.
3. Hook load considering a spreader bar and rigging weight of 0.9 MT.
4. Crane hook cleared outboard by 8 m in this step by side stepping the vessel by 15 m, keeping hook elevation the same.
5. Simulation time is time period used in OrcaFlex and not related to actual time period for operation.
6. Mudline considered is (-) 32 m below waterline.
7. Option of moving the crane outboard or moving the vessel shall be decided by the superintendent.
8. Step 1 and 2 are dummy steps to obtain the correct position of the cable and are not included in reporting.

Table 5-3: Results with Environmental Factors

Steps	Simulation Time	Bend Radius	Significant Wave Height	Wind Speed	Current Speed	Wave & Current Direction	Max. Cable Tension	Touch Down at Start/End of Step	Crane Hook Load at Start/End of Step
	sec	m	m	m/s	m/s	Degree	kN	m	kN
3	5-10	3.01	1.0	8.0	0.5	0	26.5	15.2/15.2	75.6/75.4
						45	23.6	15.2/15.2	76.3/76.1
						90	24.1	15.0/15.0	75.5/75.3
						135	22.3	15.0/15.0	75.2/75.0
						180	26.4	15.2/15.2	73.9/83.6
4	10-40	3.01	1.0	8.0	0.5	0	26.6	15.2/15.2	75.4/138.0
						45	23.3	15.2/15.2	76.1/130.4
						90	22.9	15.0/15.0	75.3/131.6
						135	23.1	15.0/15.0	75.0/130.0
						180	22.5	15.2/15.2	83.6/128.2
5	40	3.01	1.0	8.0	0.5	0	26.6	15.2	138.0
						45	23.3	15.2	130.4
						90	22.9	15.0	131.6
						135	23.1	15.0	130.
						180	22.5	15.2	128.2
6	40	3.01	1.0	8.0	0.5	0	26.6	15.2/38.1	138.0/118.0
						45	23.3	15.2/39.6	130.4/120.8
						90	22.9	15.0/38.9	131.6/118.6
						135	23.1	15.0/39.8	130.7/119.8
						180	22.5	15.2/39.9	128.2/118.4

5.5.1.2   Results for Lowering to Seabed

Table 5-4 and Table 5-5 show the results of the static and dynamic analyses, respectively, for the lowering of the joint from the deck.

187

Table 5-4: Results for Still Water Condition

Steps	Simulation Time	Bend Radius	Tension in Joint House (Max/Min) (Note 1)	Max Cable Tension	Touch down at Start/end of Step (Note 2)	Centre of Cable Joint above Mudline at Start/End of Step	Crane Hook above Waterline at Start/ End of Step	Crane Hook Paid out Length at Start/ End of Step	Crane Hook Load at Start/ End of Step (Note 3)	Vessel Horizontal wrt Step-1 at Start/ End of Step
	sec	m	kN	kN	m	m	m	m	kN	m
7	20-80	3.08	4.1/ 2.1	24.2	38.4/ 28.0	45.7/ 15.9	22.1/ -7.6	16.1/46.2	117.5/ 55.4	8.0/ 32.0
8	80	3.08	2.1	7.2	28.0	15.9	-7.6	46.2	55.4	32.0
9	80-95	3.08	2.1/ 0.5	7.2	28.0/ 18.1	15.7/ 7.9	-7.6/ -15.5	46.0/53.5	55.4/ 46.8	32.0[4]
10	95-120	3.07	1.2/ 0.4	5.2	18.1/ 16.8	7.9/ 0.0	-15.5/ -21.6	53.5/59.7	46.8/ 44.6	36.9[4]

Note:
1. (-) ve indicates compression.
2. Touchdown with respect to barge side shell is considering crane hook 8.0 m outboard the vessel.
3. Hook load considering a spreader bar and rigging weight of 0.9 MT.
4. Vessel position may be adjusted for Step 9 and 10 to suit site condition.
5. Water depth considered is 32.0 m
6. Mudline considered is (-) 32.0 m below waterline

Table 5-5: Results with Environmental Factors

Steps	Simulation Time	Bend Radius	Significant Wave Height	Wind Speed	Current Speed	Wave & Current Direction	Max. Cable Tension	Touch Down at Start/ End of Step	Crane Hook Load at Start/End of Step
	sec	m	m	m/s	m/s	Degree	kN	m	kN
7	20-80	3.06	1.0	8.0	0.5	0	24.5/-3.7	38.1/29.1	118.0/55.4
		3.01				45	25.7/-4.4	39.6/28.9	120.8/57.4
		3.08				90	25.1/-2.8	38.9/29.4	118.6/59.7
		3.08				135	25.4/-3.4	39.8/29.7	119.8/57.3
		3.08				180	24.8/-3.5	39.9/29.7	118.4/55.2
8	80	3.09	1.0	8.0	0.5	0	7.2	29.1	55.4
		3.08				45	7.6	28.9	57.4

Steps	Simulation Time	Bend Radius	Significant Wave Height	Wind Speed	Current Speed	Wave & Current Direction	Max. Cable Tension	Touch Down at Start/End of Step	Crane Hook Load at Start/End of Step
	sec	m	m	m/s	m/s	Degree	kN	m	kN
		3.08				90	8.3	29.4	59.7
		3.08				135	8.0	29.7	57.3
		3.08				180	7.2	29.7	55.2
9	80-95	3.08	1.0	8.0	0.5	0	7.2/-0.8	29.1/18.1	55.4/47.1
		3.08				45	7.6/-1.3	28.9/17.9	57.4/49.3
		3.08				90	8.3/-0.4	29.4/17.9	59.7/49.0
		3.08				135	8.0/-0.6	29.7/18.3	57.3/47.8
		3.08				180	7.2/-0.7	29.7/18.2	55.2/47.8
10	95-120	3.07	1.0	8.0	0.5	0	5.2/-0.8	18.1/16.8	47.1/43.9
		3.07				45	6.4/-1.4	17.9/16.7	49.3/43.4
		3.07				90	5.9/-0.7	17.9/16.7	49.0/41.9
		3.06				135	5.5/-0.7	18.3/16.7	47.8/42.7
		3.07				180	5.1/-0.8	18.2/16.7	47.6/44.2

It can be seen from the results that during the lifting and lowering operations of the joint, the cable experiences compressive loads. The results from the compression tests presented in Chapter 3 were used to ensure the integrity of the cable was not compromised. The results show the tension in the cable, as well as the minimum bend radius and compression limits, were within the installation limits given in Sections 0 and 4.3.1.

5.6 TESTING CONCEPT FOR OMEGA LAYING

The installation rigging arrangement shown in Figure 5-16 was proposed by the installation contractor. Therefore the same dimensions were made for the onshore simulation, as per the installation contractor's arrangement shown in Figure 5-16. In this figure, the distance between the chutes is M, the length of the offshore field joint

is L, the radius of the roller way is R and the distance between the field joint and the roller is X.

In order to mimic the conditions during the lifting operation on the vessel, the cable was bent horizontally before the lifting stage. The cable was bent 4 m after the joint housing. Note that during the lifting operation, bending occurs in the vertical plane.

The Omega deployment is simulated via three steps as follows:

1. Joint lifting: Lifting the joint from the initial position to the hanging position. The offshore field joint is lifted using a crane in the same way the lifting/rigging arrangement was used offshore. The lifting is shown in Figure 5-11.

2. Stress loading: Each cable end is connected to block weights with this load having been determined from finite element simulations. The lifting of the entire set-up then takes place. Free rotation of the cable is prevented by welding the cable ends, as illustrated in Figure 5-17 and Figure 5-18. After lifting, the load is maintained for 15 minutes.

3. Laying down on ground: Laying the joint on the ground is performed as per the offshore procedure. In this step, the cable ends are kept fastened to eliminate torsion, as shown in Figure 5-17.
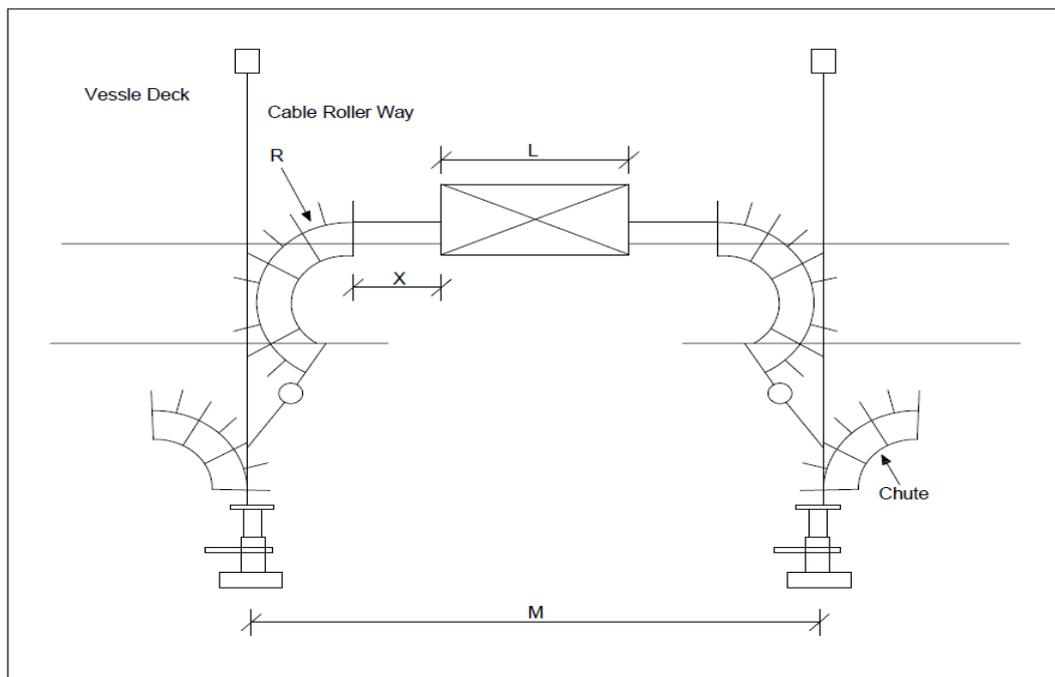
Figure 5-16: Offshore field joint arrangement on vessel (plan view).

In summary, the simulated mid-line Omega procedure consists of two separate types of tests:

- Mechanical stress test: This includes tensile force, bending, torsion and rotation of the joint during lifting.

- Non mechanical investigation/checks.

Table 5-6 summarizes the mechanical tests, which can be applied during the onshore simulation to mimic the offshore deployment procedure, in order to ensure that the mechanical integrity of the joint is not jeopardized.
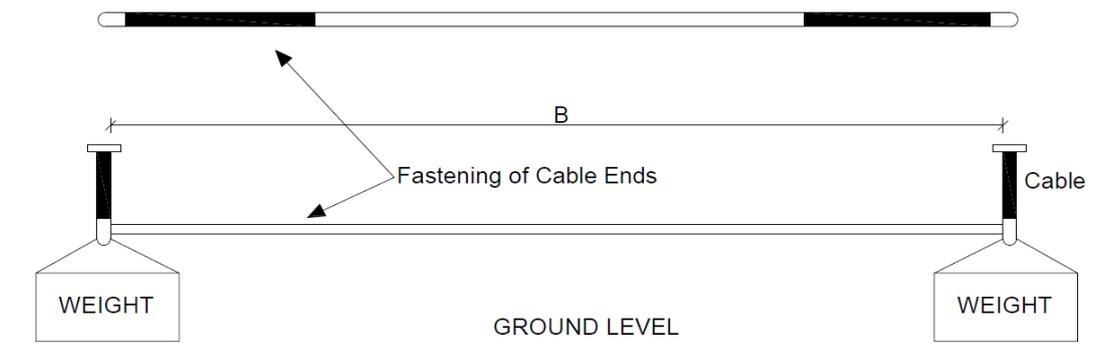
Figure 5-17: Top and front views with end fastening (with centre welding point).

Figure 5-18: Fastening of the cable end

Installation Procedure	Mechanical Stress	Values Applied	Remarks
Omega	Tensile Force	Blocks with weights equivalent to the loads obtained from finite element analysis (hold for 15 minutes)	Force by hanging load
	Bending	Approximately 90 degrees by lifting and laying down	Stresses are identical to offshore lifting/deployment procedure.
	Torsion	Torsion of the cable is prevented	Cable laid on the seabed will eliminate torsion
	Rotation of joint during lifting	No rotation due to the use of slings with choker type of lifting offshore field joint	Stresses identical to offshore lifting/ deployment procedure.

Note that before, during and after the simulations, the attenuation of the fibre optic cable was measured and recorded. During the simulation, the torsion of the cable, especially at the end of the bend restrictors, was monitored. In the circumstance where the torsion was greater than the allowable value, an additional load cycle was applied to the joint. Upon completion of the simulation, the movement of the cable at the armour pot was measured. In instances where movement had occurred beyond the allowable limit, an additional load cycle was applied to the joint. Finally, the joint was dismantled carefully to investigate the inside components to ensure that there was no sign of movement. Furthermore, a water penetration test for the pre-moulded joint was conducted, with the pre-moulded joint having been taken out of the steel casing of the joint. Other investigations were carried out to test the joint after the simulations. All the tests and the corresponding acceptance criteria are discussed in Section 5.7.4.

5.7   OVERVIEW OF TEST PROCEDURE:

5.7.1   Installation

1. The offshore field joint was installed in a straight arrangement as shown in Figure 5-16.   During the installation, the inner cores of the joint were marked in order to assist in detecting any axial movement, twisting or displacement associated with the cable cores, which may occur during the deployment simulation. Additionally, the outer yarn at the armouring pot was marked to detect any axial or angular movements of the cable at the armour pot position.

2. Both armouring cable ends were terminated by a pulling eye.

3. After installation, the cable ends were bent by 90 degrees to obtain the same condition as that on the offshore vessel. This is shown in Figure 5-19.
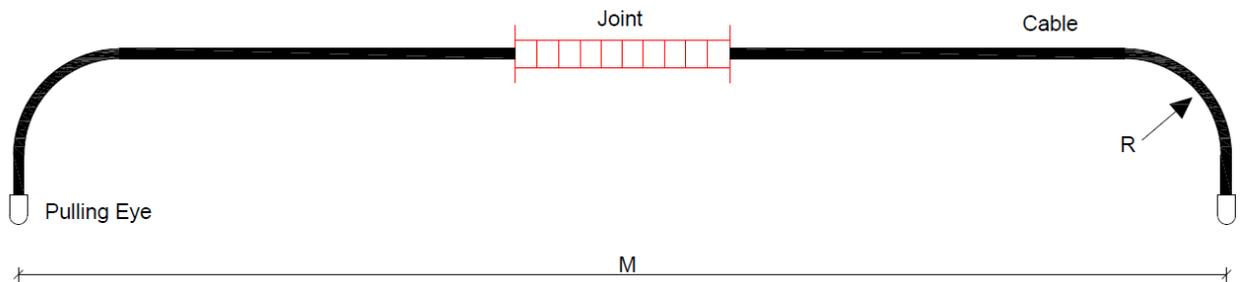
Figure 5-19: Cable-joint arrangement after installation.

5.7.2   Tests Required During Deployment Simulation

The steps involved in these tests are briefly outlined below:

1. Use the crane to lift up the beam. The lengths of fastening slings by the turnbuckles are adjusted until the final position is achieved, as highlighted in Figure 5-20. During the test, the fibre optic loop attenuation is continuously measured.

193

2. Throughout the test, the torsion of the cable is to be monitored by marking a straight line on the cable surface, as shown in Figure 5-21.

3. Once the final hanging position is achieved, additional weight is added to achieve the final load (below the Chinese finger) at each side of the cable. The final load is equal to the load obtained from the finite element analysis (refer to Figure 5-16).

4. When the configuration is in the free hanging position, as shown in Figure 5-20, it is kept in this position for 15 minutes during which time the torsion is measured. If the torsion at the end of the bend restrictor is greater than the allowable limit in circumference, then three heating voltage test cycles is to be performed as per   International Electrotechnical Commission (IEC) 60840 (2011) before conducting the test specified in Section 5.7.3.

5. In order to mimic the deployment of the Omega joint offshore, the stages shown in Figure 5-22 to Figure 5-25 are to be followed until the joint housing is laid on the ground. Once the joint housing reaches the ground, all slings are to be disconnected. The fibre optic attenuation test is then stopped.

6. Start the tests detailed in Section 5.7.3.

5.7.3   Non-Mechanical Stress Tests

1. Once the joint housing is placed on the ground, the following tests should be undertaken as per Table 5-7. The field joint housing and bend restrictor are inspected visually for any signs of damage or cracks.

2. The bend restrictor is then opened. The movement of the cable at the armour pot location is measured and compared with the measurements taken before conducting the simulation.

3. If the movement of the cable at the armour pot location is greater than the allowable limit in circumferential displacement, then three heating voltage test cycles will be performed as per IEC 60840 (2011) before conducting the remainder of the tests specified in this section. After the completion of the mechanical tests on the Omega joint, the offshore field joint is dismantled and inspected.

4. The offshore field joint is carefully dismantled and the inner cables and the pre-moulded joint is freed from the compound filling without the application of any significant bending or mechanical stress.

5. The following tests are performed:

   a. The axial and circumferential displacements of the cable cores are measured and recorded.

   b. The plumbing area located between the cable lead sheath and copper housing is visually examined for any cracks or deformations.

   c. At one pre-moulded joint, a water pressure test is carried out to investigate the tightness of the pre-moulded joint after the deployment simulation. The test is performed similar to that described in CIGRE TB 490 (2012). The end of the cable is sealed by metal covers, and the joint is placed in salty water in a pressurized vessel.

   d. After 24 hours, the joint is released from the water, and inspected for any water ingress or damage.

   e. A dimensional check is performed on the pre-moulded joint.

Figure 5-20: Final hanging position for mechanical stress tests (free hanging with additional load).

Figure 5-21: Marking on cable.
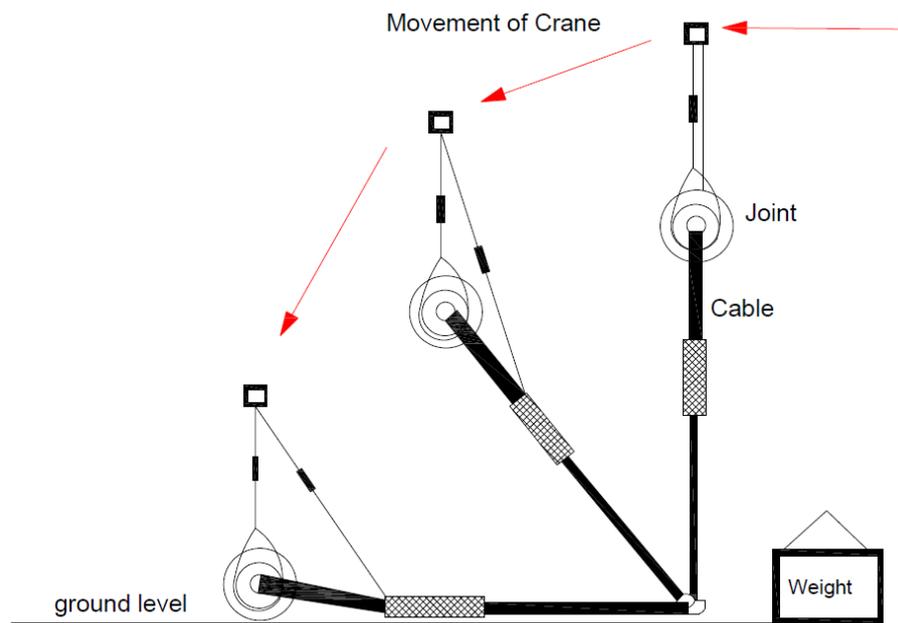
Figure 5-22: Deployment of offshore field joint (3 stages combined).

Figure 5-23: Deployment of the joint- stage-1.

Figure 5-24: Deployment of the joint- stage-2.

Figure 5-25: Joint on the ground-stage-3.

5.7.4   Mid-Line Omega Test Plan and Acceptance Criteria

Table 5-7 presents the tests performed during and after the onshore deployment simulation, alongside the acceptance criteria for each test.

Table 5-7. Summary of mid-line Omega test plan and acceptance criteria

Test	Acceptance Criteria
1. Fibre optic attenuation test Continuous fibre optic attenuation check during the test	Ensure that the increase of the attenuation before and after the test remain within the allowable limits.
2. Torsion measurements of cables Check the change of the torsion angle at the straight line marking between the bending restrictor and the pulling eye as shown in Figure 5-21:	No cable rotation during the test greater than the allowable limit at the end of bending restrictor. If cable rotation is greater than the allowable limit then three heating voltage test cycles are to be

Test	Acceptance Criteria
• before lifting • after lifting • after loading • after deployment	performed as per IEC 60840 (2011) before conducting the tests specified in Section 5.7.3.
3. <u>Visual Checks</u> Visual inspection of housing, armour pot and bend restrictor.	No visible cracks or deformation.
4. <u>Measurement of external displacement of cable at armour pot (axial and angular- angular is measured in circumferential displacement)</u> This test is to be carried out after the completion of the simulation.	No displacement caused by the test (axial and circumferential movement). If displacement has occurred then three heating voltage test cycles are to be performed as per IEC 60840 (2011) before conducting the tests specified in Section 5.7.3.
5. <u>Leakage Test</u> Leakage test on one pre-moulded joint including the plumbing area, 24 hour water pressure test.	No water inside the joint.
6. <u>Visual check of plumbing area</u> Visual check of the plumbing area. The plumbing area is located between the copper housing (three joints) and the cable sheath.	No visible cracks. No holes in the plumbing area. No visible gaps between plumbing, lead sheath and copper housing
7. <u>Dimensional check on pre-moulded and OFJ used</u>	Dimensions are in accordance with the manufacturing tolerances and drawings.

6 Chapter-6 – Paper No. 4

Title: **"Design and installation of subsea cable, pipeline and umbilical crossing interfaces".**

Authors: **Ahmed Reda, Ian M Howard, Gareth L Forbes, Ibrahim A Sultan, Kristoffer K McKee**

Journal: **Engineering Failure Analysis.**

6.1 VERTICAL POSITIVE SEPARATION IN CODES AND STANDARDS

It is evident that industry standards and recommended practices do not prohibit using the crossed pipeline as a support provided the required minimum positive separation is maintained at all times between it and the crossing assets. Furthermore, in cases where the crossed pipeline is utilized as the support, the codes and recommended practices do not explicitly prohibit the crossing configuration from being installed at a field joint coating of a pipeline.

6.2 CROSSING BEST PRACTICE

Typically, the crossing should be designed such that both the crossed pipeline and crossing pipelines/cables/umbilical are stable. If the crossing and crossed assets are not designed to be stable then the crossing design needs to take into consideration any potential lateral movement of the assets at the crossing point. Such movement can jeopardize the integrity of the pipeline/cable/umbilical and cause damage to the pipeline anodes and coatings.

Furthermore, the following critical factors must be taken into consideration when designing the crossing:

- Free span lengths must be within the allowable free span limits.

- The crossing angle with the existing pipe/cable should be greater than 30° and as close to 90° as possible.

- The cathodic protection system of the crossed pipeline and the crossing pipeline must not be compromised.

- The integrity of the coating for the crossed pipeline and the crossing assets must not be jeopardised.

- The load imposed on the crossed pipeline by the crossing assets must be within the code allowable limits.

- The axial displacement of the crossing pipeline associated with temperature fluctuations must not influence the integrity of the crossed pipeline. Taking into consideration that excessive axial displacement of the crossing pipeline

may compromise the integrity of the supports in the case where the discrete supports approach is employed.

- DNVGL-RP-F110 (2019) should be used to check the propensity of global buckling. In the case where the Ramp concept is used, it is essential to design the rock cover to prevent buckling. The cover design should be undertaken in accordance with the methodology of DNVGL-RP-F110 (2019).

- The short and long-term settlements of the support must be determined.

- Pipeline crossings must not be located in curved sections of the (new) crossing pipeline route. A 150 m length of straight pipe on either side of the crossing is recommended.

- The crossing design shall be such that the smaller pipeline crosses over the larger pipeline.

- The crossing design shall be approved by the Company and by the owner and/or operator of the pipeline being crossed.

- For the padding design, it is important to ensure that the radial and axial stresses experienced by the articulated padding will be within the material strength.

- The material of the padding should be ductile to avoid fretting fatigue and brittle fractures associated with repeated lateral movements under the influence of hydrodynamics loads.

6.3   THEORY OF ON-BOTTOM STABILITY

There are two main types of forces (as shown in Figure 6-1): the hydrodynamic forces (lift, drag and inertia) due to waves and steady currents which try to destabilize or move the cable, and the restoring forces due to soil resistance which try to restore the cable back to its initial position.

The hydrodynamic force, as illustrated in Figure 6-1, can be conveniently expressed as two components: one in-line (lateral) with the flow, drag and inertial forces, and one perpendicular to the flow (vertical), or a lift force. The in-line force acting in the flow direction per unit length of the cable, is determined using the generalized Morison's equation for drag and inertial forces, and is:

$$F_D = \frac{1}{2} \cdot C_D \cdot \rho_w \cdot D \cdot (u_w + u_c)^2$$

<div align="right">6-1</div>

$$F_I = \frac{\pi \cdot D^2}{4} \cdot C_M \cdot \rho_w \cdot a_w$$

<div align="right">6-2</div>

For pipes on the seabed, the lift force acting perpendicular to the flow direction is expressed as:

$$F_L = \frac{1}{2} \cdot C_L \cdot \rho_w \cdot D \cdot (u_w + u_c)^2$$

<div align="right">6-3</div>

To ensure on-bottom stability, an adequate stability factor of safety should be achieved in both the vertical and lateral direction. On-bottom stability design falls into two categories, namely a static two-dimensional (simplified) analysis or a dynamic analysis. The static lateral stability criterion is defined as:

$$\gamma_{st}(F_D + F_I) \leq \mu(W_{sub} - F_L)$$

<div align="right">6-4</div>

where:

F_D : drag force per unit length of cable,

F_I : inertial force per unit length of cable,

F_L : lift force per unit length of cable,

C_D : drag coefficient,

C_M : inertia coefficient,

C_L : lift coefficient,

D   : cable outer diameter,

W_{sub} : submerged weight of the cable,

ρ_w : mass density of the surrounding water,

u_w : wave induced velocity,

u_c : steady current,

μ : lateral friction factor,

γ_{st} : stability factor of safety, which shall not be taken less than 1.1.
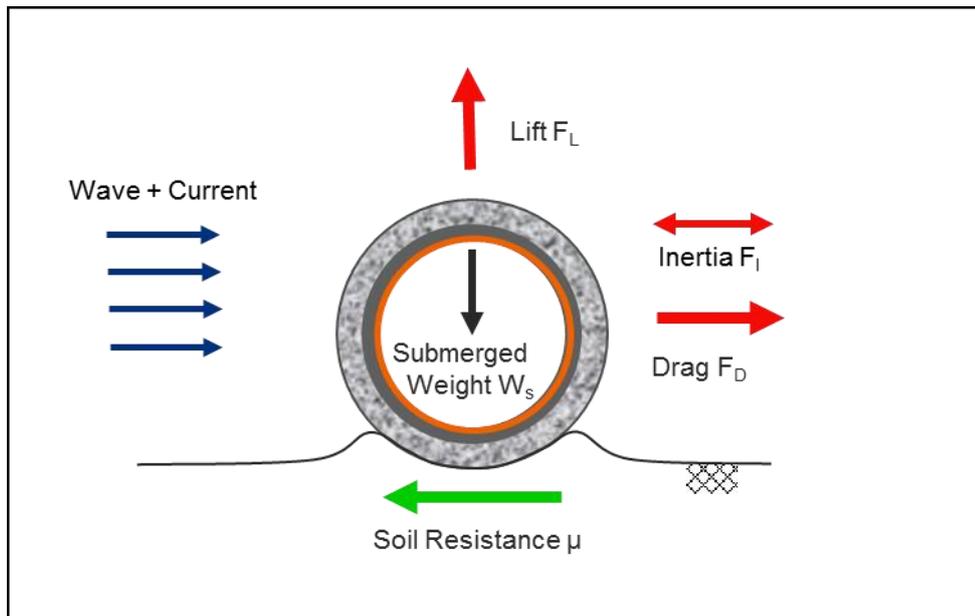
Figure 6-1 : Hydrodynamic loads on a cable.

A dynamic analysis involves the dynamic simulation of a section of cable under the action of waves and current. For a dynamic analysis, the acceptance criteria are based on allowable movement of the cable as well as the cable curvature/effective tension. Where movement is allowed, the following factors must be checked:

- Fatigue

- Outer sheath abrasion

- Interaction with other pipelines, structures etc

- Width of survey corridor

6.4 CABLE CROSSING DESIGN

This section describes the crossing system which was employed for the installation of a 132 kV subsea power cable in an existing, congested field with many dozens of crossings and without space available on the seabed to install supports.

It can be seen from Figure 6-2 that the crossed pipeline was used for support. The positive vertical separation between the crossing subsea cable and crossed assets was achieved by the use of articulated padding, as shown in Figure 6-2.

This system involves the offshore application of a specific bend restrictor and articulated padding discs on the new cable prior to installation over the crossed pipeline at the crossing location. The assembly of the system is quick and efficient as it is done concurrently with cable installation.

The articulated padding disc unit is typically made of polyurethane and is comprised of two half-shells installed around the bend restrictors at the crossing location. The half-shells are secured with bolts or using pre-cut corrosion resistant banding. The outer diameter of the articulated padding is 1.01 m, thus when the articulated padding is placed over the crossed pipeline at the crossing point, the required separation of 410 mm is maintained over the design life.

The main advantage of this design concept is that a crossing support over the crossing point is no longer necessary before installing the crossing cable. Also, the installation of the cable at the crossing location need not be as accurate as would be required when installing over a pre-installed crossing support. This allows the cable to be installed more quickly, thereby minimising costs. This option also provides greater flexibility when carrying out post-installation inspections and maintenance on the facility during its operational life because the new cable can be easily, albeit only slightly, moved laterally which enables a closer inspection of the crossing and existing pipeline or facility.

It should be highlighted that the gap between the crossed pipeline and the crossing pipeline/umbilical/cable is independent of the settlement of the crossed pipeline over time. As such, the required vertical separation will be guaranteed during the design life. Any intervention to increase the gap or separation during the operation phase is also not required. Figure 6-3 shows the deployment of the articulated padding system during cable installation.
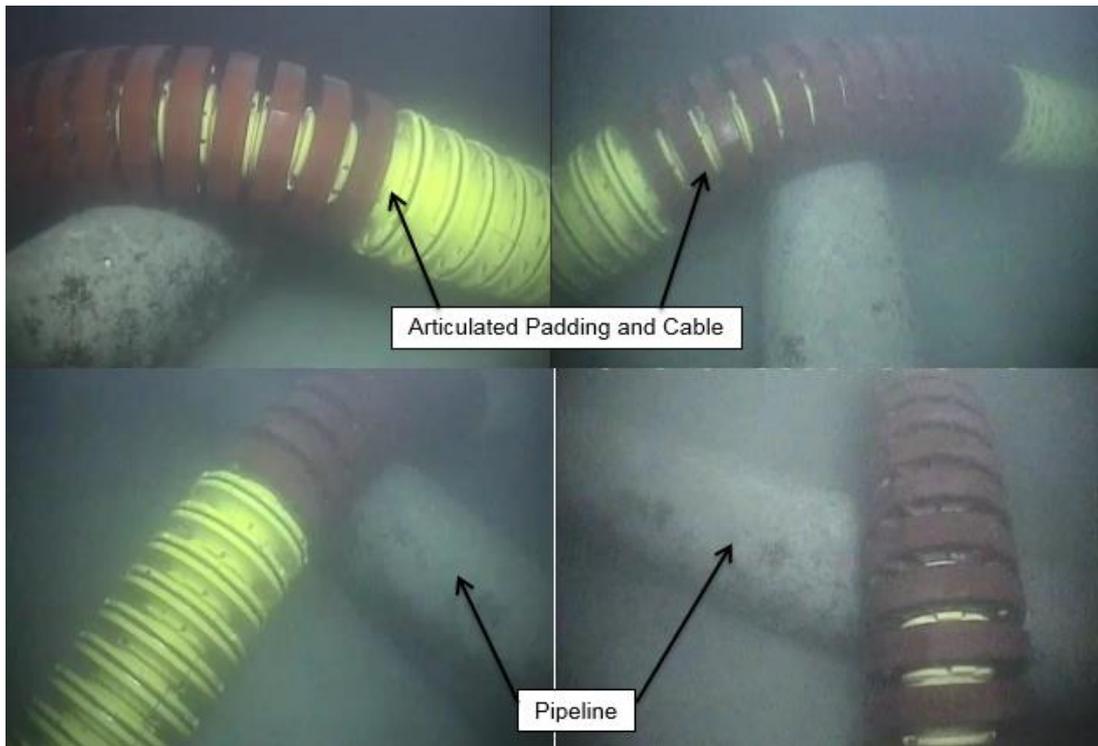
Figure 6-2: General arrangement of articulated padding crossing system.

Figure 6-3: Deployment of the articulated padding.

Figure 6-4 shows the mock-up trial undertaken on the articulated padding and bend restrictors. The mock-up test is undertaken to ensure that the offshore installation procedure provided is proven, effective and applicable to actual operation. It can be seen from the same figure that a dummy pipe was used to mimic the actual site condition where the articulated padding would be laid on an existing pipeline.

Figure 6-4: Mock-up test undertaken at the factory.

6.5   DESIGN REQUIREMENTS

Figure 6-5 illustrates the crossing design adopted for the subsea power cable using the articulated padding system and the crossed pipeline as a support. The articulated padding, which is fitted around the crossing cable, provides the required positive vertical separation of 0.41 m as determined by local regulations. As shown in Figure 6-6, the articulated padding prevents the cable from bearing directly on the crossed pipeline.
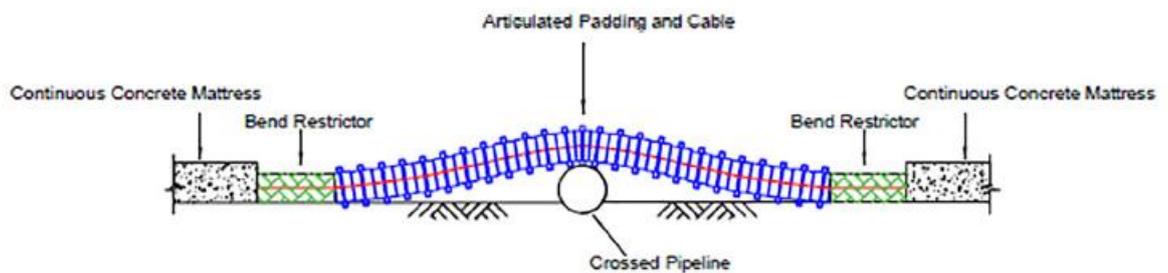
Figure 6-5: General arrangement of articulated padding crossing system.
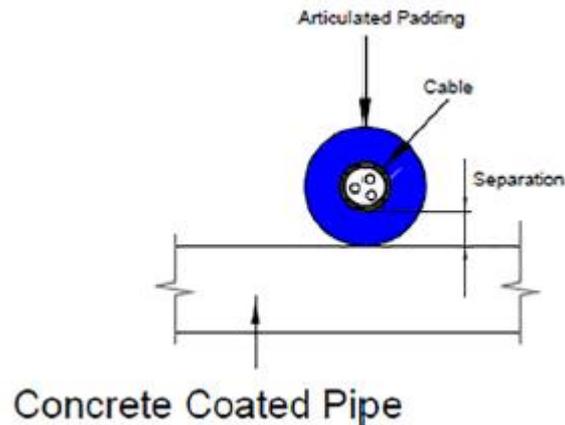
Figure 6-6: Positive separation between the crossing cable and the crossed pipeline.

The crossing design is undertaken using a commercial finite element program. The objective of the crossing design is to ensure that:

- The crossing cable curvature and effective tension resulting from all load factors (due to weight, buoyancy, residual tension and environmental forces) do not exceed the allowable curvature and effective tension specified by the cable manufacturer.

- The loads imposed on the crossed pipeline are within the allowable limits.

- The fatigue damage ratio associated with the lateral movement of the cable is within the allowable limits.

- The compression experienced by the cable is within the limits determined in Chapter 3.

- The crossing cable curvature and effective tension are acceptable without the loss of cable integrity under hydrodynamic loads as the crossing cable was not designed for absolute stability. An abrasion test (see Figure 6-7) was conducted to ensure that material loss due to abrasion of the articulated padding complies with the design life of the cable.

- The span between the two cable touchdown points will be such that in-line or cross-flow vortex induced vibration (VIV) will not take place as per the criteria given in DNVGL-RP-F105 (2017)

Figure 6-7: Abrasion test outcome.

Visual and side-scan surveys of the crossed pipelines and the seabed within 250 m of the proposed crossing point were conducted so that the crossing design could be verified prior to the installation of the cable. The survey focused on the following:

- Providing data for designing appropriate crossing locations and configurations.

- Investigating existing or crossed pipelines burial and seabed levels (the depth of burial of the crossed pipeline is measured from natural sea-bottom to top of pipe).

- Obtaining detailed bathymetry of the crossing site area.

- Determining the physical condition of the crossed assets.

- Determining the as-laid position of the crossed pipeline.

- Identifying the sacrificial anodes in the proximity of the crossing point.

If the crossing design concept involves the use of discrete supports or a ramp, as shown in Figure 1-11, then a geotechnical survey is also required at the crossing point in order to classify the soil and determine the soil strength parameters. This survey however is

not required if the design involves the use of articulated padding as the positive separation is maintained irrespective of the settlement of the crossing configuration.

During the visual survey, the anodes in the proximity of the crossing point were identified, as shown in Figure 6-8. The design of the crossing ensured that any lateral cable movement, due to hydrodynamic forces, would be away from the sacrificial anodes placed on the crossed pipeline. To ensure that the cathodic protection of the crossed pipeline is not compromised, the cable lay was arranged in such a manner that the cable crossing lay at the mid-point between anodes as per ICPC recommendation No.3 Issue 10 A (2014).

Figure 6-8: Anodes in the proximity of the crossing point.

As part of the crossing design, an induced voltage study was undertaken to:

- Ensure that the shielding around the power cables was sufficient to reduce the likelihood of electromagnetic interference to negligible levels.

- Confirm that the selected positive separation between the crossed pipeline and the crossing cable was sufficient to ensure that the induced current from the crossing cable would not interact or compromise the existing cathodic protection of the pipeline.

The crossing cable at the crossing point is designed to move laterally on the crossed pipeline. Dynamic analyses were undertaken to satisfy the limit states in Table 6-1. These limit states were developed based on the structure and guidance provided in DNVGL-ST-F101 (2017).

Table 6-1: Limit States

Design Criteria	Definition	Assessment Criteria	Return Period (Year)
Ultimate Limit State	Cable at limit of integrity	Cable minimum bend radius versus effective tension/compression load	100
Serviceability Limit State	Cable at limit of integrity of serviceability Assessment to check the degree of cable stability	Cable inoperable Extent of cable displacement	1000 100
Accidental Limit State	Cable at limit of integrity	Cable minimum bend radius versus effective tension/compression load	10,000
Fatigue limit state	Cyclic loading may lead to fatigue damage for a cable that is allowed to move laterally along the crossed pipeline. Cyclic radial loading combined loading may lead to fretting fatigue damage to the articulated padding.	Ensure that the radial and load experienced by the articulated padding are within the allowable limits of the polymer material and within the limits provided by the manufacture. The fatigue damage endured by the cable are within the allowable fatigue damage ratio.	Ambient metocean condition

The crossing analyses undertaken on the crossing arrangement shown in Figure 6-5, indicated that the lateral movement of the subsea cable at the crossing point could be eliminated. However, the lateral movement of the subsea cable can be reduced by placing concrete mattresses after the touchdown points as shown in Figure 6-5. Placing mattresses at the touchdown is required to reduce lateral movements, thus ensuring that the limit states, listed in Table 6-1, are satisfied.

6.6 FIELD JOINT COATING FAILURE

The subsea power cable (132 kV) and the crossing arrangement, as shown in Figure 6-2 was successfully installed recently. Figure 6-9 presents a snapshot from the as-

built survey undertaken after the completion of the concrete mattress installation to reduce lateral cable movement.
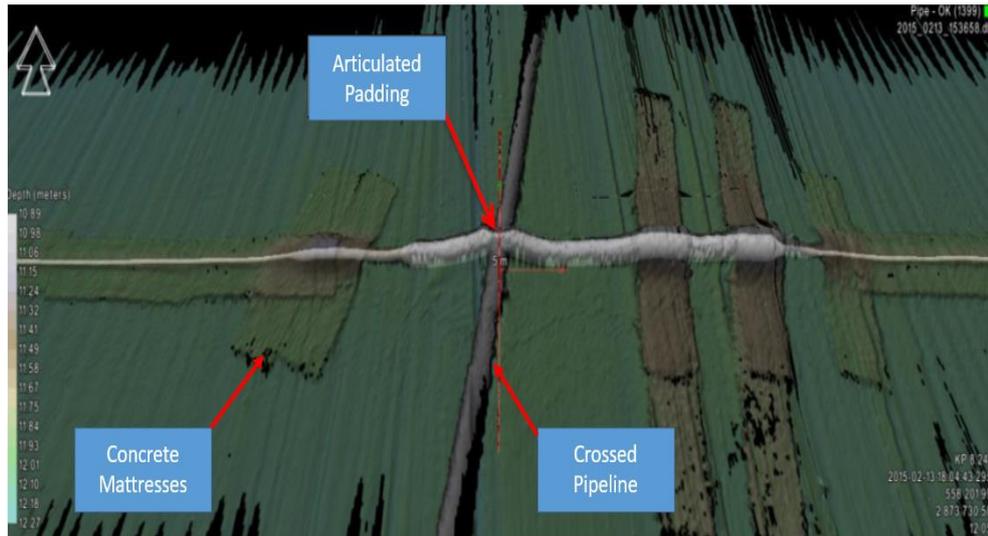
Figure 6-9: Snapshot from the as-built survey of the 132 kV -191 mm power cable at crossing area.

Figure 6-10: ROV survey at the crossing locations- The articulated padding installed on the crossed pipeline away from the field joint.

A post-installation survey was undertaken one year after the cable was installed. The survey included three dozen crossing locations similar to that shown in Figure 6-10. Visual inspections revealed that coating damage had occurred in the pipeline field joint at two crossing sites.

Figure 6-26 and Figure 6-27 illustrate the damage that occurred at the field joint as the result of the lateral movement of the cable and the articulated padding, combined with

the compressive loading exerted by the cable and articulated padding on the field joint coating.

Furthermore, Figure 6-26 shows damage in the concrete weight coating cutback. This indicates that the cable and padding were moving laterally and the concrete cutback was acting as a stopper to some extent.

6.7   DESIGN OF THE ARTICULATED PADDING

This section highlights the methodology used for designing the articulated padding. Also, it presents a summary of the methodology used for the global analysis of the articulated padding.

6.7.1   Environmental Conditions

Wave and current conditions representative of 100-year return conditions are applied to the model as detailed in Table 6-2.

Table 6-2: Metocean Parameters

Parameter	Units	Value
Wave height	m	7.4
Wave period	s	8.7
Wave direction	n/a	Perpendicular to cable lay direction
Water depth (static)	m	13.8
Water level (above static)	m	1.3
Current surface speed	m/s	1.14
Current direction	n/a	Parallel to wave

6.7.2   Global Anaylsis

The models are set-up with articulated padding protecting a cable laid over a pipeline with an outer diameter of 38 inches. The residual lay tension in the cable was set to be

10 kN. Post installation restraints were added to the sections of cable and bend restrictor that were touching down on the seabed in the static configuration. A typical base model is presented in Figure 6-11 and Figure 6-12.
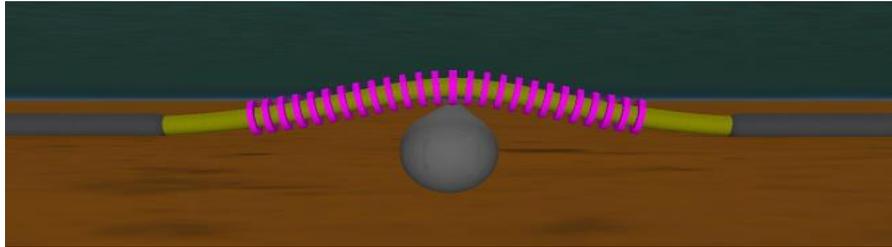
Figure 6-11: Global analysis model in static equilibrium – Elevation view.
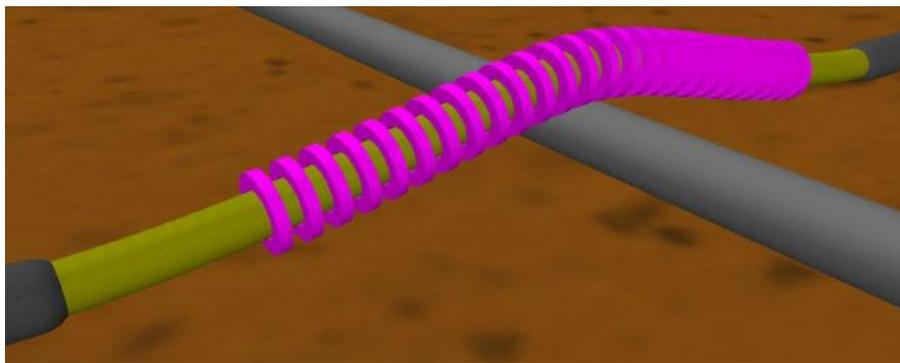
Figure 6-12:Global analysis model in static equilibrium – ISO view.

To determine the effect of not installing grout bags, additional load cases were evaluated with and without currents, configured as per the two side elevations shown in Figure 6-13.
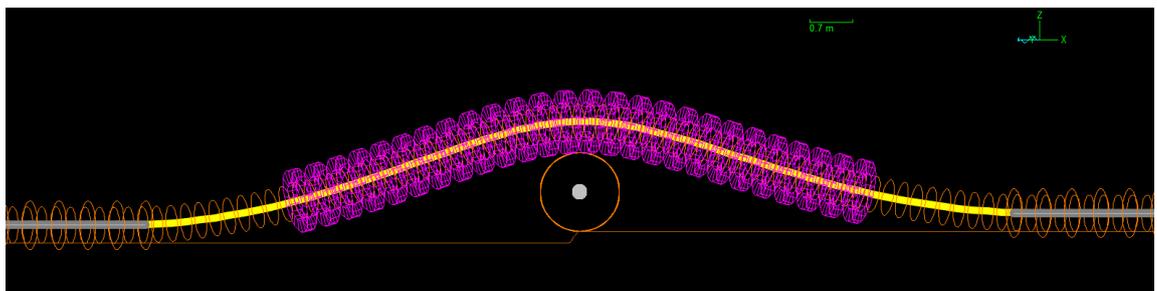
Figure 6-13: Global analysis no stabilisation (7.5m free span) – Side Elevation.

Two models were run, one with the cable crossing at 90 degrees to the pipeline, and the other with the cable crossing at 75 degrees to the pipeline. The maximum loads on articulated padding components are presented in Table 6-3.

Table 6-3: Maximum Articulated Padding Loads from Global Analysis.

System Lay Angle (Degrees)	Maximum Loads on Articulated Padding Elements	
	Radial (kN)	Axial (kN)
75	48	1.2
90	49	2.5

The reason for the difference in radial loads is because the adjacent articulated padding relieves a proportion of the load if the crossing is at 75 degrees with the asset.

6.7.3   Local Analysis

6.7.3.1   Local Analysis Model Overview

This section presents the input data and assumptions used in the local analysis of the articulated padding components.

6.7.3.2   General Modelling Considerations

The articulated padding components are intended to be installed on an assembly of interconnecting bend restrictor components.. Figure 6-14 depicts the disc or articulated padding.

The articulated padding components are expected to withstand the anticipated axial and radial loads experienced by the system during installation and from in-service environmental factors.
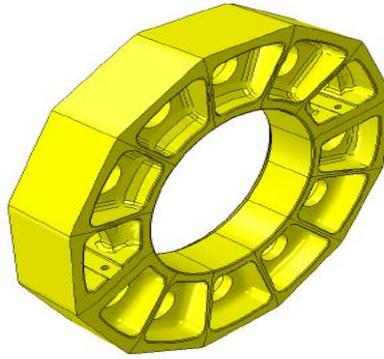
Figure 6-14: Articulated padding.

To obtain a full understanding of the way the articulated padding design responds to anticipated installation and in-service loads, several different load scenarios were analysed. A sample of those results will be presented here.

The articulated padding components are modelled in ABAQUS. For each load case, an analytical rigid surface was used to represent contact between the articulated padding and the bend restrictor component. Analytical rigid surfaces were also used to apply all additional boundary conditions. Point loads were applied to a reference point on the bend restrictor rigid surface to instigate radial and axial loading. A friction coefficient of 0.2 was applied to the contact between the articulated padding and bend restrictor. A friction coefficient of 1.0 was applied to all other contacting surfaces thereby restricting relative movement between the articulated padding and the boundary rigid surfaces.

6.7.3.3   Material Properties

The articulated padding components are constructed from polyurethane. The material properties are summarised in Table 6-4 . The limits of the material are presented in Table 6-5. The material was assumed to be linear elastic throughout the analysis.

Table 6-4: Material Properties

Material	Temperature (Deg C)	Young's Modulus (MPa)	Poisson's Ratio
Polyurethane	23	1041	0.33

Table 6-5: Material Limits

Material	Temperature (Deg C)	Allowable Stress	
		Tension (MPa)	Compression (MPa)
Polyurethane	23	28.1	33.9

Only linear elastic material properties have been applied in the ABAQUS models. The articulated padding constituent material is hyper-elastic and exhibits high strain at yield; approximately 60% tensile strain at break, at the operational temperature. Regions of high stress will deform and redistribute loads. This is not accounted for in a linear elastic material model. Therefore, the results can be considered conservative.

6.7.3.4 Local Analysis Results

The following section details the results of a local analysis of the articulated padding component for a selected case.

A specific load case was considered in order to determine the performance of the articulated padding component under in-service loading conditions. The articulated padding component was positioned directly on top of the pipe. The radial load component was resisted by the outer surface of the articulated padding component. Figure 6-15 details the ABAQUS assembly model of this selected load case.

217
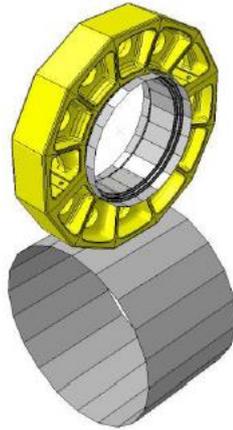
Figure 6-15: ABAQUS Model.

Table 6-6 details the peak principal stress and the resulting minimum safety factor for the articulated padding design. The articulated padding component's peak tensile and compressive stresses remain within the material limits.

Table 6-6: Finite Element Results

	Maximum Tensile Stress (MPa)	Maximum Compressive Stress (MPa)	Minimum Factor of Safety
Articulated padding	4.7	11.6	1.8

Figure 6-16 through to Figure 6-18 detail the stress distribution plot for the articulated padding design. All plots present the absolute principal stress.Excluding the contact points, the plots demonstrate that the articulated padding's stress levels remain within the allowable limits of the material.

218
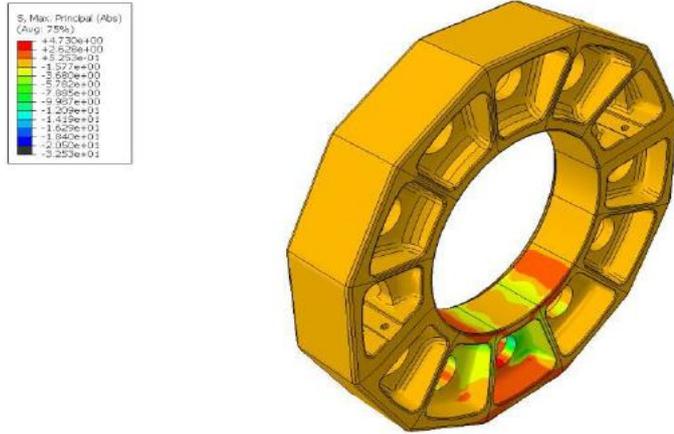
Figure 6-16: Absolute principal stress view 1.
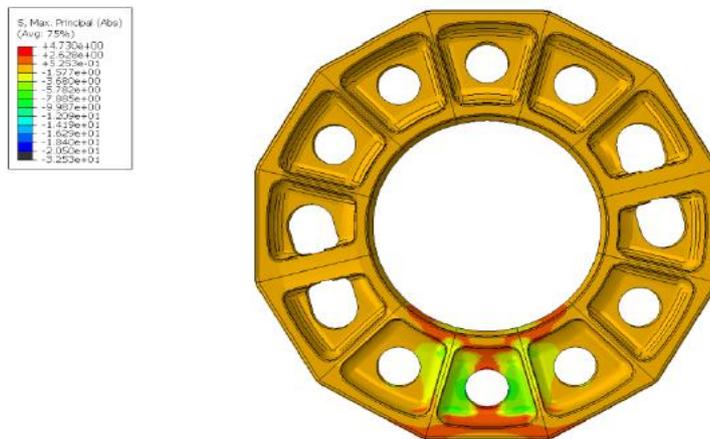
Figure 6-17: Maximum absolute principal stress view 2.
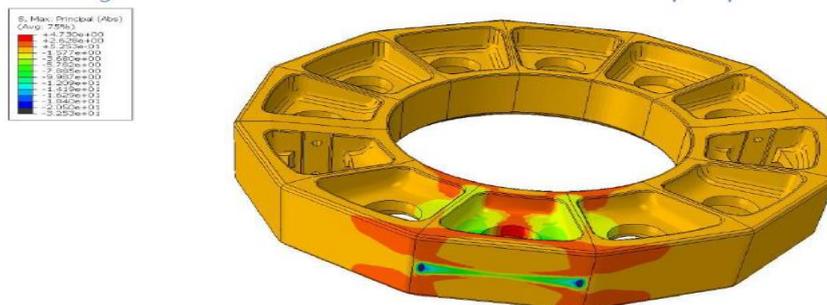
Figure 6-18: Maximum absolute principal stress view 3.

219

6.7.3.5   Physical Testing

This section presents the physical testing performed on the articulated padding to ensure that the padding was suitable for its intended purpose. The following tests were conducted:

- Axial load test
- Radial load test
- Abrasion test
- Combined radial and axial oscillation load test

1.0   **Axial Load Test**

The purpose of this test was to verify that the assembly of the articulated padding and the corresponding mating bend restrictors were able to withstand the maximum envisaged axial load in the various scenarios identified in the numerical simulations. This includes:

i.   Maximum over-boarding load as highlighted in Figure 6-19.

ii.   Maximum estimated axial load in a 100-year storm, (15°C to 25°C) as shown in Figure 6-20.

Figure 6-19: Simulated over-boarding chute (horizontal test orientation).
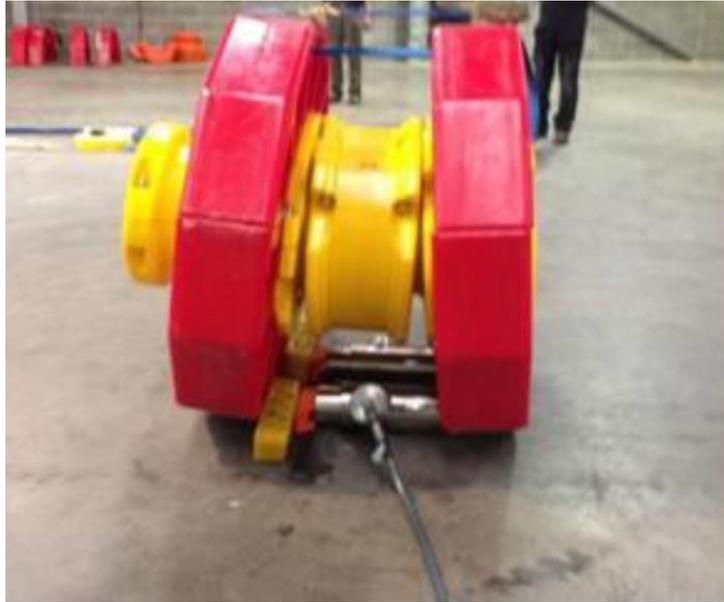
Figure 6-20: Axial load testing of articulated padding assembly.

2.0   Radial Load Test

Radial load tests, as shown in Figure 6-21 and Figure 6-22, were conducted to ensure the integrity of the assembly was not compromised during the articulated test and consequently verify the results from the finite element modelling.

Figure 6-21: Radial rig test.

Figure 6-22: Location of hydraulic cylinder.

The articulated padding assembly was placed between two structural members in a caged test rig and subjected to a direct radial load by hydraulic cylinders. To avoid localised damage caused by the hydraulic cylinder end fittings, small spreader plates were fitted between the hydraulic ram and the articulated padding parts.

3.0 Abrasion Test

The abrasion test conducted is presented in Section 6.5. After completion of the test, the padding was inspected visually to ensure that there were no signs of damage. Furthermore, the outer diameter of the padding was measured before and after the radial test to ensure that deformation had not occurred in the padding.

4.0 Combined Radial and Axial Oscillation Load Test

The purpose of the oscillation test was to simulate the contact load the articulated padding assembly would experience as a result of installation and any subsequent movement due to waves. The test replicates the 70° - 75° crossing angle of the padding over the asset, as shown in Figure 6-23 and Figure 6-24.

Figure 6-23: Crossing installation layout - side elevation.

Figure 6-24: Oscillating test (combined radial and axial) of articulated padding assembly.

Following the OrcaFlex analysis of the as-built system with typical environmental conditions (Metocean data), it was possible to predict the displacement due to the motion of the ocean. Consequently, the padding assembly was moved plus/minus 500mm at the natural lay point of the crossing. The crossing was moved by a telehandler, as indicated with the blue arrows in Figure 6-25. Both ends of the crossing were stabilised with masses.
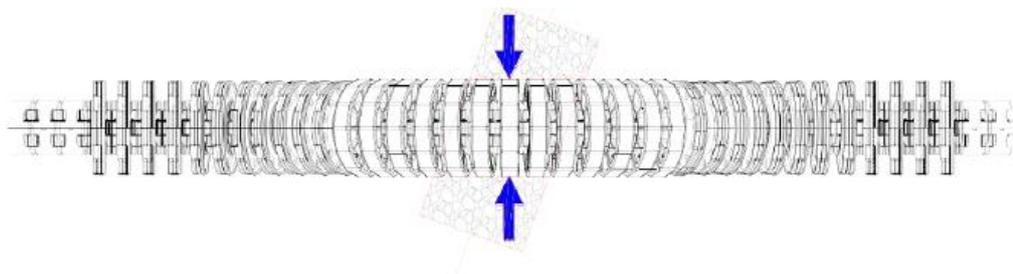
Figure 6-25: Crossing installation layout - plan view.

6.8   ENGINEERING ROOT CAUSE ANALYSIS

The engineering root cause analysis reviewed potential factors that may have contributed to the damage of the field joint coating including engineering design, manufacture, installation and environmental factors. From the root cause study, it appeared that the damage of the field joint coating was a result of the installation work, lateral cable movement and repeated dynamic impact loads. The damage to the field joint coating is illustrated in Figure 6-26 and Figure 6-27 .

6.8.1   Installation

The root cause analysis identified that prior to the finalization of the crossing design, a ROV survey was undertaken of the crossed pipelines and the seabed within 250 m of the crossing point. A survey is required to ensure that there is no anode at the crossing point. As per industry practice, the crossing survey focused on the existing pipeline burial depth, detailed bathymetry of the crossing site area seafloor levels and the physical condition of the existing pipelines. However, it did not identify the location of pipeline field joints in relation to the crossing point. The crossing design was finalised based on the results of that survey. The cable installation contractor used the side-scan and visual data from the ROV survey at the proposed crossing location during installation.

During the survey, the identification of the joint numbers and field joints was not carried out. It is not common in the cable/pipeline industry as part of the pre-lay survey to determine the location of field joints in relation to the crossing point. The joints in older pipelines may be covered in marine growth which increases the difficulty in identifying them. If pipelay records are not available then identification is extremely difficult.

The root cause investigations revealed that the codes and recommended practices are not explicit about prohibiting the installation of a crossing at a field joint of a pipeline. During the cable installation, the cable with the articulated padding was unintentionally laid on a field joint location as illustrated in Figure 6-28.

The investigation also indicated that during installation, it was difficult to identify the field joint due to the presence of marine growth. Figure 6-29 and Figure 6-30 show images of the first field joint downstream from the damaged field joints for pipeline #1 and pipeline #2. From these figures it is evident that the field joints are fully covered with the marine growth. This made it impossible to differentiate between the pipeline and the field joint.

6.8.2   Lateral Movement

Numerical simulations using finite element analysis were undertaken to estimate the radial loads generated by the articulated padding on the field joint. The finite element model used in the investigation is shown in Figure 6-31. The outcomes are provided in Table 6-7.
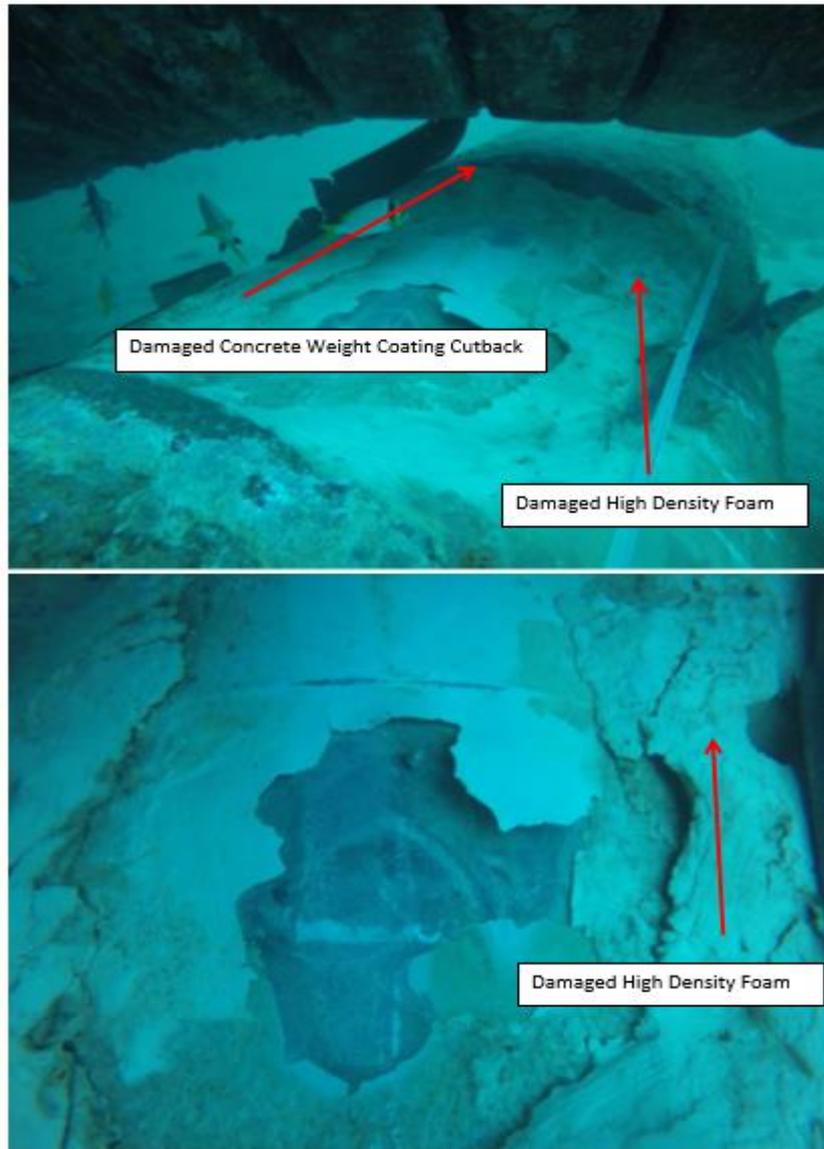
Figure 6-26: Damaged field joint coating-Pipeline # 1. Note that the cable is lifted for the purposes of inspection and this photograph.
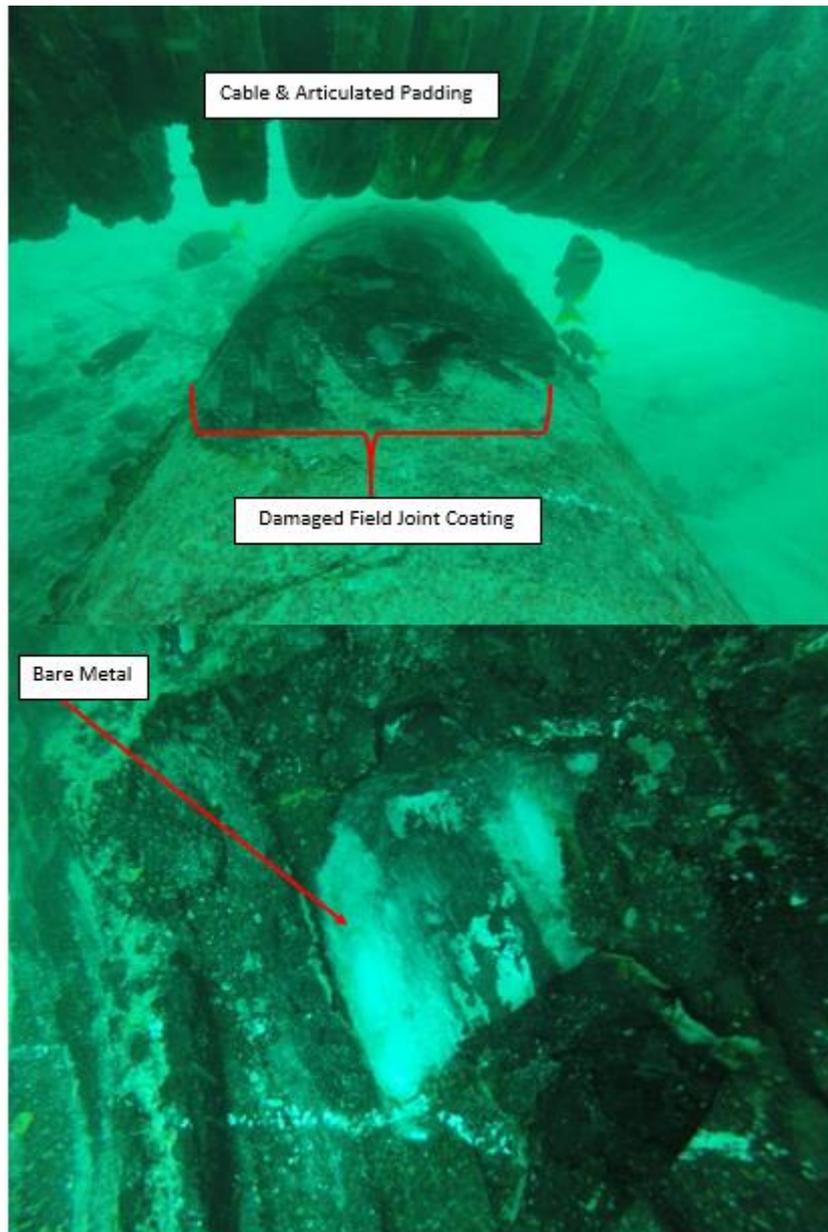
Figure 6-27: Damaged field joint coating-Pipeline # 2.
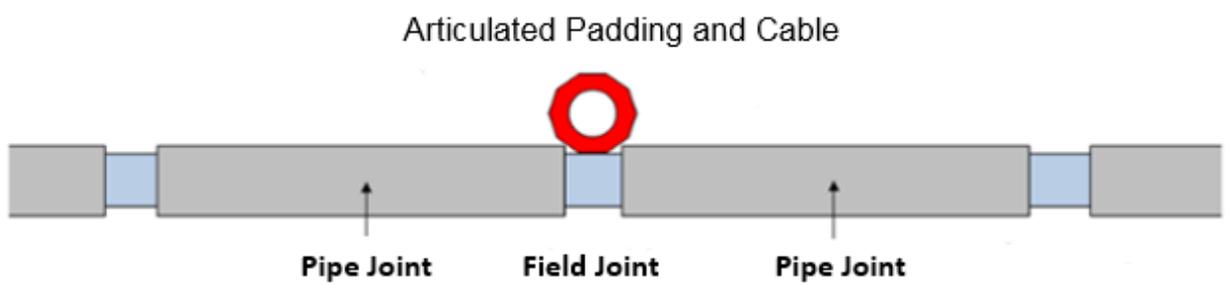
Figure 6-28: Location of articulated padding in relation to field joint.
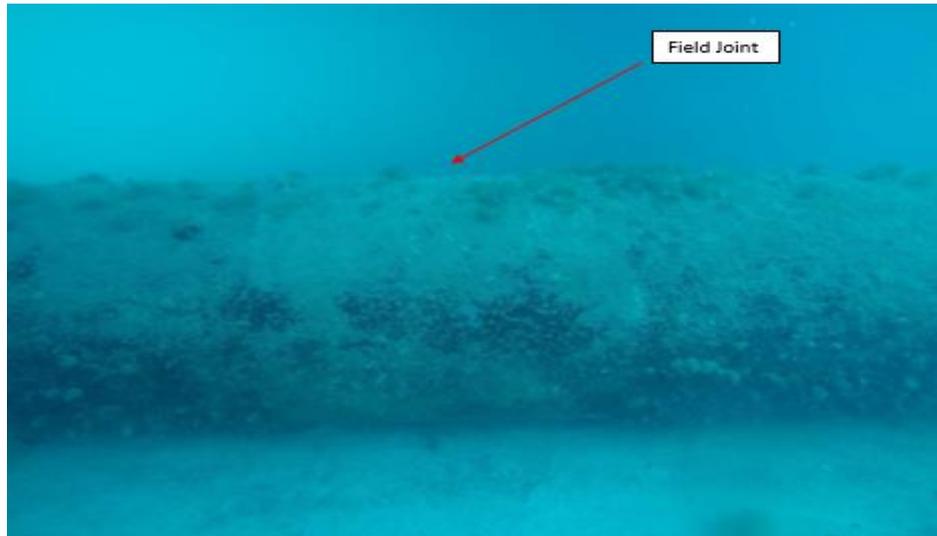
Figure 6-29: Field joint coating downstream from the damaged joint- Pipeline # 1.
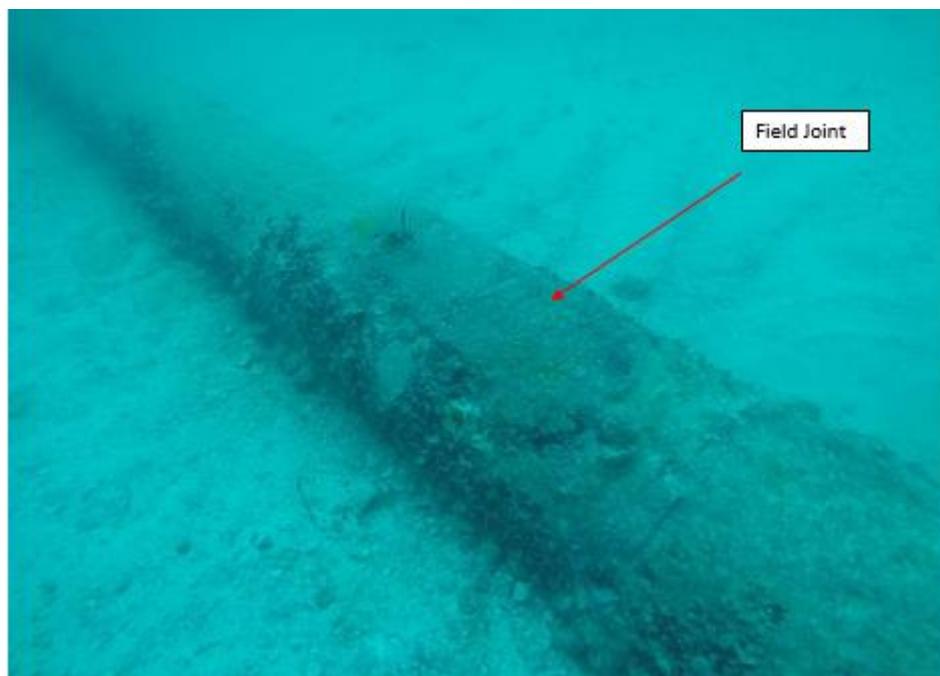
Figure 6-30: Field joint downstream from the damaged field joint- Pipeline # 2.
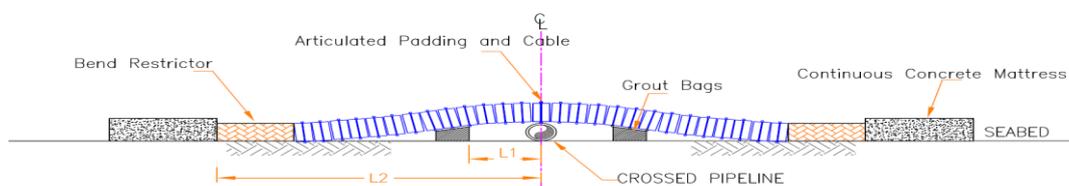
Figure 6-31: Finite element model.

228

Table 6-7: Crossing Analysis Results

Case Number	Grout bag type	Maximum radial force (kN)	Maximum axial force (kN)	Maximum lateral displacement (m)
1	No grout bags	55	6	0.65
2	Vertical support only	49	2.5	0.65
3	Cradle type	12	1	0.15

Notes:

1- **Residual lay tension (kN) used in the simulation is 6 kN and it was applied before grout bags were installed under free span.**

2- **Water depth is 22 m.**

3- **Maximum wave height and maximum wave period used in the simulation were 8.3 m and 8.6 s respectively.**

4- **Steady current at sea surface 1.25 m/s.**

5- **Pipeline centre to mattress edge (L_2) is 7.5 m.**

6- **Pipeline centre to centre of grout bag edge (L_1) is 2 m.**

The finite element analysis clearly shows that reducing the free span length from 7.5 m to 2 m (L2 and L1 respectively in Figure 6-31) by the addition of a vertical support, gives a reduction in both radial and axial load for the same maximum lateral movement. Adding cradle type bags with further horizontal restraints greatly reduces these loads.

Based on the finite element simulations undertaken, the following results were obtained.

- Increasing free span length generates significantly larger lateral movement across the crossed pipeline.

- Increased lateral displacement can significantly increase dynamic radial loads and as such must be considered as a contributing factor.

- There is a strong link between radial/axial load, support placement, type of support and lateral movement of the cable at the crossing.
- Providing cradle type grout bags (vertical and lateral restraints) on either side of the crossing reduces lateral movement.

Regarding the hydrodynamic coefficients of the articulated padding, the results from the experiments were considered individually.

- **Drag coefficient:**

The variation of the drag coefficient with the elevation of the articulated padding above the seabed was not taken into account. Thus, the drag coefficient value was considered to be constant along the section of the articulated padding over the crossed pipeline/supports. Analyses were performed with drag coefficients between 0.6 and 0.7 for the articulated padding and between 0.7 and 0.8 for the bend restrictor. Note that the drag coefficient for a bare cable is in the range of 0.9 as per DNV-RP-C205 (2014).
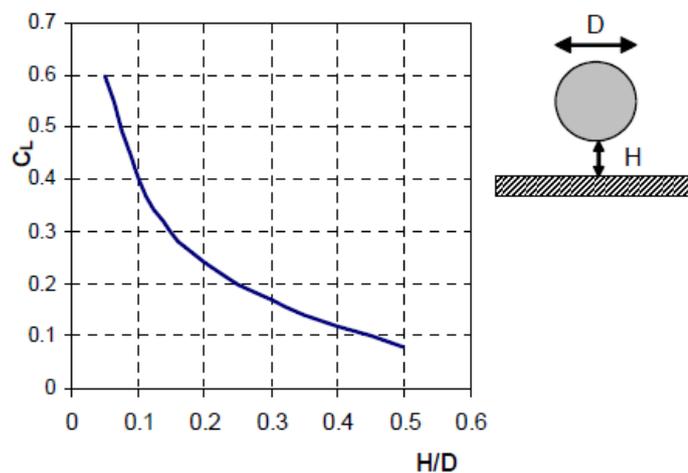
Figure 6-32: Lift coefficient (DNV-RP-C205, 2014).

For H/D ratios lower than 0.05, the lift coefficient is interpolated between the values in the curve and the value of 0.9 for the articulated padding on the seabed (i.e. H/D=0).

- **Inertia coefficient:**

Analyses were performed with an inertia coefficient of 1.8 for the articulated padding and the bend restrictor.

230

The drag force on the articulated padding is 5.6 times greater than the drag and lift forces experienced by a bare cable. This is assuming the same drag coefficient for the bare cable and the articulated padding. The difference in the drag and lift forces between the bare cable and the articulated padding can be attributed to the difference in drag area. The drag area of the articulated padding is 5 times greater than the bare cable. The outer diameter of the articulated padding is approximately 1100 mm whereas the outer diameter of the cable is 190 mm. The formulae for the hydrodynamic forces are presented in Section 6.3.

6.8.3   Repeated Dynamic Impact Loads

Dynamic impact loads due to the rolling or sliding of the articulated padding across the rough surface of the round pipeline is hard to evaluate and quantify because of the complexity of lateral motion and the involvement of many unknown force components. However, the damaged concrete at the cutback area shown in Figure 6-33 is clearly a consequence of significant impact loads.
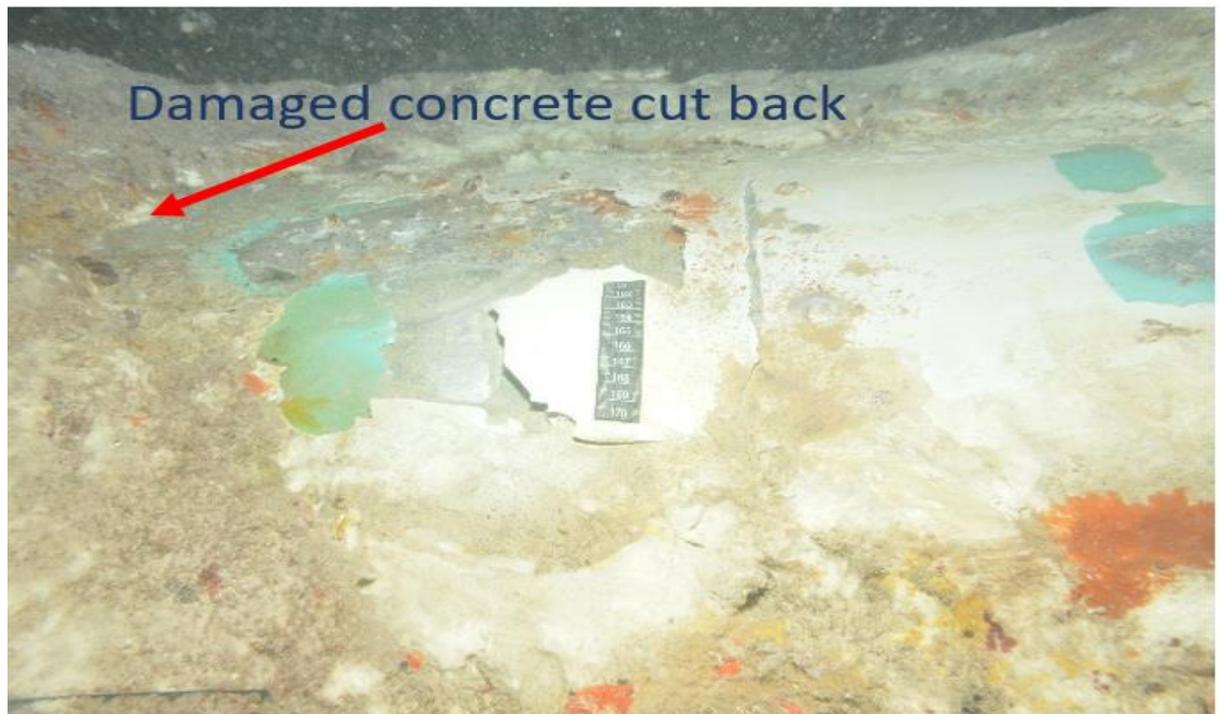
Figure 6-33: Damaged concrete cutback.

6.9   RECTIFICATION

A mitigation measure was implemented to repair the field joint coating and prevent future damage to the site. The finite element simulations undertaken demonstrated that if the cable free span length and lateral movement were reduced by the addition of vertical and horizontal constraints close to the pipeline, the global reaction forces due to self-weight and environmental factors (waves and current) can be reduced. In view of the above, it was decided to install two large cradle grout bags as shown in Figure 6-34 to avoid contact between the pipeline field joint and the cable. It can be seen from Figure 6-34 that the distance from the centre of the pipe and the edge of the bag was chosen as X. This is consistent with the finite element analysis.
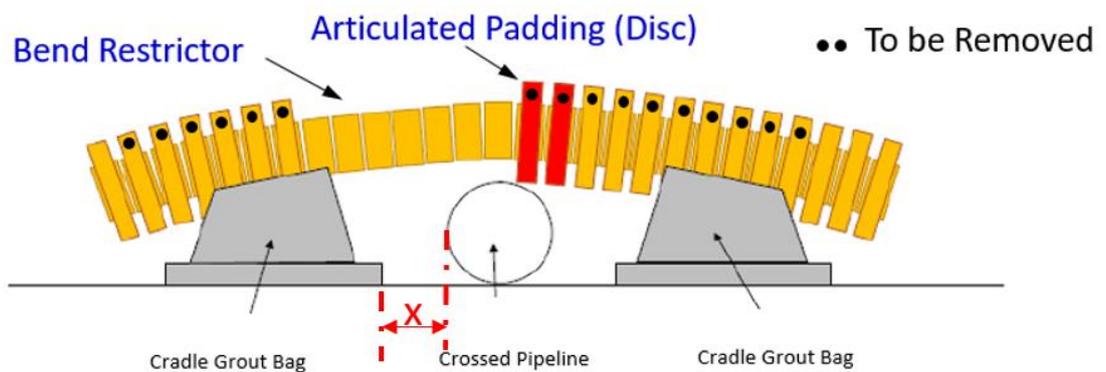
Figure 6-34: Installation of cradle grout bags.

Figure 6-35 shows that once the bags were filled with concrete, air bags were used to lift the cable off the grout bags. The discs installed around the bend restrictor were then removed and the seafloor was excavated underneath the crossed pipeline to facilitate the repair of the field joint coating.

Air Lifting bag capacity and installation location to be decided

Bend Restrictor

Gap between Cable and Existing G/B

Front View

Side View

Cradle Grout Bag

Crossed Pipeline

Cradle Grout Bag
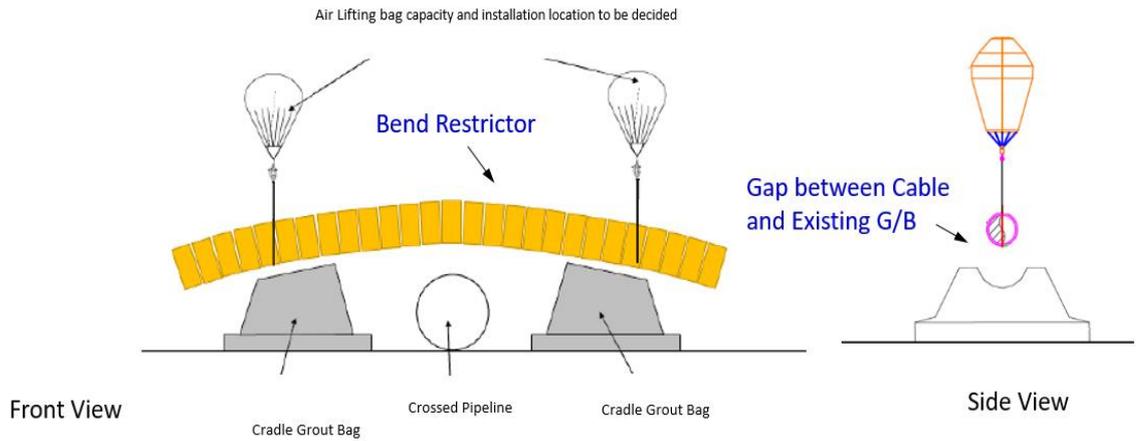
Figure 6-35: Lifting of subsea cable.

Figure 6-36 shows that after the completion of the repair, the air bags were removed, and the cable was supported by the grout cradle bags. The required vertical distance of 400 mm from the bottom of the cable to the top of the field joint was achieved by the design-specific grout bag.
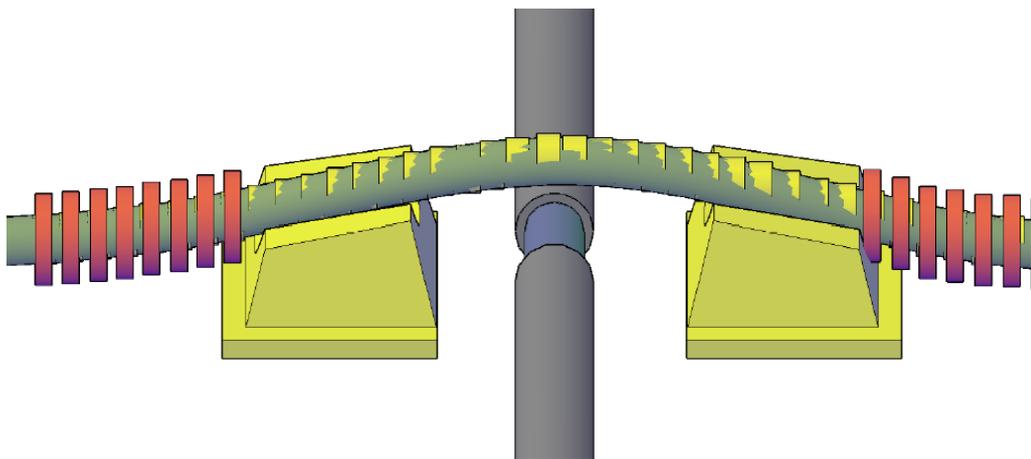
Figure 6-36: Final position.

Figure 6-37: Actual footage showing air bags lifting the cable.

The photographs in Figure 6-37 show the air bags lifting the cable. One can see that the articulated padding system has been removed. The photograph on the right shows the field joint after repair.

Figure 6-38: Photo showing the as-built vertical separation and cradle grout bag support.

The photograph on the left of Figure 6-38 shows the as-built vertical separation between the bottom of the cable/bend restrictor and the top of the field joint. The photograph on the right of Figure 6-38 shows the cable/bend restrictor sitting on the cradle grout bag. The option of shifting the cable away from the field joint was investigated but this option was found to be unviable due to the cost of relocating numerous mattresses installed at the cable touchdown point, and the risk it posed to the exposed section of cable in the crossing exclusion zone.

7 Chapter-7 – Paper No. 5

Title: **"Pipeline walking and anchoring considerations in the presence of riser motion and inclined seabed".**

Authors: **Ahmed Reda, Ibrahim A Sultan, Ian M Howard, Gareth L Forbes, Kristoffer K McKee.**

Journal: **International Journal of Pressure Vessels and Piping.**
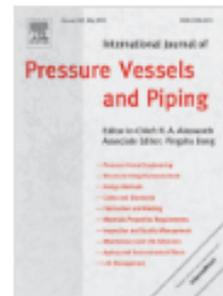
7.1 STEEL CATENARY RISER

7.1.1 Basic Steel Catenary Riser Concepts

Figure 7-1 illustrates a steel catenary riser (SCR) in the mean or neutral static position without environmental loading or vessel movement.

As SCRs are sensitive to environmental loading, the touchdown point shifts depending on vessel movement and excursions. In SCR design the touchdown zone is defined as the range of locations where the touchdown point is located. The interface between the SCR and pipeline is called the transition point. The transition point is defined as the point where there are no lateral or vertical movements due to the dynamics of the SCR. Normally, the transition point is modelled as a fixed point in the SCR design.

The axial force on the pipeline resting on the seabed is controlled by the tension imposed by the SCR at the touchdown point. Figure 7-2 shows an example of the effective tension along a pipeline during installation. Note that Y1 and Y2 denote the tensions at the SCR touchdown point and the residual lay tension of the pipeline, respectively.
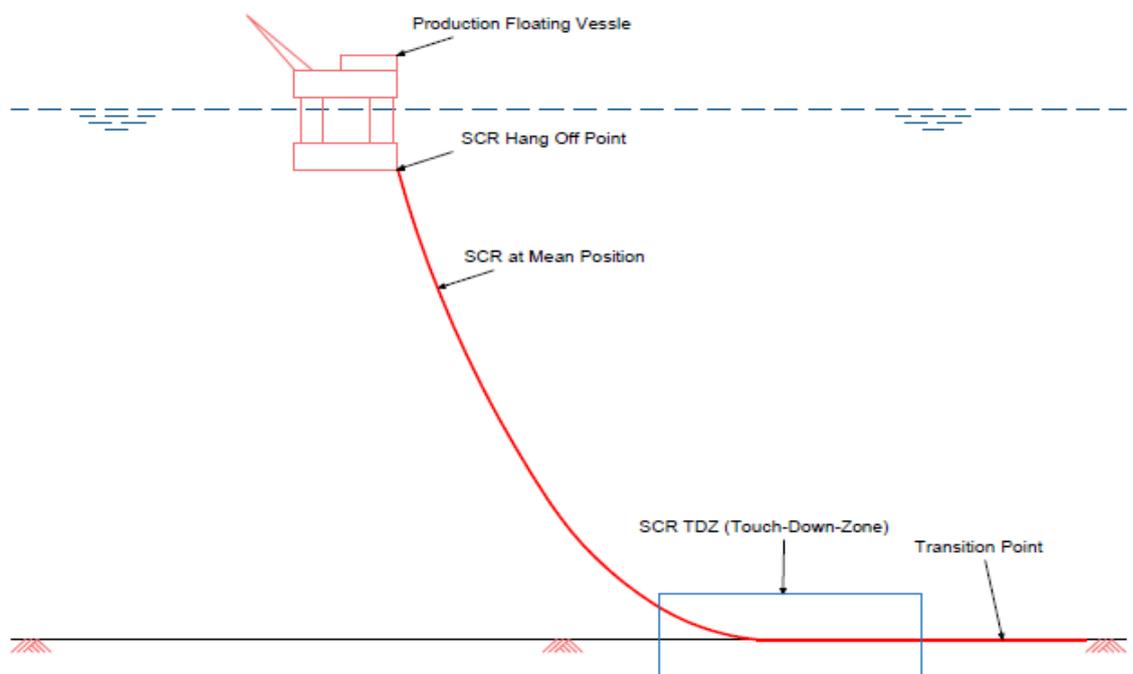
Figure 7-1. SCR in static configuration.

In this example, the tension Y1 is held by soil resistance in the axial direction. The soil resistance builds up over an expansion length. As can be seen from Figure 7-2, the tension falls from Y1 to Y2, over the expansion length. The expansion length, X2, can be determined using equation 7-1:

$$Expansion\ Length\ (X2) = \frac{Y1 - Y2}{Pipe\ Submerged\ Weight * Axial\ Friction\ Factor}$$

7-1

The force in the pipeline remains constant at the residual lay tension until the expansion zone at the end of the pipeline. As indicated in Figure 7-2, the force drops to zero at the end. However, this is not the case if the pipeline is connected to a spool or end structure, as the spool or end structure provide end resistance or reaction force. During operation, the force in the pipeline changes, as the operating fluids cause an increase in SCR/pipeline weight and consequently change the shape of the SCR, as shown Figure 7-3. However, if the departure angle, to be accommodated by the flexible joints, is fixed, the increase in the SCR weight results in a decrease in the suspended length of the SCR and generates an increase in the SCR tension.
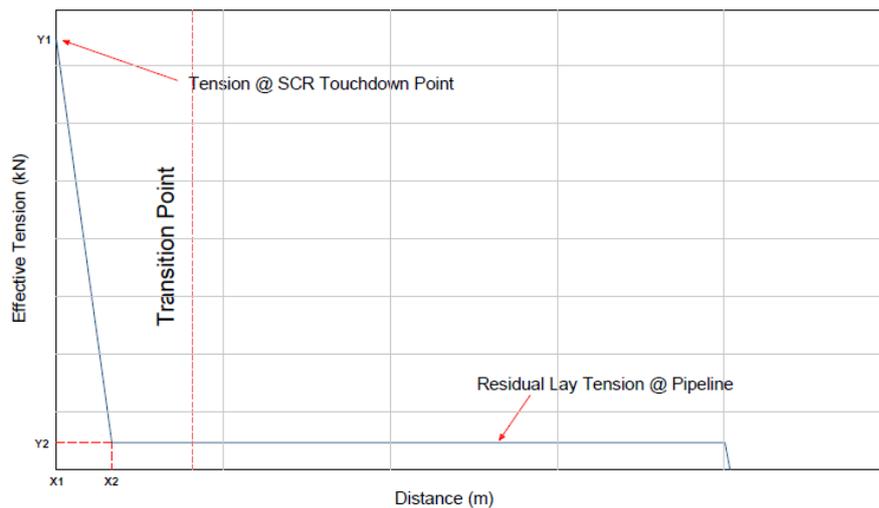
Figure 7-2. Effective tension along SCR-pipeline system.
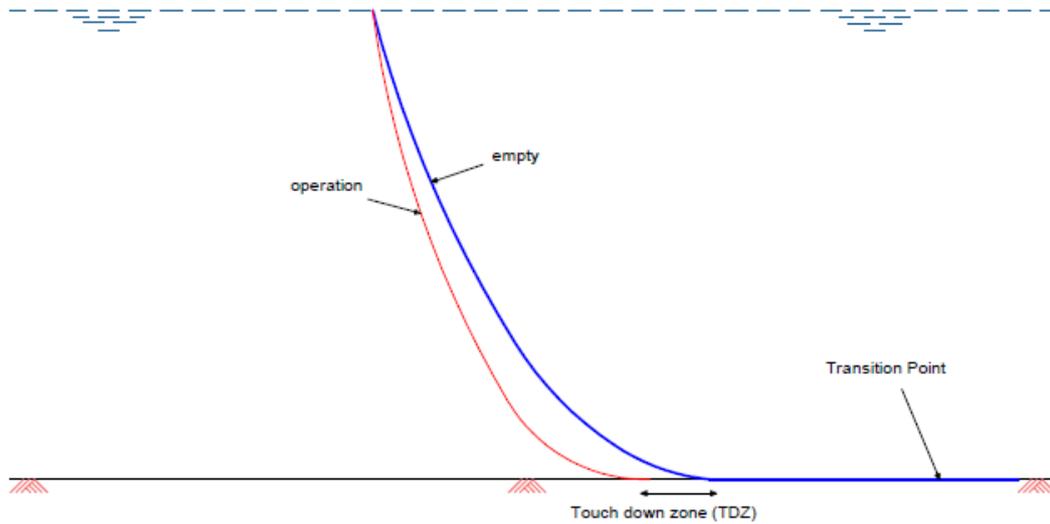
Figure 7-3: SCR configuration during installation and operation cases

7.1.2   Vessel Excursions

The floating production vessel, on which the SCR is supported, will be subject to excursions. These excursions are caused by forces associated with hydrodynamic loads. Furthermore, these excursions are influenced by the mooring system and other risers.   Horizontal movement of the vessel causes changes in the riser catenary configuration as shown in Figure 7-4.

Figure 7-4 shows that when the vessel moves to the (left) far position, the effective tension increases and the touchdown moves to the right. Hence, a shorter length of the SCR will be on the seabed. When the vessel moves to the (right) near position, the effective tension reduces and the touchdown point moves to the left, and consequently, a greater length of the SCR will be on the seabed.

238
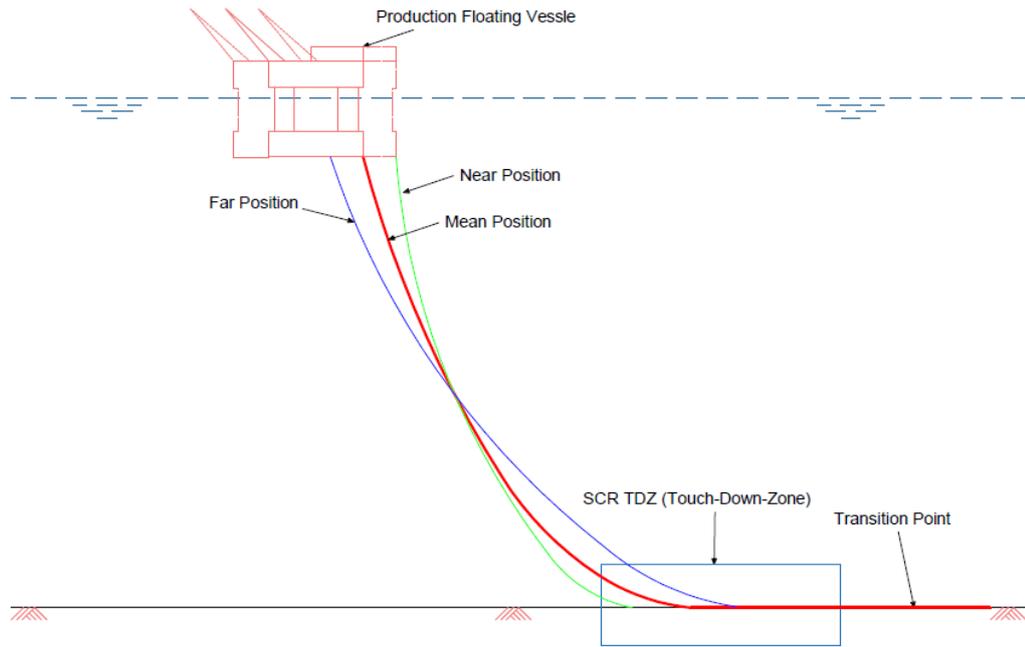
Figure 7-4. SCR configurations associated with vessel excursions.

It can be seen from Figure 7-5 that the motions of the floating vessel are transferred to the riser resulting in variable amplitude effective tension.
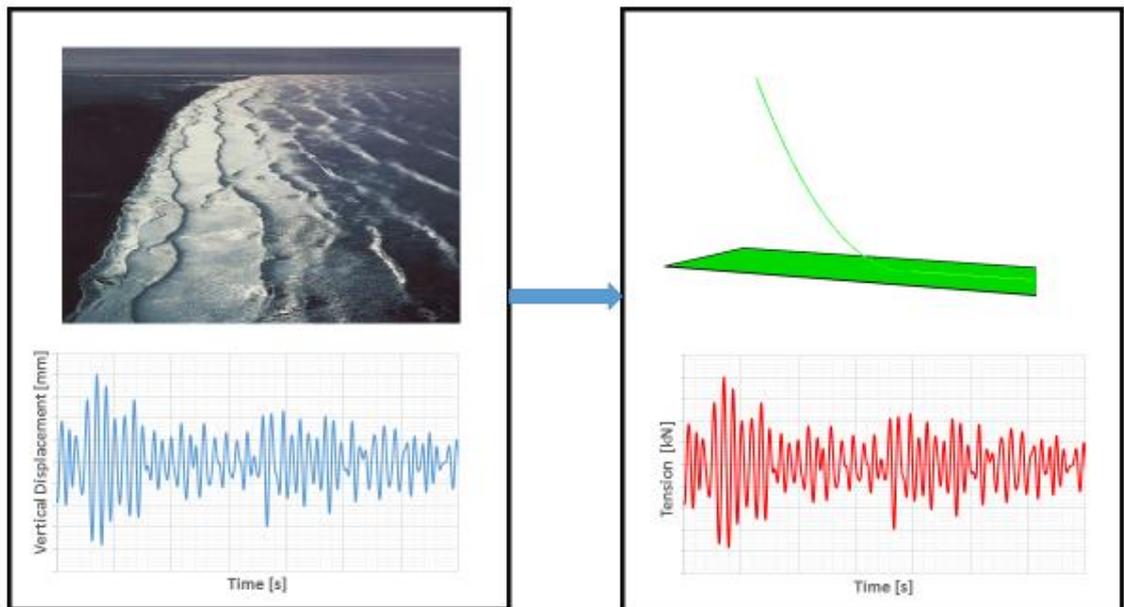
Figure 7-5: Random behaviour of sea waves translates into random amplitude loading of the SCR.

7.1.3   Selection of Basic Configuration using Static Analysis

The selection of the basic configuration is of importance in defining the SCR configuration. The purpose of this analysis is to: 1) achieve the neutral static positions of the SCR system, 2) determine the maximum stresses of the SCRs at the critical areas (touchdown area and top section area near the hang-off point), and 3) investigate the range of movements of the touchdown locations.

Figure 7-6 shows the range of SCR touchdown point locations while Figure 7-7 highlights the effective tension variations along the SCR length and in the horizontal section of SCR on the seabed.
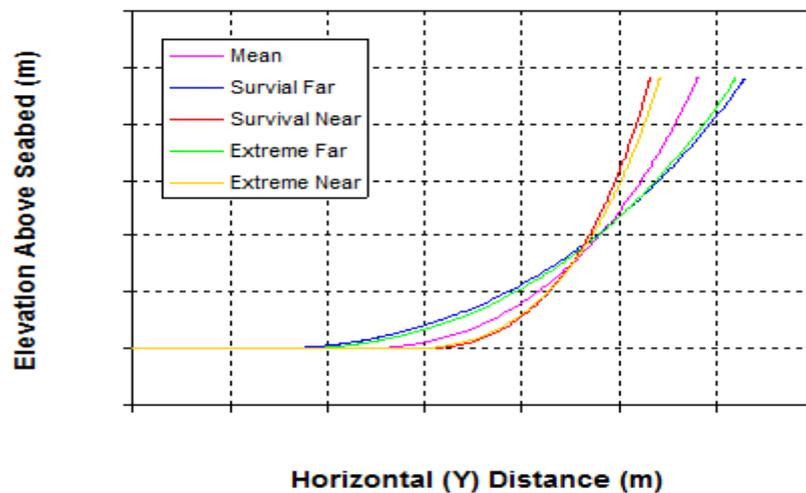
Figure 7-6. SCR configuration at different load cases.

Figure 7-6 and Figure 7-7 present some typical results for SCR configurations at different load cases. These figures should be reported to the pipeline designer for use in the pipeline system design.

As can be seen from Figure 7-6, the touchdown point varies with environmental conditions due to vessel motion. This makes the SCR prone to fatigue loading in the touchdown zone.

Figure 7-7 shows that the effective tension increases as the vessel moves towards the far position and reduces when the vessel moves in the opposite direction towards the near field.
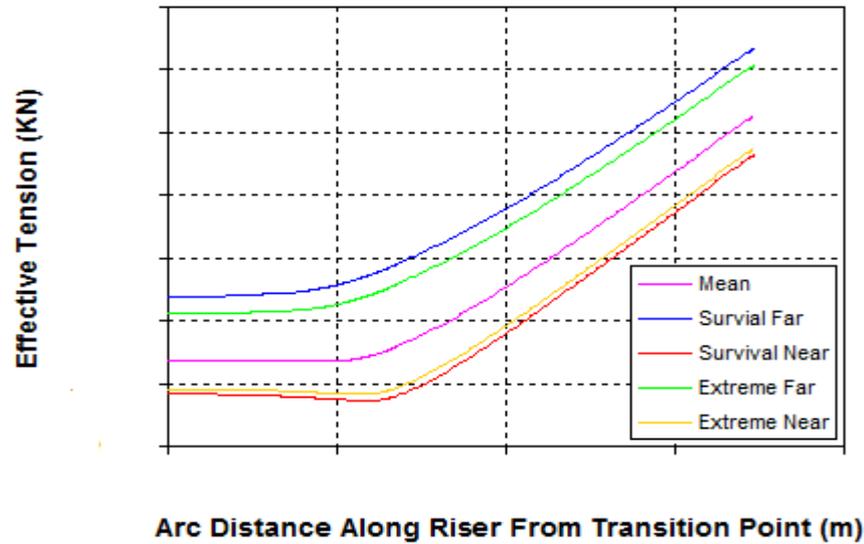
Figure 7-7. SCR effective tension distribution at different load cases.

7.1.4 Dynamic Analysis- Extreme Conditions

The riser should be designed such that it withstands the dynamic loads it will be subjected to over its design life. To ensure this, dynamic simulations should be carried out considering all design loads as per DNVGL-OS-F201 (2016) for the mean, far and near positions, depending on the environmental loading conditions.

Figure 7-8 shows an example of the on-bottom effective tension at the transition point obtained from the dynamic analysis for the survival load cases. The figure highlights the maximum and minimum effective bottom tension when the vessel is in the far field position and the near field position, respectively.

7.1.5 SCR Design Load Cases

The following loads will be defined and used during the design of the SCR. This is in accordance to DNVGL-OS-F201 (2016) and API STD 2RD (2013).

- Installation loads

- Environmental and operational loads

- Internal design pressure

241

- Other loads such as:

  o Expansion of the riser

  o Expansion of the pipeline

  o Functional loads induced by operation such as emergency shut down, slugging or pipeline pigging

- Accidental scenarios including loads associated with damaged mooring lines or loss of buoyancy of the floating facility.
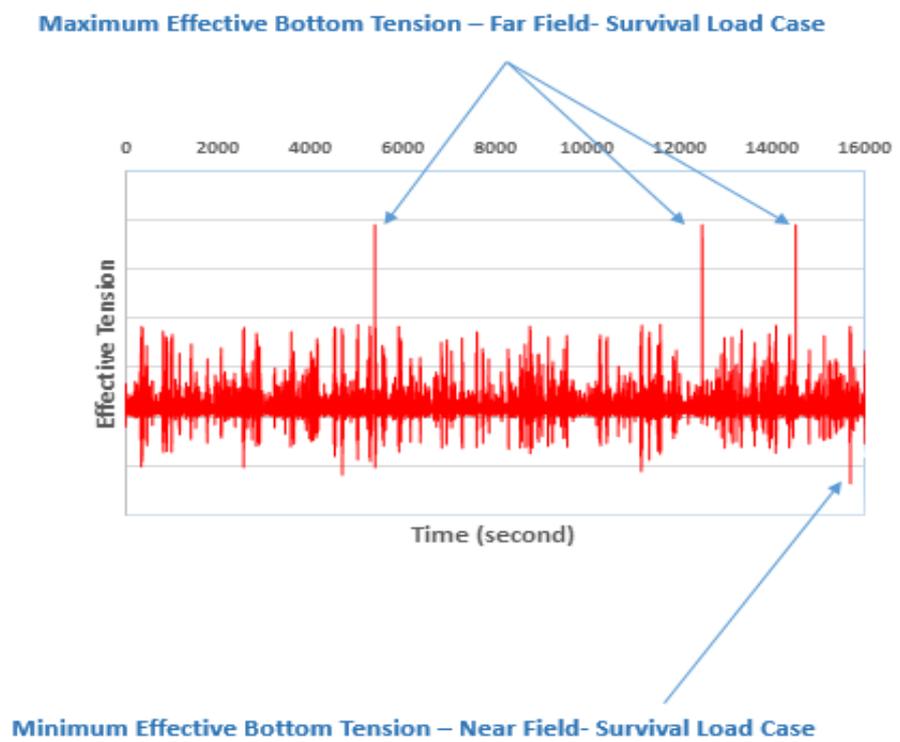
Figure 7-8: Effective tension obtained from dynamic analysis.

Table 7-1 illustrates a typical load case matrix which is normally considered by SCR designers to ensure the integrity of the SCR is not compromised.

Table 7-1: Typical Load Case Matrix for SCR Design

Load Case	Environmental Condition	Operational Condition	Mooring Condition
Installation	1-Year Return Period	Empty	Intact

Load Case	Environmental Condition	Operational Condition	Mooring Condition
Hydrostatic Test	1-Year Return Period	Water Filled	Intact
Operating	10-Year Return Period	Operation	Intact
		Shut-down	
Extreme	100-Year Return Period	Operation	Intact
		Shut-down	
	10-Year Return Period	Operation	Damaged mooring lines
		Shut-down	
Survival	1000-Year Return Period	Operation	Intact
		Shut-down	

7.1.6   Fatigue analysis of SCRs

A major consideration in the design of SCRs is the estimate of fatigue damage.

The highest fatigue damage occurs at the touchdown region of the SCR and the top region, close to the flexible joint, as shown in Figure 7-9. The other sections of the SCR are not of importance for SCR design engineers as these sections are not critical for fatigue calculations.

The top region and touchdown region are considered critical areas. The fatigue in the top region is mainly due to stress cycles induced by wave motions, whereas the fatigue in the touchdown region is caused by the continual lift off and set down of the SCR on the seabed. The significant bending stress results in an unacceptable fatigue ratio in the touchdown region.

Another source of fatigue which should be considered by the SCR designer is pipeline expansion and walking towards the SCR. The pipeline movement towards the SCR tends to shift the transition point. This shift will result in slippage of the mean position of the touchdown point, thereby reducing the static tension as well as increasing the bending moment. Consequently, characteristic concentration of fatigue damage over a very short section of the riser occurs.

7.1.7   Engineered Critical Assessment

Engineering Critical Assessments (ECA) are undertaken to determine the envelope of acceptable crack sizes of the SCR girth welds. The assessment takes into account the loads expected throughout the design life from installation till the end of design life.

The quality of SCR welds must be higher than the usual workmanship weld acceptance criteria.   However, certain small flaws have been found to be acceptable, therefore a flaw acceptance size must be developed for welds. To develop an acceptable size, a fracture mechanics analysis should be made in conjunction with level 2A of BS 7910 (2013).   This is consistent with DNVGL-OS-F201 (2016).

It should be highlighted that there are other assessments which are normally undertaken by SCR designers. These assessments are not presented here as these assessments have no influence on the pipeline.
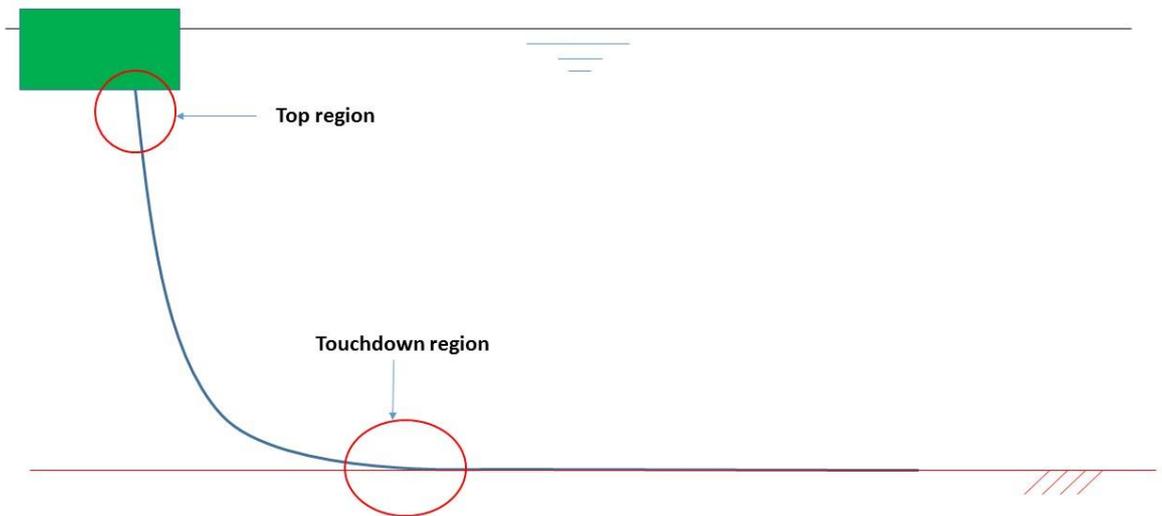
Figure 7-9: Definitions of the SCR critical regions for fatigue.

7.1.8   Initiation of SCR/Pipeline Vessel Connection Scenarios

This section presents some of the methods which are normally used to attach the pipeline or SCR to the production vessel from the pipelay vessel.

o **Scenario 1: SCR initiation at Floating platform/Vessel (First End SCR Installation)**

This method, shown in Figure 7-10, can be used in the cases where the floating vessel is on-site prior to the SCR installation. In this scenario, the floating vessel will be used as an initiation point to form the SCR directly. The sequence can be summarised by the following steps:

- Pipelay vessel to position closely to the floating vessel during the start-up of the pipelay.

- The transfer cable is handed over from the hosting facility to the pipelay vessel.

- The pipelay vessel will remain connected to the floating vessel until the entire SCR is welded and a sufficient length of the pipeline has been laid on the seabed.
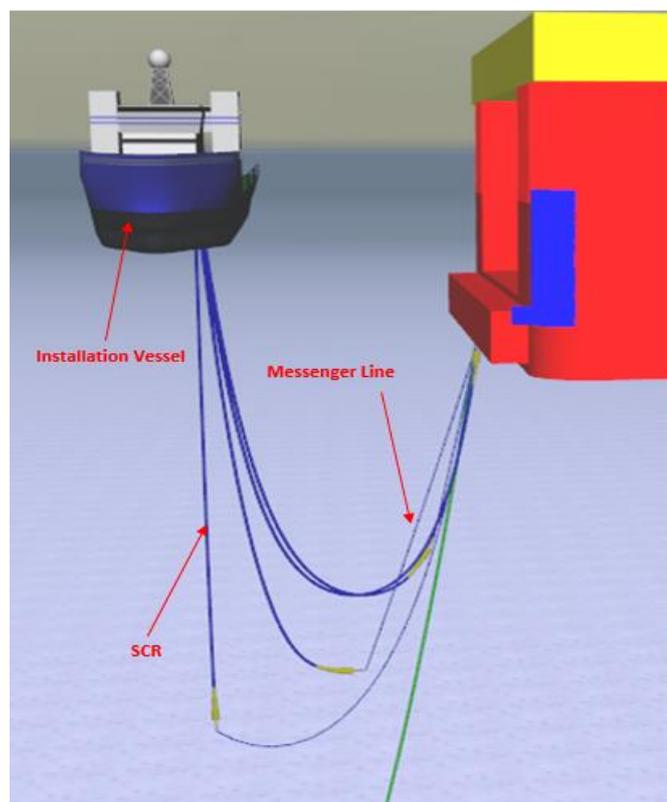
Figure 7-10: First installation sequence.

- o **Scenario 2: SCR abandonment, recovery and transfer to floating platform/vessel (Second End SCR Installation)**

In this scenario, highlighted in Figure 7-11, the pipelay vessel will initiate the pipelay using a start-up head attached to an anchor or pile. The pipelay vessel will lay the pipeline towards the floating vessel location. Then the following sequence is followed:

- The pipelay vessel is positioned close to the hosting facility.

- The transfer wire is attached to the messenger line.

- The floating platform recovers the messenger wire using its crane.

- The upper end of the riser is transferred from the installation vessel to the floating platform.

- The upper end of the riser is secured to the riser hang-off arrangement by clamp.

- The riser is paid out from the installation vessel until it reaches the touchdown point.

- o **Scenario 3: Wet stored SCR**

In this technique, as before, the pipelay vessel will initiate the pipelay using a start-up head attached to an anchor or pile. Once the start-up head has landed in the designated target box, the pipelay vessel lays away towards the intended destination. At the intended destination, the pipelay vessel will lay the pipeline down onto the seabed using an abandonment and recovery winch. From this point forward, any vessel can retrieve the SCR ends and hand the SCR over to the floating vessel's transfer system. Once the floating vessel is in control, the vessel will disconnect and the floating vessel transfer system can lower the SCR onto the SCR receptacles.

7.2 SIMPLIFIED MODEL

The model presented here is only to demonstrate the walking or creeping that can take place for any structure laid on a surface with bi-linear friction. Furthermore, this simplified model can be used to validate the user friction subroutine employed in the commercial finite element packages. The following section presents a single degree of

freedom system developed in order to demonstrate the mechanics of pipeline walking and creeping.

7.2.1   Forcing Function

Equation 7-2 presents the forcing function, F, that is used to excite the mass-spring system.

$$F = A \sum_{n=1}^{N} (t - (n-1)\tau) \, u(t - (n-1)\tau) - (t - (n-1)\tau - \Delta t) u(t - (n-1)\tau - \Delta t)$$

<div align="right">7-2</div>

Figure 7-12 illustrates the force versus time function or "forcing function". The forcing function is designed as a series of ramp inputs with a duration of Δt. Each force is applied periodically during loading cycles where the period is denoted by τ. In the above expression, n is the number of the current cycles and N denotes to the total number of cycles used in the analysis.

The function u(t) above signifies the Heaviside step function, while A refers to the slope of the ramp excitation.

7.2.2   Soil Friction Model

A bi-linear soil friction model, as shown in Figure 7-13, is employed in this section to model the resistance exerted by the soil on the pipeline axial movement, x. This model is presented below where the soil force is referred to as f_{fr}.
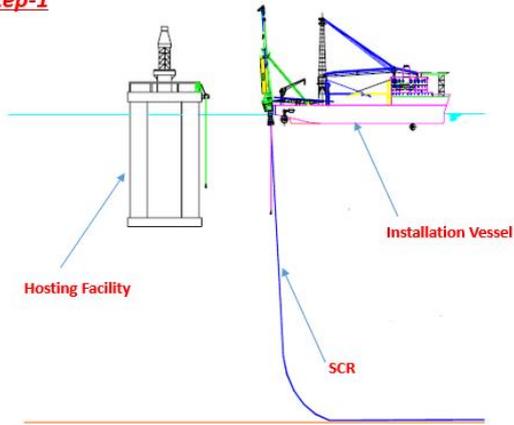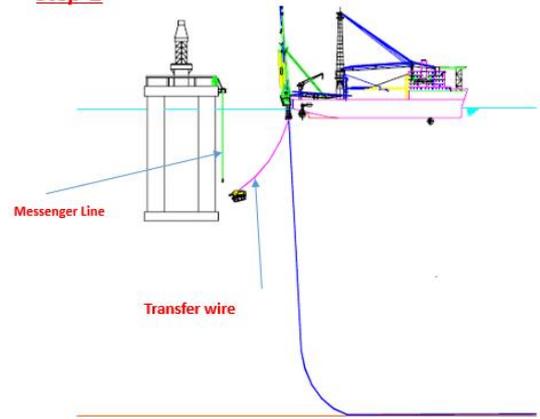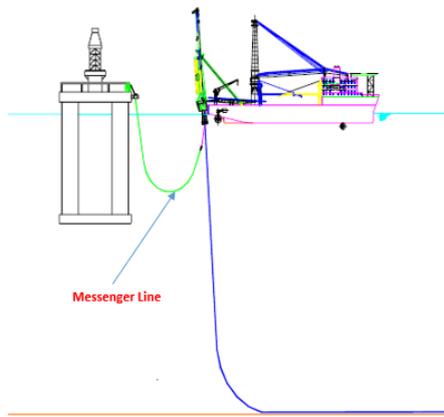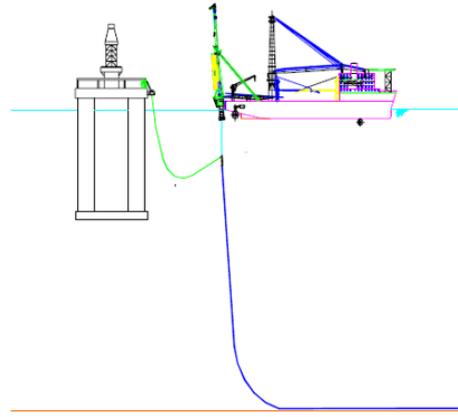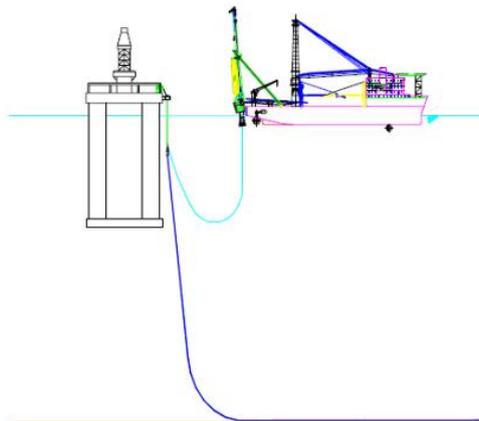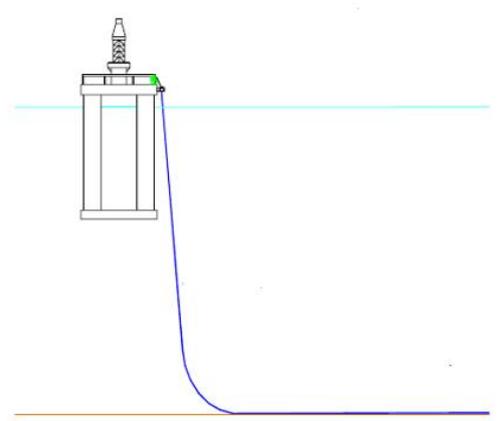
Figure 7-11: Second installation sequence.
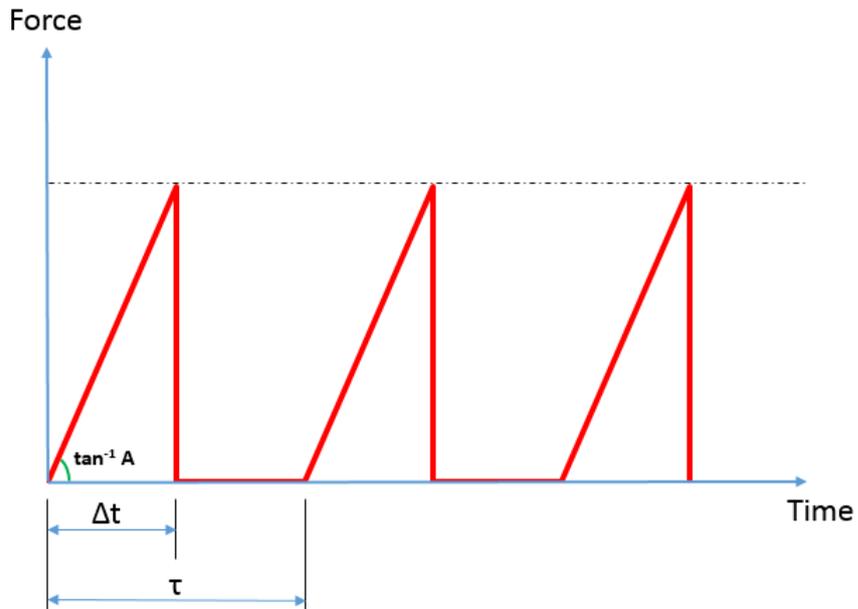
Figure 7-12: Force versus time.

In Equation 7-3, β refers to the slope of the friction force line. It should be noted that "stick behaviour" takes place as long as the friction force, f_{fr}, is below the limiting value, f_1. The soil during stick behaviour behaves as a linear spring with stiffness equal to β. The "slip behaviour" occurs when the friction force, f_{fr}, reaches the limiting value, f_1. In this situation, any increase in the displacement will no longer affect the soil friction force.

$$f_{fr} = \begin{cases} \beta \int dx & if \ \ f_1 \geq f_{fr} \geq 0 \ \ \ (Stick\ behaviour) \\ f_1 & if \ \ f_{fr} > f_1 \ \ \ \ \ \ \ \ (Slip\ behaviour\ ) \end{cases}$$

7-3
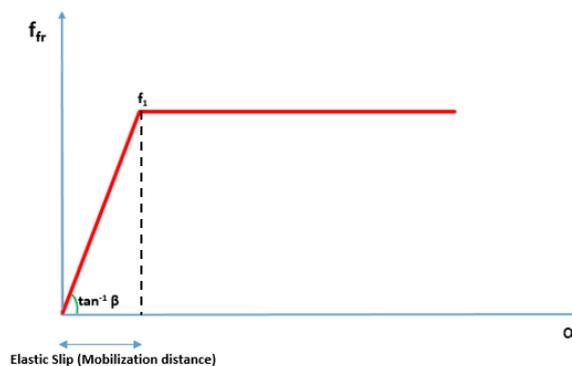
Figure 7-13: Stick-slip behaviour.

249

7.2.3 System Equation of Motion

Figure 7-14 highlights the mass spring system laid on a surface with friction. The equation of motion can be expressed as follows:

$$m\ddot{x} + C\dot{x} + Kx = F + \mu f_{fr} \; ,$$

7-4

where m, C and K are the system mass, damping coefficient and linear spring stiffness, respectively.

The forcing function, F, and f_{fr} are given in Section 7.2.2, and $\mu = -sign(\dot{x})$ is used to ensure the friction force is always acting against the direction of motion.
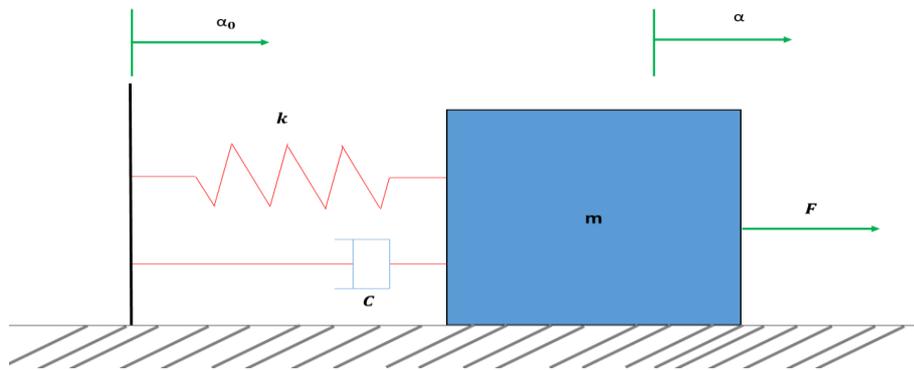
Figure 7-14: Single Degree of Freedom System (SDOF) laid on a rough surface.
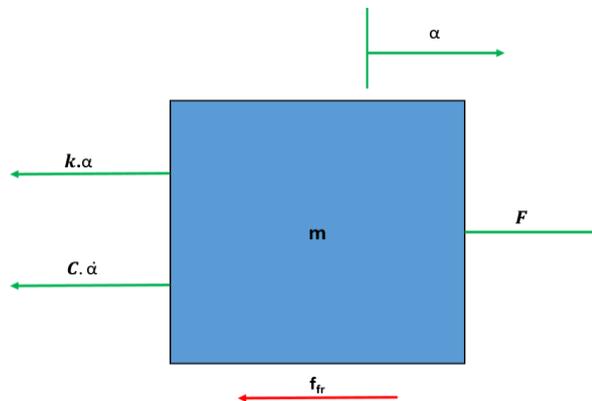
Figure 7-15: Free body diagram for the mass system.

7.2.4 Solution

The solution was derived numerically using a simple Euler iterative representation, where at iteration step number i, the acceleration of the mass, m, was calculated using:

$$\ddot{x}_i = \left(F_i + \mu_i f_{fr} - C\dot{x}_i - Kx_i\right)/m$$

7-5

Once the acceleration was calculated, the velocity at the next step number i+1 was calculated as per:

$$\dot{x}_{i+1} = \dot{x}_i + \ddot{x}_i \delta t$$

7-6

The displacement at step i+1 was calculated from:

$$x_{i+1} = x_i + \dot{x}_i \delta t$$

7-7

7.2.5 Results

In this section, two examples are shown to demonstrate the difference between walking or creeping and normal displacement. Figure 7-16 illustrates the forcing function used in the single degree of freedom system to displace the mass-spring system.
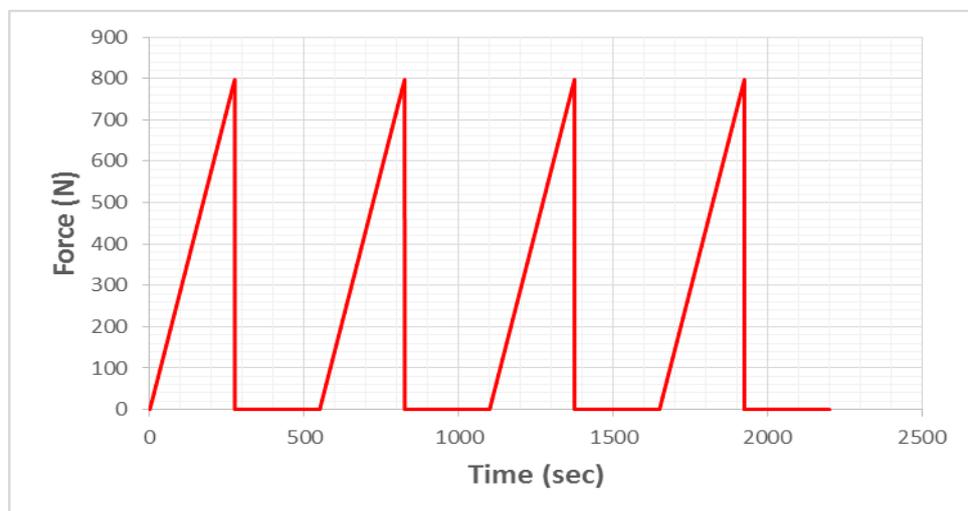
Figure 7-16: Forcing function used in this section.

Figure 7-17 highlights the displacement/time relation obtained by solving Equation 7-4 numerically. The input data in the two examples are adjusted to obtain the responses shown in Figure 7-17.

It can be seen from example-1 that the mass progressively displaces away from the original position due to the presence of the friction, the stiffness of the spring and the nature of the load. In example-2, the stiffness is increased to ensure that the mass always returns back to the original position. From the results, it can be seen that the mass in example-1 creeps or walks as time increases.
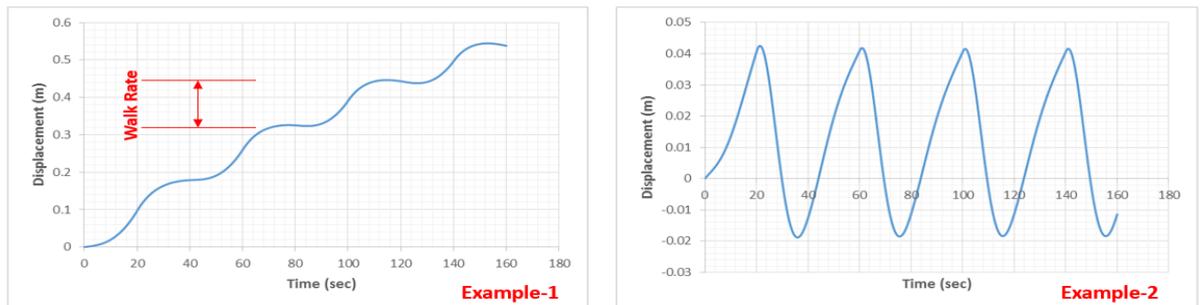
Figure 7-17: Displacement versus time relationship.

7.3   THEORETICAL MODEL

The mechanics of pipeline expansion is discussed in this section. Additionally,, the development of the analytical solution is also given. This solution is developed to validate the results from the finite element analysis.

7.3.1   Basic Equations

7.3.1.1   Effective Axial Force

The axial wall force (S_W) can be defined as the true axial force in the pipe. In other words, the true wall force is the integral of the axial stress over the cross-sectional area of the pipe. However, the effects of both internal and external pressure on the pipeline contribute to the structural response of the pipeline and this response is controlled by the effective axial force rather than the axial wall force. The effective axial force can be determined using:

252

$$S_{eff} = S_W + P_e \cdot A_0 - P_i \cdot A_i \qquad ,$$

where

S_{eff} : effective axial force (compression negative),

S_W : axial wall force (compression negative),

P_e : external pressure,

P_i : internal pressure,

A_0 : external area of pipe,

A_i : internal area of pipe.

The pressure induced axial force (S_P) can be calculated by:

$$S_P = P_e \cdot A_0 - P_i \cdot A_i$$

7-9

From Equation 7-9, it can be seen that the effective axial force is the summation of the pressure induced axial force and the pipe wall force. Based on the above, it can be seen that the pipe behaves as a beam loaded by a force equal to the effective axial force.

7.3.1.2   Fully Constrained Effective Axial Force

The model of a fully constrained pipe is normally used to describe a section of pipeline in which no axial movement takes place or where the axial strain is zero. The fully constrained force in the as-laid pipeline is given by DNVGL-ST-F101 (2017):

$$S_0 = T_{lay} - (1 - 2 \cdot \vartheta) \cdot (P_i - P_{iL}) \cdot A_i - EA.\alpha \cdot \Delta T \quad ,$$

7-10

where

S_0 : fully constrained force,

T_{lay} : lay tension,

ϑ : Poisson's ratio,

P_i : internal pressure,

P_{iL} : internal pressure during installation,

A_i : internal area of pipe,

EA : pipe axial stiffness,

ΔT : temperature change relative to the as-installed condition.

253

In any pipeline, the fully constraint force should be developed to guarantee that there is no change in strain in the pipeline, relative to the as-laid condition. Equation 7-10 indicates that the fully constrained force in the pipeline does not depend on the external pressure.

7.3.1.3 Axial Strain

The axial strain, ε_A, in a pipeline can be calculated from the effective axial force and the fully constrained effective axial force using the following equation:

$$\varepsilon_A = \frac{S_{eff} - S_0}{EA}$$

7-11

7.3.1.4 Axial Displacement

The axial displacement, $Y(x)$, at any point along the pipeline can be obtained by integrating the axial strain as shown below:

$$Y(x) = \int_{x2=V}^{x1} \varepsilon_A(x) \cdot dx$$

7-12

The integration should start from the nearest point of zero change in axial displacement (i.e. the virtual anchor point: $x_2 = v$).

7.3.2 Pipeline Expansion Analysis

The axial strain in the pipe can be obtained from Equation 7-12. The equation highlights that both the effective axial force and the fully constrained force are required to determine the axial strain. This section only considers the loading and unloading associated with pressure and temperature.

The fully constrained force in the pipe is normally calculated from the known operating conditions in terms of pressure and temperature, as highlighted in Equation

,

254

7-107-10. The effective axial force in the pipeline can be calculated using simple equilibrium concepts. At the end of a pipeline, the effective axial force is equal to the reaction provided by the end condition. If there is no reaction, then the effective axial force is zero. The effective force in the pipeline decreases (becomes more compressive) as the frictional restraint builds. The slope of the fully constrained profile is the axial pipe-soil restraint. It is important to highlight that the maximum effective force that can develop in the pipeline is the fully constrained effective force. This is simply because at this force the pipeline change in strain is zero.

The effective axial force in a short straight pipeline is shown in Figure 7-18a. In this context "short" means that there is insufficient length for the soil resistance to develop a full restraint in the middle of the pipeline and hence, there is no possibility for the pipeline to buckle laterally there.
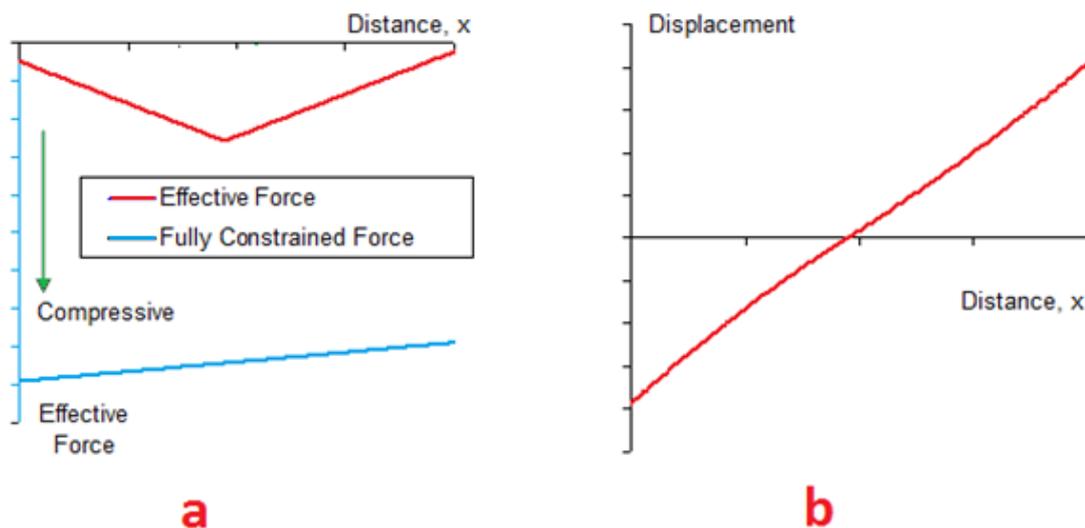
Figure 7-18: Effective axial force in a short pipeline, a) effective axial force profile, b) axial displacement.

The short pipeline has only one virtual anchor at the centre and expands from this point towards the ends. It is evident from Figure 7-18a that the maximum effective axial force is well below the fully constrained force. For the short pipeline, the effective axial force is controlled by the axial friction factor rather than the operating conditions. The axial friction factor and the pipe weight define the slope of the effective axial force.

255

In Figure 7-18a, a constant axial friction factor as well as constant submerged weight are assumed and the virtual anchor point is located at the middle of the pipeline. It should be noted that the virtual anchor point will not necessarily form exactly at the centre of the pipeline. Spool reaction, SCR tension combined with variable axial friction can all shift the virtual anchor point away from the centre.

If the pipeline has fixed ends, then the force in the pipeline will be the fully constrained force. The fully constrained force varies along the pipeline length. This is in part because the pressure and temperature tend to vary along the pipeline length.

Figure 7-18b highlights the axial displacement response along a short pipeline. It is evident that the pipeline expands from the virtual anchor point at the centre towards the free ends. The soil axial resistance opposes the pipeline expansion. Increasing the axial friction factor and the pipe weight result in a greater compressive force. This is due to the fact that frictional resistance increases until a maximum effective axial force is reached at the centre of the pipe. Beyond the centre of the pipe, the effective axial force becomes less compressive as illustrated in Figure 7-18a.
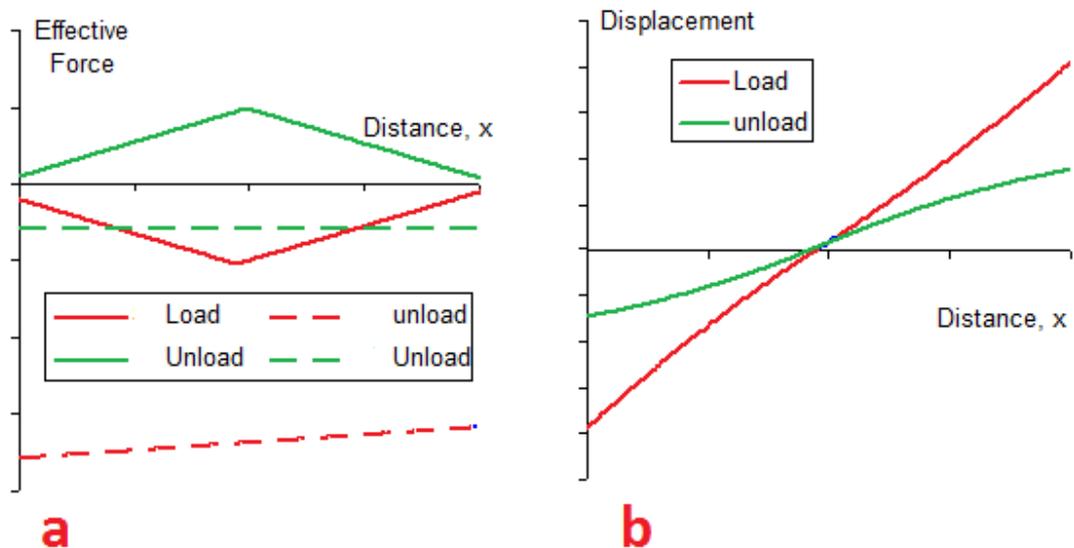
Figure 7-19: Effective axial force in a short pipeline during load/unload, a) effective axial force profile, b) axial displacement.

During unloading, the pipeline tends to contract rather than expand. Therefore, the soil friction resistance takes place in the opposite direction. Figure 7-19a shows the effective axial force during unloading .

Figure 7-19b shows the axial displacement along the pipeline during both loading and unloading. During unloading, the pipeline tends to reverse the slope of the effective axial force as indicated in Figure 7-19a and the pipe tends to contract. In spite of this, the pipeline does not return to zero or the original position as can be seen in Figure 7-19b.

Normally, the locations of the virtual anchor points during loading and unloading are different. There is an asymmetry in the pipeline force profile between loading and unloading.

7.4   FINITE ELEMENT FORMULATION

The pipeline model uses element PIPE31 in ABAQUS (2012). PIPE31 is a 2-node linear pipe element with 8 integration points around the circumference of the pipe. An element length of 1 m is employed in the model as this has been found to be sufficient in accurately modelling the walking behaviour.

The pipeline model presented is 2 km long from the transition point to the pipeline end termination (PLET). As shown in Figure 7-20, the pipeline is straight with no route bends or curves and with a global seabed slope of 2 degrees. The SCR is not modelled however the pipeline from the transition point to the PLET is modelled. The hot end of the pipeline is connected to the SCR while the cold end is connected to the PLET. The seabed slopes downhill towards the PLET. The seabed slope is modelled by adjusting the gravity vectors in the directions shown in Figure 7-20.

The operating cycles are modelled by applying start-up and shut-down transient temperature and pressure profiles as listed in Figure 7-21 and Table 7-2, respectively. Note that the temperature profiles presented in Figure 7-21 start at the pipeline inlet/ transition point.

Twenty-one temperature load/unload cycles were considered to quantify the rate of walking and expansions towards the SCR. The analysis considered the major factors that induce pipeline walking, namely: 1) SCR tension due to connecting the SCR at the hot end, 2) thermal transients associated with start-ups and shut-downs, and 3) seabed slope upon which the pipeline is laid. It is assumed that the pipeline will remain in operation during storm conditions.

257

Hereafter, nodes 1 and 2001 will refer to the transition point (hot end) and the cold end, respectively. While the tensions KP0 and KP 1160 will refer to the top tension and the SCR bottom tension, respectively.

A static analysis was undertaken and thus the inertial effects were not considered. As Carr et al. (2003) indicated, it is safe to assume that dynamic tension (short time scale) fluctuations can be ignored. This is in part because the duration of cool-down and start-up operations are expected to last several hours.

There is excellent agreement between the static and the dynamic analyses results when it comes to assessing the impact of SCR tension on pipeline end expansions and when determining the likely maximum anchor force, or the envelope of SCR loads on the anchor. However, dynamic analyses are required to assess the fatigue loading on SCR anchors due to SCR tension variations.

It should be noted that since SCR tension fluctuation is dynamic and cyclic, it will influence the axial friction response and raise concerns regarding drained versus undrained soil behaviour. The change in the axial friction response is complex and difficult to model accurately in the dynamic analysis of the SCR. Therefore, a static analysis is performed by applying the tension values given in Table 7-3 as a static load. It is important to keep in mind that in reality, the SCR tension is not constant but fluctuates with the hosting facility.

A nonlinear spring element (Spring-1) is used in the ABAQUS model to simulate the effect of an anchor. Spring-1 is an element with non-linear generalized force-deflection capabilities. The degree of freedom for this element is set to the translational nodal X direction (corresponding to pipeline axial direction). The reaction from the PLET is ignored. Refer to Table 7-4 for the anchor locations and configurations considered throughout this chapter.

The transition point is subjected to the bottom tension values presented in Table 7-3 for different load cases. This is to: 1) investigate the pipeline walking towards the SCR/PLET, 2) investigate the restraining force required to mitigate the expansion towards the SCR or towards the PLET, and 3) examine the optimal location to mitigate walking.
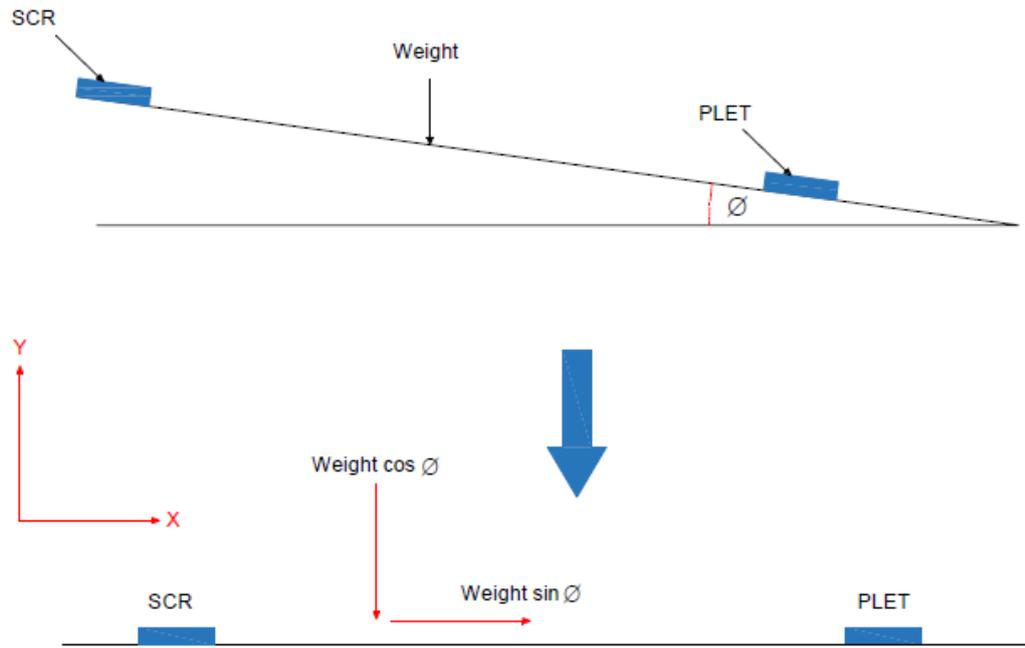
Figure 7-20: Seabed slope along the pipeline.
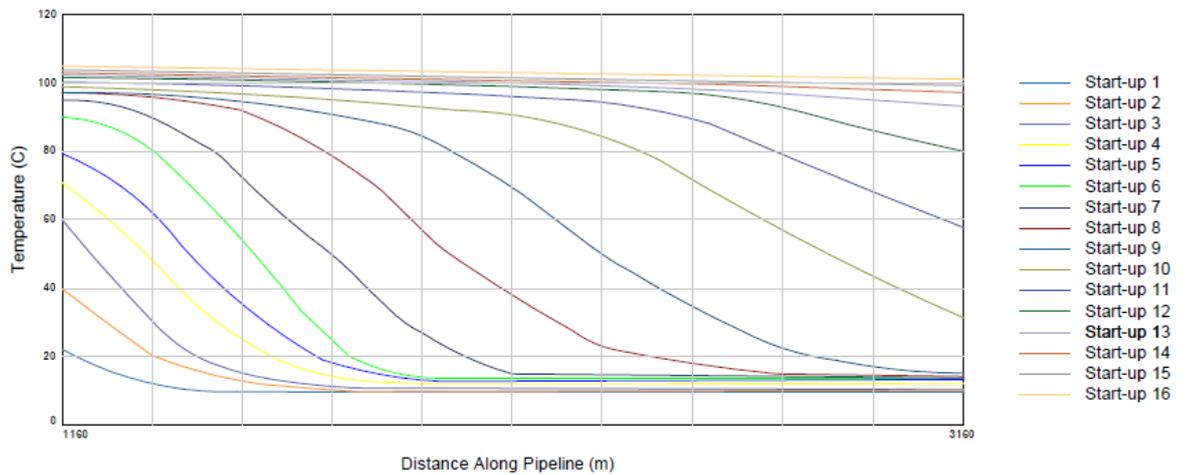
Figure 7-21: Full operating thermal cycles.

A bi-linear soil friction model, as shown in Figure 7-13 (Reda and Forbes, 2012), is employed to model the resistance exhibited by the soil on the pipeline axial movement, x.

259

7.4.1.1 Walking Direction Conventions

Figure 7-22 presents the walking direction conventions used throughout the finite element simulations.

Figure 7-22: Walking direction conventions.

7.4.1.2 Design Parameters

The pipeline and SCR physical data are listed in Table 7-2.

Table 7-2: Input Data.

Item	Value	Unit
Pipe outer diameter	mm	168
Pipe wall thickness	mm	18.3
Steel grade	-	DNV 450
Contents density	kg/m^3	200
Pipe dry weight	N/m	622.76
Pipe submerged weight	N/m	466.47
Ambient seabed temperature	°C	10
Pipeline internal pressure –load	MPa	34.5
Pipeline internal pressure –unload	MPa	21
Pipeline external pressure	MPa	10.05
Axial friction factor	--	0.4
Axial friction mobilization distance	mm	0.6

Note: At the end of the unloading condition, the pipeline internal pressure was equal to the "pipeline internal pressure (unloaded)" and the temperature exhibits the temperature profile (start-up 1), as shown in Figure 7-21 and Table 7-2.

7.4.2   SCR Tension

Table 7-3 highlights the effective tension values of different design cases.

Table 7-3: Effective Tension for SCR

Design Case	Vessel Position	Effective Tension (kN)	
		Top Tension	**at transition point**
Operating - 1-year storm	Near	234	90
	Far	690	233
Operating	Mean	60	156
Survival – 1000 year	Near	280	50
	Far	1759	677
	Lateral	1165	376

The tension values presented in Table 7-3 are obtained from the strength analyses at different load combinations. The load case selection should ensure that all aspects (from installation through to operation and accidental conditions) are considered in the SCR design.

7.5   ANCHOR LOCATION SELECTION CRITERIA

This section describes how the finite element package ABAQUS (2012) was used to determine the optimal SCR location considering the selection criteria. The cases considered in this section are as per Table 7-4. This section presents the criteria which must be considered during the design of the pipeline/SCR system to determine the requirements of holdback anchors.

The anchor types considered for limiting the pipeline expansion and walking are:

- **Unidirectional anchor:** This anchor allows axial movement in one direction only.

- **Bidirectional anchor:** This anchor limits axial movement in both directions.

Bidirectional anchors should be considered only when there is a potential for excessive walking in both pipeline directions.

There are different types of anchoring systems including anchor chain systems, rock dumping and structural anchors.

If pipeline walking is occurring then anchor chains connected to suction piles should be considered as a potential mitigation method as highlighted in Figure 7-23. This is because the anchor chain system is the most popular and proven technique for anchoring pipelines and SCRs. The chains prevent any movement in the anticipated walking direction, while still allowing expansion of the pipeline in one direction (unidirectional anchor). The piles should be sized to withstand the anticipated forces developed as a result of axial walking.

There are different types of piling systems including suction piles, driven piles, drilled or grouted piles, and plate anchors. However, suction piles, as shown in Figure 7-24, are the most popular option for mitigating pipeline walking in deep-water.
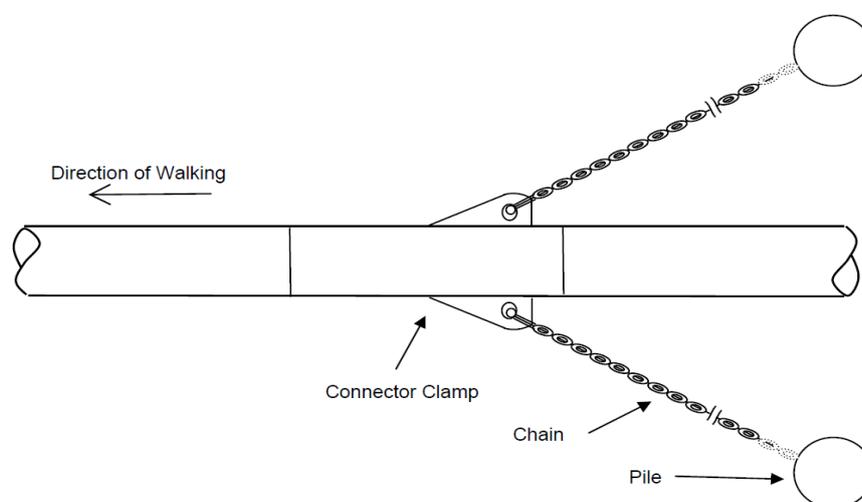
Figure 7-23: Anchor chain system concept.
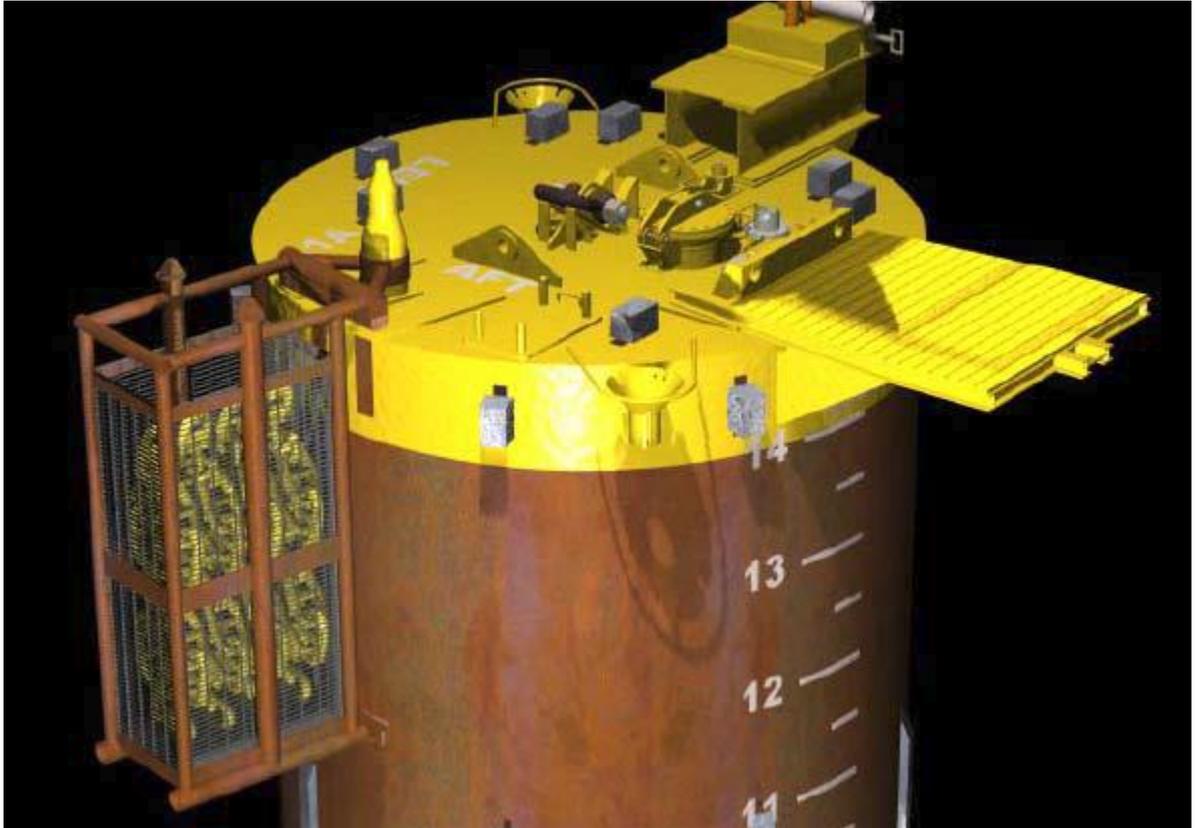
Figure 7-24: Suction pile (Colliard et al., 2006).

The optimal choice of anchor type, whether unidirectional or bidirectional, depends on the expansion and the walking behaviour of the pipeline.

The location of the anchor should be based on the following key criteria:

1- **SCR axial feed-in:** The total axial feed-in/displacement associated with the pipeline expansion and walking must be less than the SCR axial feed-in limit to ensure the integrity of the SCR is not compromised.

2- **PLET axial feed-in:** The total axial displacement of the pipeline towards the PLET should be limited to ensure the integrity of the spool is not compromised.

3- **Excessive SCR loads from the movement of the floating production facility:** It is recommended that the SCR anchor is located beyond the transition point to obviate the excessive vertical and lateral loads on the anchor. This is also to minimise the fatigue loading on the anchoring system, and possible cyclic loading and unloading of the soil around the anchor which may lead to a degradation in soil strength.

4- **Fatigue on the anchor components system due to SCR bottom fluctuations:** Fatigue is a relevant failure mode for most of the anchor structural components shown in Figure 7-23. This includes the pipeline collar (connector clamp) and the suction piles. Fatigue loading is influenced by applied stress ranges, number of stress cycles, component material, and connection geometry.

5- **Minimising the anchor loads:** Installing the anchor further downstream of the transition point, can assist in reducing the loads experienced by the anchor.

6- **Minimise the compressive load on the anchor:** This helps to minimise the buckling risk in the proximity of the anchor location.

7- **Minimise the extent of compression along pipeline:** Installing an anchor results in an increase in the compressive axial force in the pipeline and hence increases the probability of uncontrolled buckling along the pipeline.

8- **Installation constraints:** The pipeline anchor location should be selected to be compatible with the proposed pipeline installation methods. This includes considering that the floating production vessel may not be in place before the pipeline and the SCR are installed, and therefore the SCR will be wet-stored. It is easier to install anchors at the PLET side rather than at other positions along the pipeline (SCR transition point or mid-length). The effect of the dynamics of the SCR tension dampen-out as one moves away from the transition point of the SCR. Additionally, it may be easier to connect the anchor to a section of the pipeline not affected by SCR dynamics, depending on the proposed location of the pipeline anchor, and whether it is connected before or after the SCR hook-up to the floating facility.

7.5.1 Anchor Not Installed- Case 1

The incremental axial displacement (walking) presented in Figure 7-25 is based on static SCR tension. It can be seen that after 7 operating cycles, the total axial displacement towards the SCR reaches 5 m. This is beyond the design limit of the SCR. Hence, a hold-back anchor is required to avoid overstressing the spool between

the manifold and the PLET as well as to ensure that the integrity of the SCR is not compromised.
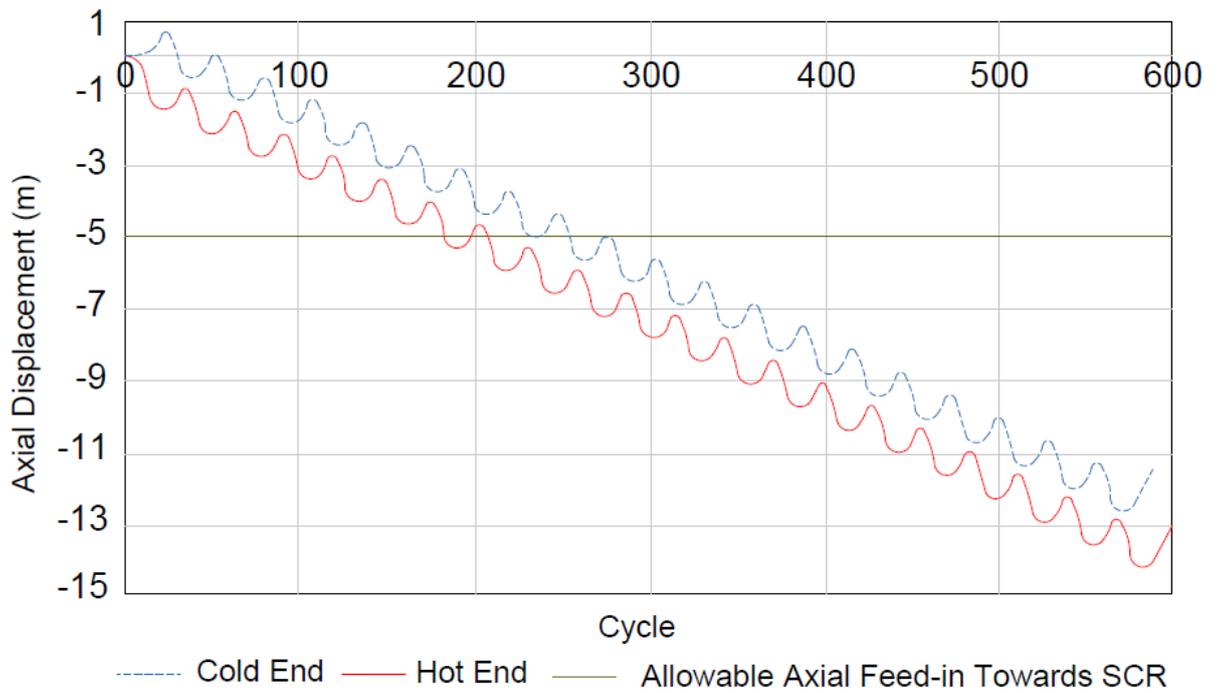
Figure 7-25: Axial displacement (walking) response vs. cycle: Case 1.

Table 7-4: Anchor Configuration

Section	Layout	Description
7.5.1		-Hold back anchor is not installed along the SCR-pipeline system.
7.5.2		-Unidirectional anchor is installed at PLET (Node-2001). - The pipeline expands towards the PLET and towards SCR. - No movement/walking towards SCR at anchor location.
7.5.3		-Bidirectional (full fixity) anchor is installed at PLET (Node-2001). - The pipeline expands towards SCR. - No movement/walking towards SCR or PLET at anchor location.

266

Section	Layout	Description
7.5.4	Node 1 Node-1001 Node-2001	-Unidirectional anchor is installed at mid-length of pipeline. -Pipeline expands towards PLET and SCR. -No movement/walking towards SCR at the anchor location.
7.5.5	Node 1 Node-1001 Node-2001	-Bidirectional anchor is installed at mid-length of pipeline. -Pipeline expands towards PLET and SCR. -No movement/walking towards SCR/PLET at the anchor location.
7.5.6	Node 1 Node-2001	-Unidirectional anchor is installed at the transition point (Node-1). -Pipeline expands towards PLET. -No movement/walking towards SCR at the anchor location.
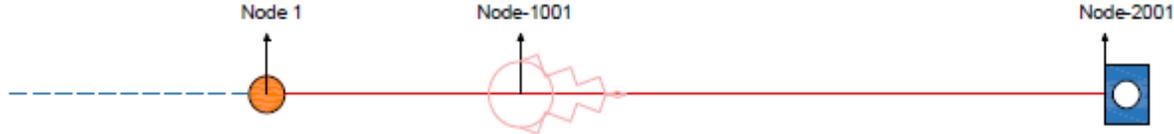
Section	Layout	Description
7.5.7		-Bidirectional anchor is installed at the transition point (Node-1). -Pipeline expands towards PLET. -No movement/walking towards SCR/PLET at the anchor location.

Key:

It is evident from Figure 7-25 that both ends (the one connected to the SCR and the one connected to the PLET) walk towards the SCR. This proves that walking due to SCR bottom tension is the dominant walking mechanism and can exceed the walking mechanisms associated with thermal transients and seabed slope, as illustrated in Figure 7-26.
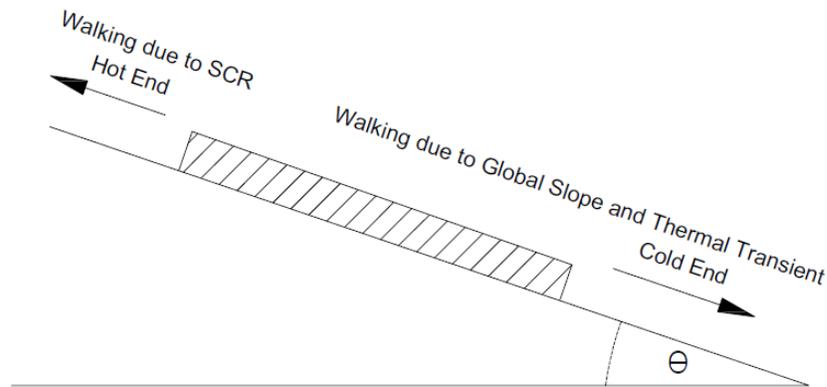
Figure 7-26: Walking directions: Case 1.

In conclusion, over several cycles, pipeline walking can lead to a significant global axial displacement of the pipeline, resulting in loss of SCR static tension and the overstressing of expansion spools and jumpers.

7.5.2   Unidirectional Anchor at PLET – Case 2

Figure 7-27 illustrates that during the "operating + static SCR tension" case, the end connected to the SCR expands towards the SCR while the other end expands towards the PLET or the anchor. The anchor does not provide any resistance to the pipeline movement towards the PLET. Therefore, the effective axial force as well as the force experienced by the anchor during this case, are both zero.

Figure 7-28 shows the effective axial force profile during the "unload + static SCR tension" case. It can be seen that initially, the pipeline contracts from both ends. Therefore, the expansion of the pipeline end connected to the PLET reduces and contracts away from

the uni-axial anchor. Over several cycles, the anchor will resist this contraction or movement and the force on the anchor gradually increases. In other words, in the initial unload case, the pipeline contracts but the effective force is not large enough to impose a load on the anchor. After a number of unloading cycles, the pipeline tends to walk towards the SCR and the force on the anchor increases gradually until it reaches its maximum value. By this time the anchor is fully activated and the force on the anchor is large enough to stop the walking towards the SCR.
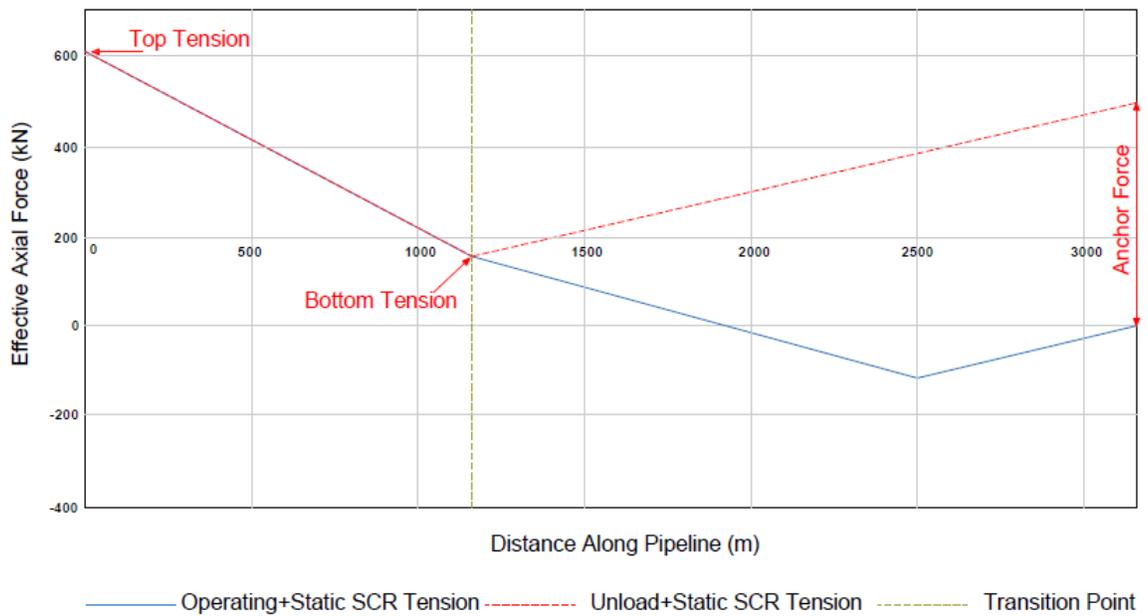
Figure 7-27: Effective axial force profile (operating and unload): Case 2.

Figure 7-29 shows that during the "operating + 1000 year far field tension" case, the bottom tension is too pronounced to be resisted by the axial soil resistance. In this case, the anchor is loaded, as shown in Figure 7-29, to prevent the pipeline walking towards the SCR.

The same figure illustrates that during the "operating + 1000 year near field tension" case, the SCR bottom tension reduces, resulting in contraction in length of the pipeline between the transition point to point A.

By examining Figure 7-27, Figure 7-28 and Figure 7-29, it can be seen that the maximum load on the anchor takes place during the unloading condition, not during the 1000 year

storm. It can be seen from the results that the load change on the anchor is cyclic. The anchor load associated with the 1000 year far tension is 300 kN while the anchor load associated with the unloading condition is 500 kN.

It is expected that the operational and unloading scenarios will take place several times during the lifespan of the pipeline. As such, the force on the anchor will fluctuate between zero and the maximum load at the start-up and shut-down and unloading scenarios respectively.

From Figure 7-30 and Figure 7-31, it can be seen that the pipeline at the end remote from the SCR (i.e. cold end) is free to expand. However, this end cannot expand towards the SCR because of the presence of the anchor. The maximum expansion towards the PLET is 0.71 m. This expansion takes place only during operation. The unidirectional anchor does not exert any compressive axial force. The maximum feed-in (expansion) towards the SCR is 2.77 m.
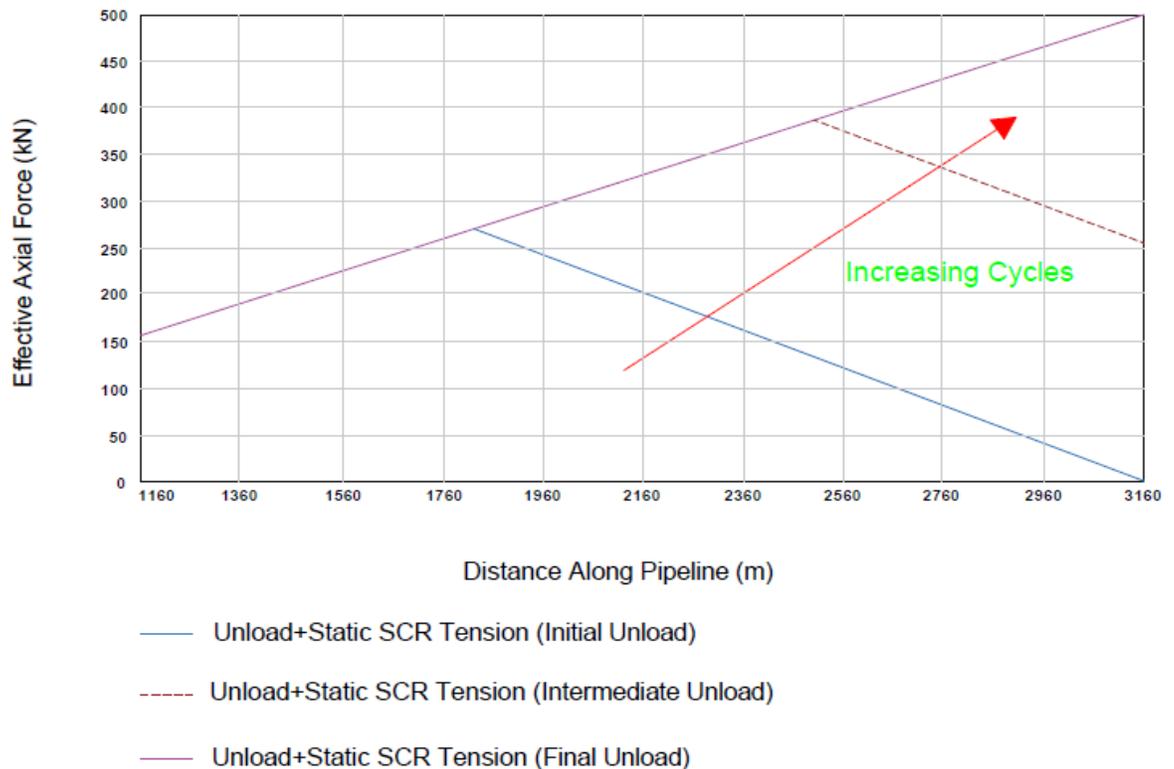
Figure 7-28: Effective axial force during unloading: Case 2.

271
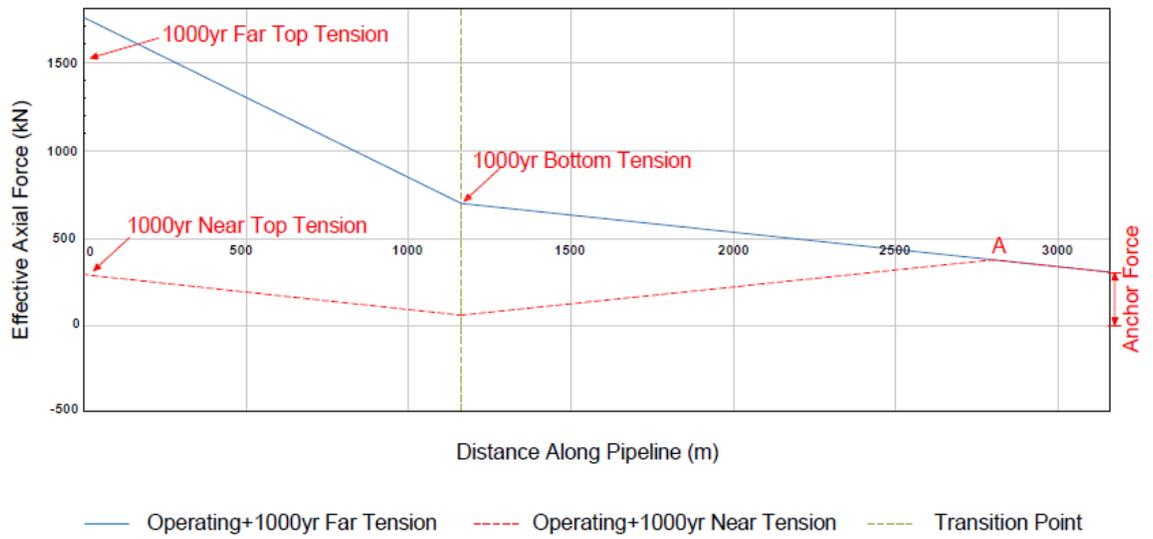
Figure 7-29: Effective axial force profile (1000 year): Case 2.
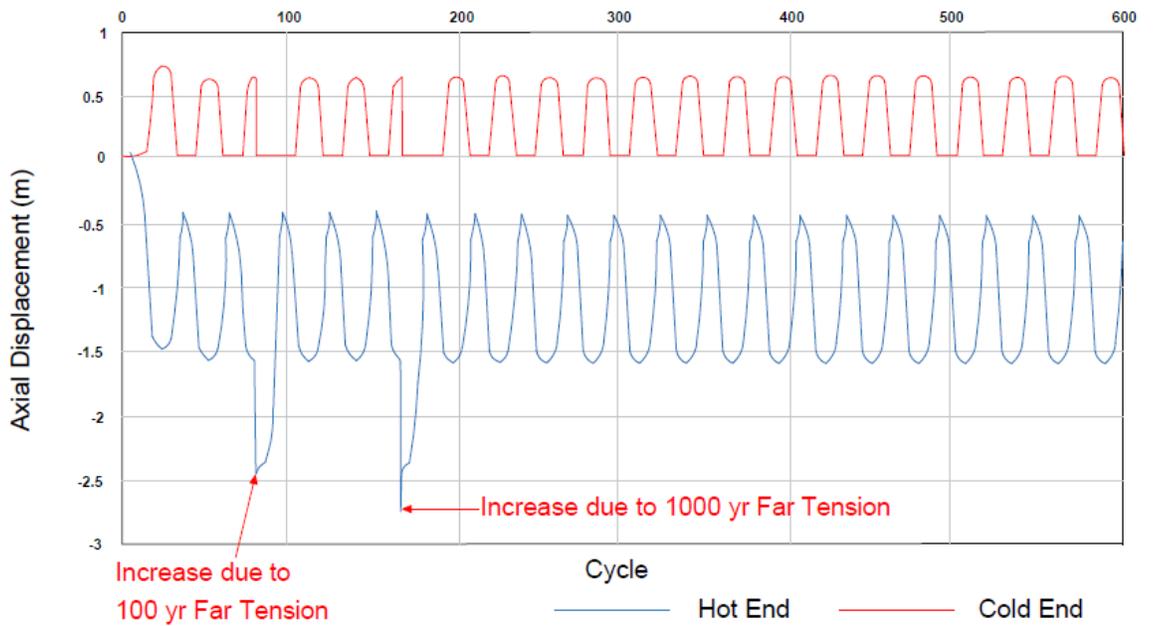
Figure 7-30: Axial displacement (walking) response vs. cycle: Case 2.

272
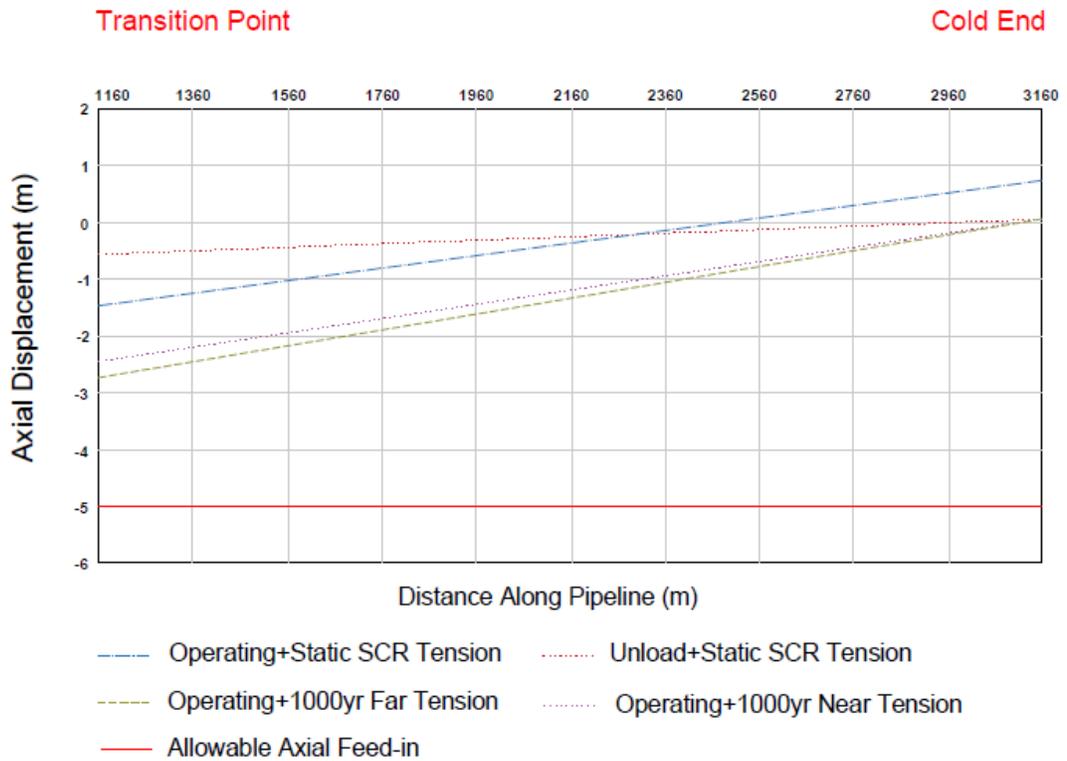
Figure 7-31: Axial Displacement along the pipeline: Case 2.

7.5.3 Bidirectional Axial Anchor at PLET – Case 3

Based on the results presented in Figure 7-32 and Figure 7-33, it can be seen that for the storm conditions and unloading conditions, the loads on the anchor are typical of the loads obtained when using an unidirectional anchor at the PLET. For normal conditions, the anchor experiences a compressive force. There is no expansion towards the PLET and the maximum feed-in towards the SCR is 2.77 m. Maximum loading on the anchor takes place during the unloading conditions not during the 1000-year storm. During normal operating cycles, the loads on the anchor fluctuate from compressive to tensile due to the operating and shut-down/unload conditions, respectively.

273
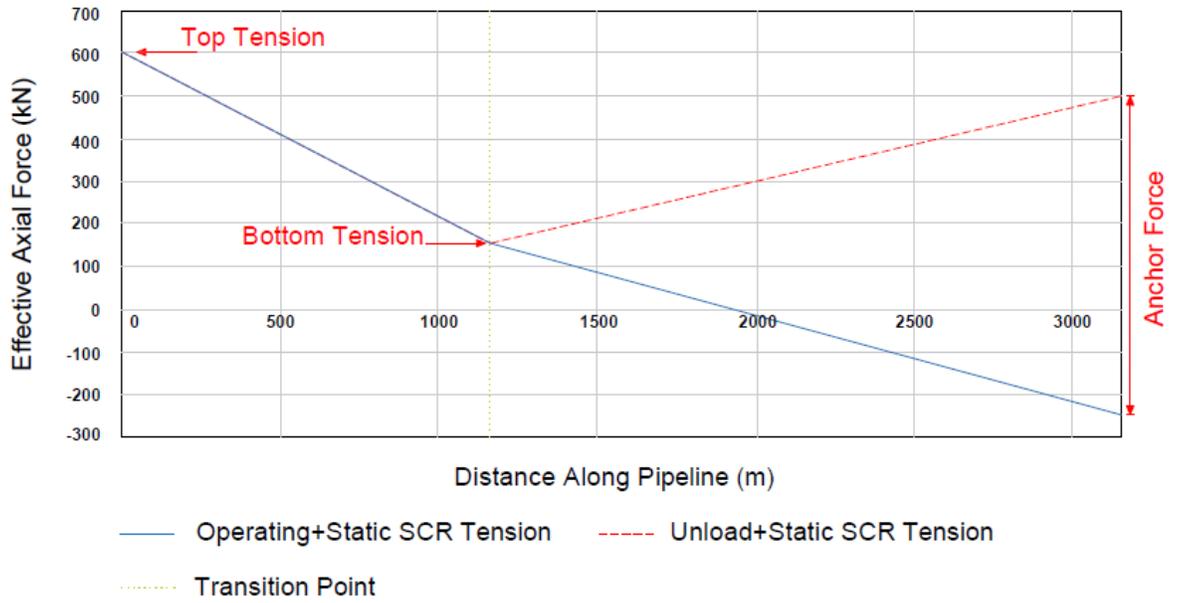
Figure 7-32: Effective axial force profile (operating and unload): Case 3.
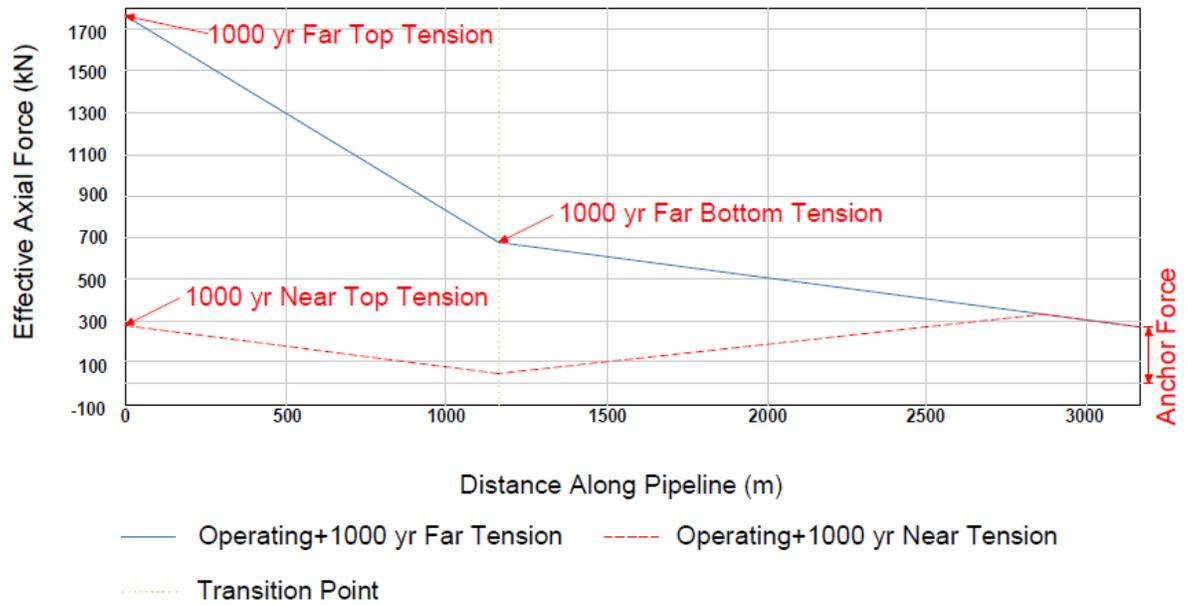
Figure 7-33: Effective axial force profile (1000 year): Case 3.

7.5.4 Mid-Line Unidirectional Anchor – Case 4

Based on the results presented in Figure 7-34 and Figure 7-35 for the unidirectional anchor installed at the middle of the pipeline, it can be seen that the maximum compressive force occurs at the anchor location. The area located upstream of the anchor is always in tension during the 1000-year storm event. The pipeline located upstream of the anchor expands towards the SCR, whereas the section located downstream from the anchor expands towards the PLET. The maximum axial feed-in towards the PLET and the SCR are 1.06 m and 1.46 m respectively. The maximum force on the anchor occurs during the 1000 year far field SCR tension.
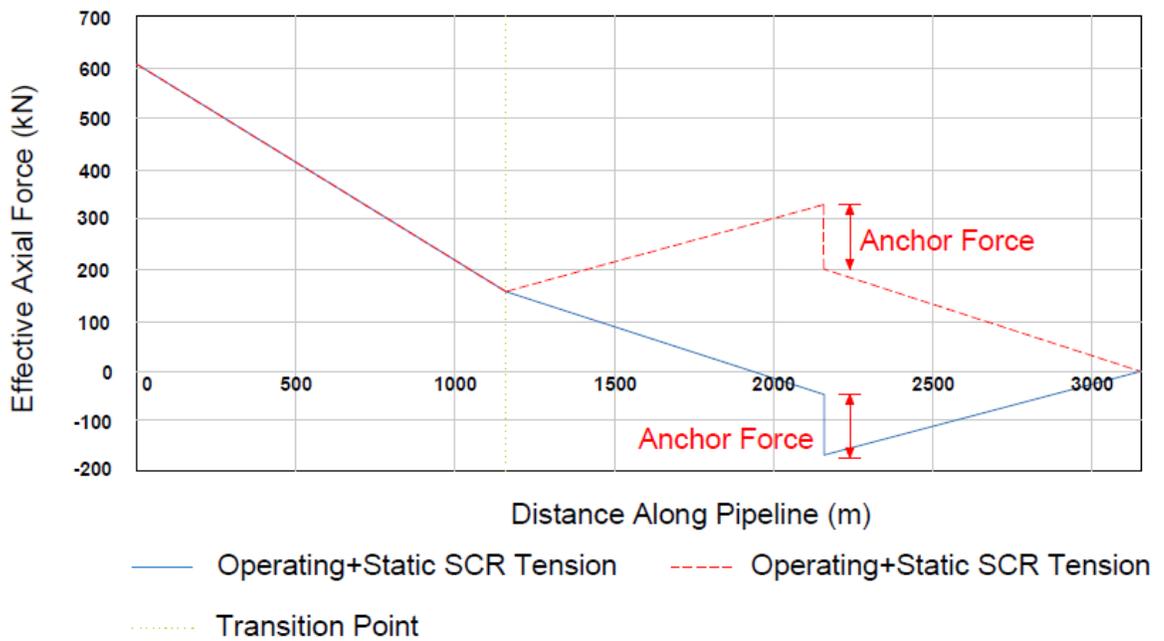
Figure 7-34: Effective axial force profile (operating and unload): Case 4.
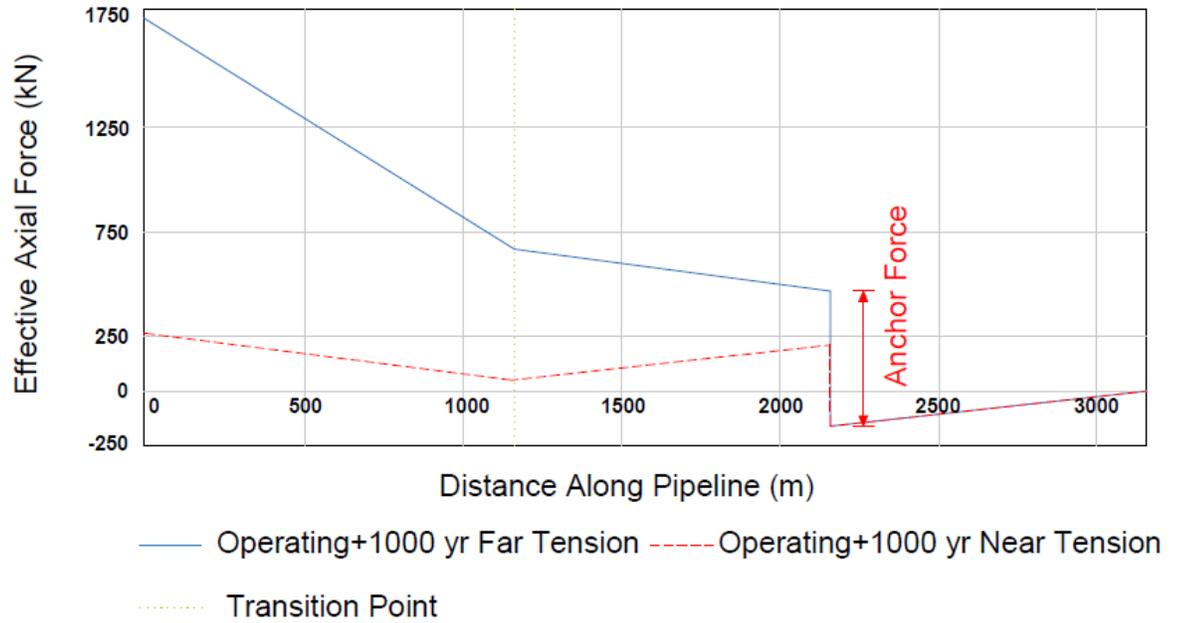
Figure 7-35: Effective axial force profile (1000 year): Case 4.

7.5.5   Mid-Line Bidirectional Anchor – Case 5

Based on the results presented in Figure 7-36 and Figure 7-37 for the bidirectional anchor installed at the middle of the pipeline, the following conclusions can be made: there is no benefit in using the bidirectional anchor at the mid-length. This is because the results are almost identical to those obtained when using the unidirectional anchor (Case 4).

276
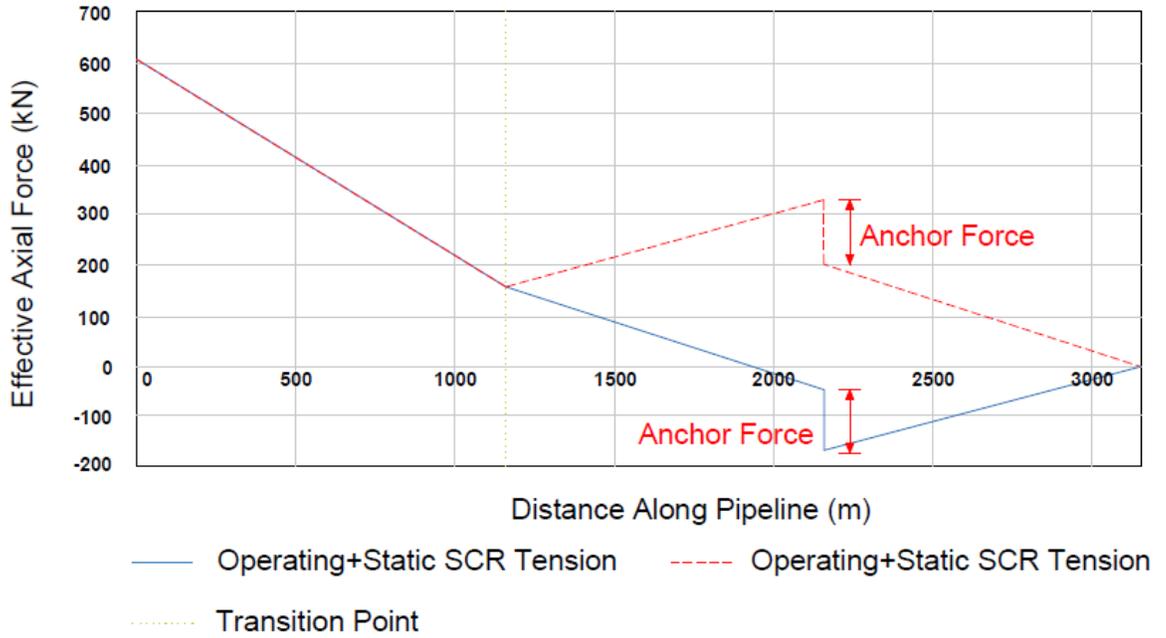
Figure 7-36: Effective axial force profile (operating and unload): Case 5.
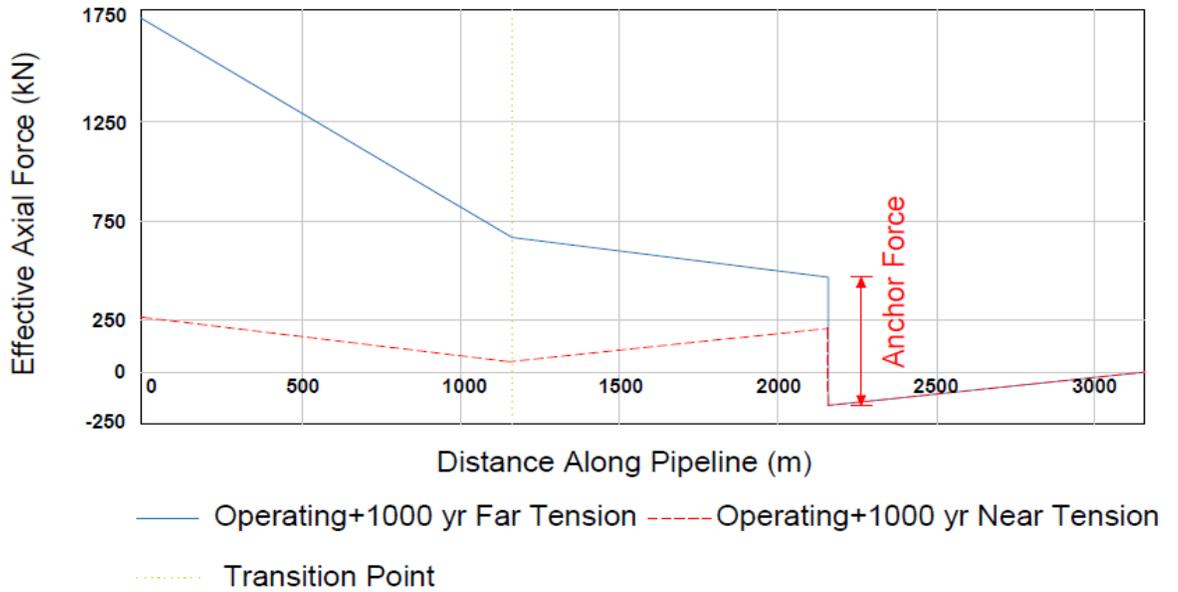
Figure 7-37: Effective axial force profile (1000 year): Case 5.

277

7.5.6 Unidirectional Anchor at Transition Point – Case 6

Based on the results presented in Figure 7-38 and Figure 7-39, compression occurs over the entire pipeline. This increases the risk of pipeline buckling. The maximum load on the anchor occurs during the 1000 year far field SCR tension. The maximum axial feed-in towards the PLET is 2.05 m.
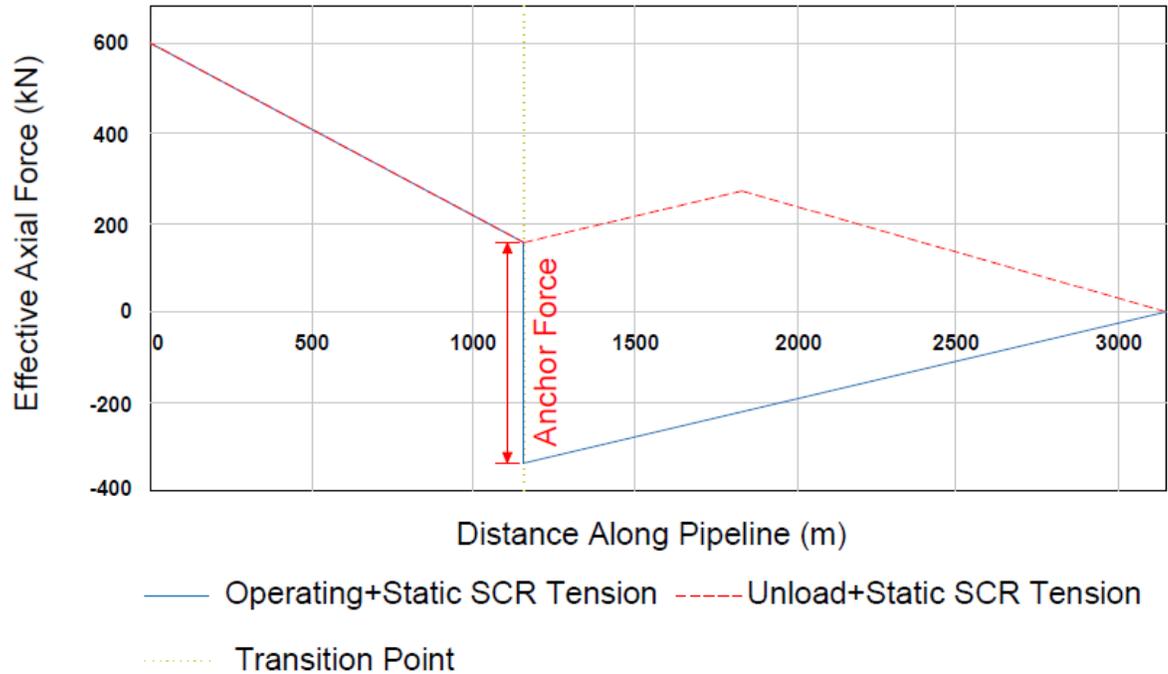
Figure 7-38: Effective axial force profile (operating and unload): Case 6.
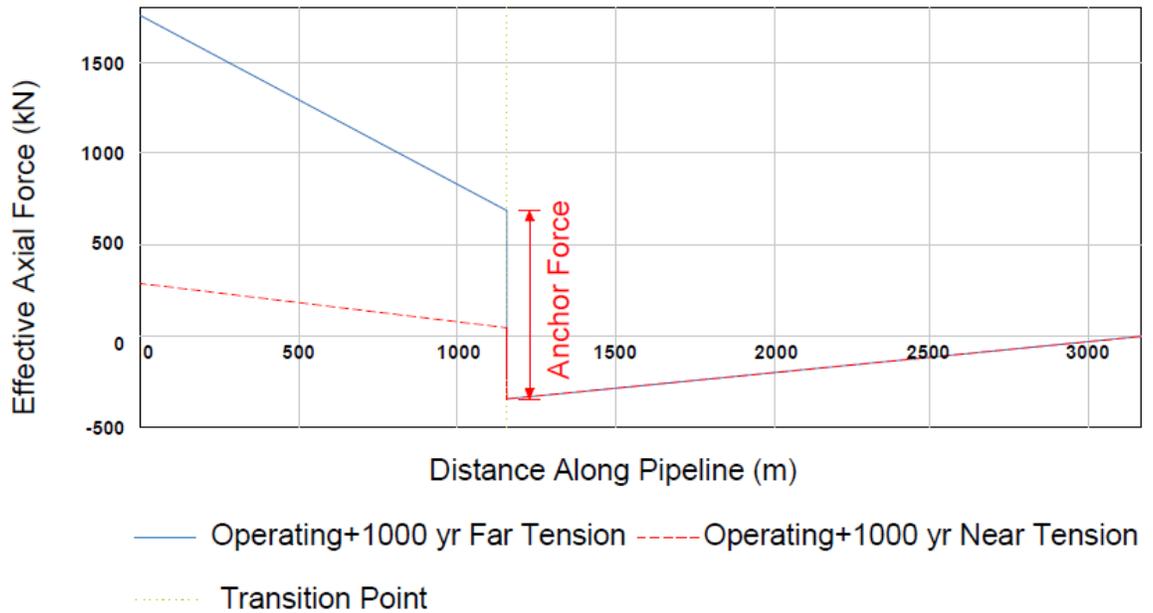
Figure 7-39: Effective axial force profile (1000 year): Case 6.

7.5.7 Bidirectional Anchor at Transition Point - Case 7

Based on the results shown in Figure 7-40 and Figure 7-41, it can be seen that there are no benefits of using the bidirectional anchor at the transition point. This is because the results are the same as those obtained when using the unidirectional anchor at the transition point. This is with the exception of the unloading force profile.
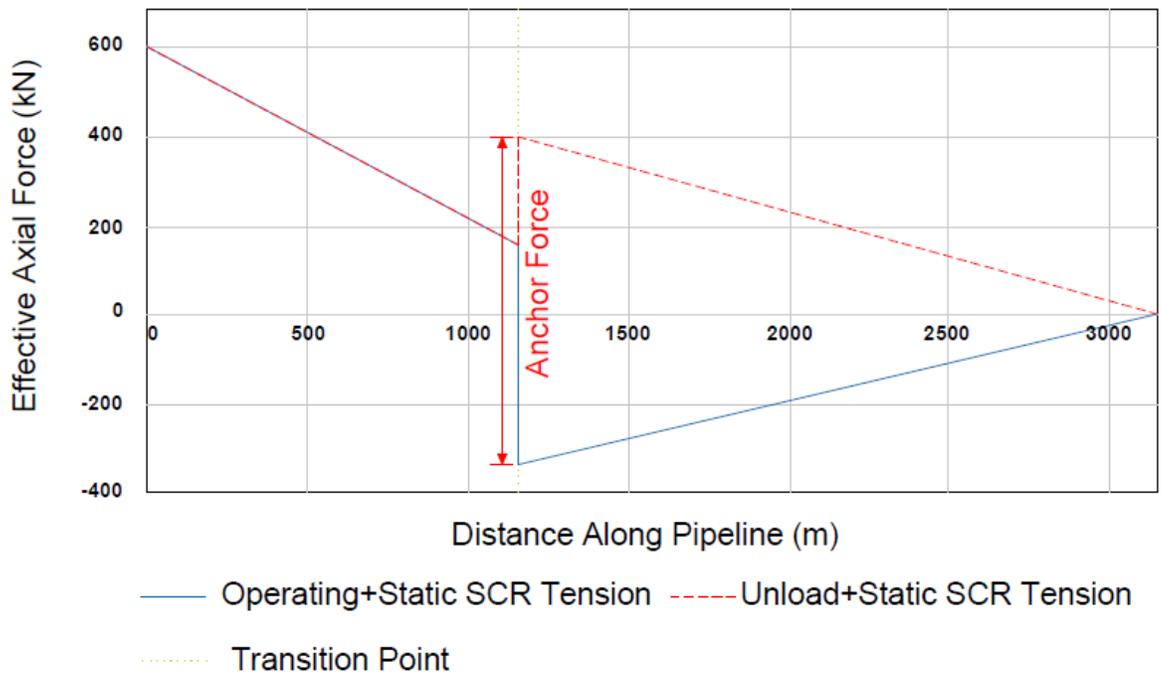
Figure 7-40: Effective axial force profile (operating ad unload): Case 7.
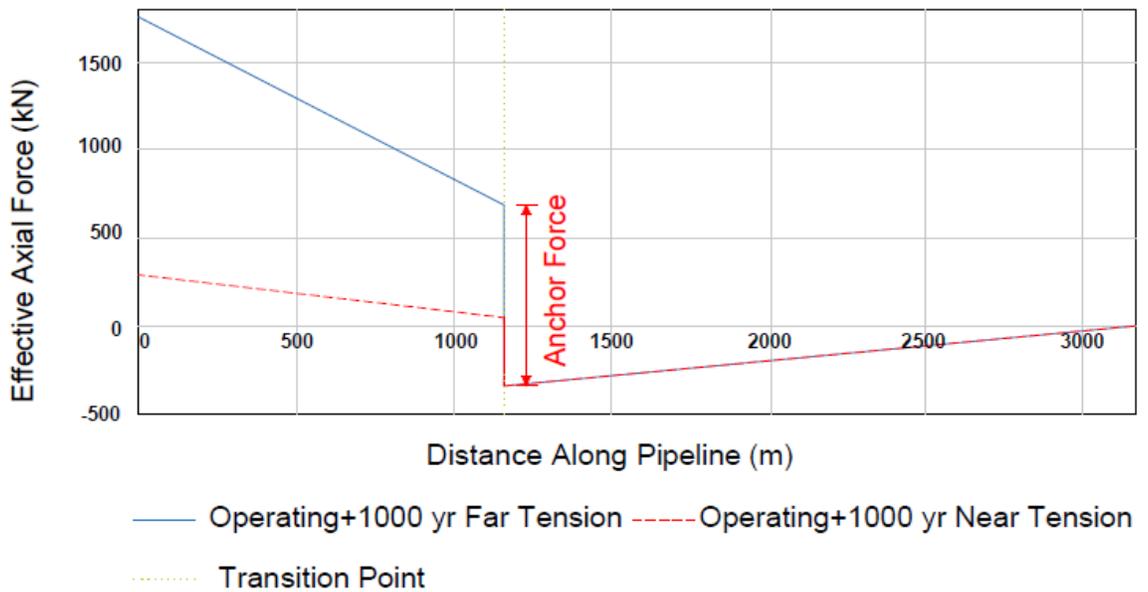
Figure 7-41: Effective axial force profile (1000 year): Case 7.

7.6 RESULTS

Table 7-5 rates each anchor configuration against the selection criteria. It should be noted that the scores here are based on the specific friction factors and pipeline dimensions used in this Chapter and may not be generalised to all cases. It is likely that some criteria, like SCR axial feed-in, PLET axial feed-in, extent of compression and anchor loads, will change with axial friction and pipeline properties. Observation of the total score for all criteria shows that unidirectional anchoring at the PLET gives the best anchoring results, with anchoring at the transition point giving the least favourable results. This cannot, however, be generalised to all pipelines, as there may situations where specific criteria may need to be adhered to during loading which results in pipeline walking, thus requiring pipeline anchoring.

Table 7-5: Anchor Location Selection Criteria

Criteria	PLET Unidirectional	PLET Bidirectional	Mid-Line Unidirectional	Mid-Line Bidirectional	SCR Unidirectional	SCR Bidirectional
SCR axial feed-in (m)	2.77	2.77	1.46	1.46	0	0
PLET axial feed-in	0.71	0	1.06	1.06	2.05	2.05
Impact of the movement of floating production vessel on the anchoring system	Low	Low	Medium	Medium	High	High
Fatigue on the anchor components system due to SCR	Low	Low	Medium	Medium	High	High

Criteria	PLET Unidirectional	PLET Bidirectional	Mid-Line Unidirectional	Mid-Line Bidirectional	SCR Unidirectional	SCR Bidirectional
bottom fluctuations						
Maximum anchor load (kN)	500[1]	750[2]	630[3]	630[4]	984[5]	984[6]
Location of maximum compressive effective axial force	Upstream the anchor	At Anchor	At Anchor	At Anchor	At Anchor	At Anchor
Buckling in the proximity of anchor	Low	Medium	Medium	Medium	Medium	Medium
Extent of compressive effective axial force (m)	1350	1350	1350	1350	2000	2000
Ease of installation of anchor	Easy (PLET can be attached by chains to suction Pile)	Medium	Medium	Medium	High	High
Hold-back anchor can be used as pipeline initiation	Can be used as an initiation for pipelay	Can be used as an initiation for pipelay	Cannot be used as initiation point	Cannot be used as initiation point	Cannot be used as initiation point	Cannot be used as initiation point
Total Score	**46**	**34**	**21**	**21**	**15**	**15**

Note: (Green = 5, Orange= 2, Red=1)

Notes:

1- Obtained from Figure 7-27.

2- Obtained from Figure 7-32.

3- Obtained from Figure 7-35.

4- Obtained from Figure 7-37.

5- Obtained from Figure 7-39.

6- Obtained from Figure 7-41.

8 Chapter-8 – Paper No. 6

Title: **"When is a subsea anchor required for a short pipeline/SCR system?"**

Authors: **Ahmed Reda, Kristoffer K. McKee, Ian M. Howard, Ibrahim A. Sultan**

Journal: **International Journal of Pressure Vessels and Piping**

8.1 STEEL CATENARY RISER

As indicated by Reda et al. (2018, p. 71-85) and Reda et al. (2019, p. 278-298), a floating production vessel on which an SCR is supported will be subject to excursions that are caused by environmental loads and influenced by the mooring system and other risers. Horizontal movement of the floating production vessel causes changes in the riser catenary configuration, which necessitate proper analysis for the riser in near, mean and far conditions, as shown in Figure 8-1.
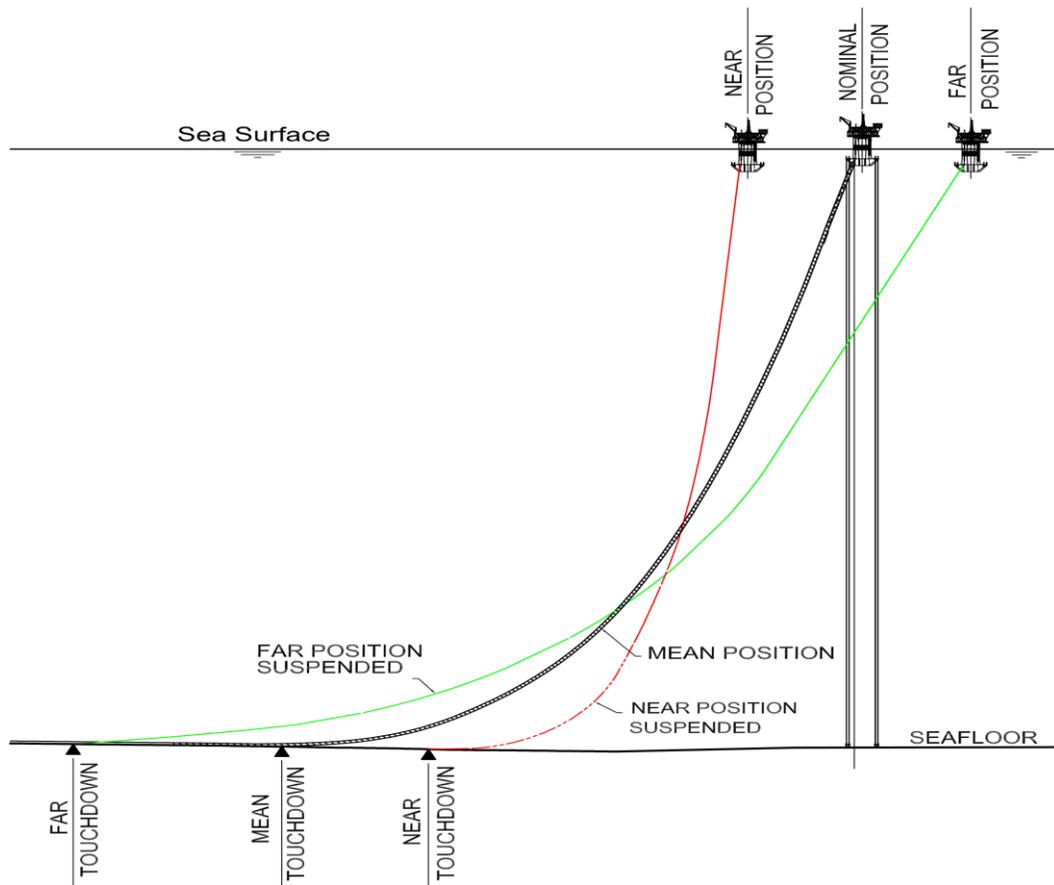
Figure 8-1: SCR configuration associated with vessel excursions.

8.2 VALIDATION AND SENSITIVITIES

This section presents the analysis undertaken to validate the finite element (FE) results against the analytical solutions presented in Subsection 8.2.1. Additionally, sensitivity assessments are undertaken to ensure the FE model behaves consistently.

8.2.1 Derivation of Force Response

For a short pipeline, the effective axial force is governed by seabed friction. The effective force profile during loading and unloading is shown in Figure 8-2. At the end of the pipeline, the effective axial force is equal to the reaction provided by the end condition.
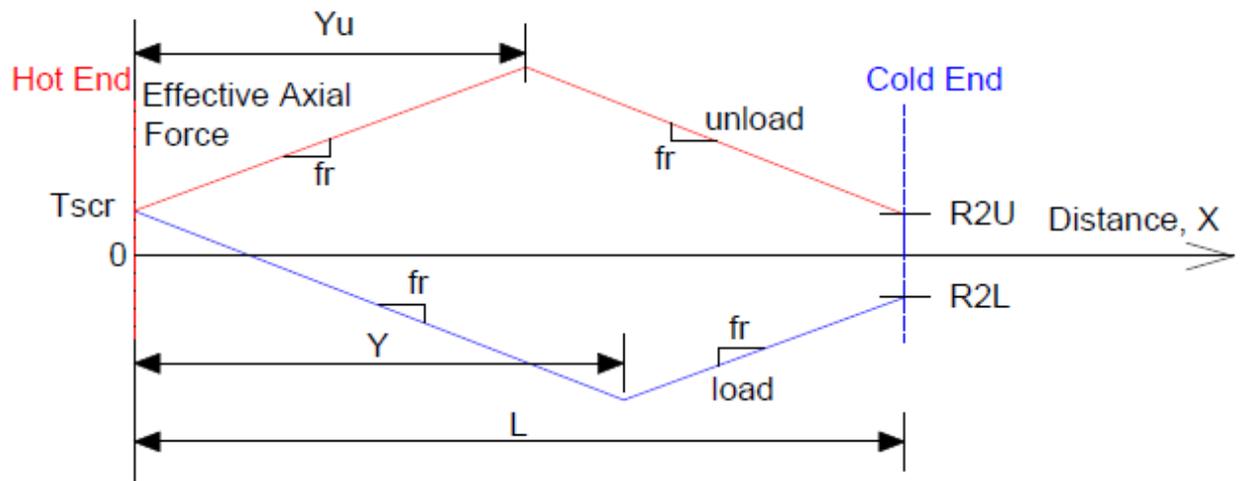
Figure 8-2: Effective axial force profile during load/unload conditions.

In the example illustrated in Figure 8-2, the hot end is connected to a steel catenary riser with static tension, Tscr, while the cold end is connected to a spool with end reaction R2L. During the loading condition, the effective axial force in the pipeline is calculated at the state of equilibrium using the following equation:

$$S_{eff} = \begin{cases} Tscr - fr \cdot x & x \le Y \\ -R2L - fr \cdot (L - x) & x > Y \end{cases} ,$$

8-1

286

where fr is the axial pipe soil resistance. The location of the virtual anchor point, Y, can be determined by the following:

$$Y = \frac{L}{2} + \frac{Tscr - R1L}{2 \cdot fr} \quad .$$

For the unloading condition, the effective axial force is determined using the following equation:

$$S_{eff} = \begin{cases} Tscr + fr \cdot x & x \leq Yu \\ R2U + fr \cdot (L - x) & x > Yu \end{cases} ,$$

where R2U is the spool reaction during unloading.

The location of the virtual anchor point during unloading can be determined by the following:

$$Yu = \frac{L}{2} + \frac{Tscr - R1U}{2 \cdot fr} \quad .$$

8.2.2   Pipeline Elastic Route Stability

Consider a curved element of pipeline on the seabed subject to the bottom tension associated with pipelay.
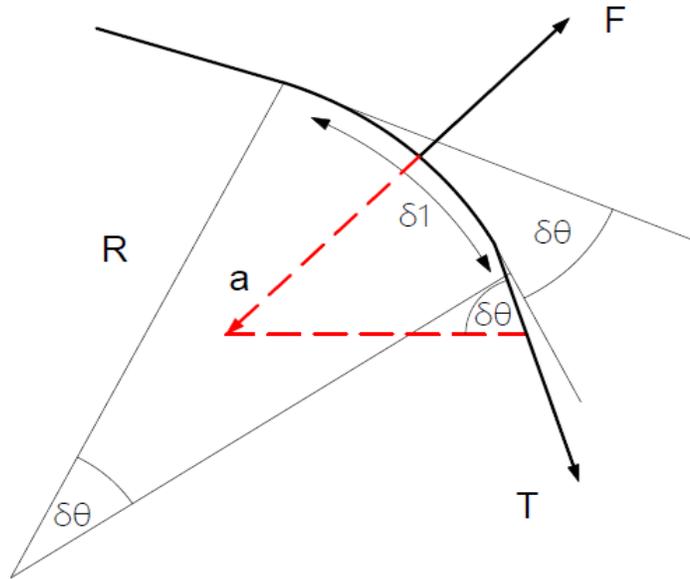
Figure 8-3: Force balance on a curved pipeline element.

The component of the tension force normal to the pipeline a is counteracted by the lateral friction, F.

The frictional force is given by:

$$F = \mu.W_S.\delta l.$$

<div align="right">8-5</div>

Resolving the tension, T, to find the component normal to the pipeline gives:

$$a = T.tan\ \delta\theta.$$

<div align="right">8-6</div>

For stability: F > a,

$$\mu.W_S.\delta l > T.tan\delta\theta,$$

<div align="right">8-7</div>

288

$$tan\delta\theta \approx \frac{\delta l}{R},$$

<div align="right">8-8</div>

$$\mu.W_S.\delta l > T.\frac{\delta l}{R}.$$

<div align="right">8-9</div>

Therefore, the radius of curvature, R, should exceed the value given by Equation 8-10:

$$R > \frac{T}{\mu.W_S},$$

<div align="right">8-10</div>

where:

F: frictional force,

Ws: submerged weight of the pipeline per unit length,

μ : coefficient of lateral friction,

T: pipeline bottom tension,

A: component of tension force normal to the pipeline,

$\delta\theta$: angle,

R: radius of curvature,

l: length of pipeline element.

8.3   FINITE ELEMENT MODEL

This section describes how the finite element package ABAQUS (2012) was used in the simulation and numerical analysis discussed in this Chapter. The parameters used in each finite element simulation are presented in Table 8-1.

The pipeline is modelled using ABAQUS PIPE31H element. The following is a list of the assumptions implemented in the finite element models:

289

1. An element length of 1 m is employed in the model. This has been found to be sufficient in accurately modelling walking behaviour.

2. The interaction between the pipe elements and the seabed is modelled as a soft, frictional contact, with decoupled axial and lateral friction. The frictional contact response is modelled in the FE analyses using a user defined subroutine that implements the non-linear monotonic response.

3. The pipe-soil interaction in the axial and lateral directions are defined using a bilinear model as illustrated in Figure 8-4, with a constant friction factor once the mobilization displacement is reached.

4. The hot end of the pipeline is connected to the SCR, while the cold end is connected to the PLET.

5. In some cases, as per Table 8-1, the pipeline is modelled as a straight segment, with no route bend or curve and with a global seabed slope of 2 degrees, as illustrated in Figure 8-5. The same figure highlights that the seabed is running down to the PLET. It also shows that the slope seabed is modelled by adjusting the gravity vectors in the direction shown in the figure.

6. In some cases, as per Table 8-1, thermal transients are modelled by applying start up and shut-down pressures and temperatures as shown in Figure 7-21.

7. The reaction of the PLET is ignored.

8. The finite element analyses undertaken are for static conditions.
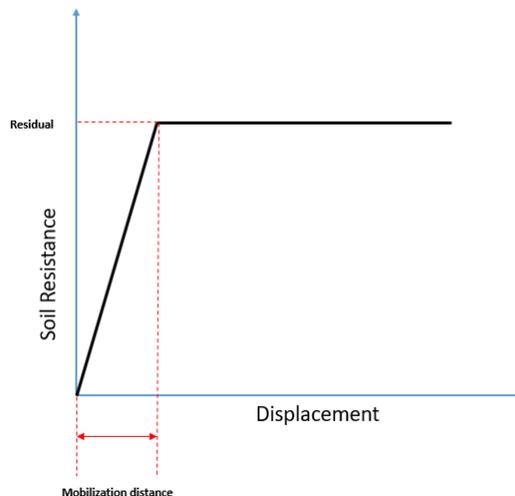
Figure 8-4: Bilinear model.
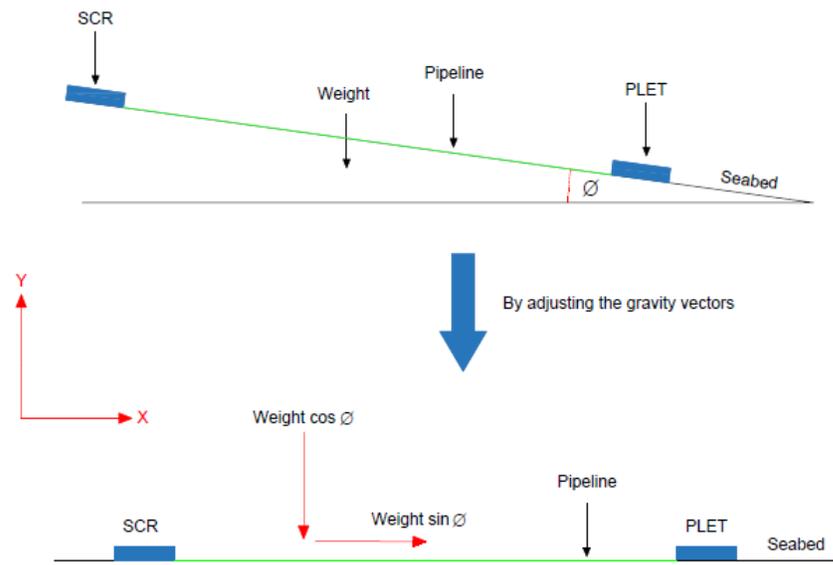
Figure 8-5: Seabed slope along the pipeline.
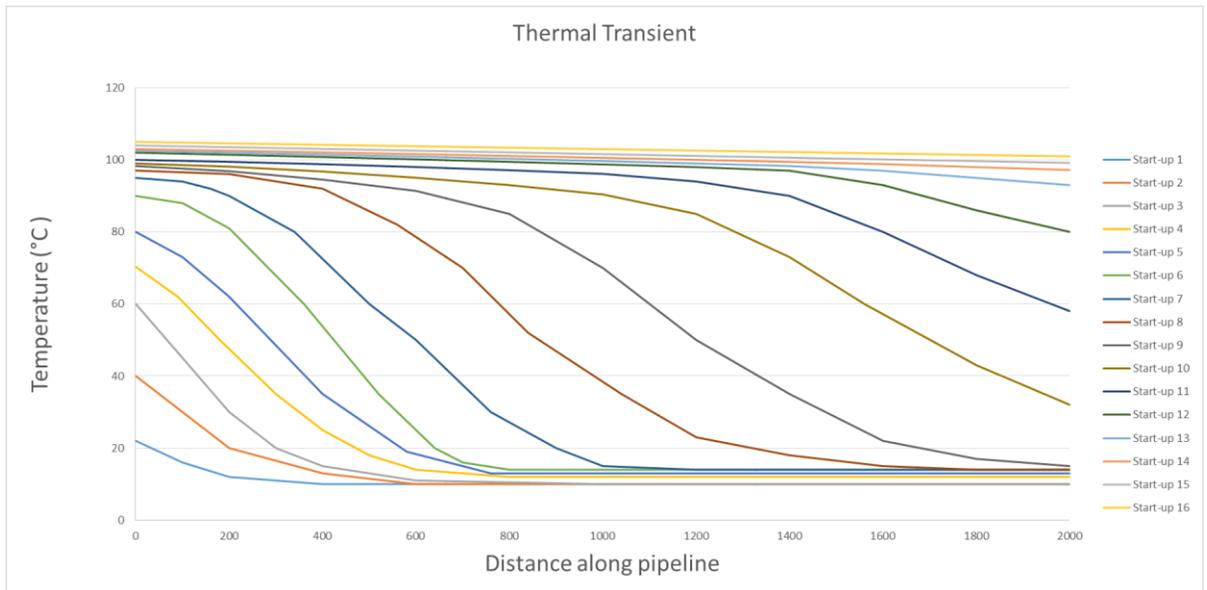
Figure 8-6: Full operating thermal cycles.

291

Table 8-1: Parameters Used in the Finite Element Simulations

	Section 3.4	Section 3.5	Section 4.1	Section 4.2	Section 4.3	Section 4.4
Seabed considered	Flat	Flat	Flat	Flat	Flat	Flat
Global slope	No	2 degrees slope	No	No	No	No
Transient considered	No	Yes	No	No	Yes	Yes
Straight pipe	Yes	Yes	Yes	No	No	Yes
Route curve	No	No	No	Yes	Yes	No

8.3.1   Comparison Between the Theoretical Solution and Finite Element Results

8.3.1.1   Effective Axial Force during Normal Operation

The finite element model used in this section is presented in Figure 8-7. The hosting vessel is connected to the pipeline via the SCR. In this example, the seabed is modelled as a flat surface.

The pipeline is 2 km long and is assumed to be straight, with no route bend or curve. The hot end is the end connected to the hosting vessel via the SCR and the cold end is free/PLET. The reaction of the PLET is ignored.
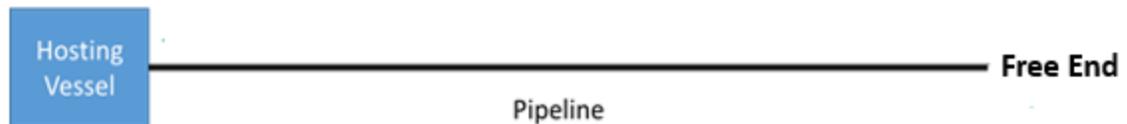
Figure 8-7: Model used in this section.

In this section, the effective axial force profile and displacement determined from the finite element is compared against the analytical solution derived using the methodology presented in Section 8.2.

Figure 8-8 shows the numerical (finite element) and analytical predictions for the effective axial force distribution along the pipeline segment. It is clear to see that the two methods are in excellent agreement. Note that points A and B on Figure 8-8 and Figure 8-9 refer to the virtual anchor points. Both the finite element model and analytical solution show that the pipeline is under the effect of the SCR tension between the SCR (distance = 0 m) and point C. The force distribution, shown in Figure 8-9, is associated with expansion from point B towards the SCR and expansion from point B towards the PLET/free end.

To validate the finite element model, the effective axial force at the cold end was checked. As can be seen from Figure 8-9, both the finite element model and analytical solution predict a net zero effective axial force at the free end. The effective axial force profile is dependent on the axial friction coefficient and the value of the SCR tension. Note that the anchor point A is not located at the centre of the pipeline. Point A is located after the mid-length of the pipeline towards the free end. This is due in part to the presence of the SCR tension.
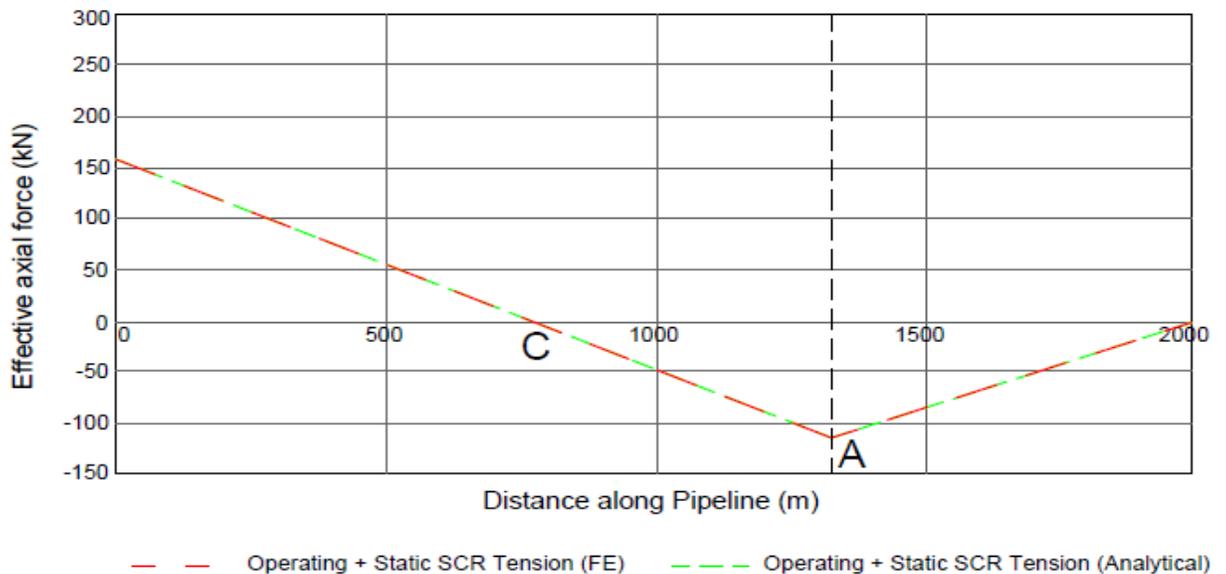
Figure 8-8: Effective axial force profile along the pipeline.
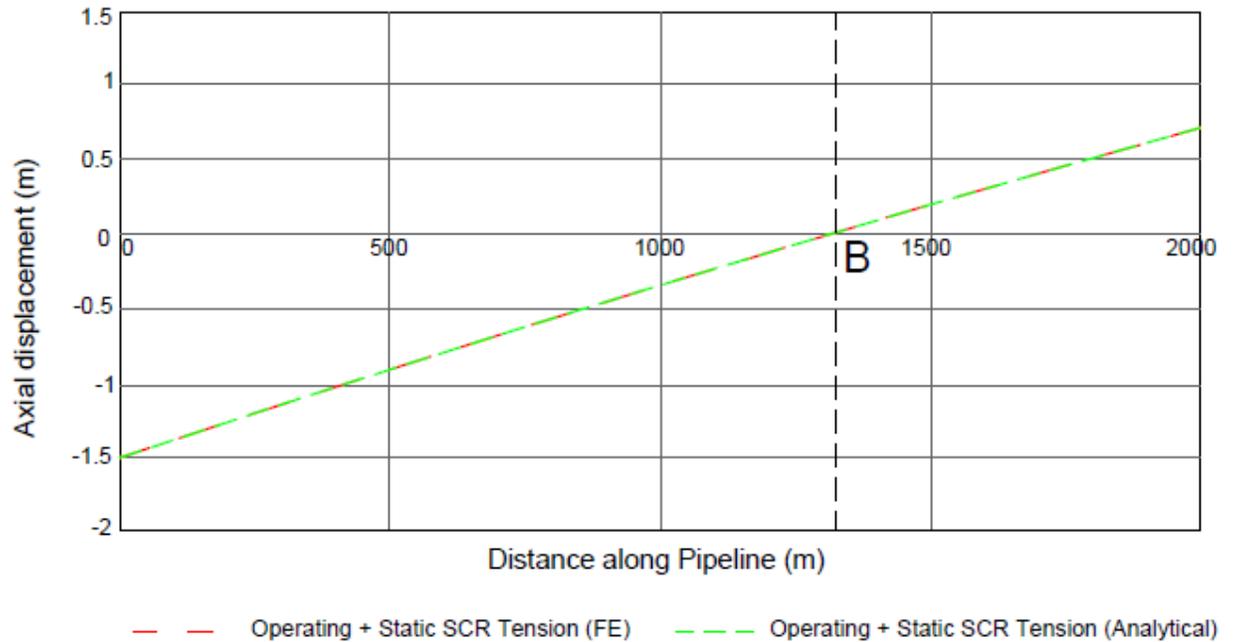
Figure 8-9: Axial displacement along the pipeline.

8.3.1.2 *Effective Axial Force during Normal Operation and Unloading: No Anchor*

To validate the effective axial force during both loading and unloading scenarios, the finite element model presented in Figure 8-7 was used, with the results given in Figure 8-10. Excellent agreement between the finite element model and the analytical solution is evident from the figure. Figure 8-10 also shows that during operation, anchor point A moves away from the SCR/hot end, and this behaviour reverses for anchor point B during unloading. Eventually, points A and B move away from the middle of the pipeline due to the action of the SCR tension force (asymmetrical load profile) and the asymmetric boundary conditions.
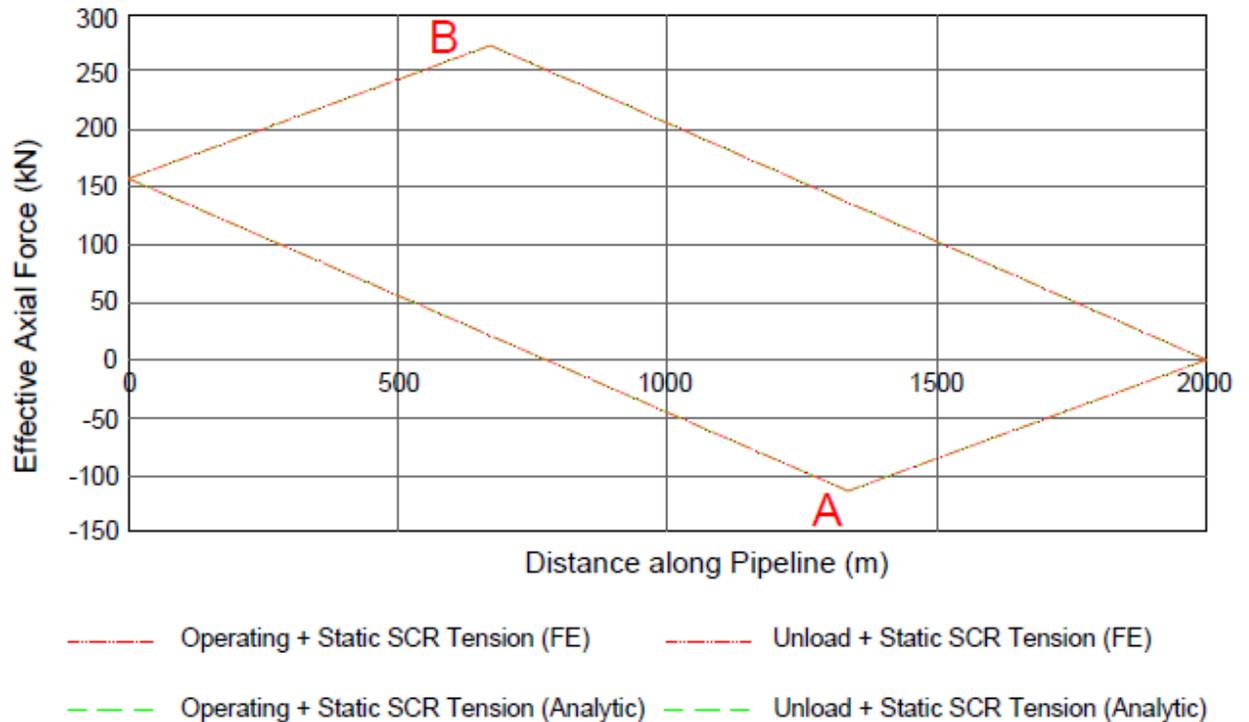
Figure 8-10: Effective axial force profile - Load/unload.

8.3.1.3   *Pipeline Response – During Normal Operation and a 1-year Storm*

Figure 8-11 predicts the effective axial force during a 1-year storm in the far field and the near field positions. During the far field position, the SCR bottom tension is resisted by the soil. In this case the anchor point A moves towards point F, resulting in a longer segment of the pipeline expanding towards the SCR. On the other hand, the SCR tension drops under near field storm positions, resulting in a contracted length of pipeline between KP0 and point N. The contraction causes the soil axial friction to progressively increase with the pipe movement (in the opposition direction of the near offset) until the virtual anchor is reformed.
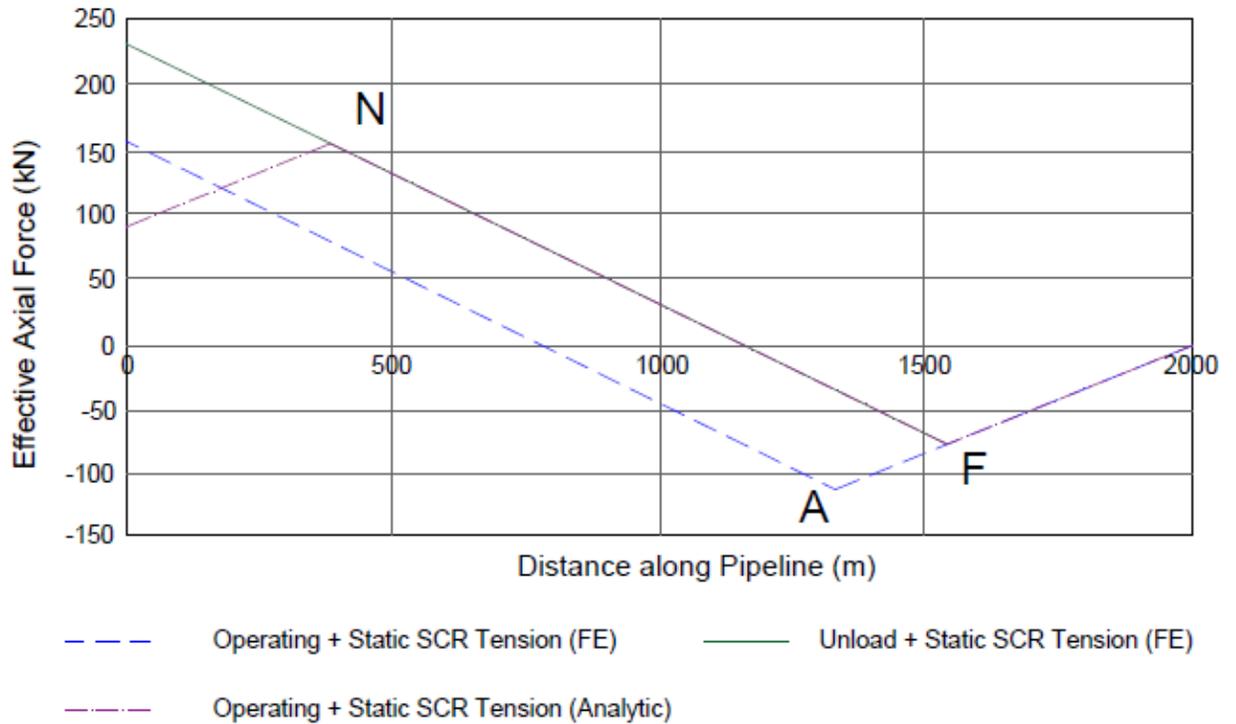
Figure 8-11: Effective axial force profile - Operation / 1-year storm.

8.3.2   Parametric Study

This section provides insight into the driving mechanisms behind pipeline design when connecting to an SCR via a sensitivity study on the effects of SCR tension, soil friction and friction mobilization distance. In this section the following three walking mechanisms are considered in the finite element simulation shown in Figure 8-5, which could result in variations in the mean position of the touchdown point:

- Tension at the pipeline end associated with the SCR

- Thermal gradients along the pipeline during the repeated start-up and cool-down cycles

- Global seabed slope along the pipeline

296

8.3.2.1   Effect of the SCR Bottom Tension

The results of this analysis are presented in Figure 8-12 to Figure 8-14. It can be seen from Figure 8-12 that the direction of the walking induced by the SCR tension force is opposite to the direction induced by both thermal gradients and the seabed slope. Specifically, the pipeline walks towards the SCR as on-bottom SCR tension overcome the effects of thermal transients and the seabed slope.
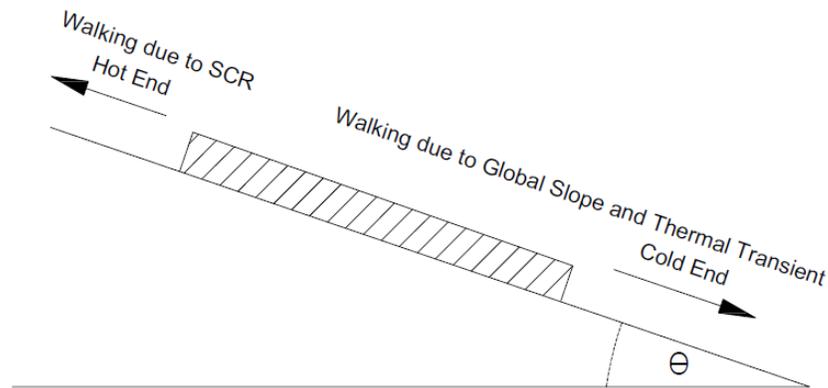
Figure 8-12: Walking directions.

A sensitivity assessment was undertaken to determine the effect of the SCR bottom tension on the rate of walking compared to the effect of thermal transients and seabed slope. A range of SCR bottom tensions were applied as per Table 8-2. In this section the axial friction coefficient was set to 0.4 with a mobilization distance of 0.00005 m. Refer to Figure 8-4 for the definition of "mobilization distance".
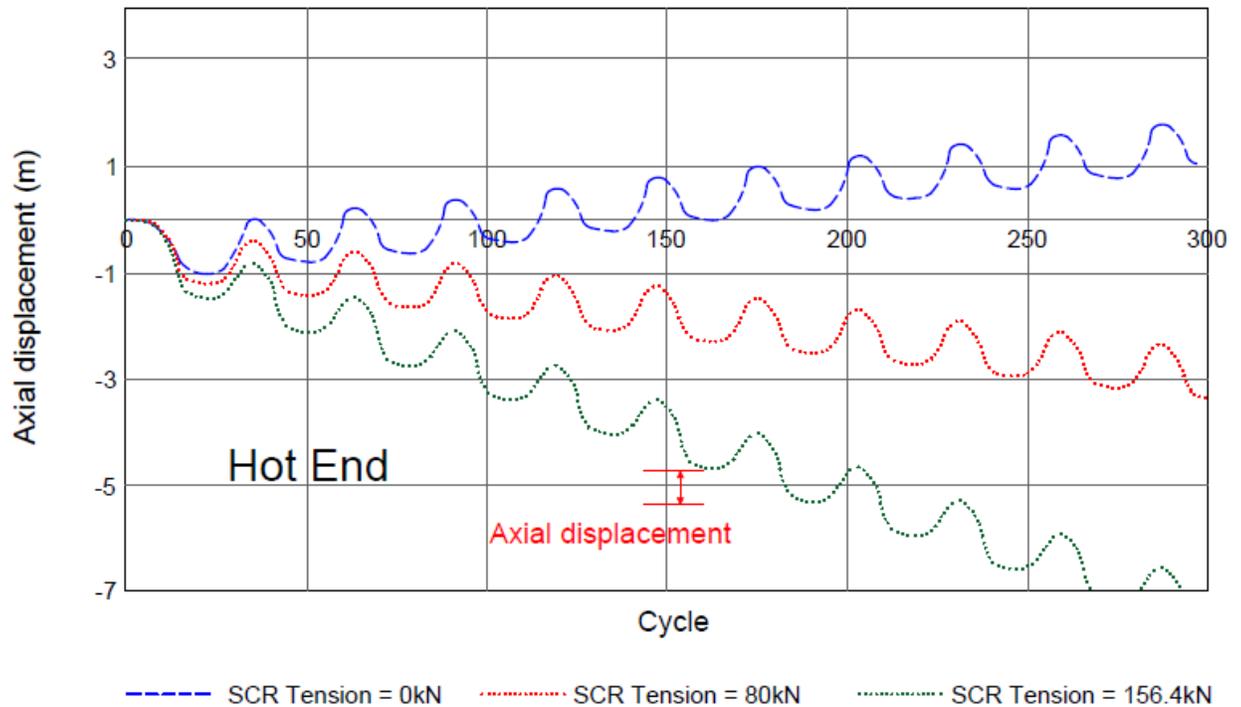
Figure 8-13: Walking response – Hot end.

Table 8-2: Pipeline Walking Distance for Range of SCR Bottom Tensions

SCR Bottom Tension (kN)	Walk Rate per Cycle (m)	
Zero tension	+0.23	(away from SCR)
80	-0.20	(towards SCR)
156.4	- 0.63	(towards SCR)

Looking at the results given in Table 8-2, Figure 8-13 and Figure 8-14, it is obvious that the displacement per cycle for the mean tension value of 156.4 kN is significant and that the total displacement towards the SCR would not be acceptable even for a small number of cycles.

As can be seen from the results given in Figure 8-13 and Figure 8-14 for all cases, the displacement per cycle for the hot end is equal to the displacement per cycle for the cold

298

end. This is another way to validate the finite element model used to establish the results in the thesis.

If the maximum allowable axial feed-in towards the SCR is assumed to be 5 m, the results associated with a tension of 156.4 kN (from Figure 8-13) show that after a few cycles the displacement towards the SCR would greatly exceed this limit. This deviation would jeopardize the integrity of the SCR if a hold back anchor is not used. The results given in green in Figure 8-14 show that the cold end moves towards the hot end and this can cause over-stressing of the spool.
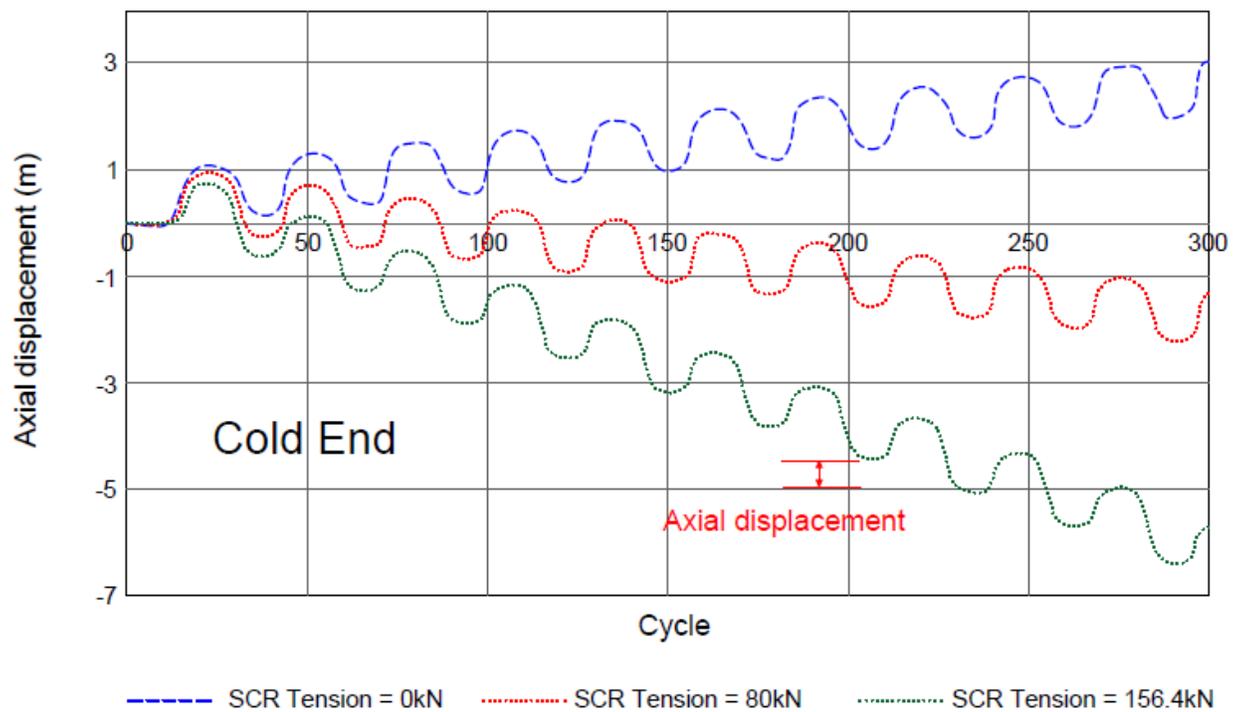
Figure 8-14: Walking response – Cold end.

For a tension value of 80 kN, the whole pipeline moves towards the SCR, but to a lesser extent than that obtained with the SCR tension of 156.4 kN. For the case without SCR tension, the entire pipeline moves towards the cold end as expected. This is due to the combined effect of the thermal transients and the seabed slope. In the absence of SCR tension, the walking induced by the transient profile and seabed slope is still present. In this case, the entire pipeline moves towards the cold end (down the slope). The results

299

above also show that an ideal SCR tension could be obtained to counteract any pipeline walking.

8.3.2.2   Effect of Axial Friction

The model used in this section is presented in Figure 8-5. A range of axial friction coefficients were applied as per Table 8-3. In this section the SCR tension was set to 156.4 kN with a mobilisation distance of 0.00005 m. Based on the results presented in Table 8-3, Figure 8-15 and Figure 8-16, it can be concluded that the walking was very sensitive to axial friction. The walking behaviour was found to change substantially with changes in friction coefficients.

Table 8-3: Pipeline Walking Distance for a Range of Friction Coefficients

Axial Friction Coefficient	Walk Rate per Cycle (m)
0.4	-0.63 (towards SCR)
0.8	-0.21 (towards SCR)
1.2	-0.05 (towards SCR)
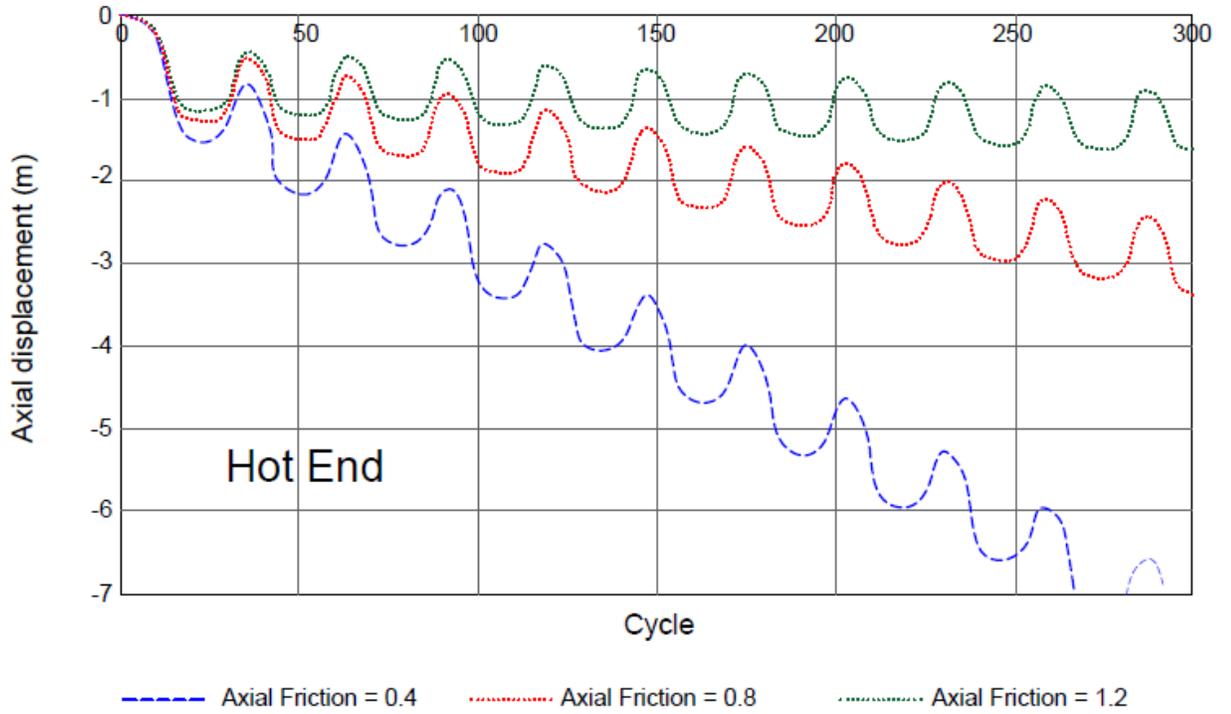
Figure 8-15: Walking response – Hot end.
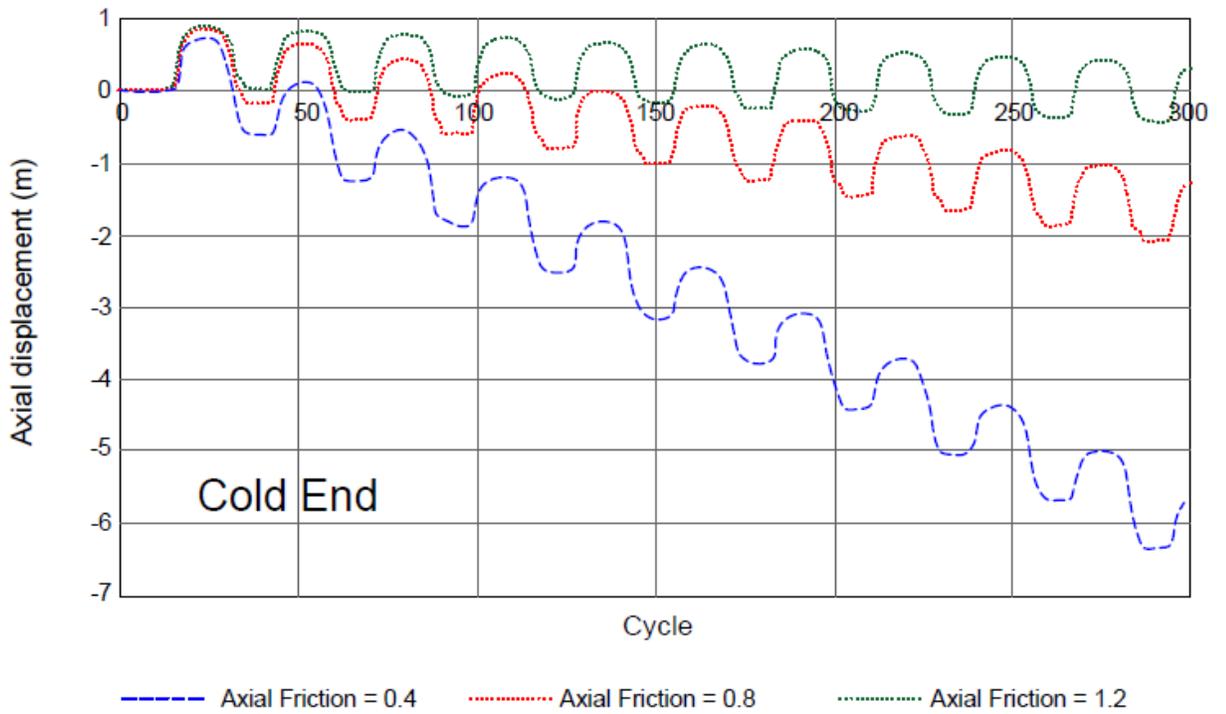
Figure 8-16: Walking response – Cold end.

301

8.3.2.3   Effect of Axial Mobilisation Distance

The model used in this section is presented in Figure 8-5. A range of axial mobilisation distances were applied as per Table 8-4. In this section the SCR tension was maintained at 156.4 kN throughout with an axial friction coefficient of 0.4.

Table 8-4: Pipeline Walking Distance for a Range of Mobilisation Distances

Mobilisation Distance (mm)	Walk Rate per Cycle (m)
0.05	-0.613 (towards SCR)
3.36	-0.610 (towards SCR)
8.4	-0.600 (towards SCR)
90	-0.49 (towards SCR)

The results in Table 8-4, Figure 8-17 and Figure 8-18 show that the rate of axial walking decreases with an increase in mobilisation distance. Furthermore, it is evident from Table 8-4 that the mobilisation distance could have a substantial impact on shorter pipelines.
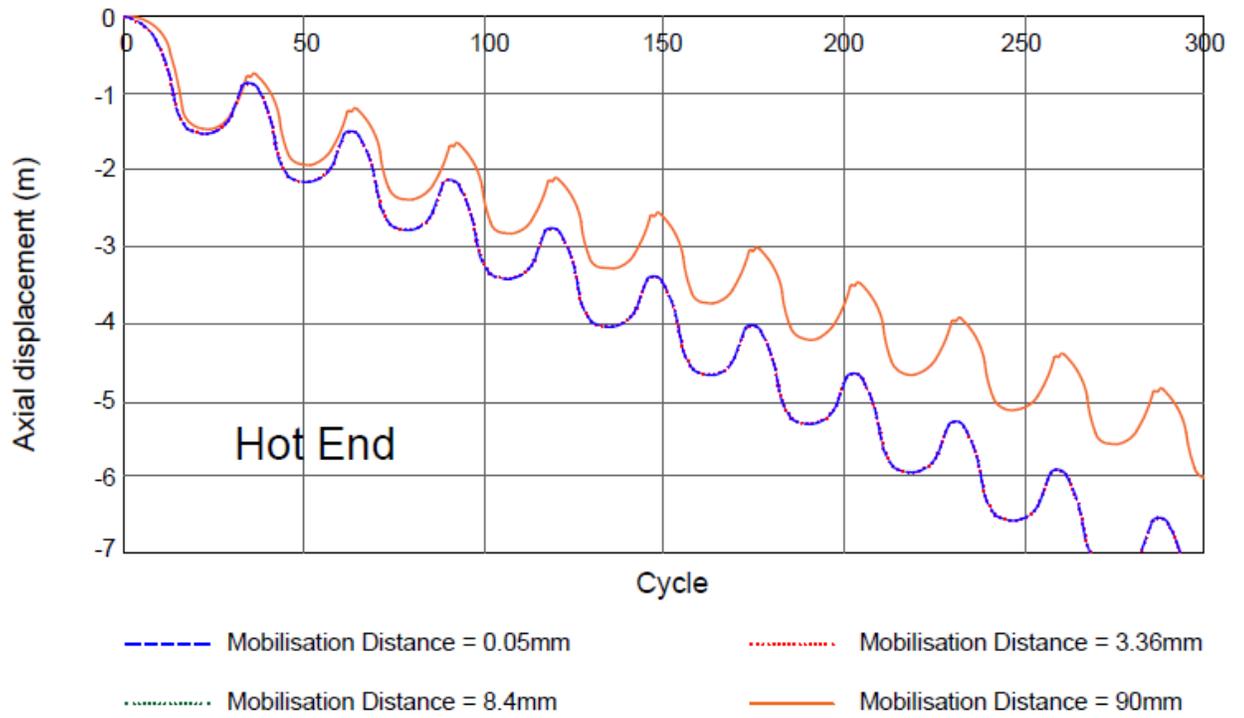
Figure 8-17: Walking response – Hot end.
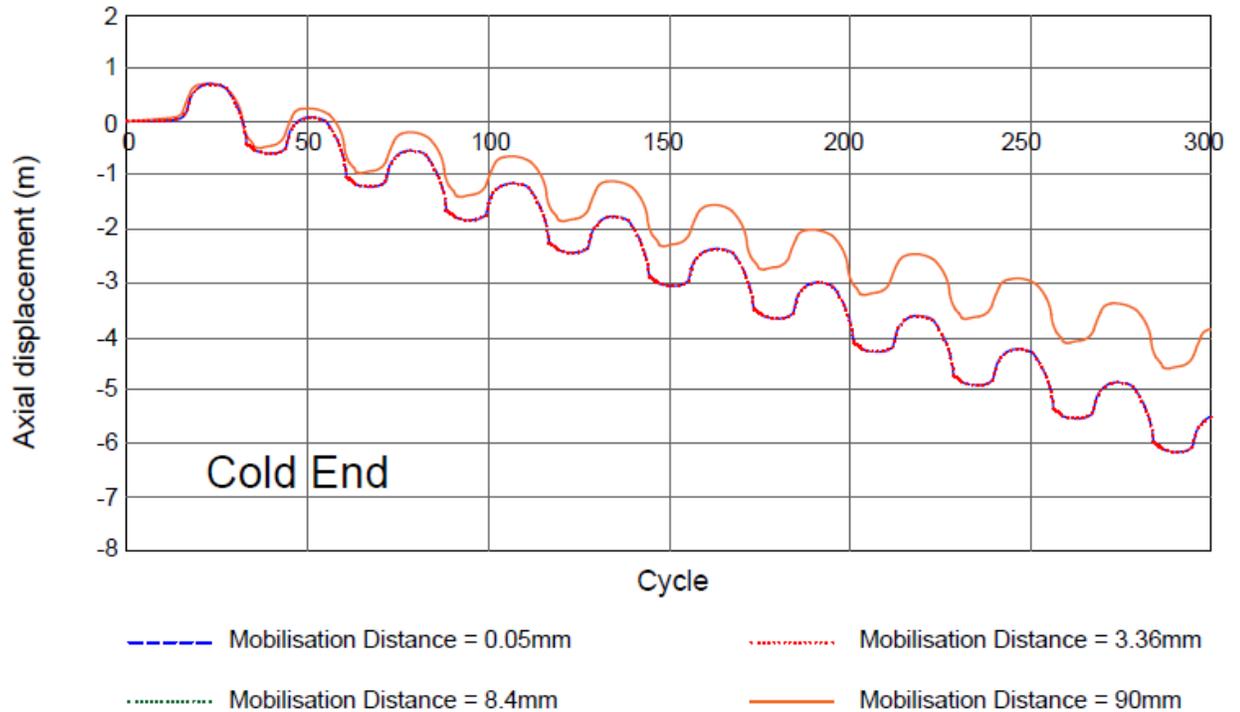
Figure 8-18: Walking response – Cold end.

8.4 REQUIREMENTS FOR ANCHORAGE

This section presents the criteria that must be satisfied during the design of the pipeline/SCR system when using hold-back anchors along the pipeline.

8.4.1 Pipeline Slippage

The thesis considers the following question: is a pipeline connected to an SCR susceptible to slippage due to SCR tension?

It is understood that a short pipeline connected to a SCR is prone to slippage by the SCR during storm conditions (extreme and survival design load cases).

Furthermore, the pipeline length, the axial friction coefficient as well as the SCR bottom tension in the far field position govern pipeline slippage. Pipeline slippage causes the

pipeline to move axially towards the SCR, thereby compromising the integrity of the SCR and the expansion spool installed at the PLET.

8.4.1.1 Illustrative Example

The example considered in this section illustrates the phenomenon of pipeline slippage due to SCR tension. In this example, a short pipeline is connected to a SCR as shown in Figure 8-19. The pipeline is straight without any route curves. The SCR is subject to the vessel offset in the far field position.
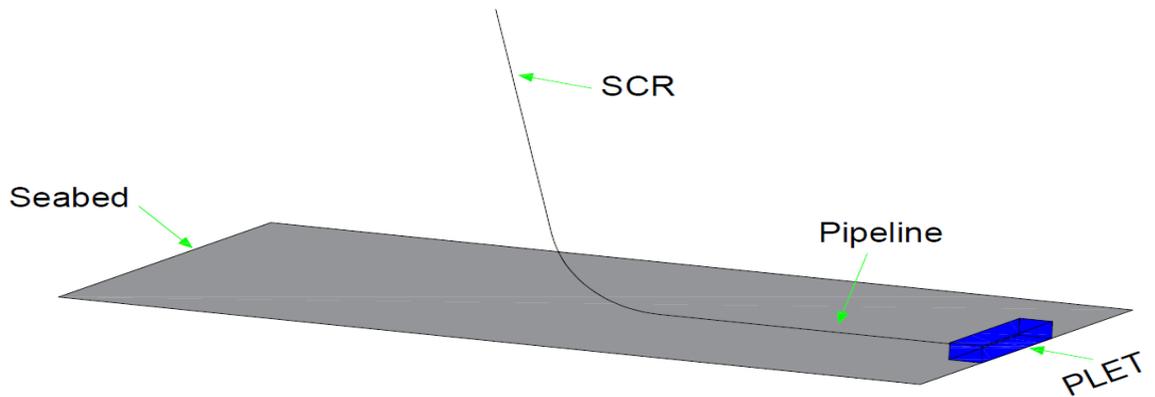
Figure 8-19: Slippage demonstration.

Figure 8-20 shows the effective axial force obtained from finite element modelling using ABAQUS (2012) for different axial friction coefficients. The effective axial force profile is dependent on the combined effect of the axial friction coefficient and the value of the SCR tension. In this example, coordinate values 0 and 2000 on the x-axis refer to the transition point and the free end, respectively.

It can be seen from Figure 8-20 and Figure 8-21 that the pipeline is prone to slippage only for the lower bound value of the axial friction coefficient. In this case, the whole pipeline moves axially towards the SCR. Figure 8-21 shows that the pipeline expands approximately -1.5 m and +0.8 m towards the SCR and the free end, respectively, when the upper bound axial friction coefficient is used. When the best estimate value of axial friction coefficient is used on the other hand, the end expansions are -1.9 m and +0.5 m

305

towards the SCR and the free end, respectively. The positive and negative signs indicate expansion towards the free end and the SCR, respectively. Figure 8-22 shows that the entire pipeline displaces towards the SCR with a value of -29.8 m.
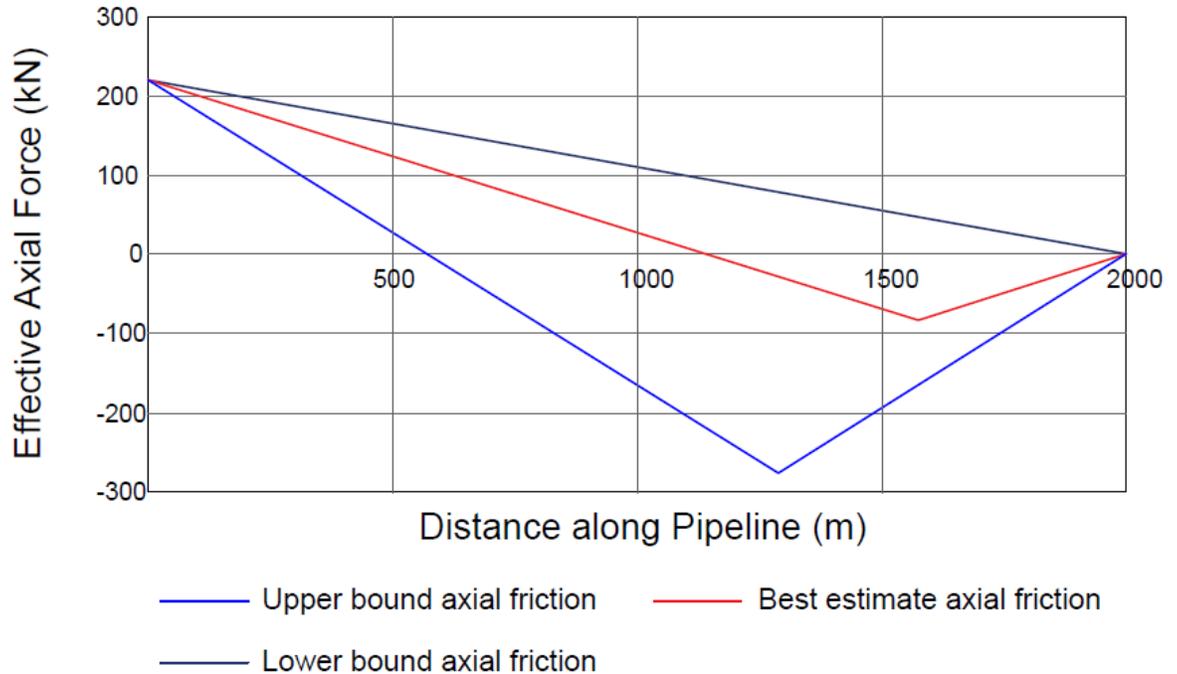
Figure 8-20: Effective axial force vs. distance for different axial friction coefficients.

In order to prevent the pipeline from slipping towards the SCR, it is recommended to install a hold-back anchor either at the PLET side away from the SCR transition point or at the SCR transition point. The optimal position is determined by the SCR axial feed-in limit. If the pipeline expansion associated with pressure and temperature changes in the direction of the SCR is less than the SCR axial feed-in limit, then the recommended anchor location will be at the PLET side as per Reda et al. (2018 p. 71-85). If the pipeline expansion towards the SCR is greater than the SCR axial feed-in limit, then the hold-back anchor should be installed at the SCR transition point. The transition point is the point where there are no lateral or vertical movements due to the dynamics of the SCR (Reda et al., 2018 p. 71-85).
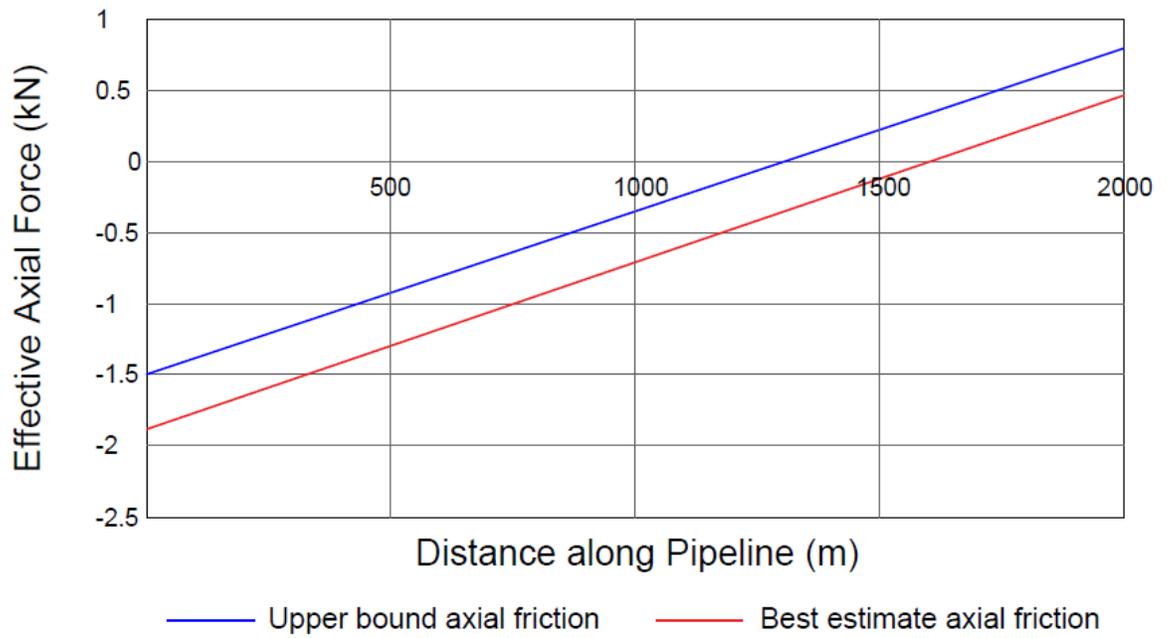
Figure 8-21: Axial displacement vs. distance for upper bound and best estimate axial friction coefficients.
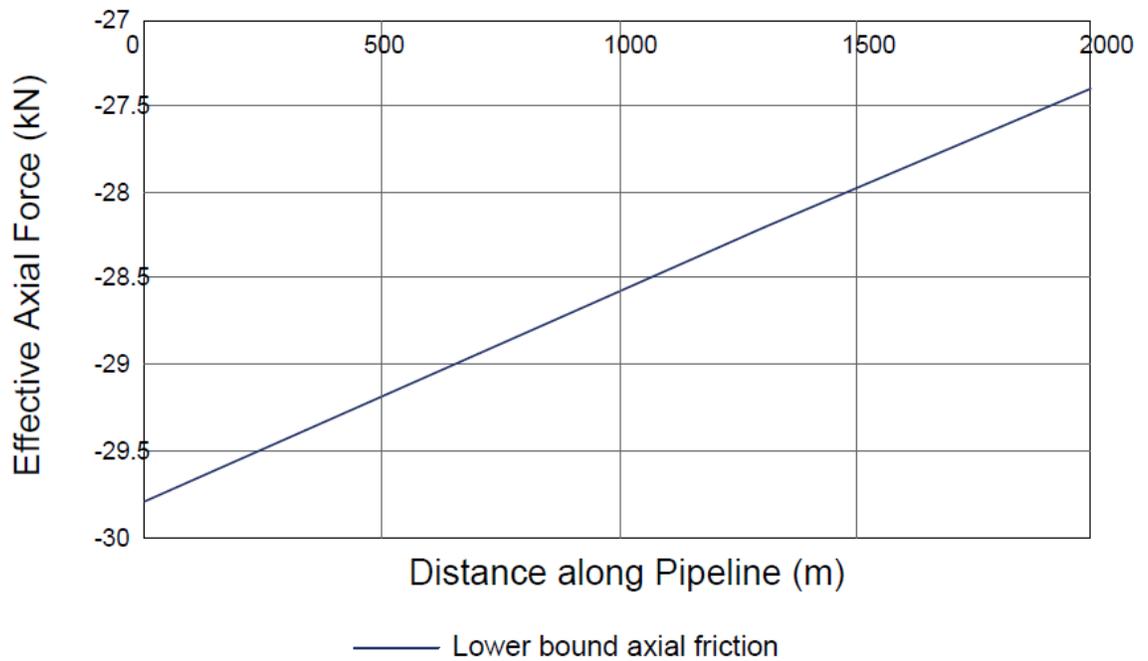
Figure 8-22: Axial displacement vs. distance for lower bound axial friction coefficient.

The following equation can be used to determine whether a short pipeline that is connected to a SCR is susceptible to pull-out or slippage:

SCR Tension (T) ≤ Straight Axial Resistance (R$_a$)

$$8\text{-}11$$

Where:

$$R_a = L \times W_s \times \mu_a$$

$$8\text{-}12$$

and

L: straight pipeline length,

μ_a: axial friction coefficient,

W$_s$: pipe submerged weight.

Hence, the pipeline length required to prevent pull-out can be calculated as follows:

$$L = \frac{T}{W_{s*}\mu_a}$$

$$8\text{-}13$$

It can be seen from Equation 8-13 that a high axial resistance and a high pipe submerged weight are generally beneficial in suppressing pipeline slippage and can obviate the need for an anchoring system. The axial resistance can be increased with an increase in the surface roughness of the pipeline coating.

8.4.2   Route Bend Pull-Out Due to SCR Tension Associated with Storm Conditions

A significant design issue that must be considered is whether or not the route bend is susceptible to pull-out in association with SCR tension. Route curves are generally used to align the approach angles of the field to the floating host facility riser hang-off. Route bend pull-out can occur as a result of excessive tension transmitted from the SCR to the route bend during storm conditions. Route bend pull-out should be obviated for the following reasons:

1. Straightening the route bends can result in the development of non-recoverable end expansion towards the SCR. Hence, slippage or pull-out of the mean position of the SCR touchdown point can occur towards the floating production vessel. Conversely, straightening the route bends could potentially increase the end expansion towards the spool installed at the other end, thereby compromising the integrity of the spool.

2. Straightening the route bend could lead to significant implications on the field architecture.

8.4.2.1   Illustrative Example

In the example shown in Figure 8-23, a SCR is connected to a pipeline with a route curve. In the finite element analysis, the SCR is subjected to the vessel offset in the far field position. It is assumed that the pipeline will remain in operation under storm conditions. The objective of this analysis is to show whether the curve/bend is prone to pull-out under the influence of excessive transmitted tension associated with storm conditions. In this example, coordinate values 0 and 3500 on the x-axis refer to the transition point and the free end, respectively.

Figure 8-23: Curved pipeline connected to floating production vessel via SCR.

The results presented in Figure 8-24 and Figure 8-25 show that excessive SCR tension associated with storm conditions could indeed result in route bend pull-out.

In situations where the pipeline is found to be prone to route bend pull-out, the following solutions should be considered first, before adopting the holding back anchor solution:

- Relocation of the route bend

- Introduction of a straight pipeline section prior to the route bend

- Increase of the bend radius of the route bend

If the above solutions are not successful in preventing the bend pull-out, a hold-back anchor should then be employed. The anchor can be installed at the transition point of the SCR.
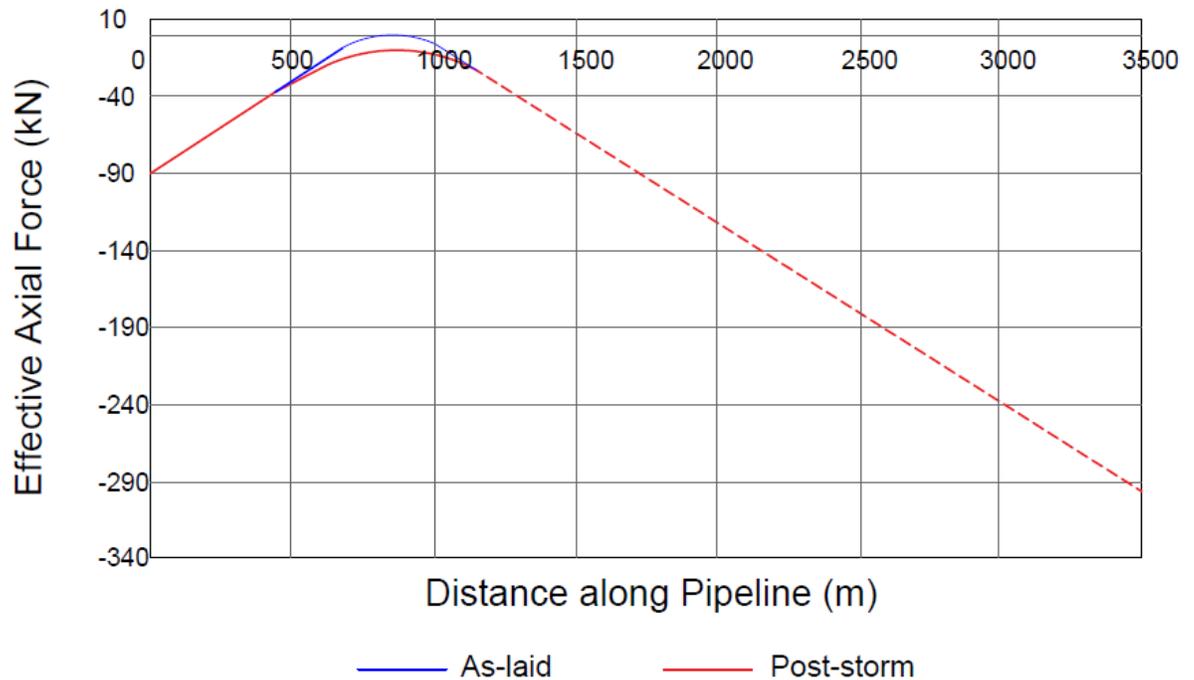
Figure 8-24: Pipeline route after the application of SCR far tension.

310
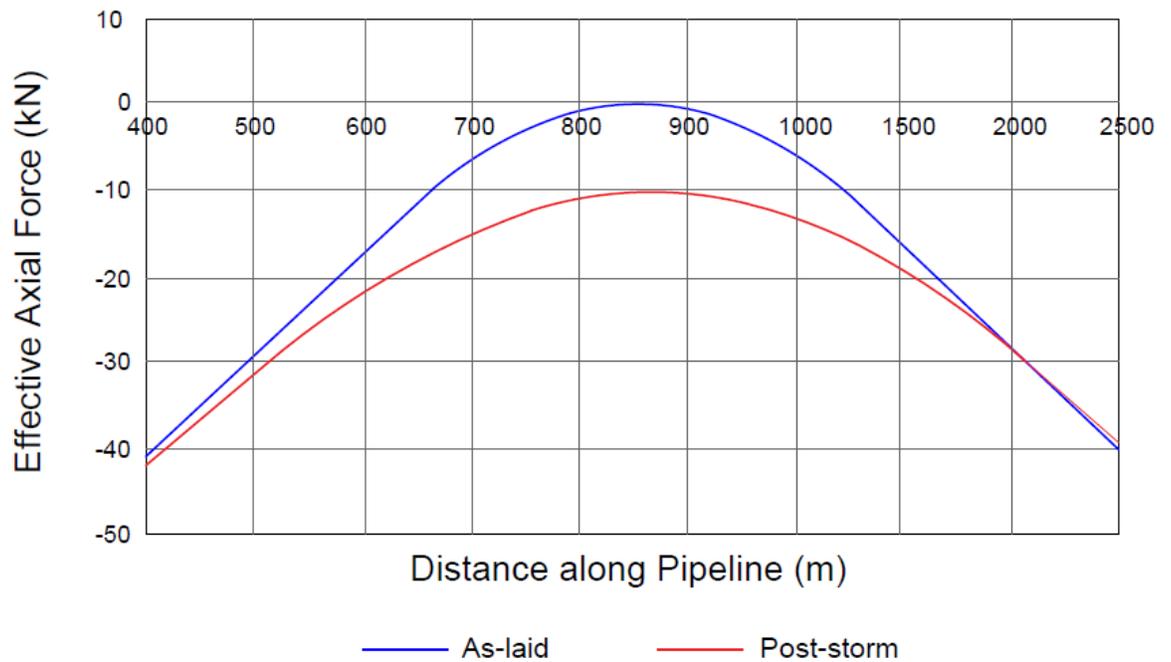
Figure 8-25: Snapshot of route bend.

As per Equation 8-14, the maximum tension, T, that can be resisted by the route bend is calculated by:

$$T = \frac{R \times \mu_L \times W_s}{SF}$$

8-14

Where:

R: route bend radius,

μ_L: lateral friction coefficient (lower bound value is recommended),

W_s: pipe submerged weight,

SF: factor of safety.

311

8.4.3 Is the Route Bend Susceptible to Pull-Out Associated with Tension Build-Up During Repeated Operational Start-Ups and Shut-Downs?

Route bend stability under repeated shut-downs is an important requirement during the design of "short" or "ultra-short" high temperature pipelines in deep water. The tension that can result along the length of the pipeline from shut-down conditions can be significantly greater than that resulting from pipe lay. This increase in pipeline tension can force the route bend to straighten if the radius is not large enough to provide the required amount of resistance. This problem is further exacerbated with the presence of riser bottom tension in the pipeline.

8.4.3.1 Illustrative Example

The example shown in Figure 8-26 is designed to assess the susceptibility of the route curve to pull-out associated with tension build-up during repeated start-up and shut-down cycles. The SCR tension applied in this model is the static SCR tension. The pipeline is subjected to eight cases of repeated start-ups and shut-downs. Figure 8-27 illustrates the effective axial force induced during the loading and unloading conditions for the pipeline system. The red and black dotted lines refer to the centre of the route bend and tensile force at which the route bend becomes unstable, respectively.
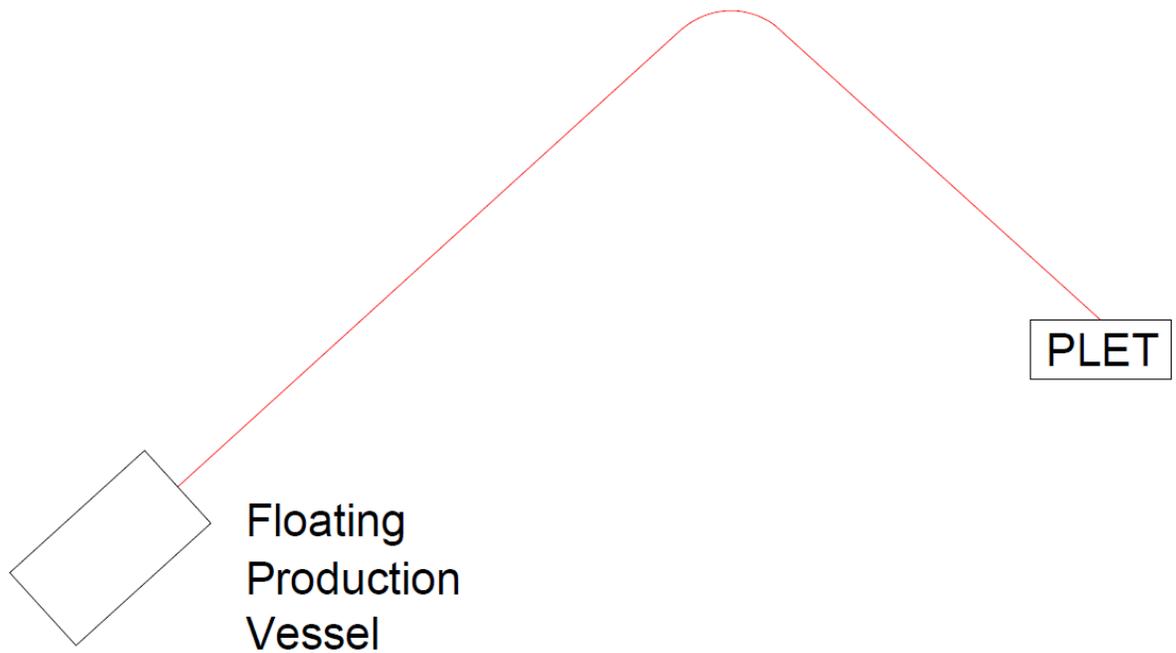
Figure 8-26: Curved pipeline connected to floating production vessel via SCR.

In this example, the destabilising force ($N_{unstable}$) is equal to 110 kN, calculated using Equation (8-14).
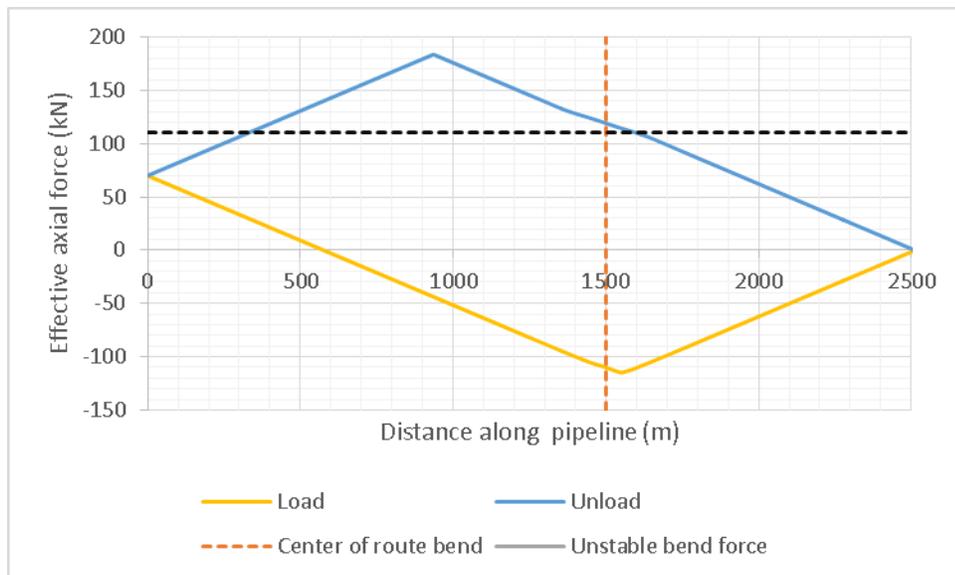
Figure 8-27: Effective axial force during loading and unloading conditions.

Figure 8-27 shows that the effective axial tension at the centre of the bend during the unloading condition is 120 kN, which is greater than the destabilising force, $N_{unstable}$. Hence, the route bend will become unstable. This can be explained further by looking at Figure 8-28, which demonstrates that the route bend is unstable under the repeated loading and unloading (start-ups and shut-downs) conditions in the presence of the static SCR tension.

Figure 8-29 shows the distribution of the axial displacement along the pipeline. It can be seen that the end expansion towards the free end increases with the progress of the route bend pull-out. This proves that the imposed tension would cause a pull-out of the route bend, thereby allowing the pipe to feed-in towards the spool or the SCR, compromising the integrity of the spool and the SCR if not duly controlled.

In the event that the pipeline proves to favour a route bend pull-out event, the pipeline/SCR design should then be reconsidered to investigate the possibility of increasing the bend radius. Alternatively, the consequences of the route bend pull-out should be investigated. The consequences of a route bend pull-out event are:

1.   Significant implications on the field layout architecture.

2.   Increasing the axial feed-in towards the SCR beyond the allowable limit, hence compromising the integrity of the SCR.

3.   Allowing more pipe segments to feed-in towards the spool, hence overstressing the spool.

If the route cannot be adjusted and the consequences are unacceptable, then a hold-back anchor is mandatory.
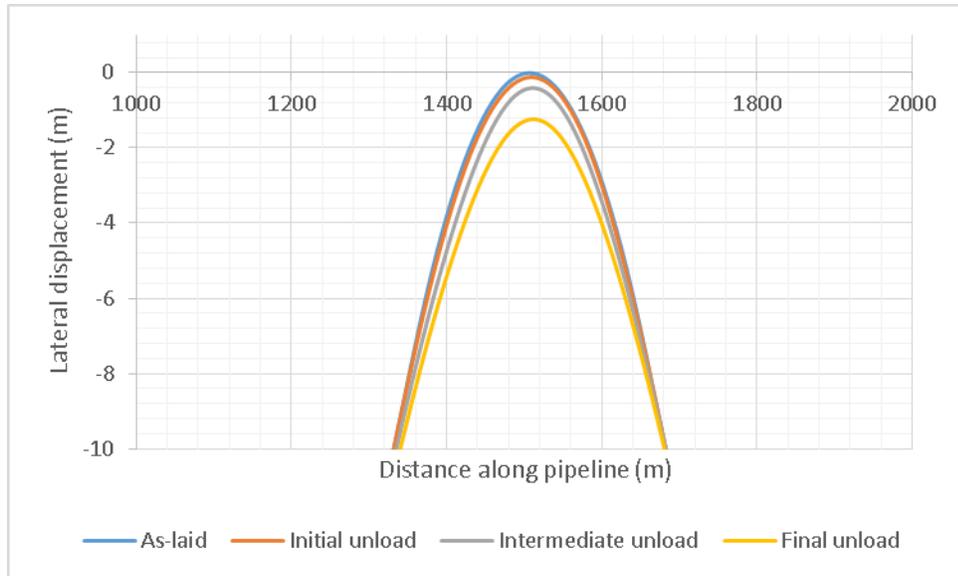
Figure 8-28: Route bend pull-out.
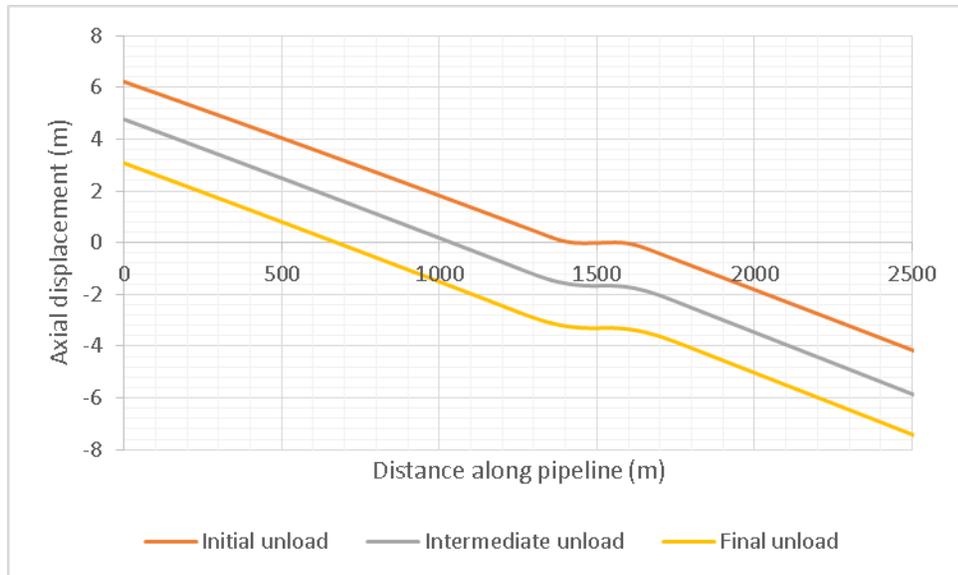
Figure 8-29: Axial displacement along the pipeline.

It should be noted that lateral friction coefficients considered in this chapter are residual/breakout lateral friction coefficients.

In real conditions, as the route bend moves laterally, the influence of SCR tension as well as cyclic start-up/shut-down decreases. With each cyclic sweep, the route bend tends to sweep the surface soil ahead of it, building up into berms at the extremes of the pipeline

displacement. These soil berms could offer a significant lateral resistance to route bend lateral movement. The subsequent cycles of the lateral movement of the route bend could lead to a steady increase in the lateral resistance provided by the soil berms.

The rate of the embedment is governed by the vertical pipe load and the shear strength of the soil under the pipeline. However, it should be indicated that the pipeline-seabed contact condition for the route bend is different from the pipeline-seabed contact condition resulting from the lay process of a straight pipeline.

Considering the soil berm during the simulation is likely to reduce the rate of lateral ratcheting of the route bend. Hence, it is conservative to ignore berm build-up during the evaluation of pull-out due to tension build-up from repeated operational start-ups and shut-downs.

In this section, the residual axial friction coefficient was employed during the simulation. It can be assumed that the peak (breakout) axial friction coefficient does not affect lateral ratcheting behaviour of the bend. This is because typically, the soil beneath the pipeline (including the bend) will not have time to reconsolidate between subsequent cool down and heat-up cycles. However, considering that reconsolidation may only take a few hours, this may be enough for the reestablishment of the peak resistance between cycles.

If peak resistance is experienced during transient temperature changes, it is well known that this can significantly modify the lateral ratcheting and pull-out behaviour of the route bend. It is recommended that sensitivity checks using the peak (breakout) axial friction coefficient are carried out to investigate the susceptibility of the route to lateral ratcheting and pull-out.

8.4.4 Pipeline Expansion towards SCR/PLET

A further important consideration is whether the total pipeline expansion towards the SCR over the design life is acceptable. In other words, it is important to consider whether or not the stress on the spool located at the other end of the pipeline is acceptable.

As per Reda et al. (2018, p. 71-85) and Reda et al. (2019 p. 278-298), the incremental axial displacement (walking) over the design life towards the SCR should be kept within

316

the allowable maximum limit specified by the SCR design. Pipeline anchoring will be needed if the through-life expansion towards the SCR cannot be kept within this limit

The model presented in Figure 8-19 was used to investigate the rate of walking and expansion towards the SCR under repeated start-ups and shut-downs. The results are given in Figure 8-30. The figure shows that both ends (the hot end that is connected to the SCR and the cold end that is connected to the free end) expand towards the SCR. The rate of walking presented here is based on the static SCR tension. It can be seen that after 10 operating cycles, the total expansion towards the SCR reaches 7 m. In this example, the allowable axial feed-in towards the SCR is assumed to be 5 m.

It can be seen from Figure 8-12 that walking due to the SCR is in the opposite direction to the walking mechanisms of both thermal gradients and the seabed slope. The results show that the pipeline walks towards the SCR, that is, on-bottom SCR tension was shown to dominate the walking behaviour over the thermal transient effects and the seabed slope. In the scenario discussed above, a hold back anchor was required to avoid overstressing of the spool between the manifold and the PLET and to ensure that the integrity of the SCR was not compromised.

In conclusion, pipeline walking over several cycles can lead to significant global axial displacement of the pipeline, resulting in loss of SCR static tension and overstressing of the expansion spools and jumpers. Thus anchoring would be required. The anchor can be installed at the PLET away from the SCR transition point as per Reda et al. (2018, p. 71-85).

Note that the axial friction coefficient considered in this section was the residual axial resistance. This is conservative, since the breakout axial friction tends to reduce the rate of pipeline walking. Furthermore, the breakout axial resistance may not affect axial walking behaviour, as typically the soil beneath a pipeline will not have time to reconsolidate between subsequent start-up and shut-down cycles.
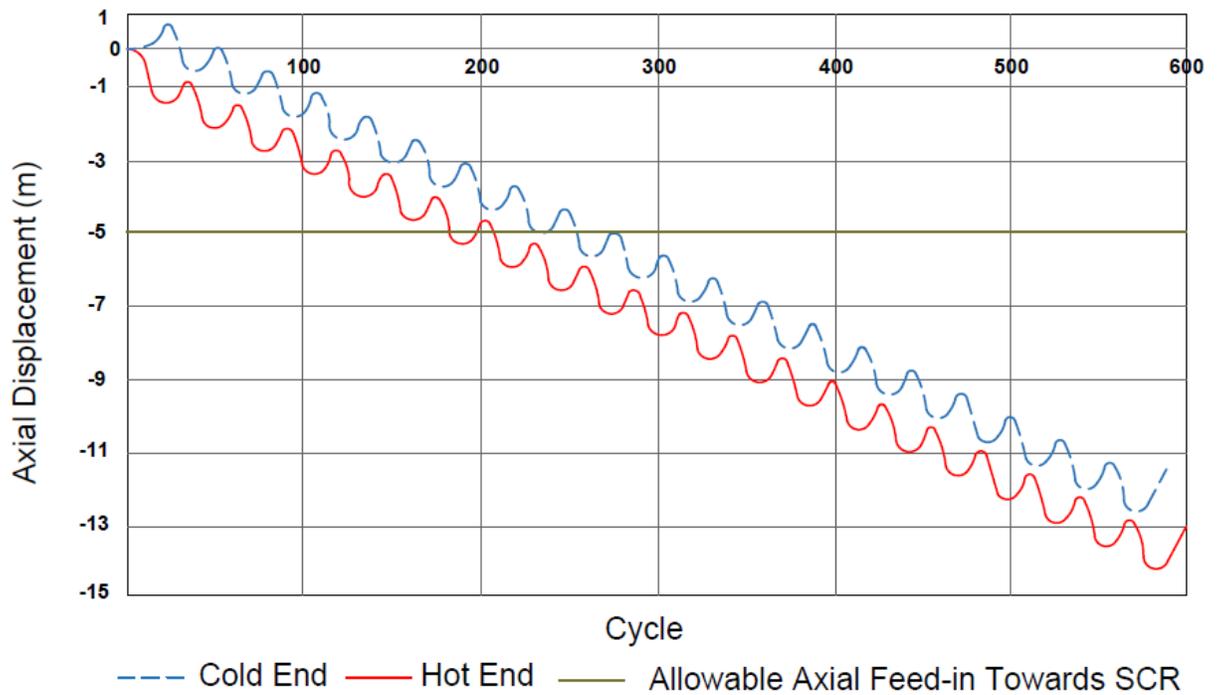
Figure 8-30: Total expansion over design life.

8.5   INFLUENCE OF PIPE-SOIL INTERACTION

Table 8-5 highlights the importance of the axial and lateral friction coefficient in the criteria presented in Section 8.4. Sensitivity assessments should be undertaken using the lower and upper bounds of friction in order to determine the requirements for anchoring along a short pipeline connected to a SCR.

Table 8-5: Influence of Pipe-Soil Interaction

Friction	Bound	Short pipeline slippage	Route bend pull-out due to SCR tension associated with storm conditions	Route bend pull-out associated with tension build-up during the repeated operational start-ups & shut-downs	Pipeline expansion towards SCR/PLET
Residual axial friction coefficient	Lower	Anchor is more likely	Anchor is more likely	Less tension Anchor is less likely	Anchor is more likely
	Upper	Anchor is less likely	Anchor is less likely	More tension Anchor is less likely	Anchor is less likely
Residual / breakout (peak) lateral friction coefficient	Lower	No concern	Anchor is more likely	Less stable Anchor is more likely	No concern
	Upper	No concern	Anchor is less likely	More stable Anchor is less likely	No concern
Lateral (berm) / cyclic	Lower	No concern	More restrained Anchor is less likely	More restrained Anchor is less likely	No concern
	Upper				

Notes: 1- Orange indicates "Of limited concern".

2- Blue indicates "Least concerning".

3- Red indicates "Most concerning"

Pipe-soil interaction is essential in determining the requirements of the anchor. Therefore, it is important to ensure that before evaluating the criteria given in Table 8-5 sufficient soil data are available to determine the pipe-soil friction coefficient.

8.6   EVALUATION OF THE ANCHORING CONCEPT

Anchors may be required for various reasons, including pipeline initiation during laying, limiting pipeline walking and providing on-bottom tension for SCRs. Geotechnical input is needed for the design of anchors, for end termination foundations, and for connection manifolds. There are different types of anchoring system, including:

1.   Anchor and chain

2.   Anchor and stab

3.   Structural anchor

4.   Rock dumping

Table 8-6 is a list of the main advantages and drawbacks of each anchoring type.

Table 8-6: Evaluation of different anchoring systems.

Anchoring Type	Advantages	Drawbacks
Anchor and Chain	✓ Can be installed before or after pipeline installation. ✓ Can be installed anywhere along the pipeline (i.e. pipeline end or middle of the pipeline). ✓ Has a good track record, especially in the Gulf of Mexico. ✓ Comprises of a relatively simple design when compared to	✘ Size of the pile is proportional to the load experienced by the anchor. ✘ Large piles require more cautious handling during installation and operation. ✘ Installing the piles after the completion of the pipeline construction may pose a risk to the

320

Anchoring Type	Advantages	Drawbacks
	other concepts such as structural anchors and anchor/stab concepts. ✓ The anchor and chain concept is relatively inexpensive.	installed pipeline associated with the dropped object.
Anchor and Stab	✓ Can be utilised to initiate the pipelay as well as to restrain pipeline ends from walking and/or expanding.	✗ There is insufficient track record and operational data for SCR anchoring. ✗ Stab and hinge operation requires high precision. ✗ May only be suitable at the pipeline first end (initiation), as it requires a tight installation tolerance. ✗ Piles are required to be installed prior to the pipeline installation. ✗ Large piles require more cautious handling during installation and operation.
Structural anchor	✓ Can be used for pipeline initiation during pipeline installation. In particular, a system incorporating a PLET structure and piles.	✗ The structural anchor is required to be pre-installed before the pipeline installation campaign. During the pipeline installation, the pipeline will be guided onto the bearing arrangement via guide members. The collars connected to the pipeline are then engaged with the bearing arrangement. ✗ Complex design.

Anchoring Type	Advantages	Drawbacks
		✖ Large piles require more cautious handling during installation and operation.
Rock Dumping.	✔ The calculation/design of the total weight/volume of rock dumped per rock grading and the number of passes required to achieve the required cover are simple when compared to other anchoring concepts.	✖ High costs may be associated, due to the large quantity of graded rock required, particularly in locations where it is difficult to source rocks. ✖ High costs may be involved with mobilising a vessel suitable for rock dumping in deep-water.

There are several available methods to control or limit axial walking. The most viable and appropriate solution is chosen based on the following factors:

1.   The outcome from the walking assessments

2.   Field layout constraints

3.   Cost

4.   Constructability

5.   Adaptability to different SCR installation methods and schedules

6.   Compatibility with soil type

The typical distribution of costs for a SCR system-only is as follows (note that the range in quotes is due to the riser outer diameter ranging from 6 to 26 inches):

- Materials and transport 30-35%

- Engineering and project management 20-10%

- Installation 50-55 %

The material costs included above do not account for the following components:

- PLETs and anchors

- Topside piping including pig launching and receiving facilities

- Riser hang off structural assemblies

The cost of the anchoring system is typically around 10-15% of the total cost of the SCR system (materials/transport, engineering/project management and installation).

8.6.1 Anchor and Chain

An anchor and chain system utilises holdback chains that are attached to a collar on the pipeline. The other end of the chain is connected to a pile. Figure 8-31 and Figure 8-32 show examples for the anchor/chain concept as well as the connector clamp.
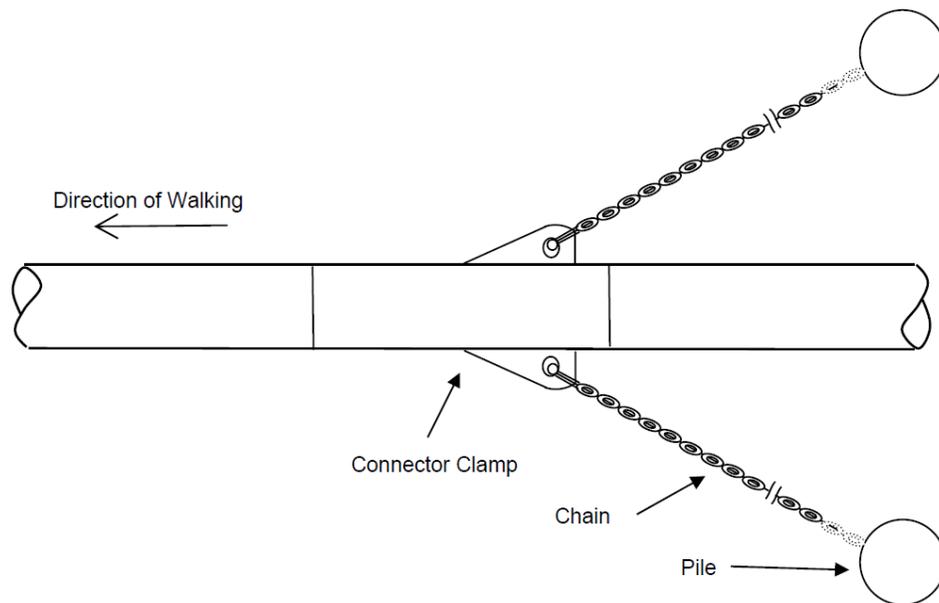
Figure 8-31: Dual anchor pile at pipeline centre/transition point.
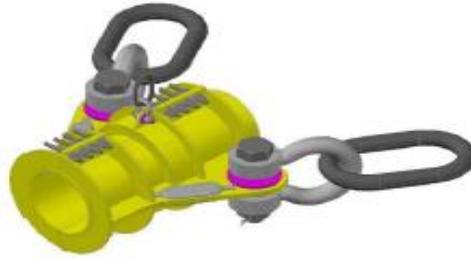
Figure 8-32: Connector clamp.

8.6.2 Anchor and Stab

The stab and hinge anchor system (Figure 8-33) can be utilised to anchor a pipeline and prevent the axial feed-in towards the SCR. This can be achieved by using a tee bar arrangement to provide a mechanical connection between the pipeline end and the suction pile. The tee bar arrangement provides a rigid connection of the pipeline to the piles and axially limits the pipeline from expanding or moving in either direction.
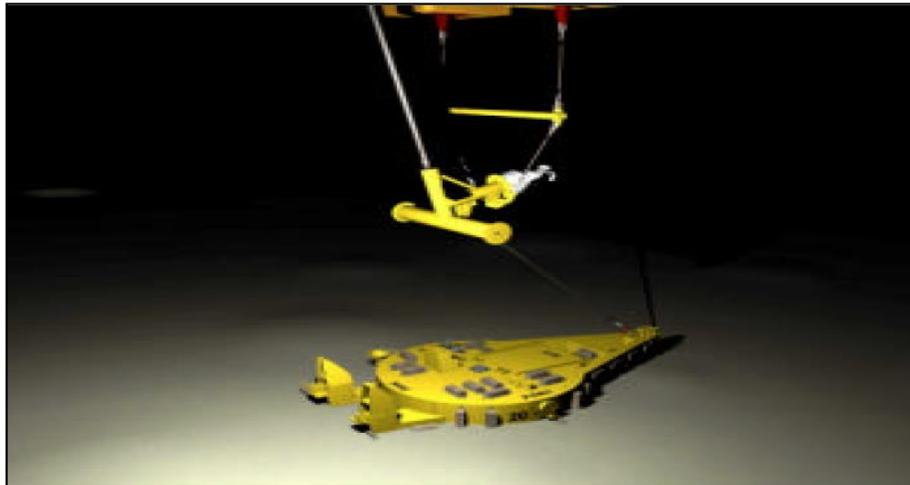
Figure 8-33: Anchor with hinge and stab (Perinet et al., 2011).

8.6.3 Structural Anchor

A structural anchor, as illustrated in Figure 8-34, utilises a rigid frame mounted on piles and includes a bearing arrangement to control axial feed-in of the pipeline towards the SCR.
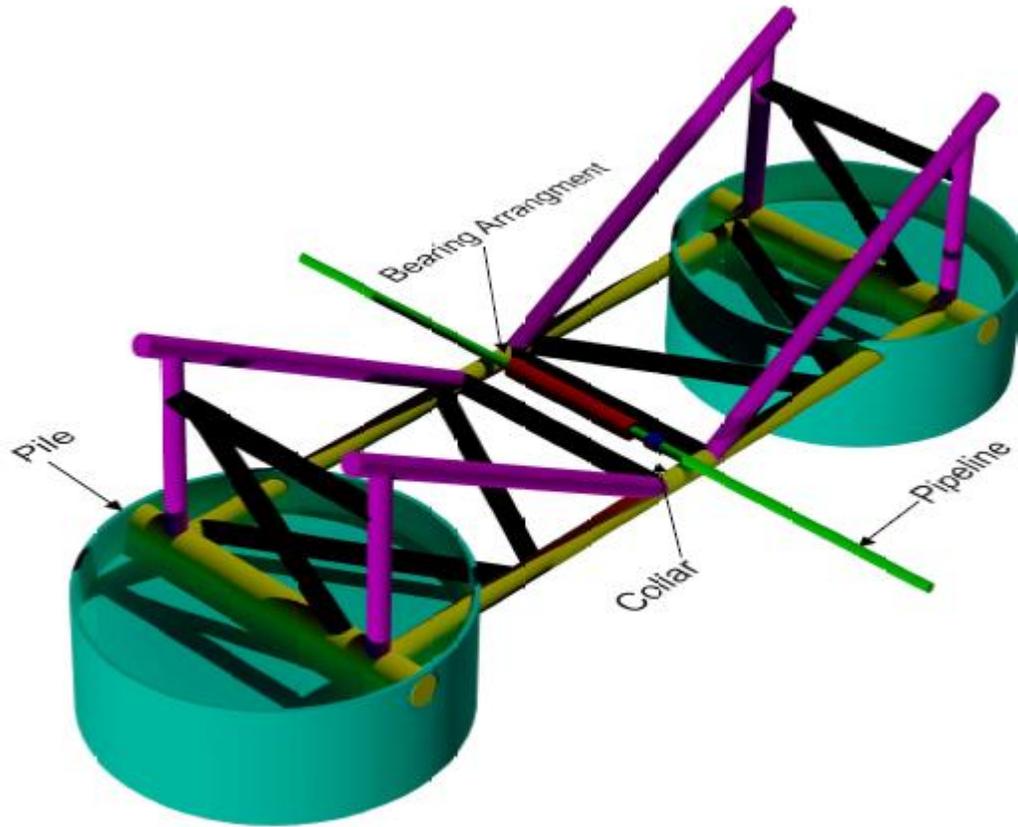
Figure 8-34: Structural anchor.

8.6.4   Rock Dumping

Rock dumping (Figure 8-35) can be utilised along a pipeline in order to anchor the pipeline in the proximity of the SCR to reduce axial feed-in towards the SCR.
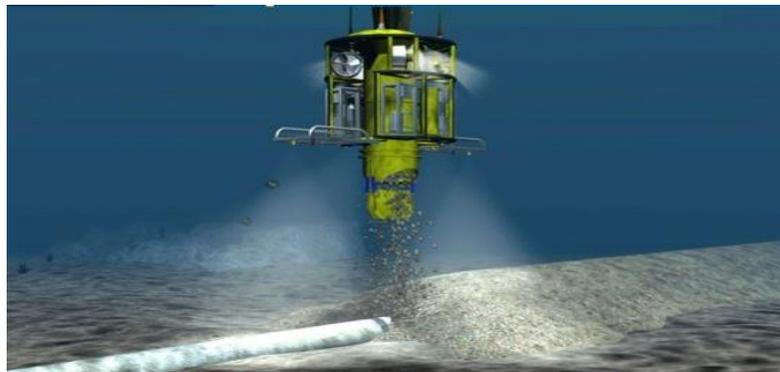
Figure 8-35: Rock dumping.

8.7   TYPE OF PILING

The type of piling which can be considered for SCR anchors are as follows:

1.   Suction piles
2.   Driven piles
3.   Drilled and grouted piles

Suction piles may be used in soft clay deposits. Soft soil with sand and aggregate may require driven piles, whereas harder seabeds may require drilled and grouted piles.

Soil boring should be undertaken to assess the geotechnical characteristics of the seabed material for the piles in order to select the most suitable piling system.

The pile configuration and sizing are typically based on soil condition and pile capacity. There are other factors that should be accounted for during the selection of the optimal pile configuration, such as the load on the anchor that is required to prevent or reduce the axial feed-in towards the SCR or the PLET, constructability, complexity of the piling design and the pile's failure mode.

The pile configuration options are as follows:

- Single pile, dual piles or multiple piles (cluster)
- Fixed or free head configurations

Single piles are less complex than dual/multi-cell piles.

Fixed head piles (see Figure 8-36 and Figure 8-37) are when the pile head cannot rotate because it is connected to a very rigid cap. The bending moment here is non zero under lateral loads applied at the pile head level. Also, the rigidity of the pile influences the degree of the rotation.

Free head piles (see Figure 8-38, Figure 8-39 and Figure 8-40) are when the pile head can rotate freely with no restraints. This occurs when the pile head is not attached to any structure, or when the head is connected to a flexible structure that does not prevent rotation. The bending moment at the pile head is zero unless an external moment is applied.

During the assessment of the holding capacity for the pile, the effect of the installation tolerances (i.e. anchor tilt and orientation) on the ultimate holding capacity of the pile should be taken into consideration.
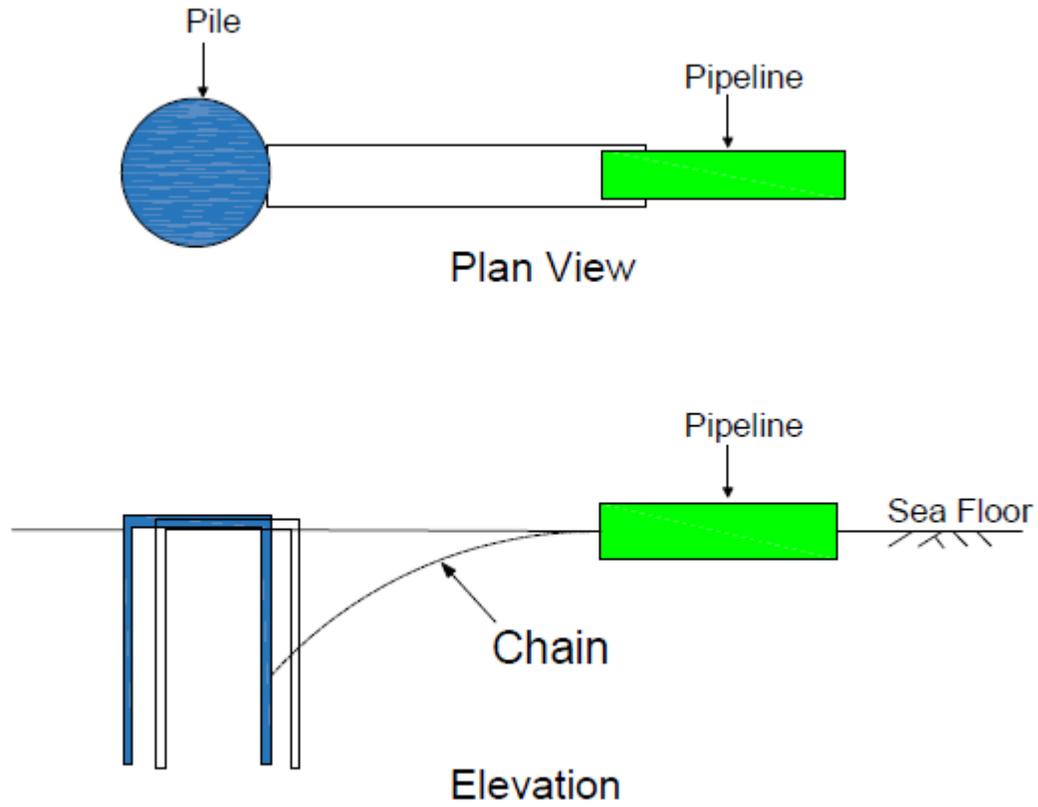
Figure 8-36: Fixed-head (single pile).
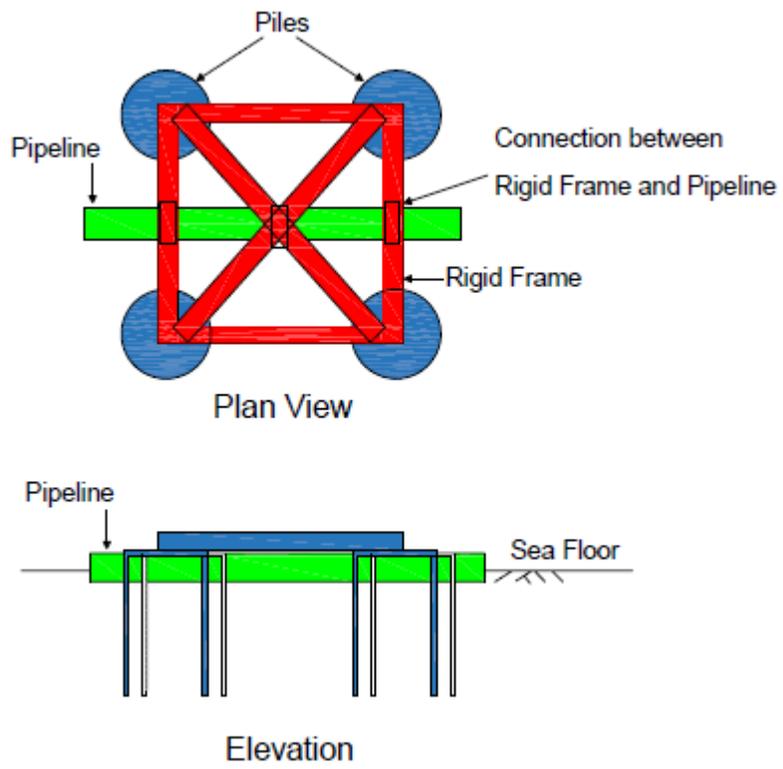
Figure 8-37: Fixed-head (cluster type).
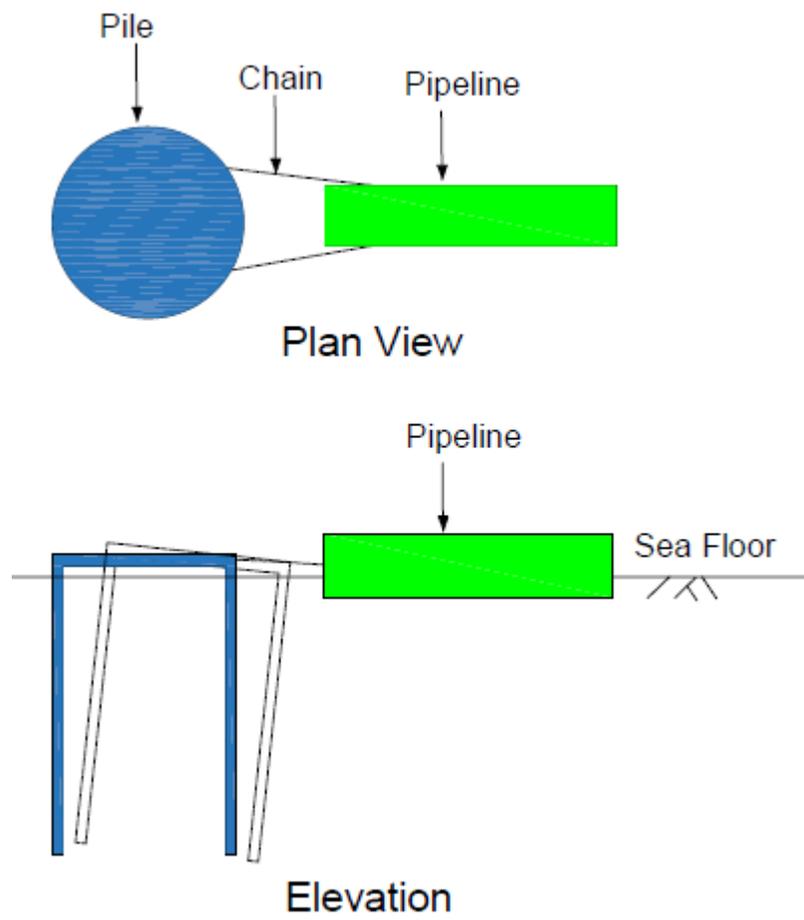
Figure 8-38: Free-head (single pile).
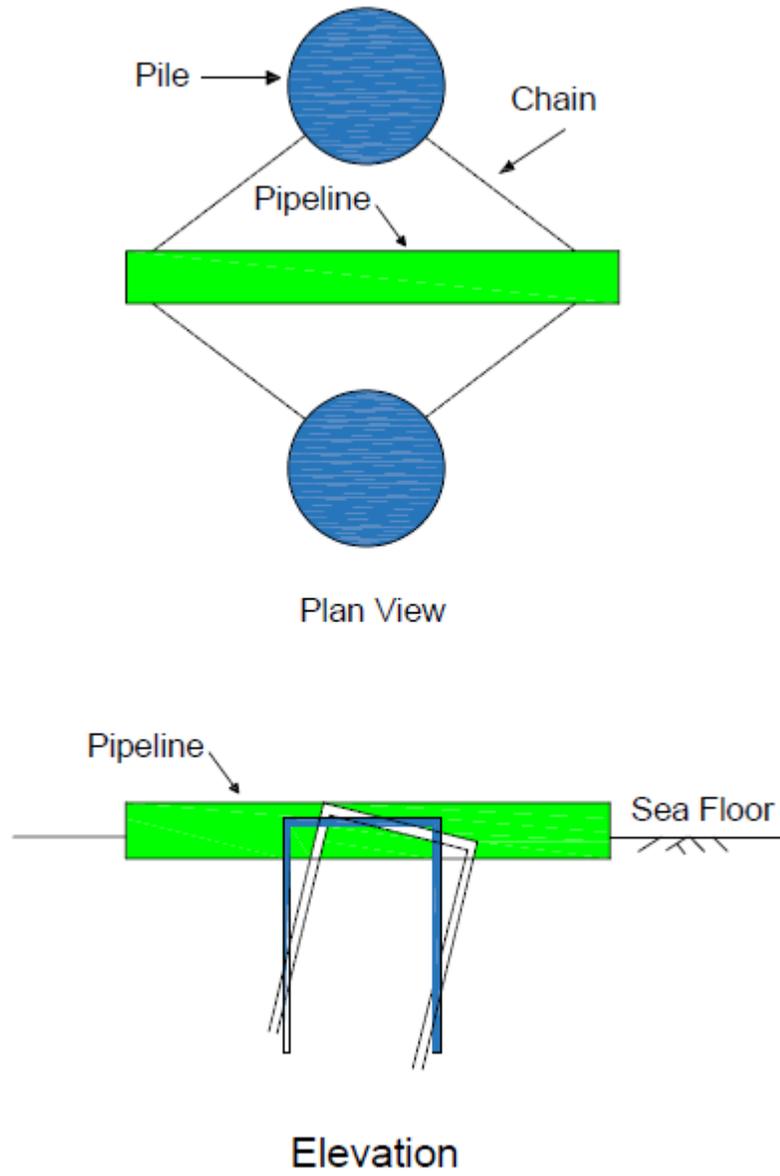
Figure 8-39: Free-head (dual piles).
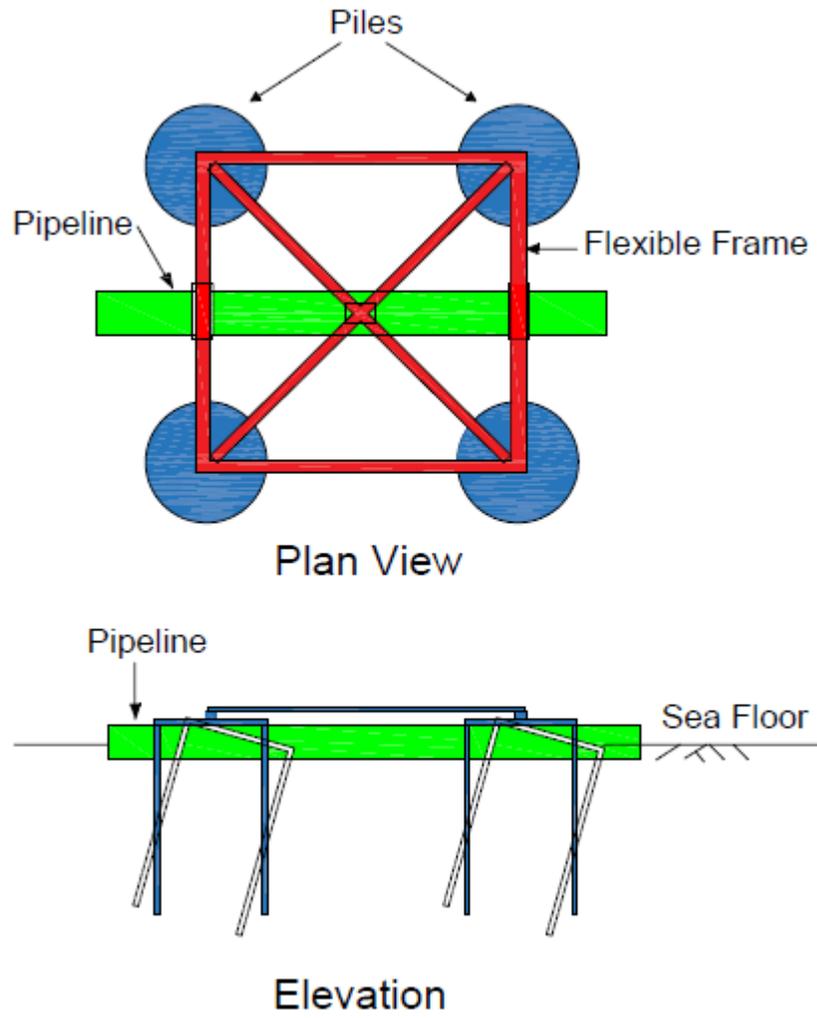
Figure 8-40: Free-head (cluster piles).

9 Chapter-9 – Paper No. 7

9.1 NOMENCLATURE

A	Pipe cross section
E	Material Young's modulus
I	Moment of inertia
K	Expansion of Fourier sine integral transformation
L	Span length
u_{cr}	Critical speed
u	Speed of slug
ρ	Steel density
α	Speed parameter

9.2 VALIDITY OF NORMALIZATION

Reda et al. (2011) demonstrated that the response of a simply supported beam under either a moving mass or a moving force, displays a response that is qualitatively similar to the single degree of freedom system. This is true provided the structure has light damping and the vibration modes are well separated. As a result, a more rational design methodology was adopted by relating two non-dimensional parameters: the dynamic load factor (DLF) and the speed parameter. The purpose of this section is to verify whether or not the relationship between the maximum normalized DLF and the speed parameter changes with span length and pipeline cross-section for the case of a moving mass. This is in order to validate the applicability of the normalization of the results obtained from the finite element analysis of the moving mass model. The verification is carried out at different slug mass to beam mass ratios and uses the moving concentrated mass model. The input data used for this comparative study is given in Table 9-1.

Table 9-1: Input Data.

Parameter	Units	Value
CASE-1		
Pipe outer diameter	mm	323.9
Wall thickness	mm	12.7
Material Young's modulus	GPa	205
Steel density	kg/m^3	7850
Total damping ratio	--	0.02
Speed parameter	--	0.1–2
Span length	m	30
CASE-2		
Pipe outer diameter	mm	406.4
Wall thickness	mm	15.7
Material Young's modulus	GPa	205
Steel density	kg/m^3	7850
Total damping ratio	--	0.02
Speed parameter	--	0.1–2
Span length	m	50

It is evident from Figure 9-1 and Figure 9-2 that the maximum normalized bending moment DLF for Case 1 and Case 2 is the same despite the different mass ratios. It can also be shown that for the moving mass model, the non-dimensionalization of the problem is shown to be valid, as is the case of a moving force across a beam span (Reda et al., 2011).
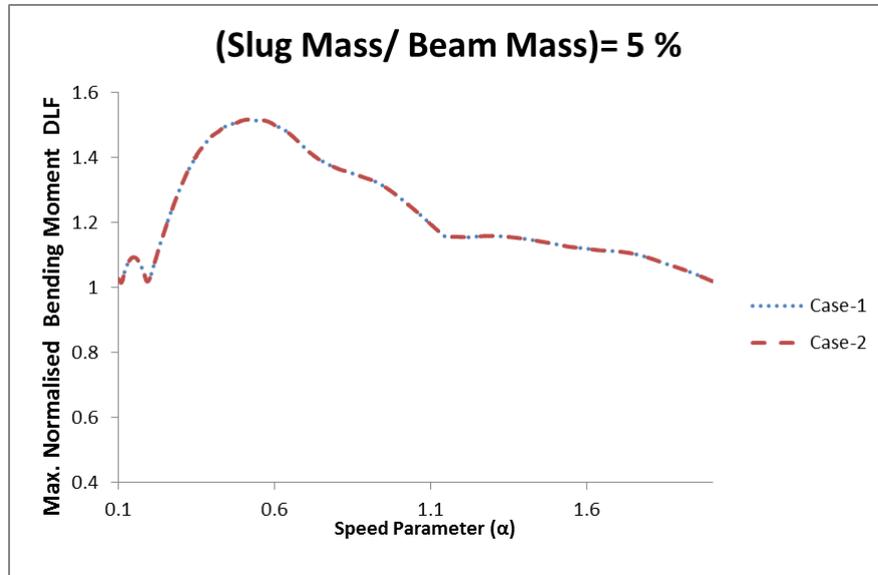
Figure 9-1: Validation of bending moment normalization at slug/beam mass = 5%.
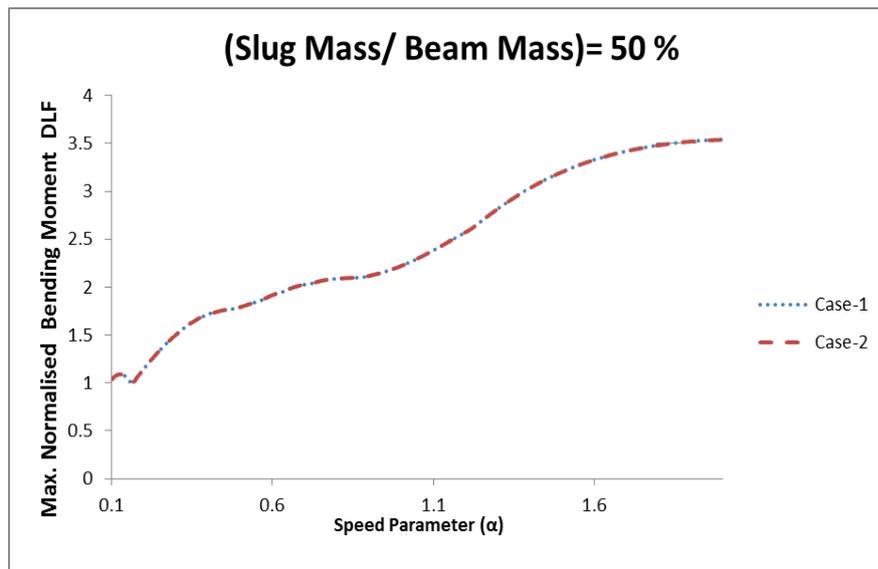
Figure 9-2: Validation of bending moment normalization at slug/beam mass = 50%.

9.3 INFLUENCE OF HIGHER MODES OF VIBRATION ON MAXIMUM NORMALIZED DLF OF DISPLACEMENT/BENDING MOMENT FOR MOVING FORCE MODEL

Reda et al. (2011) presented a solution for the governing equation of a simply supported beam subjected to a moving force. The solution was given in the form of a Fourier sine (finite) integral transformation (refer to Equations 9 and 10 in Reda et al. (2011)).

The aim of this section is to investigate the effect of higher modes of vibration, represented by the expansion of the Fourier sine integral transformation, on the maximum normalized DLF of displacement and bending moment.

Figure 9-3 illustrates the speed parameter versus the maximum normalized DLF of bending moment. By comparing the curve of K=1 with K=7 and K=40, one observes that the effect of the higher modes of vibration on the bending moment is significant. It is clear that using a single mode of vibration in the expansion series may not correctly predict the maximum normalized DLF of bending moment.
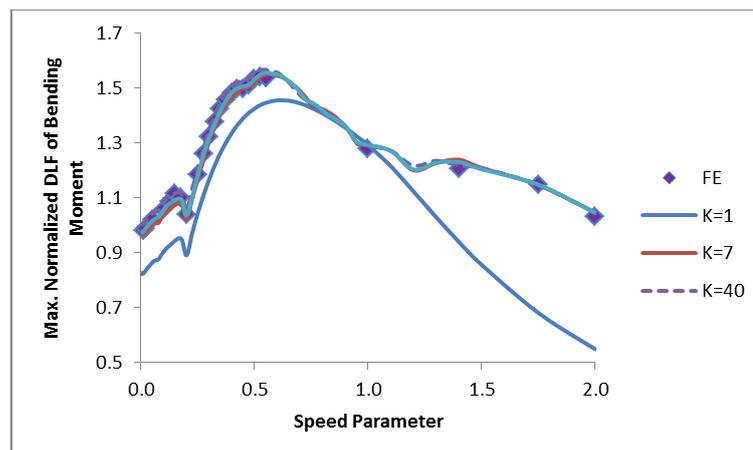
Figure 9-3: Impact of higher modes of vibration on maximum normalized DLF of bending moment for moving force model.

It is evident from Figure 9-3 that the finite element solution allows the effects of multi-vibration modes to be considered, as the finite element moving force results match the analytical solutions for K=7 and K=40. Note that the finite element model employed in this section is for the same span traversed by a moving concentrated force.

336

Conversely, as can be seen from Figure 9-4, the impact of higher modes of vibration in the expansion series on the displacement is not as significant as the bending moment. The maximum normalized DLF of displacement versus speed parameter relationships for K=1, K=7 and K=40 are in good agreement for all values of the speed parameter below 1.4. The only deviation occurs at speed parameters above 1.4, i.e. when the higher order modes in the expansion series become more dominant.
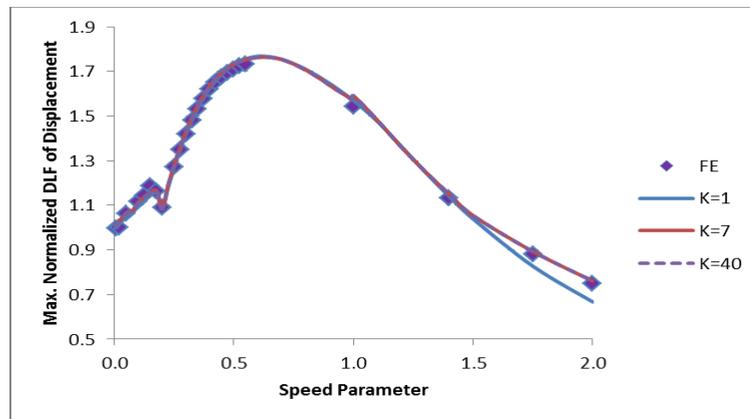
Figure 9-4: Impact of higher modes of vibration on maximum normalized DLF of displacement for moving force model.

Once again, the finite element model of the concentrated moving force yield excellent results when compared with the analytical solutions for K=7 and K=40. This further strengthens the assertion that the finite element model sufficiently accounts for higher modes of vibrations.

9.4   DISCRETIZATION CONSIDERATIONS IN MOVING FORCE FINITE ELEMENT BEAM MODEL

This section investigates the discretization errors induced in the finite element analysis of the moving concentrated force model. This is to help guide the development of a suitable mesh density for a beam type structure.

Discretization involves dividing the simply supported beam under consideration into an equivalent system of elements with associated nodes. The discretised geometry can, however, affect the accuracy and validity of the results significantly.

Proper discretization within a given structure is often a matter of engineering judgment. A careful balance must be maintained between accuracy and computation time.

Table 9-2 and Table 9-3 present the maximum normalized DLF for both bending moment and displacement, respectively, for different numbers of elements. They also present the maximum normalized DLF for both displacement and bending moment calculated using the analytical solution presented in Reda et al. (2011). In the following calculations, a 30 m long simply supported beam with damping ratio of 0% and a speed parameter of 0.8 was used.

Table 9-2: Maximum Normalized DLF Errors for Bending Moment for Different Number of Elements

Number of Elements	FE (DLF)	Analytical Solution (DLF)	Error [1] (%)	Error [2] (%)
2	0.948		32.909	--
4	1.290		8.705	26.512
8	1.363		3.539	30.448
16	1.393	1.413	1.415	31.945
32	1.393		1.415	31.945
64	1.395		1.274	32.043

Note:

1. Percentage error between the maximum normalized DLF, calculated using FE, and the analytical solution.
2. Percentage error between the maximum normalized DLF, calculated at a given number of elements, and the maximum normalized DLF corresponding to two elements.

Number of Elements	FE (DLF)	Analytical Solution (DLF)	Error [1] (%)	Error [2] (%)
2	1.422		16.647	--
4	1.659		2.755	14.286
8	1.672		1.993	14.952
16	1.674	1.706	1.876	15.054
32	1.682		1.413	15.453
64	1.682		1.407	15.458

Note:

1. Percentage error between the maximum normalized DLF, calculated using FE, and the analytical solution.
2. Percentage error between the maximum normalized DLF, calculated at a given number of elements, and the maximum normalized DLF corresponding to two elements.

It was observed that the bending moment was more sensitive than the displacement to mesh density. The results are shown for a single speed parameter and damping ratio, however for a complete mesh convergence test all speed parameters and damping ratios should be analysed as they both impact the displacement/bending moment shape and thus may necessitate different mesh densities.

With that said, the results presented in Table 9-2 and Table 9-3 are generally indicative of the mesh convergence for all speed parameters and damping ratios presented in this

paper. The results are also in good agreement with the discretization considerations for a moving force across a beam-like structure given in Rieker et al. (1996).

9.5   STATIC OR DYNAMIC ANALYSIS

The objective of this section is to provide guidance in order to determine at what speed a slug flow produces a dynamic amplification that is considerably over and above the static loading. This is to help determine the level of analysis required, before embarking on a more complex and expensive dynamic finite element analysis.

For any given speed parameter and damping ratio, the deviation of the maximum normalized DLF between a moving mass model and unity, is calculated using Equation 9-1:

$$\boldsymbol{Deviation}\ (\%) = \frac{(\boldsymbol{Maximum\ DLF})_{\boldsymbol{Moving\ Mass}} - 1}{(\boldsymbol{Maximum\ DLF})_{\boldsymbol{Moving\ Mass}}}$$

9-1

Figure 9-5 and Figure 9-6 highlight the deviations in the displacement and bending moment for the moving mass model, calculated using equation 9-1, at a damping ratio of 0.04.
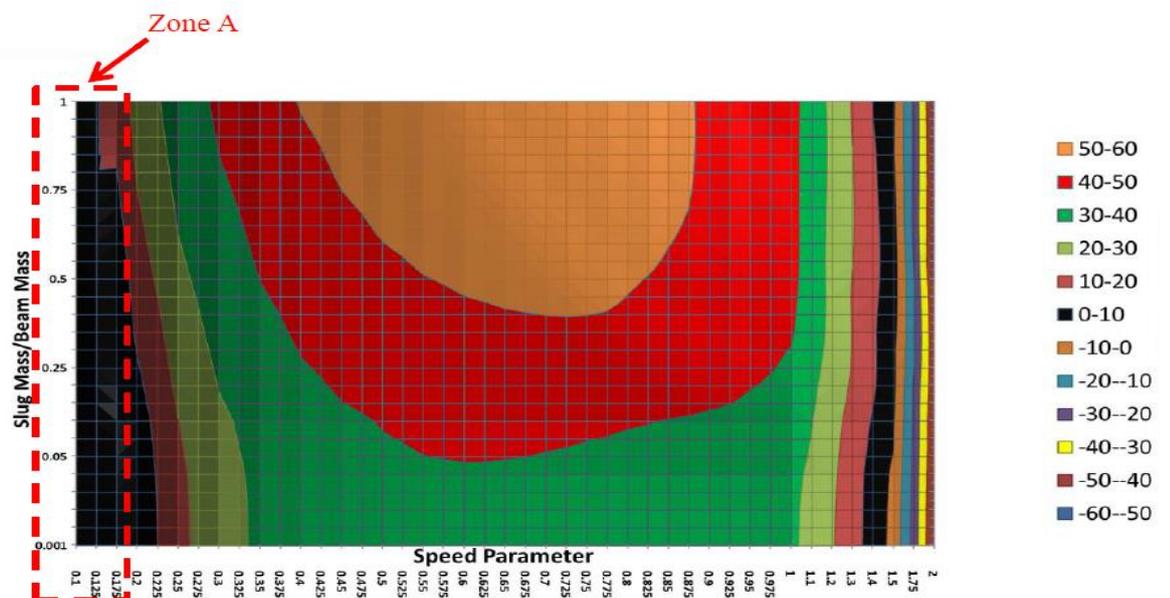
Figure 9-5: Deviations of maximum normalized DLF of displacement at a damping ratio of 0.04.

340
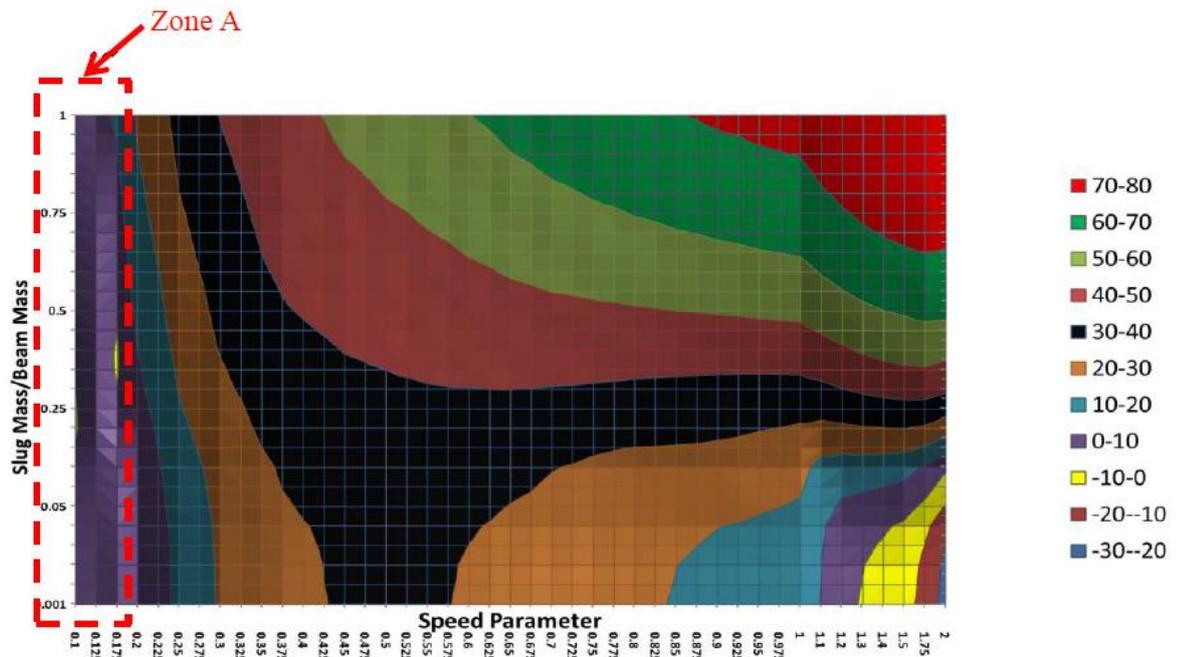
Figure 9-6: Deviations of maximum normalized DLF of bending moment at a damping ratio of 0.04.

The maximum normalized DLF for the moving mass model is determined from the finite element analysis of a simply supported beam with a point mass as per Reda et al. (2011).

It is worth mentioning that static and dynamic analyses were undertaken for various total damping ratios varying from 0 to 0.2, however for brevity, the results presented here are for a damping ratio of 0.04 only. The damping ratios selected were typical of a pipeline free span with two shoulders resting on a seabed (DNVGL-RP-F105, 2017; Gareth & Reda, 2013). Damping of a pipeline free span arises from the presence of structures, soil and fluid. Moreover, it is noted that the trend in deviation given in Figure 9-5 and Figure 9-6 are indicative of all damping ratios between 0 and 0.2.

From Figure 9-5 and Figure 9-6, the following conclusions are drawn:

- Negative deviation values denote that the dynamic analysis generates a smaller displacement/bending moment than the static analysis. Accordingly, a static analysis would be acceptable and indeed conservative.

- Deviation values equal to or less than +10% have been chosen as the limit to indicate that the use of static analysis is acceptable.

341

- It is concluded that a static analysis is sufficient for any speed parameter equal to, or less than, 0.175 for any given slug mass to beam ratio. This zone is highlighted in the figures and is denoted as Zone A.

- Deviation values greater than +10% indicate that the use of a static analysis is not acceptable and therefore the use of dynamic analysis would be required to obtain an acceptable approximation of the real displacement/bending moment within the system.

The results from the static and dynamic analyses quantitatively identify the following:

- Conditions under which a moving point mass across a simply supported beam can be adequately modelled as a static system, thus negating the need to undertake a dynamic analysis of the system.

- Dynamic analysis is not required for slug speeds below 0.175 of the beam span's critical speed. This is because the deviation, determined as per equation (9-1), is less than a 10% increase from the maximum static case. This criteria is denoted as a Zone A loading category in Figure 9-5 and Figure 9-6.

- Although the results shown in Figure 9-5 and Figure 9-6, have only been derived for a point mass, these results would also be applicable for slug lengths less than 10% of the span length. This is based on the work presented in Reda and Forbes (2011) and Rieker and Trethewey (1991). Nevertheless, these results may be conservative for slug lengths greater than 10% of the span as indicated by Reda and Forbes (2011).

In an effort to develop a quick tool to determine whether or not a particular span subjected to a moving load lies within Zone A, a design chart, as shown in Figure 9-7, was developed. The design chart has the following advantages:

- Allows easy interpretation of whether or not a particular slug speed, span length and pipe outer diameter, would lie within the Zone A loading category.

- Allows easy visualization of whether or not a decrease in span, change in pipe outer diameter or revised slug speed estimate would push the current pipe design outside of the Zone A loading category.

Figure 9-7 depicts the relationship between slug speed and span length for a group of pipe outer diameters with an upper limit of 0.175 non-dimensional speed parameter (note that this could be changed if the 10% DLF limit was increased or decreased). Figure 9-7 is beneficial in identifying which parameter can be changed for the pipeline span to lie within the Zone A loading category. As changing the length of the span or the pipe wall thickness will change the natural frequency of the span, the non-dimensional speed parameter, will consequently also change.
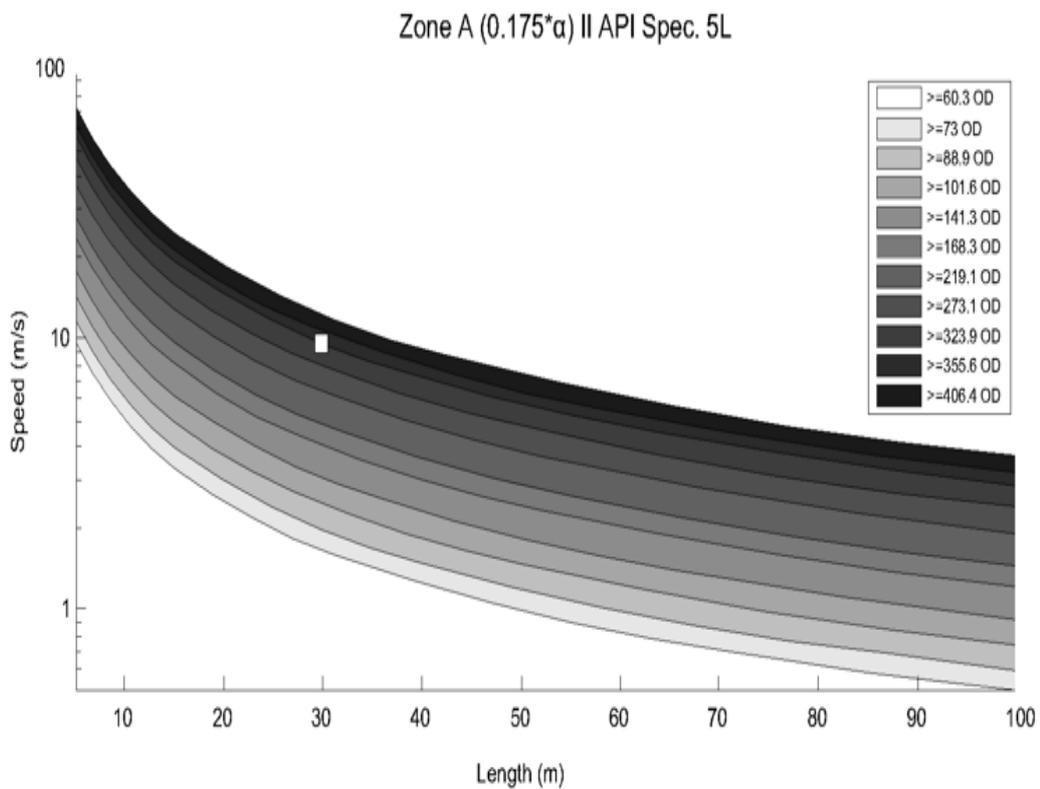
Figure 9-7: Zone A loading category graph for API Spec 5L.

To demonstrate how Figure 9-7 can be used, the limit for the requirement of dynamic analysis is marked for a slug speed of 10 m/s and 323.9 mm OD pipe. This is based on the dynamic response within 10% of the static loading. This indicates that for span lengths of less than 28.9 m no dynamic analysis would be required. The same conclusion is also valid for larger diameter pipes at the same speed and span length. However, for smaller diameter pipes (less than 323.9 mm OD) the span length would need to be reduced as per Figure 9-7.

343

It is important to highlight that Figure 9-7 may only be valid for span length to outer diameter ratios (L/OD) of less than 100. It is envisaged that future publications will deal with the extension of free spans into the regime of higher L/OD ratios.

It should be noted that the likely maximum slug velocity will not exceed the maximum permissible velocity of gas in a pipeline which is 40 m/sec. However, the results shown in Figure 9-7 are up to a maximum velocity of 80 /sec. The results above 40 m/sec are presented for interest.

9.6 APPLICABILITY OF THE MOVING CONCENTRATED FORCE MODEL AND THE MOVING CONCENTRATED MASS MODEL

The intention of this section is to help distinguish the conditions under which the two different models of a traversing concentrated force/mass over a structure should be used, and indeed, whether a dynamic analysis should even be pursued.

In the previous Section, conditions were introduced where the dynamic effects of the moving slug across a pipe span were negligible. A similar approach will be used here to discriminate between a moving force analysis and moving mass analysis. This will clarify when it is appropriate to simplify the moving load problem to a simplified moving force analysis with little loss of accuracy.

In this Section, an analytical moving concentrated force model and a finite element moving concentrated mass model are used. Both models are used to determine the maximum displacement/bending moment for any given speed parameter and damping ratio and slug mass to beam mass ratio. The maximum displacement/bending moment is then divided by the static displacement/bending moment in order to determine the maximum normalized DLF of displacement/bending moment.

It should be noted that both the maximum dynamic load and static load are calculated for the same cross-section of the pipe and the same concentrated force/mass.

For any given speed parameter and damping ratio, the deviation between the maximum normalized DLF, calculated from the moving concentrated force and moving concentrated mass models, is obtained using Equation (9-2):

344

$$Deviation\ (\%) = \frac{(Maximum\ DLF)_{Moving\ Mass} - (Maximum\ DLF)_{Moving\ Load}}{(Maximum\ DLF)_{Moving\ Mass}}$$

Once again, the applicability assessment of the moving concentrated force model and the moving concentrated mass model is undertaken using damping ratios varying from 0 to 0.2. The results presented here are for a damping ratio of 0.04 only.

Figure 9-8 highlights the deviation of maximum normalized DLF of displacement at a damping ratio of 0.04.
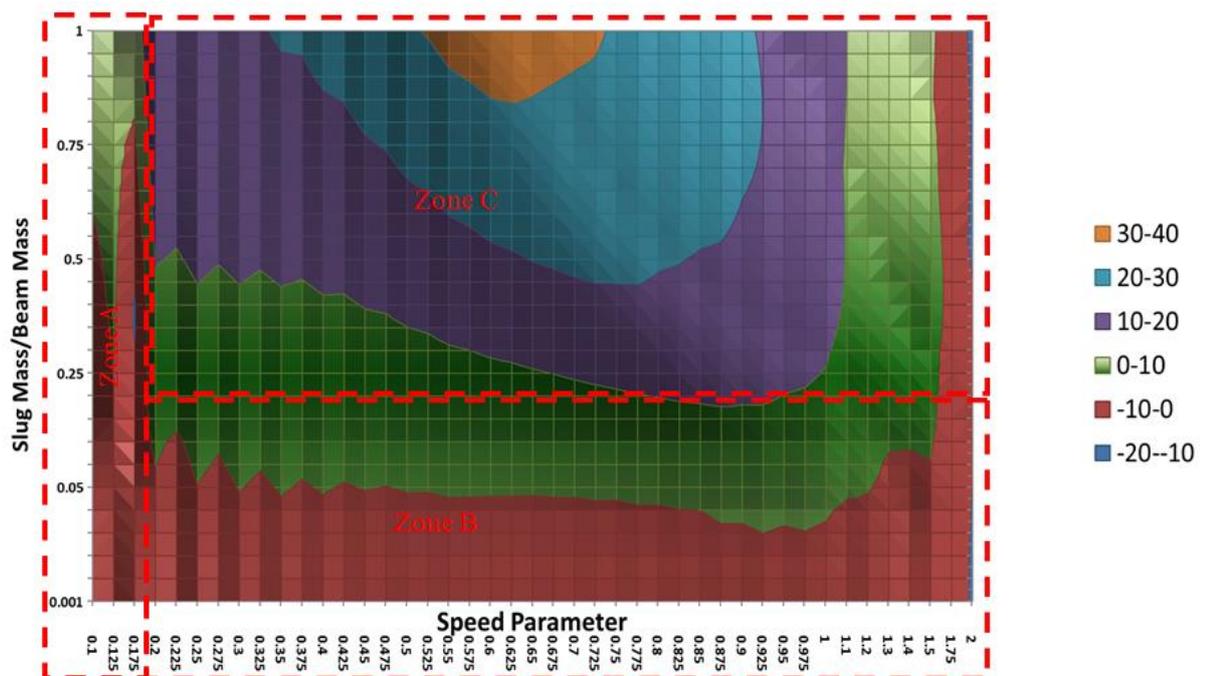
Figure 9-8: Deviation of maximum normalized DLF of displacement at a damping ratio of 0.04

Based on Figure 9-8, the following conclusions are drawn:

1a.   A negative deviation indicates that the moving force model over-predicts the normalized maximum DLF.

2a.   The moving concentrated force model over-predicts the maximum normalized DLF of displacement between the speed parameters of 0 and 0.175, irrespective of the slug mass/beam mass ratio.

3a.   The moving concentrated force model over-predicts the maximum normalized DLF of displacement between the speed parameters of 1.75 and 2, irrespective of the slug mass/beam ratio.

4a.   The moving concentrated force model over-predicts the maximum normalized DLF of displacement between the speed parameters of 0 to 2 when the slug mass/beam mass ratio is less than 5 %.

5a.   The green area indicates that the moving concentrated force model can still be used with a reasonable level of confidence, since the deviation is between 0 and +10%.

6a.   The deviation results indicate that the moving concentrated mass model should be used in the purple, light blue as well as the orange areas, as the deviation is greater than +10%.

From Figure 9-8 one can see that the deviation alternates between positive and negative for certain mass ratios across the lower speed regions. An example of this oscillation can be seen in the sudden step change from the red area to the green area between the speed parameters of 0.175 and 0.2. This occurs only when the slug mass/beam mass ratio is greater than 7.5 %. This could be due to the fact that for small slug mass/beam mass ratios (less than 7.5%), the moving force and moving mass critical speeds are very close. This may be because the added mass in the moving mass model is small and can be disregarded in comparison to the beam mass. This will be further explained in Figure 9-9 and in Figure 9-10.
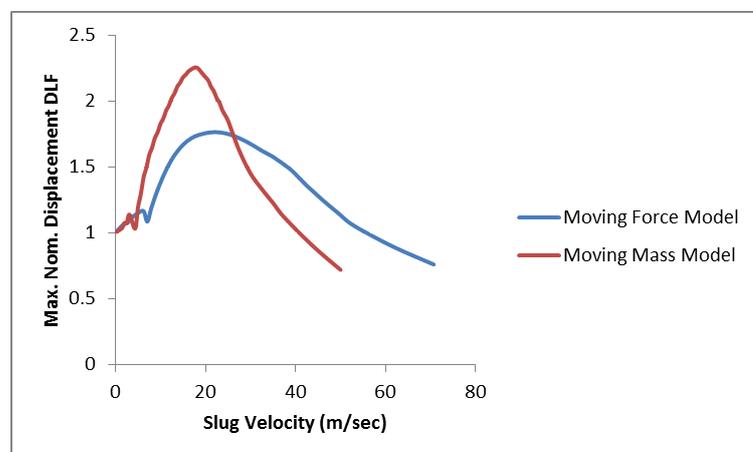
Figure 9-9: Moving mass versus moving force displacement DLF at a slug/beam mass ratio = 0.5.
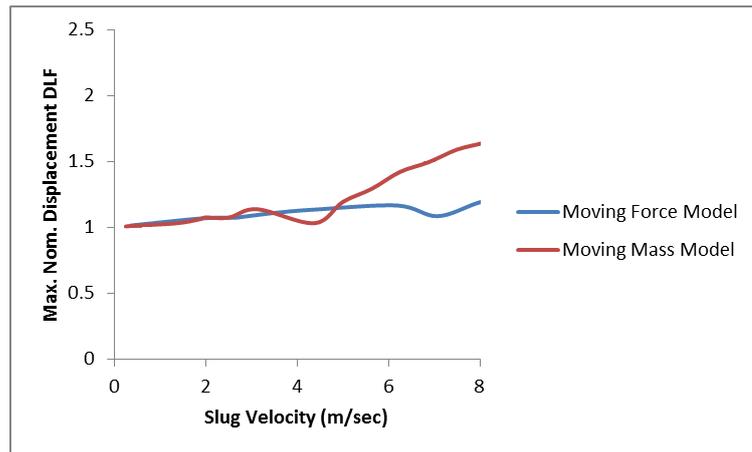
Figure 9-10: Close-up of moving mass versus moving force displacement DLF at a slug/beam mass ratio = 0.5.

Figure 9-9 and Figure 9-10 were developed to help visualize the difference between the predictions of the moving force model DLF and the moving mass model. In Figure 9-9 , for low speeds (close to 1 m/sec), the moving force and moving mass models are relatively similar in their predictions. As the speed increases, the moving force model under-predicts the moving mass model until this changes at higher speeds. In general, the shape of the two graphs for both the moving force and moving mass models are similar, with the peak occurring at a lower speed for the moving mass model due to the lower natural frequency of the system. This is because the moving mass is added to the mass of the underlying beam structure. It is evident that for slug velocities between 5 m/sec and 27 m/sec, the moving mass is more conservative. This is, however, reversed at high velocities.

One can see from Figure 9-10 that for a speed velocity in the range of 1 m/sec to approximately 5 m/sec, there is a dip and then rise in the DLF for the moving mass model, thus causing an alternating over and under-prediction of the moving force model as compared to that of the moving point mass. A similar result is observed when viewing the bending moment DLF in Figure 9-11.

Figure 9-11 depicts the deviation of maximum normalized DLF of bending moment at a damping ratio of 0.04. The bending moment deviations are only investigated for speed parameters between 0.1 and 2. This is due, in part, to the long computation time

347

associated with speed parameters of less than 0.1. However, it is expected that the moving force model will be a valid model for all ratios below 0.1.
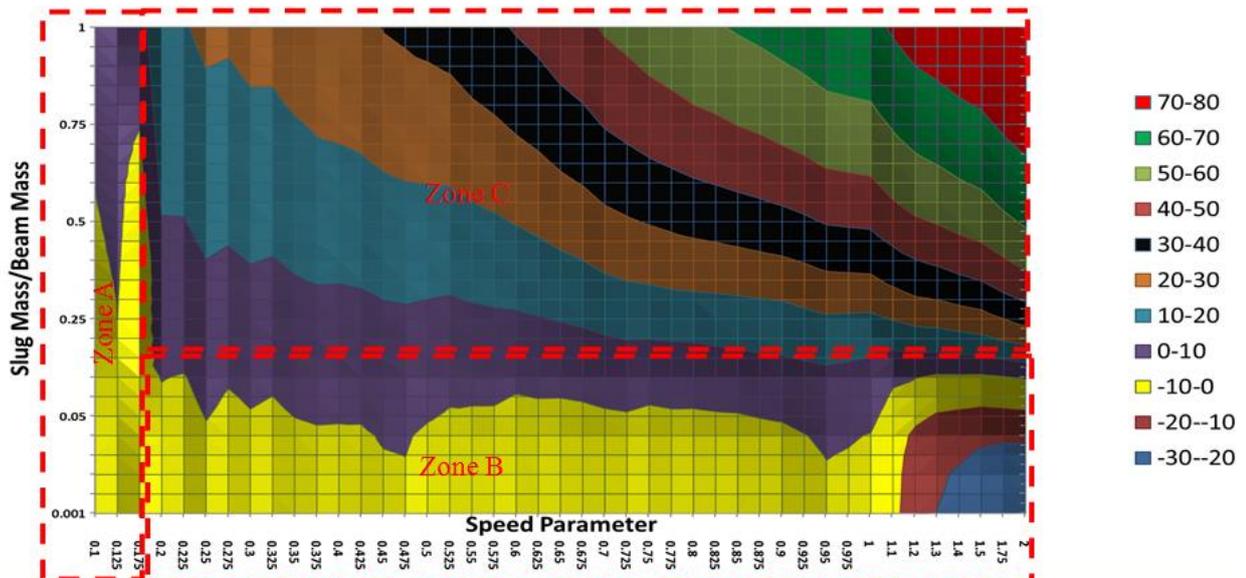
Figure 9-11: Deviation of maximum normalized DLF of bending moment at a damping ratio of 0.04.

Based on Figure 9-11, the following conclusions were drawn:

1b   A negative deviation indicates that the moving force model over-predicts the normalized maximum DLF.

2b   The deviation results show that the moving concentrated force model over-predicts the maximum normalized DLF of bending moment between the speed parameters of 0 and 0.175, irrespective of the slug mass/beam mass ratio.

3b   The moving force model is still valid for the area that represents errors between 0 and +10%.

4b   The moving concentrated force model over-predicts the maximum normalized DLF of bending moment between the speed parameters of 0.1 to 2. This is only true when the slug mass/beam mass ratio is less than 5%.

5b   Deviations of less than +10% indicate that the moving concentrated mass over-predicts the maximum normalized DLF by less than 10%. This proves that the moving concentrated force model can still be used with a reasonable level of confidence.

348

6b   The areas with deviations greater than +10% indicate that the moving concentrated mass model has to be used.

From the observations of Figure 9-8 and Figure 9-11, it is proposed that two additional loading categories are given in conjunction with the Zone A loading category above.

- **Zone B:** a moving force analysis is needed to adequately model the dynamic effects of a moving slug to within a 10% deviation of the actual loading. This zone is bounded by mass ratios less than 0.2 and speed parameters greater than 0.175.

- **Zone C:** a moving mass analysis is needed to adequately model the dynamic effects of a moving slug. This zone is bounded by mass ratios greater than 0.2 and speed parameters greater than 0.175.

The above zone boundaries are generally applicable to all damping ratios and can be altered to represent limits of the dynamic application factor other than the 10% deviation limit used here.

10   Chapter-10 – Paper No. 8

Title: **"Vibration of a curved subsea pipeline due to internal slug flow"**

Authors: **Ahmed Reda, Gareth Forbes, Kristoffer McKee, Ian Howard**

Journal: **Proceedings of the 43rd International Congress on Noise Control Engineering**

Publication date: **2014**

Publisher: **Australian Acoustical Society**

10.1 SLUG FLOW

Slug flow is an unstable flow phenomenon that occurs in multiphase pipelines under certain conditions. Slug flows can pose considerable challenges in terms of pipeline design and operability. Near horizontal pipelines, at low to moderate gas and liquid flow rates, can experience a number of various slug flow regimes which are characterized by alternating periods of high liquid production rates (slugs) followed by high gas production rates (gas bubbles), as shown in Figure 10-1. The likelihood of slug flows occurring is a function of both the incoming fluid as well as the pipeline layout. Processing of these slugs in topside separator facilities can be extremely difficult if the slugs become excessively long.
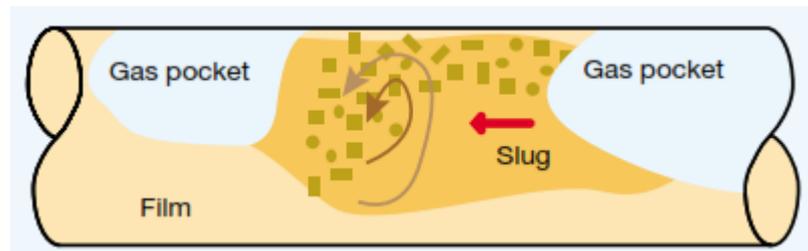
Figure 10-1 Internal slug flow schematic (Havre (1072000107)).

10.2 MOVING POINT FORCE

10.2.1 Moving Point Force

In order to investigate the vibration and dynamic motion of a pipe span due to internal slug flow, the moving slug will be modelled as a moving point force across a beam span. This modelling procedure has been shown to be an adequate simplification of the real distributed moving mass of internal pipe slug flow (see Reda et al. (2011) and Reda and Forbes (2011)).

10.2.2 Moving Point Force Across a Straight Beam

For a moving point force across a single straight beam span, shown schematically in Figure 10-2, the general form of the finite element equations of motion are given by:

351

$$[M]\{\ddot{u}\} + [C]\{\dot{u}\} + [K]\{u\} = \{F(t)\}$$

<div align="right">10-1</div>

The force vector due to a moving point force, F(t), has been previously derived by Wu et al. (2000), and can be written as the following:

$$\{F(t)\} = \{000...f_1^{(s)}(t)\,f_2^{(s)}(t)\,f_3^{(s)}(t)\,f_4^{(s)}(t)...000\}$$

<div align="right">10-2</div>

where $f_i^{(s)}(t)(i = 1-4)$ represents the equivalent nodal forces on element 's' which the force is traversing at that particular time. Additionally, $\{N\}$ is the element shape function matrix (see Wu et al., (2000)) such that:

$$\{f^{(s)}(t)\} = \left\lfloor f_1^{(s)}(t)\,f_2^{(s)}(t)\,f_3^{(s)}(t)\,f_4^{(s)}(t)\right\rfloor^T = P\{N\}$$

<div align="right">10-3</div>

10.2.3 Moving Point Load on a Curved Beam

For a moving force across a curved beam of arbitrary shape, the distance between two sets of nodes on the finite element model needs to be calculated in a more sophisticated manner than that of a simple straight beam. Additionally, the nodal force needs to be converted into the local coordinate system for the element of interest and the inclusion of an axial deformation term in the element formulation needs to be considered, as shown in Figure 10-3. The derivation of the force vector due to a curved beam with a moving vertical force will be calculated below.
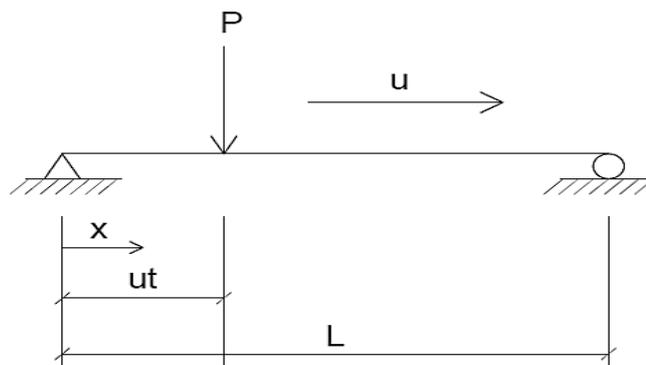
Figure 10-2: Schematic of a moving force 'P' moving across a simple straight beam span.

Consider a curved beam under the influence of a force, P, traveling at a constant speed relative to the pipe, as shown in Figure 10-3. The distance, $S_p(t)$, travelled by the force can be shown to be:

$Sp(t)=m.V.\Delta t$

10-4

where:

V = slug load speed,

Δt = time step size.

m = time step.
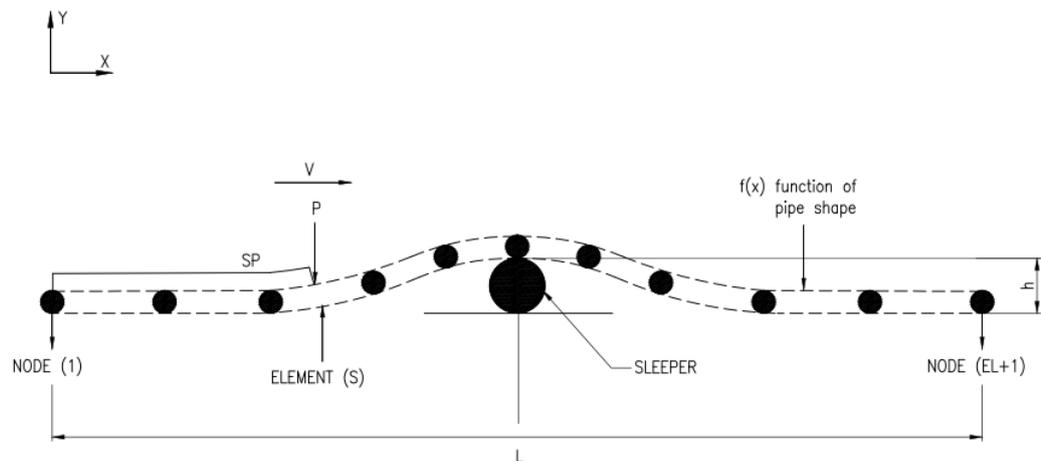
Figure 10-3: Curved beam subjected to a slug load, P, moving with velocity, V.

In order to find the distance that the force has travelled across element 's' at any given time, the length of the curve needs to be calculated. The length of each element 'arc_length(j)' can be shown to be (see Figure 10-4 for definition of arc length as a function of node x and y coordinate):

$$arc_{length}(s) = \sqrt{\Delta x\,(k)^2 + \Delta y\,(k)^2}$$

10-5
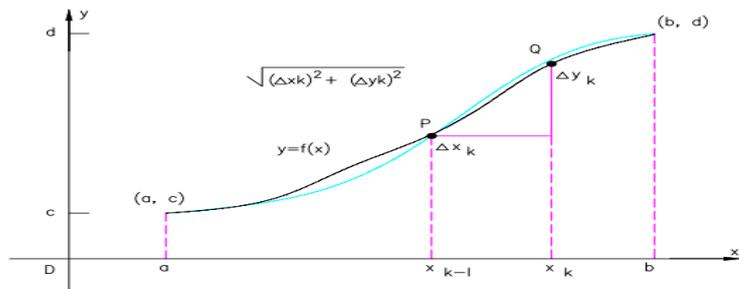
Figure 10-4: Schematic of arc length of a curve.

The non-dimensional distance, ξ, that force, P, has travelled across element 's' can now be described as the following:

$$\xi = \frac{S_p(t) - \sum_{j=1}^{s} arc_{length}(j)}{arc_{length}(s)}$$

10-6

Now that the location of the force at any given time has been derived, the force vector for all nodes can be calculated as the vertical force traverses the curved span as shown in Figure 10-5:

$$\{F(t)\} = \{0 \ldots F(t)_1{}^Q \ F(t)_2{}^Q \ F(t)_3{}^Q \ F(t)_4{}^Q \ F(t)_5{}^Q \ F(t)_6{}^Q \ldots 0\}$$

10-7

where:

$$F(t)_1{}^Q = (P \sin(\emptyset)).N_1$$

10-8

$$F(t)_2{}^Q = (F_C + P \cos(\emptyset)).N_2$$

10-9

$$F(t)_3{}^Q = (F_C + P \cos(\emptyset)).N_3$$

10-10

$$F(t)_4{}^Q = (P \sin(\emptyset)).N_4$$

10-11

354

$$F(t)_5{}^Q = (F_C + P\cos(\emptyset)).N_5$$

$$F(t)_6{}^Q = (F_C + P\cos(\emptyset)).N_6$$

Here I have introduced two coordinates systems: a local one, (X,Y), directed along the length of the element, and a global one $(\overline{X},\overline{Y})$. The global coordinate is selected such that it is best suited to the whole sleeper model. The forces shown above were derived in the local coordinates, where P and F_C are the magnitude of the slug force and the centrifugal force, respectively. Using the mass of the moving slug, m_{slug}, the tangential speed, V, and the radius of curvature of the span, ρ, the force terms P and F_C can be expressed as the following:

$$P = m_{slug}.\text{g}$$

$$F_C = \frac{m_{slug}.V^2}{\rho}$$

If N_i $(i = 1 - 6)$ represents the shape function for a straight beam element, then the shape functions for a cubic beam element can be defined as (Przemieniecki,1985):

$$N_1 = 1 - \xi$$

$$N_2 = 1 - 3\,\xi^2 + 2\,\xi^3$$

$$N_3 = (\xi - 2\,\xi^2 + \xi^3).L$$

$$N_4 = \xi$$

$$N_5 = 3\,\xi^2 - 2\,\xi^3$$

$$N_6 = (-\,\xi^2 + \xi^3).L$$

The local forces must be transformed to the global coordinates. The global forces are dependent on the location of the slug. Assuming that the slug load is located between node 1 and node 2, as shown in Figure 10-5, then the global forces can be expressed as the following:

$$F_{\bar{X}} = F(t)_1{}^Q.cos(\emptyset) - F(t)_2{}^Q.sin(\emptyset) + F(t)_4{}^Q.cos(\emptyset) - F(t)_5{}^Q.sin(\emptyset)$$

10-22

$$F_{\bar{Y}} = F(t)_1{}^Q.sin(\emptyset) + F(t)_2{}^Q.cos(\emptyset) + F(t)_4{}^Q.sin(\emptyset) + F(t)_5{}^Q.cos(\emptyset)$$

10-23
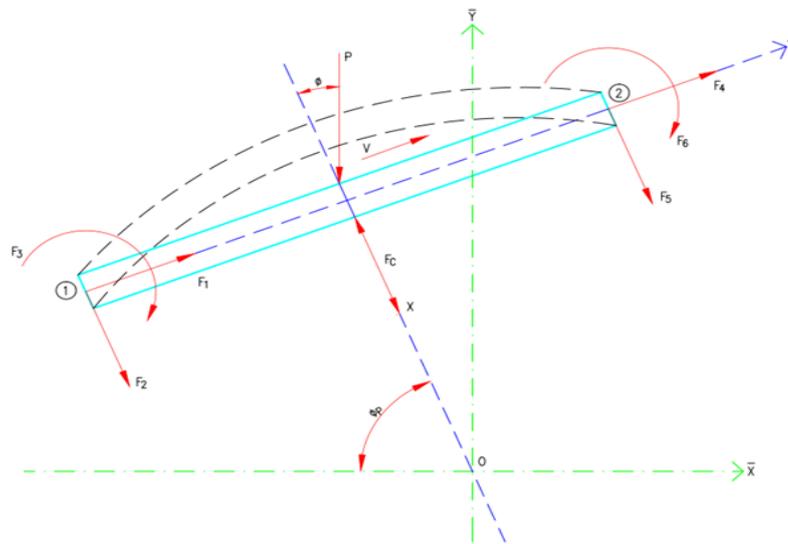
Figure 10-5: External and nodal forces on element 's'.

10.2.4 Non-dimensional Centrifugal Force Parameter

The difference in nodal forces between a straight beam and a curved beam is a result of both the curvature of the beam that changes the direction of the applied vertical load, as well as the centrifugal force that arises due to the fluid flow now following a curved path. This suggests that the effect of curvature on the nodal forces will be a function of both the degree of curvature and the velocity of the traversing force.

356

The centrifugal force is given as:

$$F_c = \frac{mv^2}{\rho}$$

10-24

For a simple half sine wave, the shape of the pipeline lying over the sleeper is defined as:

$$f(x) = \frac{h}{2}\left[1 - \cos\left(\frac{2\pi x}{L}\right)\right]$$

10-25

The radius of curvature is simply the inverse of the second derivative of the pipeline shape, and can be shown to be:

$$\rho = \frac{2}{h}\left(\frac{L}{2\pi}\right)^2 \sec\left(\frac{2\pi x}{L}\right)$$

10-26

Therefore, the maximum centrifugal force exerted by the slug will occur at the centre of the span, and have the value of:

$$F_{Cmax} = \frac{2mV^2 h\pi^2}{L^2}$$

10-27

A new non-dimensional parameter, γ, is introduced to describe the percentage contribution of the maximum centrifugal force compared to the original vertical force of the slug, and is:

$$\gamma = \frac{F_c}{mg} = \frac{2V^2 h\pi^2}{gL^2} * 100 \%$$

10-28

It can be seen that γ is a function of the span curvature (h/L^2) and the traversing speed of the force (V^2). For small γ values, the effect of curvature will not have any significant change on the applied nodal forces as compared to a straight beam.

357

10.3 FINITE ELEMENT MODEL

Notwithstanding the sophistication of commercial finite element packages such as ABAQUS and ANSYS, a large amount of effort is still required to model a moving force using these commercial software packages. This thesis utilized the commercial finite element package ABAQUS to model the pipeline and run the FE analysis, but the input force was applied using an in-house subroutine that employed the above derivation of the nodal forces.

Initially, the general-purpose FE implicit solver ABAQUS was used to lay the pipeline over the sleeper and on the seabed. This was in order to obtain the correct as-laid shape for the pipeline over a span (note that the previous derivation for the centrifugal force was for a sinusoidal type lay shape). Once the static analysis was completed, the pipeline coordinates were exported to a subroutine (developed in-house) to generate a force input file.

Upon completion of the static analysis, a dynamic analysis was performed to investigate the dynamic behaviour of an unbuckled pipeline over the buckle initiator sleeper. The dynamic analysis was undertaken using the implicit Hiller Hughes Taylor operator for integration of the equation of motion.

The pipe was modelled using PIPE31H, a 2-noded hybrid formulation pipe element. The reason for selecting this pipe element is because it is well suited to modelling long slender pipelines with better convergence behaviour than standard pipe elements. An element length of 0.5 m was used.

The seabed and sleeper were modelled using an analytical rigid cylindrical surface. Contact between the pipe and the seabed was modelled as soft contact. Friction between the pipeline and the seabed was assigned to the seabed in the axial and lateral directions. The standard ABAQUS friction model was employed in the analysis. The friction between the pipe and the sleeper was modelled using a simple Coulomb friction model. The contact between the pipeline and sleeper was modelled using contact elements. Figure 10-6 shows a representation of the resultant finite element model.

The following loading sequence was employed in the finite element model to investigate the dynamic response of a pipeline span to time variant moving loads:

1. Apply a small lateral out of straightness (OOS) to the straight pipe.

2. The value considered in the analysis is the maximum allowed OOS in a single pipe joint as defined below. This is consistent with DNV-OS-F101.

   OOS $\leq$ 0.15 % Pipe Joint

3. Apply external pressure.

4. Apply gravity to settle the pipe on the seabed.

5. Reset the boundary conditions.

6. Apply internal operating pressure (internal pressure is assumed to be equal to external pressure).

7. Restart dynamic analysis to determine the stress ranges and span displacements.
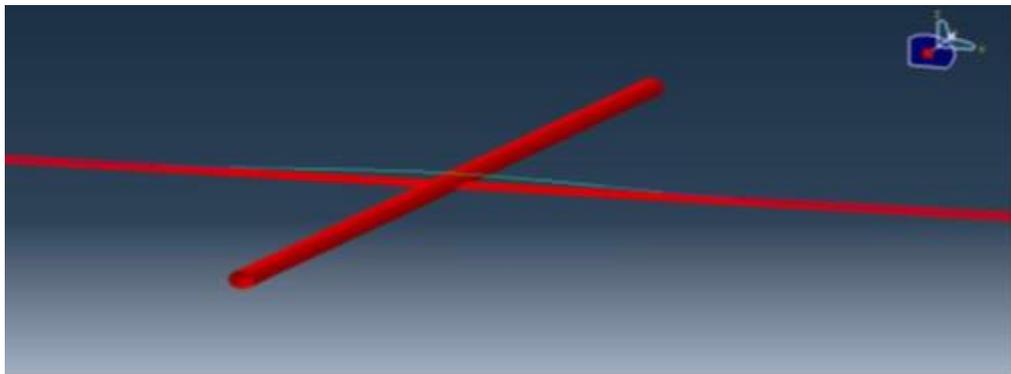
Figure 10-6: ABAQUS finite element model showing the sleeper and ground contact surface in red. The pipeline is shown in blue.

10.3.1 Input Data and Assumptions

The input data used in this thesis is shown in Table 10-1.

Table 10-1: Input Data

Parameter	Unit	Value
Pipe outer diameter	mm	219.1
Wall thickness	mm	15.9
Steel density	kg/m^3	7850
Pipe unit submerged weight	N/m	456.6

Slug load	kg	100
Modulus of elasticity	GPa	207
Sleeper height	m	1.2
Slug speed	m/s	8, 15 & 30

The following assumptions have been made:

- The pipe is of constant cross section and constant unit mass per length.

- The mass of the moving load is smaller than the mass of the beam.

- The velocity of the slug is constant along the span.

- The slug is modelled as a point load.

- Vibration due to slugs passing through the pipeline span will only incur in the vertical pipe plane.

10.3.2 Results

A modal analysis to determine the mode shapes and the natural frequency of the span was conducted. The first 3 natural frequencies are listed in Table 10-2, with the mode direction being either transverse to the span plane (in-line) or in-plane with the span (cross-flow). The mode shapes generally came in in-line/cross-flow pairs with only a slight difference in frequency, as would be expected for an axisymmetric structure with only a small amount of out of straightness (due to the pipeline bending over the sleeper). The mode shapes for the corresponding in-line and cross-flow modes are almost identical, as can be seen with mode 1 and mode 2 overlapping one another in Figure 10-7.

Table 10-2 - Mode Shape Natural Frequencies

Mode #	frequency (Hz)	Mode direction
1	0.85175	Inline
2	0.88617	Cross-flow

Mode #	frequency (Hz)	Mode direction
3	1.1634	Inline
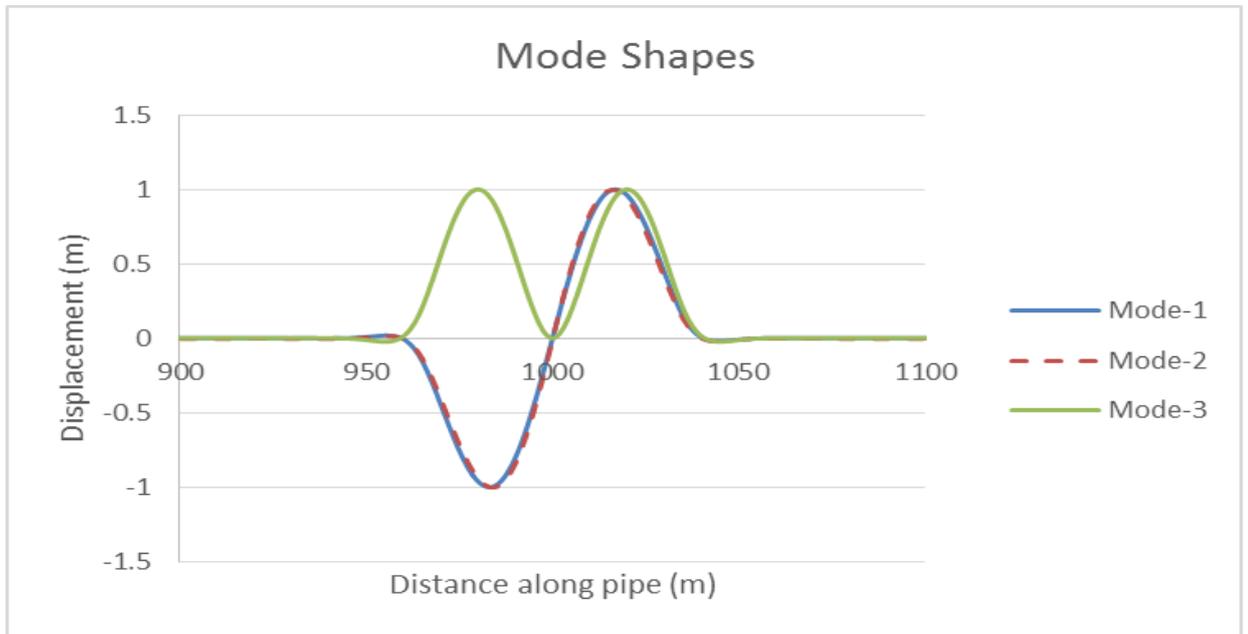
Figure 10-7: First 3 mode shapes of pipeline.

The finite element model was run for three different pipe span and velocity cases to determine the effect of the pipeline out of straightness on the dynamic response of the pipeline. Table 10-3.

For each velocity case, the centrifugal force parameter was removed so that the effect of the span out of straightness could be assessed. The vertical and axial displacement and axial stress in the pipeline with and without the centrifugal force are given in Figure 10-8 to Figure 10-13. It can be seen that the inclusion of the centrifugal force does not have any significant impact on either the maximum stress or the deflection (at any location along the length of the span) for the speeds of 8 m/s and 15 m/s. This result was expected due to the fact that the non-dimensional centrifugal force parameter for both these cases was less than 10%. In other words, the combined effect of the out of straightness and the slug velocity only changes the applied force by approximately 10% as compared to a simple straight span.

An example of just how greatly slug speed and span out of straightness can affect results can be seen in the case where the slug speed is 30 m/s. The stress at the centre

of the span is reduced due to the increased slug speed. The force slug speed increases as a result of the centrifugal force vector being in the positive vertical direction thereby offsetting some of the weight force of the slug. In particular, as can be seen in Figure 13 and Figure 14, the axial stress changes only slightly with the inclusion of the centrifugal force for slug speeds of 8 m/s and 15 m/s. This is contrast with the slug speed of 30 m/s, where the stress is reduced by approximately 40%. This is in reasonable correlation with the non-dimensional force parameter of $\gamma = 34\%$.

In conclusion, the stress pattern of the pipeline span is reasonably complex for all slug speeds and is not easily described by the simplified non-dimensional force parameter. This implies that there is a need for the finite element modelling of the pipeline span and force interaction if accurate stress values are required.

Table 10-3 – Results and Case Parameters

	v (m/s)	L (m)	h (m)	f(x)	γ	Fc included
Case 1	8	80	1.2	natural lay	2.4%	Yes
Case 2	8	80	1.2	natural lay	2.4%	No
Case 3	15	80	1.2	natural lay	8.5%	Yes
Case 4	15	80	1.2	natural lay	8.5%	No
Case 5	30	80	1.2	natural lay	34%	Yes
Case 6	30	80	1.2	natural lay	34%	No
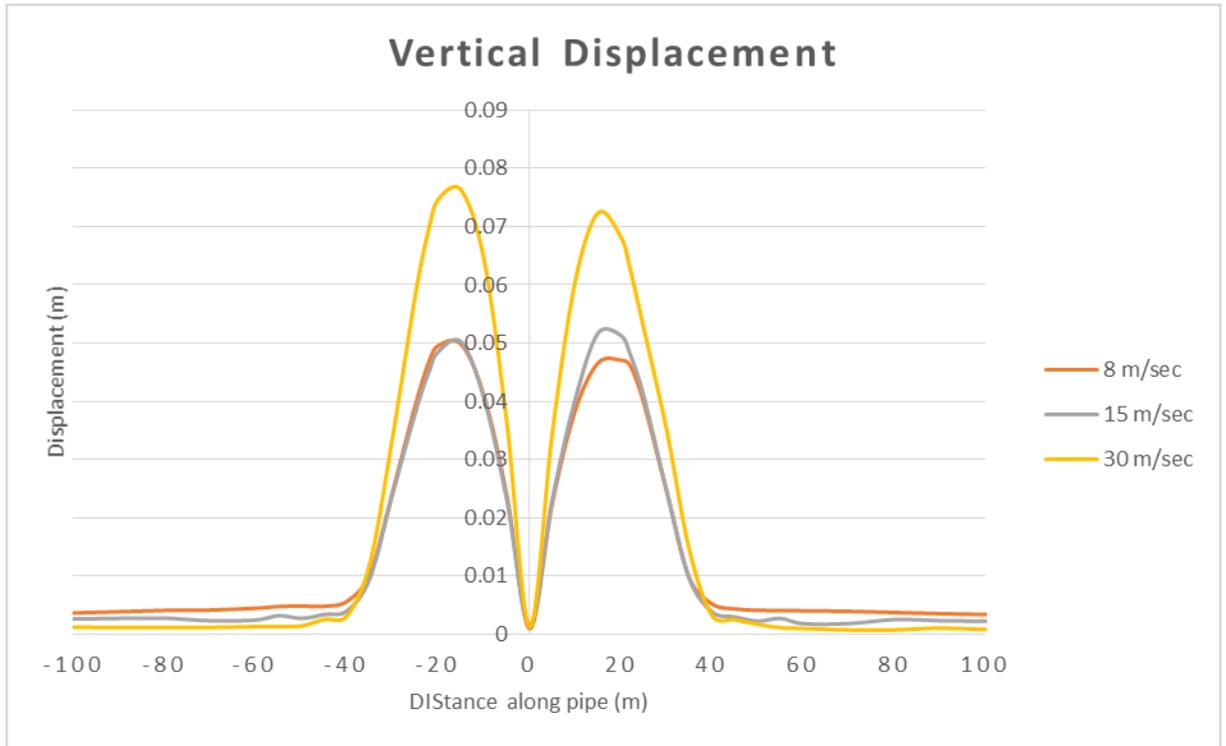
Figure 10-8 Maximum vertical span deflection across the span length as the force traverses the span. Centrifugal force included.
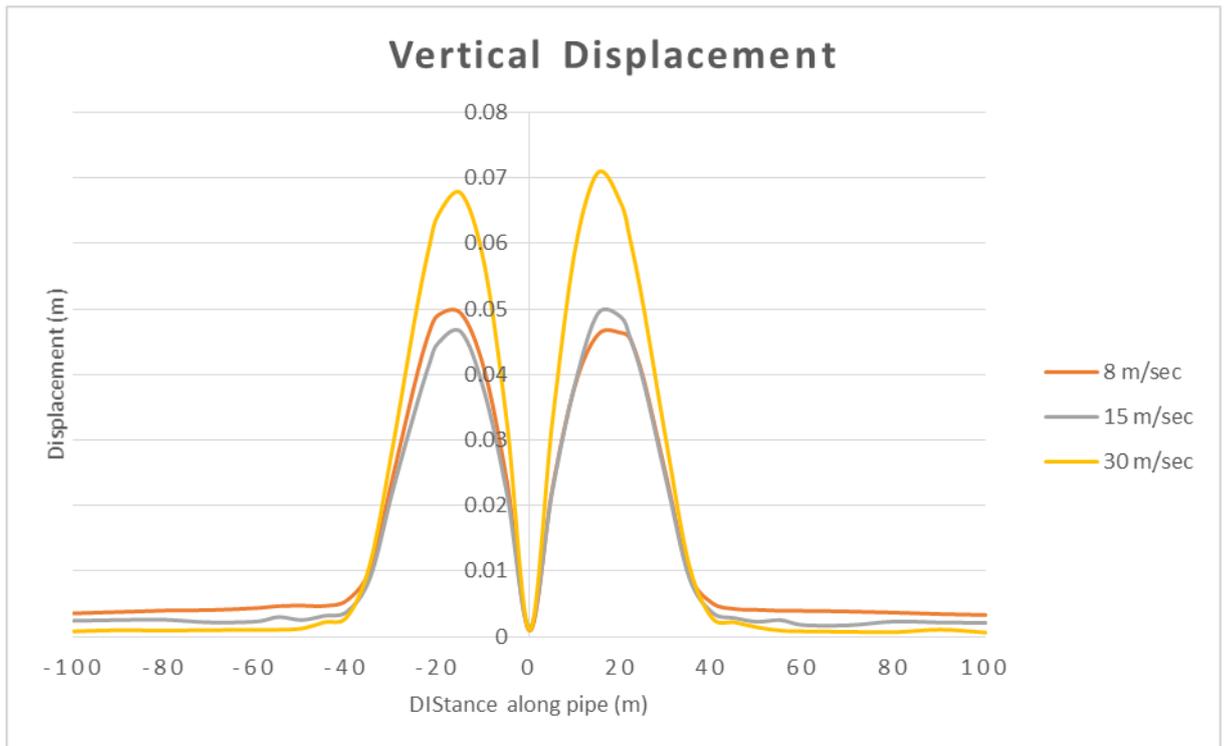
Figure 10-9 Maximum vertical span deflection across the span length as the force traverses the span. Centrifugal force not included.

363
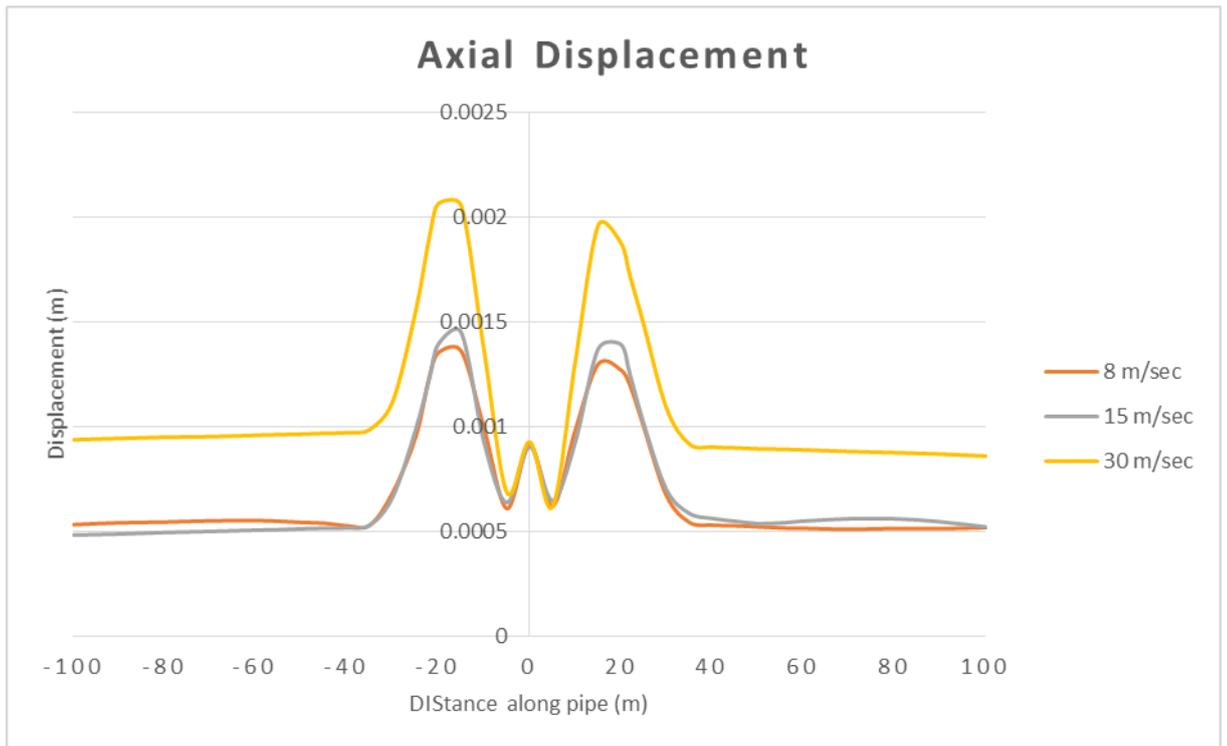
Figure 10-10 Maximum horizontal span deflection across the span length as the force traverses the span. Centrifugal force included.
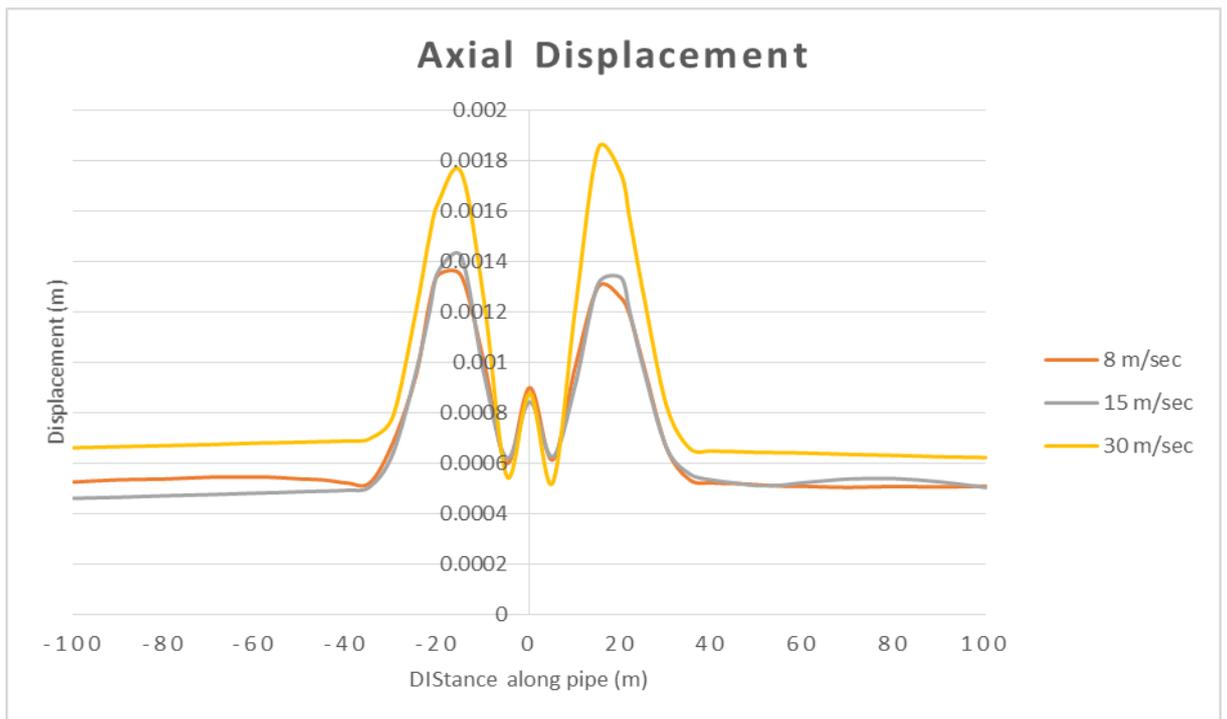
Figure 10-11 Maximum horizontal span deflection across the span length as the force traverses the span. Centrifugal force not included.
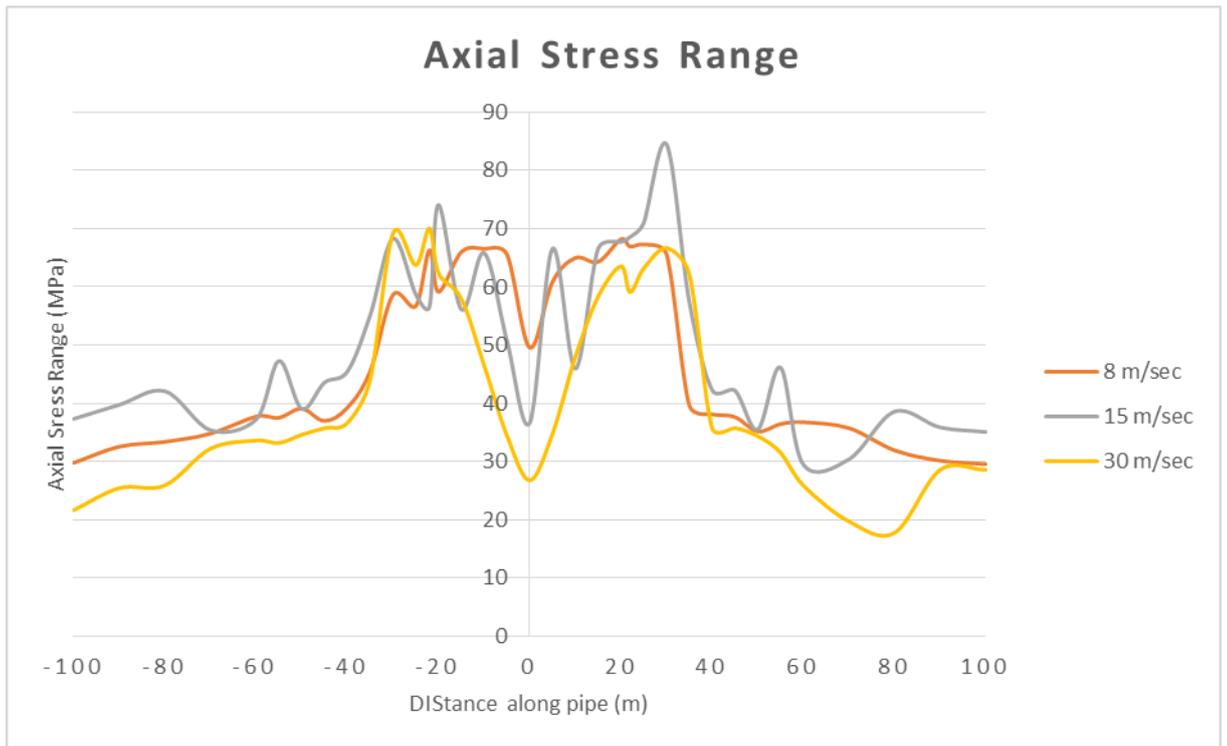
Figure 10-12 Maximum axial stress range across the span length as the force traverses the span. Centrifugal force included.
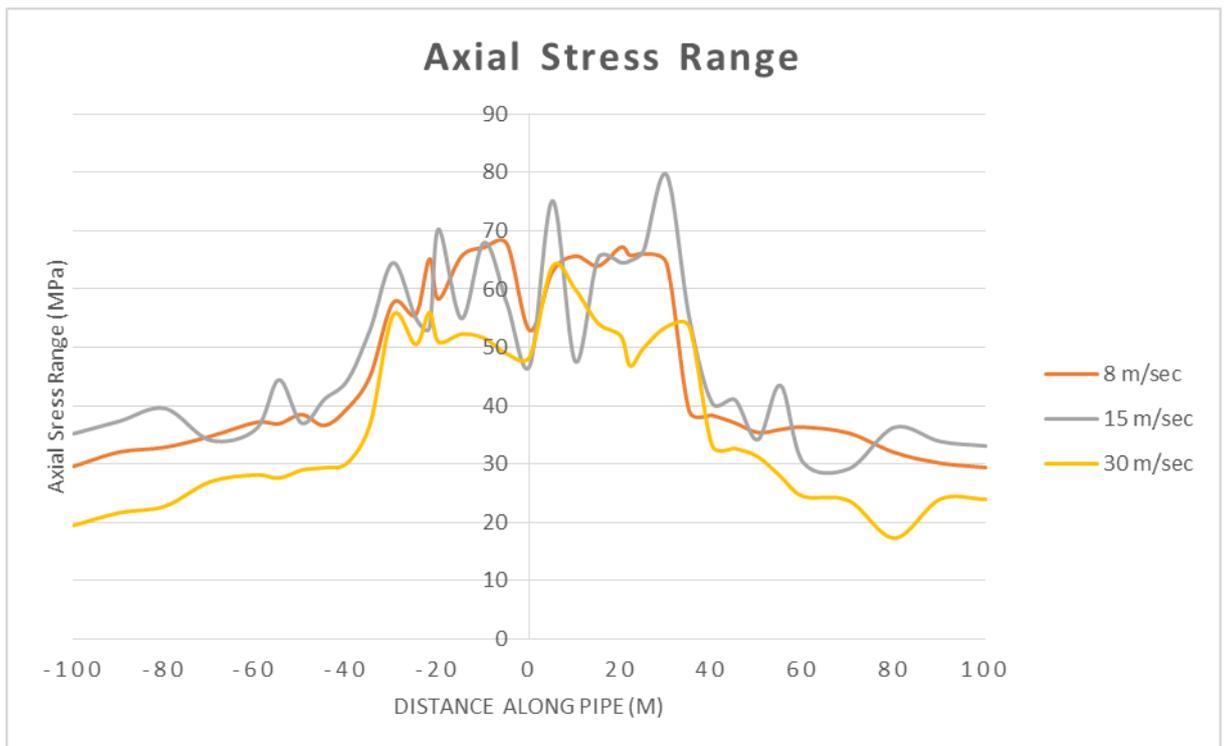
Figure 10-13 Maximum axial stress across the span length as the force traverses the span. Centrifugal force not included.

11   Conclusions and Recommendations

11.1 CONCLUSIONS

Topic 1: Compression Limit of High Voltage alternating Current Cables

1. The increase in demand for cable installation under difficult environmental conditions, in areas with high concentrations of subsea assets, as well as the costs involved with the usage of vessels, place stringent demands on understanding the compression limits of subsea cables.

2. During the dynamic installation analysis, it was discovered that the bare cable experienced high compression loads at the touchdown point as well as at the sag-bend due to the presence of articulated padding.

3. The vast majority of subsea cables are designed to function without any problems under their allowable tensions. However, under compression loads, the cable tends to deflect over any free length. When the subsea cable deflects under the compression load, the steel armours will become slightly unstable in torsion and the cable may kink into a loop depending on the cable length paid out from the installation vessel.

4. This thesis developed an empirical method for determining axial compression in a given cable, which can also be applied to other cable cross-sections and designs. A new test arrangement for the compression was presented herein. This compression method can be implemented in future projects to determine the axial compression limits of the subsea cable.

5. The test arrangement can be presented by CIGRE and DNVGL recommendations for subsea cables. The same test can also be used to determine the allowable compression limits of subsea umbilicals and flexible pipes.

6. The allowable compression limit data needs to be made available as part of the supply data for the installation and on-bottom stability analyses of the subsea cable.

7. The test shows that the axial compression limit can be taken as 10–12% of the allowable tension on the allowable minimum bend radius. It should be highlighted that the results presented in this thesis are for 3 Phase HVAC cables. A direct current, DC, cable which has a single internal core will probably behave differently in the given testing regime due to its different cable assembly lay-up. Nevertheless, the new test arrangements presented in this thesis can be used to determine the allowable compression limit for any subsea cable with any cable assembly lay-up.

8. The allowable axial compression loads can be determined using the proposed bending test. However, pure axial compression limits cannot be used on their own in case the cable is subjected to bending in conjunction with tension. For pure axial compression, Euler buckling theory can be used to determine the pure axial compression limits after considering a safety factor. The safety factor represents the worst compression case seen in the cable where the effect of the steel armour is negligible.

9. It was essential after conducting the axial compression test to determine whether the cable sample was damaged during the test. A high voltage test would be an appropriate way to ensure that the integrity of the cable was not jeopardised. However, in practice, high voltage testing is impossible due to the cable sample length and available resources.

10. This thesis presented steps which could be adopted during the visual inspection of a subsea cable cross-section.

11. It was found that the axial stiffness in compression was 32 times slower than the axial stiffness in tension. Hence, it is recommended that analyses should use different values for the axial stiffness whether it is for tension or compression. This is to obtain realistic results for the compression loads.

12. Cable and umbilical manufacturers can use the results presented herein and from future tests to develop analytical models to determine allowable axial compression

limits. The analytical model can be calibrated by gathering test results from several umbilicals and cables.

Topic 2: Development of a Testing Scheme to Improve Cable-Joint Integrity:

1. This thesis presents a set of standardised onshore testing regimes which improves both the reliability and affordability of cable joints implied.

2. The thesis presents the design process which involves a series of steps. These design steps can be followed to determine the loads which can be applied during the onshore testing to mimic the installation conditions for in-line rigid joints. Also, an analytical method is presented to calculate the loads experienced by the in-line joint during deployment.

3. The new testing arrangement uses the design loads, determined from the engineering simulations, to test the offshore rigid joint on-land, simulating the actual installation conditions. Once the load tests are completed, the joint, including the plumbing area, is subjected to a water penetration test. In the water radial penetration test, one pre-moulded joint, including plumbing areas, is submerged in pressurised water for 24 hours. This is followed by an examination to detect seawater ingress where a visual inspection is conducted of the plumbing area between the cable lead sheath and copper housing. This is to ensure that the plumbing area is clear of any cracks or holes.

4. It is possible that the seawater ingress potential would be greater when the joint is loaded and under external pressure, than in the simulation where the loads on the joint are applied on-land with the radial water penetration test conducted only after and without loading. To overcome this issue the external pressure employed in the RWP corresponds to the maximum water depths along the pipeline plus an additional 50 m. This is consistent with Electra 171 (1997) that recommend employing an external pressure in the RWP corresponding to the maximum water depths along the cable plus 50 m in the case where the water depth is less than 500 m and maximum water depth plus 100 m for water depths over 500 m.

5. The new testing arrangement offers an alternative to subsea immersion testing for subsea cable joints and offshore deployment simulations.

6. This thesis summarizes a rigid cable joint onshore testing scheme for Omega deployment. The proposed testing scheme can be employed to confirm that the integrity of the offshore field joint during the deployment process is not compromised.

7. The proposed testing platform for Omega deployment uses the design loads, determined from finite element analysis, to qualify the joint on land. After the load tests are applied the joint is subjected to a water penetration test

8. The proposed testing arrangements can be used to replace the sea simulations and trials to determine if the proposed field jointing procedure is acceptable. The test could be implemented in conjunction with the typical mechanical tests listed in CIGRE TB 490 (2012).

Topic 3: Design and Installation of Subsea Cable, Pipeline and Umbilical Crossing Interfaces:

1. The crossing analysis performed has established there is a strong link between radial and axial loads, vertical and horizontal support placement and lateral movement of the crossing.

2. The coating at the field joint can get damaged due to high radial and axial loads combined with high residual lay tension. The radial and axial loads are the results of the interaction between the free span and the lateral movement.

3. It was found that industry accepted standards, related to the design and construction of submarine cable crossings, do not provide guidance for the case in which the crossed pipeline is used as a support. The industry standards also do not consider the consequence of field joints being in close proximity to the crossing.

4. It is recommended that industry consider revising the relevant codes and practices to emphasise the potential risks of installing a crossing near a field joint and to recommend undertaking dynamic analyses of the crossing line.

369

5. In the case where the crossed pipeline is used as a support, it is important to ensure that the crossing pipeline/cable/umbilical does not bear on the field joint of the crossed pipeline. The contact load and lateral movement under severe environmental loading conditions can compromise the integrity of the field joint coating.

6. During the pre-lay survey of the crossed pipeline and the seabed, it is essential to survey the proposed crossing point to ensure that it is not at a field joint. As part of the crossing agreement, it is important that the owner of the crossing umbilical or cable obtains the installation pipe tally sheet which contains the coordinates of the field joints of the existing, crossed pipeline. However, for the pipelines installed using first generation barges, the tally sheet may not include the coordinates of the field joints. In this case, additional efforts are needed by installation contractors to identify field joint locations during routing surveys. The industry may require practical ways to determine the location of the field joint in reference to the crossing point. This may be by close inspection of the site using a competent ROV and instrumentation.

7. The results presented in this thesis enable the pipeline designer to relate to the contact loads and cable tensions that can cause field joint coating damage if they need to check their own crossing designs. As older pipelines do not include a sheet steel cover on the field joints, damage will be greater on those than on modern field joint coating systems.

8. The articulated padding is a good crossing design concept especially for the subsea cable and umbilical. However, it is important to ensure that the material used for the articulated padding can accommodate repeated lateral movement.

Topic 4: Pipeline walking and Anchoring Considerations in the Presence of Riser Motion and Inclined Seabed:

1. This thesis utilized finite element modelling to evaluate the interaction between the SCR and the pipeline system, in order to 1) quantify the rate of walking and expansion towards the SCR under different loading conditions, 2) understand the

370

mechanisms driving the walking, and 3) make recommendations for the pipeline, subsea structures and SCR designs to ensure the integrity of both the pipeline system and the SCR are not compromised.

2. It is evident from the results that the walking due to SCR bottom tension is the dominant walking mechanism and can exceed other walking mechanisms associated with thermal transients and seabed slope. For a short pipeline, in the range of 2- 3km, where there is no lateral buckling, it is recommended to install the anchor at the PLET side and away from the SCR transition point.

3. It is important for the SCR/ pipeline system design to ensure that the maximum expansion towards the SCR is controlled and kept below the allowable axial feed-in towards the SCR as this may result in comprising the integrity of the SCR.

4. The studies conducted herein show that there may be conflicting requirements between the anchor loads imposed by the SCR and the pipeline operating loads. For instance, the SCR design normally assumes that the maximum anchor load will take place during extreme storm conditions. The research contained herein show that this is not always the case. It was demonstrated that the maximum anchor loads occur during storm conditions except for the case when an anchor is installed at the PLET side. In this case, the maximum anchor load takes place during the unloading operational cycle rather than during extreme storm scenarios. For the anchor at the PLET, the load on the anchor changes or is cyclic.

5. This thesis also highlighted that the anchor location, in reference to the SCR, has a significant impact on the load imposed on the anchor. Additionally, the load imposed on the anchor is driven by the SCR anchor configuration, vessel execution, pipeline operating conditions and the pipeline expansion and walking behaviour. Fatigue loading on the SCR anchors, due to pipeline start-up and shut-down events and SCR tension variations, should be evaluated during the anchoring system design.

6. In this thesis, a roadmap was presented to determine requirements for anchoring a short pipeline connected to a SCR in the absence of lateral buckling. Figure 11-1 illustrates a flowchart that can be used to determine the necessity of a hold-back anchor of a short pipeline connected to a SCR with no lateral buckling.

7. For a short pipeline connected to the SCR, the on-bottom SCR tension was shown to dominate the walking behaviour over both the thermal transient effects and seabed sloping.

8. The expansion towards the SCR should be minimised, as this can result in shifting at the touchdown point, which can eventually reduce the static tension in the SCR and change the curvature in the sag-bend region.

9. During the design stages, it is important to determine the requirements of anchoring to arrest the axial walking. This is in order to guarantee the integrity of the tie-in spool between the PLET and manifold is not compromised.

10. Excessive SCR tension associated with storm conditions may result in route curve pull-out, which could lead to significant implications on the field layout.

Topic 5: Pipeline Slug Flow Dynamic Load Characterization.

1. The results presented herein act as a guideline for the complex analysis required for a particular span and slug flow arrangement before any dynamic analysis is entered into, if in fact it is even deemed necessary.

2. The results presented in this thesis cover a wide range of applications such as railways, road bridges and many other structural situations that involve a moving load problem. The results show the differences between a moving concentrated force and a moving concentrated mass model for a simply supported beam. Based on the results presented, three loading categories are proposed:

   - **Zone A:** no dynamic analysis needs to be undertaken. A design chart for a set of pipe schedules comparing slug speed and span length for various pipe geometries is given such that it can be easily determined if a set of speed/length scenarios will lie within this first loading category.

   - **Zone B:** moving force analysis should be undertaken.

   - **Zone C:** moving mass analysis should be undertaken.

;

Figure 11-1: Anchoring Requirements

3. The acceptable deviation limit from the full dynamic response can be set as desired. In this thesis, a limit of 10% under-prediction was set, resulting in the following loading category zone limits.

- **Zone A:** no dynamic analysis needs to be undertaken. Slug speed is below 0.175 non-dimensional critical speed of the span, and is valid for any slug/span mass ratio.

- **Zone B**: moving force analysis should be undertaken. Slug speed is greater than 0.175 non-dimensional critical speed of the span, and the slug/span mass ratio is less than 0.2.

- **Zone C:** moving mass analysis should be undertaken. Slug speed is greater than 0.175 non-dimensional critical speed of the span, and the slug/span mass ratio is greater than 0.2.

4. It is crucial to highlight that all the conclusions derived in this paper are only valid for free spans into the regime of span length to outside diameter (L/OD) ratios that are less than 100. It is envisaged that future studies will deal with the extension for free spans into the regime of higher L/OD ratios.

5. Within this thesis, internal pipeline slug flow was modelled as a moving force across a pipeline span, with the effect of the span out of straightness specifically investigated.

6. The effect of span out of straightness causes centrifugal forces and must be included due to fact that the moving slug follows a curved path. The severity of the centrifugal force impact was shown to be a function of both the slug velocity and the span out of straightness.

7. A non-dimensional centrifugal force parameter, γ, was developed which can be used to assess whether the combination of out of straightness and slug velocity will have any appreciable influence on the pipeline vibration over and above that of a straight pipe span.

8. The results showed that for a non-dimensional centrifugal force parameter, $\gamma < 10\%$, the out of straightness has little effect. Additionally, the stress pattern over the pipeline span is relatively complex even if $\gamma < 10\%$, indicating that if detailed stress values are required across the pipeline, a finite element analysis with a transient force applied due to the slug motion should be conducted.

11.2 RECOMMENDATIONS FOR FURTHER STUDIES

The following recommendations are presented for further research:

1- It is recommended to use the results from the testing of the full-scale axial compression to validate a three-dimensional finite element model. Once there is a good correlation between the full-scale testing and the finite element model, the finite element model can be used to establish a parametric assessment to understand the importance of some parameters such as friction/contact between the components of the cable.

2- The testing of the full-scale axial compression should be extended for other cable sizes to understand the consequences of excessive compression on the integrity of subsea cables.

3- The proposed testing arrangement for determining the axial compression limit of subsea cables should be implemented in the relevant standards and codes.

4- More studies should be undertaken to understand the requirements of anchoring medium and long pipelines.

5- The impact of the dynamic SCR tension on a lateral buckle, in the proximity of a SCR, in terms of fatigue should be investigated.

6- The available analytical walking models should be updated to account for the axial mobilization distance.

7- The pipeline and cable standard should be updated to cover the scenario where the crossed pipeline is used as a support in cable and umbilical crossings.

8- Standards and codes for on-bottom stability requires that zero-lateral movement at the crossing locations occurs. Based on the findings herein, it was concluded that achieving zero lateral movement at the crossing locations for the cable or umbilical is difficult. These are for the cases where the crossed pipeline is used as a support. It is thus important that the stability criteria at the crossing location is updated.

9- Investigate the effects of axial forces and initial sagging on the dynamic response of a horizontal pipeline span under the slug flow.

10- Assess the effect of the pipe/soil friction on the dynamic response of a horizontal pipeline span under the slug flow.

11- Investigate the phenomenon of vibration cancellation and resonance for a pipeline span operating under a series of slugs.

12- Develop a finite element formulation to assess the dynamic response of curved beams under a distributed load.

12 Reference

1. Worzyk, T. (2009). Submarine power cables: design, installation, repair, environmental aspects. Springer Science & Business Media.

2. Reda, A. M., Forbes, G. L., Al-Mahmoud, F., Howard, I. M., McKee, K. K., & Sultan, I. A. (2016). Compression limit state of HVAC submarine cables. Applied Ocean Research, 56, 12-34.

3. Reda, A., Howard, I. M., Forbes, G. L., Sultan, I. A., & McKee, K. K. (2017). Design and installation of subsea cable, pipeline and umbilical crossing interfaces. Engineering Failure Analysis, 81, 193-203.

4. Manual, OrcaFlex (2014). "Version 9.8 a." Cumbria: Orcina, Ltd.

5. Bectarte, F., & Coutarel, A. (2004). Instability of tensile armour layers of flexible pipes under external pressure. In International Conference on Offshore Mechanics and Arctic Engineering (Vol. 37459, pp. 155-161).

6. CIGRÉ TB 490 (2012). Recommendations for testing of long AC submarine cables with extruded insulation for system voltage above 30 (36) to 500 (550) kV.

7. Knouk, I. (1998). Expansion of pipelines under cyclic operational conditions: Formulation of problem and development of solution algorithm. In OMAE 1998: 17 th International Conference on Offshore Mechanics and Arctic Engineering (p. 1998).

8. Tørnes, K., Ose, B. A., Jury, J., & Thomson, P. (2000, February). Axial creeping of high temperature flowlines caused by soil ratcheting. In Proceedings of the Conference on Offshore Mechanics and Arctic Engineering, ASME, OMAEPIPE5055.

9. Reda, A. M., Forbes, G. L., & Sultan, I. A. (2011). Characterisation of Slug Flow Conditions in Pipelines for Fatigue Analysis. In International Conference on Offshore Mechanics and Arctic Engineering (Vol. 44366, pp. 535-547).

10. Cooper, P., Burnett, C., & Nash, I. (2009). Fatigue design of flowline systems with slug flow. In International Conference on Offshore Mechanics and Arctic Engineering (Vol. 43437, pp. 207-212)

11. Electra 171 (1997). Recommendations for Mechanical Tests on Submarine cables.

12. Feld, G., Owen, D. G., Reuben, R. L., & Crockett, A. E. (1995). Mechanical behaviour of the metallic elements of submarine cables as a function of cable loading. Engineering structures, 17(4), 240-253.

13. DNV-RP-J301(2014). Subsea power cables in shallow water renewable energy applications.

14. IEEE Standard 1120 (2004). "Guide for the Planning, Design, Installation, and Repair of Submarine Power Cable Systems".

15. ISO-13628-5 (2009). "Design and operation of subsea production systems-Part-5: Subsea umbilicals".

16. API-RP-17B (2014) . Recommended practice for flexible pipe.

17. API-RP-17J (2014). Specification for Unbonded Flexible Pipe.

18. McCann, D., Smith, F., & O'Brien, P. (2003). Guidelines for compression modeling in flexible risers for deepwater applications. In Offshore Technology Conference. Offshore Technology Conference.

19. MCS - Marine Computational Services (1999): "FLEXCOM-3D Non-linear Three-Dimensional Time Domain Finite Element Analysis Software", Version 5.1.

20. Clarkston, B., Valenzuela, E., Worman, P. J., & Williams, P. (2009). Frade Field Dynamic Umbilicals Design and Testing. In Offshore Technology Conference. Offshore Technology Conference.

21. Alexander, W. L., Wu, M., & Chang, S. H. M. (1999). Dynamic performance comparison of deepwater riser systems for a turret-moored FPS. In Offshore Technology Conference. Offshore Technology Conference.

22. Nesje, J. D., Aggarwal, R. K., Petrauskas, C., Vinnem, J. E., Keolanui, G. L., Hoffman, J., & McDonnell, R. (1999). Risk assessment technology and its application to tanker based floating production storage and offloading (FPSO) systems. In Offshore Technology Conference. Offshore Technology Conference.

23. Yasseri, R., Yasseri, S., & Wang, B. (2014). Integrity of subsea control umbilical. In International Conference on Offshore Mechanics and Arctic Engineering (Vol. 45462, p. V06AT04A053). American Society of Mechanical Engineers.

24. Aranha, J. A. P., Pinto, M. O., & Da Silva, R. M. C. (2001). On the dynamic compression of risers: an analytic expression for the critical load. Applied ocean research, 23(2), 83-91.

25. Rabelo, M. A., Pesce, C. P., Santos, C. C., Junior, R. R., Franzini, G. R., & Neto, A. G. (2015). An investigation on flexible pipes birdcaging triggering. Marine Structures, 40, 159-182.

26. Marta, M., Mueller-Schuetze, S., Ottersberg, H., Isus, D., Johanning, L., & Thies, P. R. (2015). Development of dynamic submarine MV power cable design solutions for floating offshore renewable energy applications.

27. DNV-RP-F401 (2012). Electrical power cables in subsea applications.

28. Balena, R., & Williams, P. (2009). Risk-based structural analysis of frade umbilical cables. In 20th International Congress of Mechanical Engineering.

29. Loos, B. (2017). Operability limits based on vessel motions for submarine power cable installation.

30. International Cable Protection Committee (2009). Damage to submarine cables caused by anchors. Loss Prevention Bulletin.

31. Reda, A. M., Al-Yafei, A. M. S., Howard, I. M., Forbes, G. L., & McKee, K. K. (2016). Simulated in-line deployment of offshore rigid field joint–A testing concept. Ocean Engineering, 112, 153-172.

32. CIGRE, T. (2009). 379 Update of service experience of HV underground and submarine cable systems. WG B1-10.

33. Skog, J. E., Van Asten, H., Worzyk, T., & Andersrød, T. (2010). NorNed – World's longest power cable. CIGRE Session, Paris, France.

34. Karlsdóttir, S. H. (2013). Experience in transporting energy through subsea power cables: The case of Iceland (Doctoral dissertation).

35. Reda, A., Abu-Siada, A., Howard, I. M., & McKee, K. K. (2019). A testing platform for subsea power cable deployment. Engineering Failure Analysis, 96, 142-157.

36. Electra 189 (2000). Recommendations for tests of power transmission DC cables for a rated voltage up to 800 kV.

37. Woo, J., Kim, D., & Na, W. B. (2015). Safety analysis of rock berms that protect submarine power cables in the event of an anchor collision. Ocean Engineering, 107, 204-211.

38. Yoon, H. S., & Na, W. B. (2013). Safety assessment of submarine power cable protectors by anchor dragging field tests. Ocean engineering, 65, 1-9.

39. Skog, J. E., Van Asten, H., Worzyk, T., & Andersrød, T. (2010). NorNed – World's longest power cable. CIGRE Session, Paris, France.

40. The CIGRE Paper (1986). Methods to Prevent Mechanical Damage to Submarine Cables, presented by Cigré Working Group 21 as Session Paper 21-12 at the 1986 Cigré Session, Paris, France.

41. Rosevear, R. D., Choquette, M., Fairhurst, M., Jorgensen, H. J., Larsen, J. E., Mampeay, B., ... & Waschk, V. (2009). Update of service experience of HV underground and submarine cable systems. CIGRE TB, 379, 1-84.

42. Ventikos, N., & Stavrou, D. I. (2013). Submarine power cables: laying procedure, the fleet and reliability analysis. Journal of Marine Engineering & Technology, 12(1), 13-26.

43. Featherstone, J., Cronin, A., Kordahi, M., & Shapiro, S. (2001). Recent trends in submarine cable system faults. In Proceedings SubOptic.

44. Ericsson, A., Thunwall, B., Gustafsson, A., & Svahn, J. (2003). Qualification of a highly electrically and mechanically stressed AC cable system. In Proceedings JICABLE (pp. 38-43).

45. Palmer, A. C., & King, R. A. (2004). Subsea pipeline engineering. PennWell Books.

46. Bai, Q., & Bai, Y. (2014). Subsea pipeline design, analysis, and installation. Gulf Professional Publishing.

47. Standard, D.O., DNVGL-ST-F101 (2017). "Submarine Pipeline Systems." Det Norske Veritas, Norway.

48. API RP-1111 (2015). Construction, Operation, and Maintenance of Offshore Hydrocarbon Pipelines (Limit State Design).

49. ISO 15589-2 (2012). Petroleum, petrochemical and natural gas industries -- Cathodic protection of pipeline transportation systems -- Part 2: Offshore pipelines.

50. ISO 13623 (2009). Petroleum, petrochemical and natural gas industries -- Pipeline transportation systems.

51. ICPC (2014). Recommendation 3 Telecommunications Cable and Oil Pipeline / Power Cables Crossing Criteria.

52. Reda, A., Forbes, G., McKee, K., & Howard, I. (2014). Vibration of a curved subsea pipeline due to internal slug flow. In Proceedings of the 43rd International Congress on Noise Control Engineering. Australian Acoustical Society.

53. Reda, A., Sultan, I. A., Howard, I. M., Forbes, G. L., & McKee, K. K. (2018). Pipeline walking and anchoring considerations in the presence of riser motion and inclined seabed. International Journal of Pressure Vessels and Piping, 162, 71-85.

54. Reda, A., McKee, K. K., Howard, I. M., & Sultan, I. A. (2019). When is a subsea anchor required for a short pipeline/SCR system?. International Journal of Pressure Vessels and Piping, 171, 278-298.

55. Guha, I., White, D. J., & Randolph, M. F. (2019). Subsea pipeline walking with velocity dependent seabed friction. Applied Ocean Research, 82, 296-308.

56. Bruton, D. A., Bolton, M., Carr, M., & White, D. (2008, January). Pipe-soil interaction with flowlines during lateral buckling and pipeline walking-The SAFEBUCK JIP. In Offshore Technology Conference. Offshore Technology Conference.

57. Perinet, D., & Simon, J. (2011, January). Lateral buckling and pipeline walking mitigation in deep water. In Offshore Technology Conference. Offshore Technology Conference.

58. Carr, M., Bruton, D., & Leslie, D. (2003). Lateral buckling and pipeline walking, a challenge for hot pipelines. In Offshore Pipeline Technology Conference (pp. 1-36).

59. Carr, M., Sinclair, F., & Bruton, D. (2006). Pipeline walking-understanding the field layout challenges, and analytical solutions developed for the SAFEBUCK JIP. In Offshore technology conference. Offshore Technology Conference.

60. Bruton, D. A., Carr, M., Sinclair, F., & MacRae, I. (2010). Lessons learned from observing walking of pipelines with lateral buckles, including new driving mechanisms and updated analysis models. In Offshore technology conference. Offshore Technology Conference.

61. Phifer, E. H., Kopp, F., Swanson, R. C., Allen, D. W., & Langner, C. G. (1994). Design and installation of auger steel catenary risers. In Offshore Technology Conference. Offshore Technology Conference.

62. Quintin, H., Legras, J. L., Huang, K., & Wu, M. (2007). Steel catenary riser challenges and solutions for deepwater applications. In Offshore technology conference. Offshore Technology Conference.

63. Drumond, G. P., Pasqualino, I. P., Pinheiro, B. C., & Estefen, S. F. (2018). Pipelines, risers and umbilicals failures: A literature review. Ocean Engineering, 148, 412-425.

64. Wu, M., & Huang, K. (2007). The Comparison of Various SCR Configurations for Bow Turret Moored FPSO in West Africa. In The Seventeenth International Offshore and Polar Engineering Conference. International Society of Offshore and Polar Engineers.

65. Belik, M. (2016). Innovative developments and managerial factors as key enablers of deepwater riser project delivery (Master's thesis, University of Stavanger, Norway).

66. Ogbeifun, A. M., Oterkus, S., Race, J., Naik, H., Decnop, E., & Dakshina, M. (2019, June). The Branched Riser Systems: Concept Development. In International Conference on Offshore Mechanics and Arctic Engineering (Vol. 58813, p. V05BT04A029). American Society of Mechanical Engineers.

67. Mekha, B., & Bhat, S. (2013). Newer frontiers in the design of steel catenary risers for floating production systems. In International Conference on Offshore Mechanics and Arctic Engineering (Vol. 55379, p. V04BT04A056). American Society of Mechanical Engineers.

68. Mansour, A. M., Bhat, S., Pasala, D., & Kumar, D. (2014). Field development using semisubmersible floating production system with steel catenary risers in Western Australia harsh environment. In Offshore Technology Conference. Offshore Technology Conference.

69. Clukey, E. C., & Zakeri, A. (2017). Recent advances in nonlinear soil models for fatigue evaluation of steel catenary risers SCRs. In Offshore Technology Conference. Offshore Technology Conference.

70. Shoghi, R., & Shiri, H. (2019). Modeling touchdown point oscillation and its relationship with fatigue response of steel catenary risers. Applied Ocean Research, 87, 142-154.

71. Taheri, A., & Siahtiri, R. (2017). Steel Catenary Riser-Seabed Interaction Due to Caspian Sea Environmental Conditions. Journal of Rehabilitation in Civil Engineering, 5(2), 36-48.

72. Serta, O. B., Mourelle, M. M., Grealish, F. W., Harbert, S. J., & Souza, L. F. A. (1996, January). Steel catenary riser for the marlim field FPS P-XVIII. In Offshore Technology Conference. Offshore Technology Conference.

73. Wang, J., Fu, S., Baarholm, R., Wu, J., & Larsen, C. M. (2014). Fatigue damage of a steel catenary riser from vortex-induced vibration caused by vessel motions. Marine Structures, 39, 131-156.

74. Wang, J., Fu, S., Baarholm, R., Wu, J., & Larsen, C. M. (2015). Out-of-plane vortex-induced vibration of a steel catenary riser caused by vessel motions. Ocean Engineering, 109, 389-400.

75. Elosta, H., Huang, S., & Incecik, A. (2013). Dynamic response of steel catenary riser using a seabed interaction under random loads. Ocean Engineering, 69, 34-43.

76. Li, F. Z., & Low, Y. M. (2012). Fatigue reliability analysis of a steel catenary riser at the touchdown point incorporating soil model uncertainties. Applied Ocean Research, 38, 100-110.

77. Shiri, H. (2014). Response of steel catenary risers on hysteretic non-linear seabed. Applied ocean research, 44, 20-28.

78. Hawlader, B., Dutta, S., Fouzder, A., & Zakeri, A. (2015). Penetration of steel catenary riser in soft clay seabed: finite-element and finite-volume methods. International Journal of Geomechanics, 15(6), 04015008.

79. Reda, A., & Forbes, G. (2012). Investigation into the dynamic effects of lateral buckling of high temperature/high pressure offshore pipelines. Proceedings of Acoustics 2012-Fremantle.

80. Sultan, I. A., Reda, A. M., & Forbes, G. L. (2012). A Surrogate Model for Evaluation of Maximum Normalized Dynamic Load Factor in Moving Load Model for Pipeline Spanning due to Slug Flow. In International Conference on Offshore Mechanics and Arctic Engineering (Vol. 44908, pp. 601-610). American Society of Mechanical Engineers.

81. Sultan, I. A., Reda, A. M., & Forbes, G. L. (2013). Evaluation of slug flow-induced flexural loading in pipelines using a surrogate model. Journal of offshore mechanics and Arctic engineering, 135(3).

82. Reda, A. M., Forbes, G. L., & Sultan, I. A. (2012). Characterization of Dynamic Slug Flow Induced Loads in Pipelines. In International Conference on Offshore Mechanics and Arctic Engineering (Vol. 44908, pp. 185-197). American Society of Mechanical Engineers.

83. Reda, A., & Forbes, G. (2011). The effect of distribution for a moving force. Proceedings of Acoustics 2011.

84. Rieker, J. R., & Trethewey, M. W. (1999). Finite element analysis of an elastic beam structure subjected to a moving distributed mass train. Mechanical Systems and Signal Processing, 13(1), 31-51.

85. Rieker, J. R., Lin, Y. H., & Trethewey, M. W. (1996). Discretization considerations in moving load finite element beam models. Finite elements in analysis and design, 21(3), 129-144.

86. Casanova, E., Pelliccioni, O., & Blanco, A. (2009). Fatigue life prediction due to slug flow in extra long submarine gas pipelines using fourier expansion series. In International Conference on Offshore Mechanics and Arctic Engineering (Vol. 43437, pp. 549-557).

87. Casanova, E., & Blanco, A. (2010). Effects of soil non-linearity on the dynamic behavior and fatigue life of pipeline spans subjected to slug flow. In International Conference on Offshore Mechanics and Arctic Engineering (Vol. 49132, pp. 185-192).

88. Kansao, R., Casanova, E., Blanco, A., Kenyery, F., & Rivero, M. (2008). Fatigue life prediction due to slug flow in extra long submarine gas pipelines. In International Conference on Offshore Mechanics and Arctic Engineering (Vol. 48203, pp. 685-692).

89. Lin, Y. H., & Trethewey, M. W. (1990). Finite element analysis of elastic beams subjected to moving dynamic loads. Journal of sound and vibration, 136(2), 323-342.

90. DNV, G., DNV-RP-C205 (2014). Environmental conditions and environmental loads. DNV GL, Oslo, Norway.

91. GL Noble Denton (2016). 0030/ND Guidelines for Marine Transportation.

92. Gere, J. M., & Timoshenko, S. P. (1984). Mechanics of Materials 2nd edn (Monterey, CA: Brooks/Cole Engineering Division).

93. Ju, G. T., & Kyriakides, S. (1992). Bifurcation and localization instabilities in cylindrical shells under bending—II. Predictions. International journal of solids and structures, 29(9), 1143-1171.

94. ABAQUS, U. S. M. (2012). Version 6.12. Dassault Systemes Simulia Corp, Rhode Island, USA.

95. Attwood, J. R., Dickinson, M., Gregory, B., Hampton, R. N., & Svoma, R. (1998). Development of high stress HV and EHV XLPE cable systems. In Cigré.

96. IEC 60840 (2011). Power Cables with Extruded Insulation and Their Accessories for Rated

Voltages above 30 kV (Um = 36 kV) up to 150 kV (Um = 170 kV) – Test Methods and Requirements.

97. DNVGL-RP-F110 (2019). Global Buckling of Submarine Pipelines, Structural Design due to High Temperature/High Pressure.

98. DNVGL-RP-F105 (2017). Free spanning pipelines.

99. Standard, DNV Offshore (2016). "DNVGL-OS-F201." Dynamic Risers, Det Norske Veritas.

100. API (2013). STD. "2RD,"." Dynamic Risers for Floating Production Systems".

101. BS-7910 (2013). British Standards Institution. Guide on methods for assessing the acceptability of flaws in metallic structures. British Standard Institution.

102. David Colliard, Jérôme Anton (2006). Lessons learned from the design and installation of suction piles in West Africa, DOT.

103. Perinet, D., & Frazer, I. (2006). Mitigation methods for deepwater pipeline instability induced by pressure and temperature variations. In Offshore Technology Conference. Offshore Technology Conference.

104. Forbes, G. L., & Reda, A. M. (2013). Influence of axial boundary conditions on free spanning pipeline natural frequencies. In International Conference on Offshore Mechanics and Arctic Engineering (Vol. 55362, p. V04AT04A017). American Society of Mechanical Engineers.

105. Wu, J. J., Whittaker, A. R., & Cartmell, M. P. (2000). The use of finite element techniques for calculating the dynamic response of structures to moving loads. Computers & Structures, 78(6), 789-799.

106. Przemieniecki, J. S. (1985). Theory of matrix structural analysis. Courier Corporation.

107. Havre, K., Stornes, K. O., & Stray, H. (2000). Taming slug flow in pipelines. ABB review, 4, 55-63.

Appendix-1 (Paper-1)

https://www.sciencedirect.com/science/article/abs/pii/S0141118716000031

Appendix-2 (Paper-2)

https://www.sciencedirect.com/science/article/abs/pii/S0029801815006733

Appendix-3 (Paper-3)

Appendix-4 (Paper-4)

Appendix-5 (Paper-5)

https://www.sciencedirect.com/science/article/abs/pii/S0308016117303824

Appendix-6 (Paper-6)

https://www.sciencedirect.com/science/article/abs/pii/S0308016118304204

Appendix-7 (Paper-7)

Appendix-8 (Paper-8)

Appendix-9 (Co-authors' Attribution Statements)